On Prediction of Wave-Induced Loads and Vibration of Ship Structures with Finite Volume Fluid Dynamic Methods

Von der Fakultät für Ingenieurwissenschaften,
Abteilung Maschinenbau und Verfahrenstechnik,
der Universität Duisburg-Essen
zur Erlangung des akademischen Grades
eines Doktors der Ingenieurwissenschaften
Dr.-Ing.
genehmigte Dissertation

von

Jan Oberhagemann
aus
Braunschweig

Gutachter: Univ.-Prof. Dr.-Ing. Ould el Moctar
Univ.-Prof. Dr.-Ing. Heinrich Söding (emerit.)
Univ.-Prof. Ph.D. Odd Magnus Faltinsen

Tag der mündlichen Prüfung: 17. Juni 2016

Preface

The present thesis is submitted as part of the requirements for obtaining the degree Doktor-Ingenieur from the University of Duisburg-Essen. The work has been conducted at the Institut für Schiffstechnik, Meerestechnik und Transportsysteme under supervision of Prof. Ould el Moctar. I am grateful for the continued guidance and motivation, especially in times when I was about to resign; thanks for all the support and encouragement. Thanks also to Profs. Heinrich Söding and Jørgen Juncker Jensen for their advice and inspiration; to Profs. Odd Faltinsen and Heinrich Söding for the discussions and the willingness to review my work.

I want to thank all colleagues at the institute and at Germanischer Lloyd for fruitful and stimulating discussions, in particular Jens Ley, Jens Neugebauer, Jan Kaufmann, Daniel Schmode, Jochen Hundemer, Christoph Hungershöfer, and last but not least Ole Hympendahl for his review; special thanks go out to Vladimir Shigunov for always having excellent ideas and critical comments. I am also much obliged to Elzbieta Bitner-Gregersen, Andreas Brehm, Jörg Brunswig, Ingo Drummen, Jens Bloch Helmers, Sa Young Hong, Adrian Kahl, Matthias Krömer, Šime Malenica, Holger Mumm, Miguel Onorato, Helge Rathje, Thomas Schellin, Clemens Schiff, Gaute Storhaug and many more for the collaboration and the discussions we had. There are of course many more to be listed, please excuse for not being mentioned personally.

Further, I want to express my gratitude to the small army of nameless computers who dedicated their lives to crunching my numbers. Despite being imprisoned in the darkness of server rooms, these restless slaves did a pretty good job.

Finally, I want to thank my family for their continued support throughout the last years. Please excuse me for the times when I was absent, physically or mentally. Judith and Hanne, I promise you a significantly larger share of my time in the future.

This work was funded by former Germanischer Lloyd SE, now DNV GL SE. The financial support is gratefully acknowledged.

Jan Oberhagemann
June 2016

Abstract

Rational assessment of wave loads for ultimate strength of ship structures requires appropriate numerical tools capable of dealing with physical phenomena related to severe environmental conditions. In addition to low frequency wave loads, vibration caused by wave action adds to the total wave loading of the primary hull structure.

The thesis presents a numerical method for determining ship hull structural loads due to the action of waves, including the contributions from vibration of the fundamental vertical vibration modes of the hull. The proposed numerical method is based on a coupled numerical solution of the dynamics of fluid and structure. The fluid dynamics method is based on solution of the Reynolds-Averaged Navier-Stokes (RANS) equations combined with a multiphase fluid formulation, whereas the structural dynamics method relies on a simplified representation of the hull girder with a finite element beam. The fluid dynamics method is in principle well suited to capture nonlinear flow features relevant for time domain simulation of ships in severe or extreme environments due to the capability of capturing complex flows including highly disturbed free surfaces. Wave-wave interaction, wave breaking and wave impacts are implicitly accounted for. The coupled method presented here implicitly and consistently accounts for complex resonant excitation of hull girder vibrations in waves as well as impulsive vibratory excitation due to slamming.

Fundamental tasks of the work documented herein are the improvement and validation of the coupled numerical method, including investigations of required computational accuracy and estimations of numerical uncertainties. Available computational procedures for obtaining statistical properties of ship loads in irregular waves are adopted to the needs of the computationally expensive numerical method, and applied in case studies.

Declaration

Part of the work described in this dissertation has previously been published in the following references.

- el Moctar, O., J. Oberhagemann and T.E. Schellin (2011): Free-Surface RANSE Method for Hull Girder Springing and Whipping. *SNAME Transactions 119*, pp. 48-66.
- Oberhagemann, J. and O. el Moctar (2012): Numerical and Experimental Investigations of Whipping and Springing of Ship Structures. *Int. J. Offshore and Polar Engineering 22(2)*. pp. 108-114.
- Oberhagemann, J., J. Ley and O. el Moctar (2012): Prediction of Ship Response Statistics in Severe Sea Conditions using RANS. In *Proc. 31st Int. Conf. on Ocean, Offshore and Arctic Engineering*. Rio de Janeiro, pp. 461-468. Paper No. OMAE2012-83995.
- Oberhagemann, J., J. Ley, V. Shigunov and O. el Moctar (2012): Efficient Approaches for Ship Response Statistics using RANS. In *Proc. 22nd ISOPE Conference*. Rhodes, pp. 1133-1140.
- Oberhagemann, J., V. Shigunov and O. el Moctar (2012): Application of CFD in Long-Term Extreme Value Analyses of Wave Loads. *Ship Technology Research 59(3)*. pp. 4-22.
- Oberhagemann, J. V. Shigunov and O. el Moctar (2013): First-Order Reliability Analogies of Nonlinear Bending Moments in Ships. In *Proc. 32nd Int. Conf. on Ocean, Offshore and Arctic Engineering*. Nantes. Paper No. OMAE2012-10547.

Nomenclature

BEM	Boundary Element method
CD	Central Differencing scheme
CEHIPAR	Canal de Experiencias Hidrodinámicas de El Pardo
CFD	Computational Fluid Dynamics
COMET	Continuum Mechanics Engineering Tool
CRRW	Conditioned Random Response Wave
CRS	JIP Cooperative Research Ships
CSD	Computational Structure Dynamics
CSR	Common Structural Rules
DNV GL	classification society, merger of former DNV and GL
DoF	degree of freedom
ERDW	Equivalent Regular Design Wave
ExtremeSeas	EU project Design for Ship Safety in Extreme Seas
FEM	Finite Element method
FORM	First Order Reliability method
FVM	Finite Volume method
GL	Germanischer Lloyd
HRIC	High Resolution Interface Capturing scheme
IACS	International Association of Classification Societies
IE	Implicit Euler time marching scheme
interDyMFoam	OpenFOAM free-surface flow solver on dynamic grids
ISSC	International Ship Structures Congress
ITTC	International Towing Tank Conference
ITTL	Implicit Three Time Level time marching scheme
JONSWAP	Joint North Sea Wave Project
KRISO	Korean Research Institute for Ships and Offshore; formerly named MOERI
KVLCC	KRISO Very Large Crude Oil Carrier
LNPE	logarithmic number of periods between exceedances
MARIN	Maritime Research Institute Netherlands
MLRW	Most Likely Response Wave

MOERI	Maritime Ocean Engineering Research Institute
MULES	Multidimensional Universal Limiter with Explicit Solution
NA	North Atlantic
NBA	Narrow-Band Approximation
NS	Navier-Stokes (equations)
OpenFOAM	Open Source Field Operation and Manipulation
PCA	probability corrective approach
PIMPLE	Combination of PISO and SIMPLE
PISO	Pressure-Implicit with Splitting of Operators
PM	Pierson-Moskowitz (spectrum)
RANS	Reynolds-Averaged Navier-Stokes (equations)
RAO	Response Amplitude Operator
RCA	response corrective approach
SIMPLE	Semi Implicit Method for Pressure-Linked Equations
SORM	Second Order Reliability method
UD	Upwind Differencing scheme
UDE	University of Duisburg-Essen
VBM	vertical bending moment
VoF	Volume of Fluid
WILS	JIP Wave Induced Loads on Ships

List of symbols

A_S	effective shear area
A_W	wave amplitude
B	moulded breadth
C_C	Coefficient of Contribution
χ	upcrossing rate
$\mathbf{D}$	damping matrix
δ	discretisation error
E	Young's modulus
G	shear modulus
g	gravity acceleration
H_S	significant wave height
I	area moment of inertia
$\mathbf{I}$	mass moment of inertia
$\mathbf{J}$	Jacobian of motion
$\mathbf{K}$	stiffness matrix
k	wave number
LC	loading condition
Λ	logarithmic number of periods to exceedance
L	ship's length
$\vec{L}$	angular momentum
$\mathbf{M}$	mass matrix
μ	mass per unit length
μ	wave encounter angle
m	mass
$\bar{\mu}$	mass moment of inertia per unit length
$\vec{\xi}$	position vector in global reference frame
$\vec{P}$	momentum
p	pressure
φ	roll motion
Ψ	planar shear rotation
ψ	yaw motion

γ	peak enhancement factor
$\mathbf{r}$	motion state vector
ρ	density
S	energy density spectrum
$\mathbf{S}$	rotation matrix
t	time
τ	stress tensor
T_D	total service life time at sea
θ	pitch motion
T_S	simulation duration
T_z	zero-upcrossing period
Υ	refinement ratio
$\mathbf{u}$	vector of nodal degrees of freedom
$\vec{v}$	vector of velocities
v	ship speed
ω	frequency
$\vec{\omega}$	vector of angular velocity
$\vec{x}$	position vector in local reference frame
$\mathbf{y}$	motion state vector
z	vertical bending deflection
ζ_W	wave elevation

Contents

Nomenclature vi

List of symbols viii

1 Introduction 1
- 1.1 Background and Motivation . . . 3
- 1.2 Thesis Structure . . . 6

2 Numerical Method 9
- 2.1 Fluid Dynamics . . . 10
  - 2.1.1 Pressure-Velocity Coupling . . . 12
  - 2.1.2 Free Surface Flows . . . 14
  - 2.1.3 Finite Volume Discretisation . . . 15
- 2.2 Structure Dynamics . . . 17
  - 2.2.1 Kinematics and Dynamics of Moving Bodies . . . 18
  - 2.2.2 Extension to Flexible Bodies . . . 25
  - 2.2.3 Finite Element Timoshenko Beam . . . 27
  - 2.2.4 Time Integration . . . 31
- 2.3 Solver Coupling and Communication . . . 32
  - 2.3.1 Mesh Morphing . . . 33

3 Wave Load Statistics 37
- 3.1 Statistical Description of Waves . . . 37
  - 3.1.1 Spectral Wave Energy Distribution . . . 38
  - 3.1.2 Discretised Wave Elevation Process . . . 40
  - 3.1.3 Wave Climate . . . 41
- 3.2 Linear Ship Responses to Waves . . . 43
- 3.3 Nonlinear Response Statistics . . . 46
  - 3.3.1 Equivalent Regular Design Waves . . . 49
  - 3.3.2 Response-Conditioned Wave Sequences . . . 50
  - 3.3.3 Monte-Carlo Simulations . . . 52
  - 3.3.4 Extrapolation of Upcrossing Rates . . . 53

3.3.5 Coefficient of Contribution 56

4 Validation **59**
4.1 Assessment of Numerical Errors and Uncertainties 61
4.1.1 Grid Refinement for Transient Problems 63
4.2 Free Vibration Decay Simulations 68
4.3 Motions and Loads in Waves 85
4.3.1 Regular Waves 85
4.3.2 Irregular Waves 106

5 Method Application **133**
5.1 Extrapolation of Upcrossing Rates in Stationary Sea States . . 137
5.2 Extrapolation of Grid Independent Solutions 147

6 Discussion **157**
6.1 Concluding Remarks 162
6.2 Suggestions for Future Work 163

Bibliography **165**

Appendix A Ship Particulars **175**

Appendix B Angular Momentum of Flexible Bodies **179**

Appendix C Example of Dynamic Response Amplification **182**

Appendix D Additional Figures **190**

1 Introduction

The continuous action of water surface waves is, besides the load effects of cargo, one of the key loading processes that ship hull structures are designed to withstand. The long-term (life-cycle) maxima of loads are, e. g., used in structural design to define the required ultimate strength of primary members of the hull girder structure. Corresponding wave loads are typically experienced in severe sea states, where full scale measurement data are scarce. Rational assessment of design loads for ultimate strength thus requires appropriate numerical tools capable of dealing with physical phenomena related to severe environmental conditions. The slowly-varying (at wave frequency) loads are relatively well understood, and numerous approaches exist to compute these wave loads numerically with adequate accuracy. For the assessment of the wave frequency loads, the ship may be idealised as a rigid body.

In addition to low frequency wave loads, full-scale measurements revealed a contribution of vibration caused by wave action which adds to the total wave loading of the primary hull structure. Wave-induced vibrations may account for a significant part of the total wave loads, see Storhaug et al. (2003), Storhaug (2007), Kahl and Menzel (2008), Andersen (2014). Sources of wave-induced vibration are, e. g., short impulses when parts of the hull impact on the water surface (called slamming), or waves encountered in resonance with natural frequencies of the ship structure. Such wave-induced vibrations modulate the structural stress fluctuations caused by wave action, and can be observed in virtually all time series of measured stresses. The vibratory modulations increase the load extremes and adversely affect the fatigue life through increased numbers of load cycles, Heggelund et al. (2011), Rathje et al. (2012). Frequencies of vibration correspond to the fundamental natural frequencies of the hull and are typically in the order of $0.3\,Hz$ to $1.5\,Hz$.

Wave-induced vibrations of ships have been frequently reported for decades, and serious concerns about consequences were already raised in the seventies when Great Lakes bulk carriers experienced severe fatigue problems. It is also about that time when numerical methods were developed to address resonant wave-induced vibration, Söding (1975), Bishop and Price (1979). For long time,

however, attention paid to wave-induced vibration was limited.

In the recent past, vibrations of the ship hull girder have again gained increased attention, and concerns were raised mainly regarding fatigue failure, but also regarding strength failure of the hull girder in severe weather conditions. The hull girder collapses of the containerships *MSC Napoli* in 2007 and *MOL Comfort* in 2012 often serve to witness the relevance of wave-induced vibration. The official incident reports of these accidents indeed list wave-induced vibration amongst the contributions to the failures, MAIB (2008), ClassNK (2014), although the root causes were insufficient buckling strength capacities of the hull girder in both cases. However, from measurements it is evident that wave-induced vibration amplifies the overall loading of ship structures, and it significantly contributes to hull girder load extremes. Hence, effort must be made towards reliable prediction of the consequences of wave-induced vibration. This necessitates the development and continuous improvement of numerical tools and computational procedures to assess the contribution of wave-induced vibration to extreme loads.

Wave-induced vibration is a complex and non-linear phenomenon involving structure and fluid dynamics, so the physics are difficult to model numerically. This thesis aims at contributing to further establish the use of advanced simulation methods in extreme value predictions of ship loads. The proposed method implicitly accounts for relevant nonlinearities and is well suited to address extreme wave loads.

Wave loads are random processes. Determination of a minimum required structural capacity therefore requires to establish the long-term probability distribution of the corresponding load. Classical long-term statistical calculations based on spectral methods, however, are not suited for extreme value analyses of the combined action of low frequency wave loads and vibration. Also, well-established procedures that find a non-linear correction to a linear long-term value from a single deterministic simulation are inappropriate in this context. On the other hand, there exist no reliable nonlinear methods that are suited for direct long-term simulations, so strategies are sought to cut down the required computation times. This thesis will explore more advanced simulation strategies, investigate the related requirements on the numerical methods, and discuss necessary computational resources.

Probabilistic modelling plays an increasingly important role in engineering design of structures. The safety of a design is assessed in modelling the exerted load and the load capacity in terms of stochastic functions. The structure is said

to be safe when the probability of the load exceeding the capacity is below a defined threshold level. The load exerted on ship structures can be subdivided in two fundamental contributions. The first of these is a slowly varying process basically caused by cargo loading and unloading, and changes of bunkers and ballast. This load contribution is commonly called the still water load. The second constribution owes to the action of ocean waves and is a continuous non-stationary stochastic process. Other contributions exist such as wind and thermal loads as well as the quasi-static hydrodynamic loads due to forward speed and manoevering, but these are typically small or act locally, and are disregarded in hull girder strength requirements of standard commercial ships.

This thesis exclusively deals with the numerical determination of the wave loading contribution.

Nonlinearities of waves, wave-structure interaction and dynamic structural response cannot be neglected when dealing with the wave load extremes relevant for structural design. This makes accurate numerical extreme load predictions a demanding task even when assuming rigid ships, and it is fair to say that wave-induced vibrations are among the most complex contributions to the overall structural loading.

1.1 Background and Motivation

The present thesis arose from the continued efforts at former Germanischer Lloyd (GL) not only to incorporate numerical methods in classification rule development processes, but also to improve computational procedures to establish design loads for structural design assessments. The thesis reflects the results of a research cooperation between GL and the University of Duisburg-Essen (UDE).

The numerical method presented here is based on a solver of the Reynolds-Averaged Navier-Stokes (RANS) equations combined with a multiphase fluid formulation. Such fluid dynamics methods are in principle well suited to capture nonlinear flow features relevant for time domain simulation of ships in severe or extreme environments due to the capability of capturing complex flows including highly disturbed free surfaces. Wave-wave interaction, wave breaking and wave impacts are implicitly accounted for.

Back in the 1990s, GL was one of the first ship classification societies to introduce numerical methods based on the solution of the RANS equations

in studies of slamming loads, Muzaferija et al. (1998), Sames et al. (1999). Applications were extended to assess loads in waves based on imposed motions, el Moctar et al. (2004), and later on based on the simultaneous solution of nonlinear equations of motions, el Moctar et al. (2005). Consequently, GL relatively early attempted to use these methods also to address dynamic structural responses, el Moctar et al. (2006).

Oberhagemann (2006) proposed a method to iteratively couple the RANS solver with a simplified structural representation of the ship's hull girder. The flow solver is coupled to a nonlinear motion solver for six degrees of freedom and a linear motion solver to compute the linear elastic flexural response of the ship structure according to the Finite Element Method (FEM). The threefold coupled method allows to include nonlinearities of wave-structure interaction which is essential for realistic simulations of slamming and green water effects on the structural response.

In the literature, one will often find a clear distinction between hull girder vibration in response to impulsive loading, referred to as *whipping*, and resonant vibration excitation, referred to as *springing*. However, several authors discuss the difficulties to categorise the type of vibration from measured data, see e.g. Storhaug et al. (2003). In this respect, the merits of a consistent first-principle approach to all types of vibration excitation are clear. The coupled method presented here implicitly accounts for higher order resonant excitation of hull girder vibrations in waves and impulsive vibratory excitation due to slamming, el Moctar et al. (2011). Nonlinearities related to hydrodynamic added mass and damping are implicitly captured to account for forward speed effects, instantaneous wave elevations, etc.

Computational Fluid Dynamics (CFD) methods are beneficial in applications where nonlinearities are of major concern, e. g. in predictions of extreme value distributions of wave loads acting on ships and other marine structures. As a flip-side, direct long-term simulations covering the whole ship's life will not become realistic within the foreseeable future since available resources only allow for simulations of relatively short sequences.

Therefore, screening of relevant environmental conditions in terms of ship responses and their probability distributions is a very important prerequisite. Once representative scenarios are identified, corresponding ship responses are computed with more involved numerical methods to obtain improved extreme ship response distributions. Simpler and faster numerical hydrodynamic methods are

employed to screen for critical conditions, so application of the computationally expensive CFD methods may be restricted to a few simulations of limited duration.

The most simplifying way to establish simulation conditions is the concept of equivalent design waves. Harmonic regular waves are established in a way that they excite a response corresponding to the target design level, according to linear theory. The nonlinear simulation is then limited to this single harmonic wave. While the ease-of-use of these so-called Equivalent Regular Design Waves (ERDW) has made them the predominant wave scenarios for CFD computations, it comes at the price of some shortcomings due to their simplistic definition. Irrespective of the nonlinearities included in such simulations, the assumptions made during establishing the wave load scenarios affect the results to a high degree, often putting their informational value for design and dimensioning of the structure in question.

Various alternative approaches have been proposed and tested in recent years that aim at identifying relevant scenarios, e. g. Baarholm and Moan (2000), Dietz (2004), Kim and Troesch (2010), Jensen (2011). See Jensen (2009) and Schellin et al. (2013) for reviews of selected approaches. Seng and Jensen (2012), Oberhagemann et al. (2012) and Oberhagemann et al. (2013) give examples of application of coupled CFD-CSD methods to extreme load predictions beyond traditional ERDW.

The most suitable role of CFD and coupled CFD-CSD methods needs further clarification but could in principle cover three different aspects: First, application of CFD methods may directly provide load magnitudes or improve present rule load assumptions; second, such methods may be used to calibrate or validate simpler methods; third, CFD simulations may be an integral part of computational procedures defined in the rules. The thesis intends to provide guidance for future decisions on these options. Fundamental tasks of the work presented here are therefore the improvement and validation of existing methods; investigation of required computational accuracy and estimations of numerical uncertainties; adoption of available computational procedures and application of the methods in case studies; provision of decision support for rule development.

It may be prospected that the use of RANS methods for coupled solvers will become more popular in the near future. Paik et al. (2009), Seng and Jensen (2012), Craig et al. (2015) and Robert et al. (2015) are examples of similar non-commercial implementations, and Lakshmynarayanana et al. (2015) report attempts to use a commercial software package. Besides the availability of such

methods to a larger number of users, one important precondition for a more wide-spread use is the existence of appropriate load prediction procedures.

1.2 Thesis Structure

This thesis presents a numerical method based on the solution of the Navier-Stokes (NS) equations to asssess large wave-induced ship motions and corresponding loads. Nonlinearities of wave excitation and ship response are included. The thesis concentrates on vertical vibration modes. The more complex torsional, transverse and mixed vibration modes are excluded although the coupled solver implementation basically allows their inclusion, Oberhagemann et al. (2012). The exclusion helps to limit the complexity of the topics to be covered. The restriction to less demanding vertical vibrations may be justified with observations from measurements indicating that the the fundamental two-node vertical bending vibration is most contributing to the overall vibration stresses. Although the natural frequency for one-node torsion is typically lower for container ships with large deck openings, related vibrations are less pronounced.

The thesis gives evidence to the following statements:

- First principle methods such as RANS CFD combined with finite element computational structure dynamics (CSD) capture relevant wave loading and response processes to investigate wave-induced vibration.
- Discretisation errors and numerical uncertainties are inevitable when using numerical methods, except for academic cases. Good engineering practice is to be aware of this and give estimates of the uncertainty. By its nature, the discretisation error is relatively larger for local quantities, and smaller for integral values.
- It is not always meaningful to attempt to minimize the discretisation uncertainty a priori by using very fine grids. Instead, it can be advantageous to use coarse discretisations and thus save computation time, while spending more effort on assessing the inherent bias and uncertainty.
- CFD-CSD methods can be embedded in more advanced procedures than simplistic regular design waves when investigating wave-induced vibration, at the price of increased computational costs.

Chapter 2 covers the theoretical background of the numerical methods used in this thesis. This comprises the derivation of the numerical fluid and structure

dynamics methods and a description of their combination to a coupled solver. The governing equations solved in the fluid and structure domains are given as well as their implementation in a coupled solver.

Chapter 3 deals with the description of ship responses to wave excitation. Starting with linear wave theory and the fundamentals of ship responses, linear short- and long-term statistics of responses based on the Narrow-Band Approximation (NBA) are derived. This chapter further discusses issues of determining ship response statistics from nonlinear simulations. Numerous approaches of different complexity are available for establishing relevant simulation scenarios.

Validation of the numerical method is presented in chapter 4, comprising comparisons of computation results with model scale experimental data in regular and irregular waves, taken from model test campaigns at KRISO, CEHIPAR and MARIN, see appendix A. Attention is paid to uncertainties and errors introduced by insufficient space and time discretisation. Certain flow features require fine spatial resolution and small enough time steps to obtain reasonably accurate predictions. Fine grid and time step resolutions, on the other hand, strongly increase the computational effort as well as corresponding CPU and memory requirements. This chapter discusses a reasonable balancing of accuracy and efficiency. In addition, strategies for estimating grid independent solutions are tested and discussed.

Hydrodynamic vibratory damping is particularly sensitive to grid resolution since it is mainly caused by radiation of short waves at inclined sections in the bow and stern regions. Further, accurate prediction of local pressure peaks is related to large computational effort as well when simulating ships in waves. Still it is less demanding to compute sufficiently accurate integral quantities like impact-related slamming forces, and these forces are crucial to determine global high-frequency hull girder response.

Simulations in irregular waves covering relatively long time intervals are compared with experimental data and allow to assess short term statistical properties of the ship responses. Numerical results are in good agreement with model test data, both showing significant deviations from Rayleigh-distributed response amplitudes, especially for hull girder loads including effects of structural elasticity.

Despite savings in computational time through the use of relatively coarse grid resolutions and estimates of the grid dependent error, the computational costs for direct simulations of long-term load distributions are still orders of

magnitude too high to render such applications feasible. Strategies for further reducing the required computation time based on reducing the required lengths of simulations were discussed chapter 3. Based on these strategies, chapter 5 explores options for computing nonlinear load statistics within more practical computation times.

Definitions

All terms the reader may not be familiar with will be defined at their earliest occurrence in the text. However, a few terms are already given a definition here. This is to avoid ambiguity because they are commonly used in both regulatory and numerical computing contexts but with a different meaning.

- **Code**
  The entitity of rules, guidelines and recommendations specified by a classification society or any other regulatory body is denoted a *code*. A *code* intends to safeguard the fitness of a construction for a specific purpose. It may provide distinct descriptive design formulae (rules) or settle *procedures* to establish design requirements. It usually has mandatory character but may include voluntary parts (e. g., in the sense of recommendations).
- **Method**
  Method in this context refers to an algorithm that can be implemented in computer programs. In turn, any computer program implements at least one method.
- **Procedure**
  A *procedure* is the modus operandi for a specific type of investigation. It usually involves the use of a certain *method* or of several *methods* in a sequence, and comprises a defined way of data processing and data evaluation. A *procedure* is therefore a formally specified computational approach.

2 Numerical Method

The basic concept of the numerical method is a straight-forward splitting of the transient coupled problem of fluid and structure dynamics into two distinct solution domains. Dedicated CFD (Computational Fluid Dynamics) and CSD (Computational Structure Dynamics) solvers are assigned to these domains. A coupling and communication layer calls these solvers alternatingly and iteratively in each time step and manages the exchange of information at the domain boundaries, i. e., fluid forces acting on the structure, and displacement of the fluid boundaries caused by structural deformation and motions.

For the solution of the fluid dynamics equation systems, two solvers are used in the scope of this thesis, namely COMET and a solver interDyMFoam from the software package OpenFOAM. Both methods use discretised formulations of the Navier Stokes (NS) equations based on the finite volume method (FVM). They largely rely on the same numerical approaches. The most important differences of the solvers are the algorithms for the iterative solution of the coupled NS equations of mass and momentum conservation, and the treatment of the numerical difficulties related to free-surface flows. The governing equations are given in section 2.1, along with strategies to derive a solution algorithm. Further on, the implemented numerical methods are explained and their differences highlighted.

The structure dynamics method is further divided into parts consisting of rigid-body motions on the one hand, section 2.2.1, and elastic deformation motions on the other hand, section 2.2.2. The former can be of arbitrary amplitude and are formulated nonlinearly using the kinematics of an inertial mass point. Large amplitude motions may, e. g., occur during manoevering or in case of large roll motions. Although this feature is of minor relevance for the applications in this thesis, it allows for more flexibility in the application of the method. In turn, deformations are assumed to have small amplitude - which is a good assumption for ships - and are linearized.

The linear structural solver implemented here relies on a simplified approach; the ship hull is reduced to a beam, accounting for vertical bending and shear deformation. This allows to model the global flexural response of the ship only,

but fundamental characteristics of the hull structure are well approximated when doing so. Especially planar vibration modes, e.g., vertical bending vibration, can be easily modelled with sufficient accuracy. More complex vibratory modes such as torsion of ships with large deck openings require a more detailled modelling.

Splitting of the structure solvers allows a simplification of the problem and consider only motions of a rigid body. Further on, the division intuitively appears reasonable in the context of wave loads on ships, as the motions typically are larger than elastic deflections by an order of magnitude.

Both linear deformations and rigid-body motions are formulated for transient problems. The coupled method combines both structure solvers with the fluid solver, see section 2.3. In each time step, several iterations over all solvers assure a converged and consistent coupled solution.

2.1 Fluid Dynamics

For the purposes of this thesis, the fluids are assumed Newtonian. In this case, the flow is governed by the following equations of momentum conservation and mass conservation, here written for an arbitrary fluid parcel:

$$\left[\frac{\partial(\rho\vec{v})}{\partial t}+((\rho\vec{v})\cdot\nabla)\,\vec{v}\right]=-\nabla p+\nabla\tau+\vec{b} \tag{2.1.1}$$

$$\frac{\partial\rho}{\partial t}+\nabla\cdot(\rho\vec{v})=0, \tag{2.1.2}$$

with the vector of velocities $\vec{v}$, density ρ, pressure p, volumetric forces $\vec{b}$, and the Cauchy stress tensor τ,

$$\tau=\mu\left(\nabla\vec{v}+(\nabla\vec{v})^T\right)-\frac{2}{3}\mu\,(\nabla\cdot\vec{v})\,\mathbf{I}, \tag{2.1.3}$$

where μ is the dynamic viscosity. In case of an incompressible fluid, the divergence of the velocity must equal zero, $\nabla\cdot\vec{v}=0$, so the stress tensor simplifies to the deviatoric stress tensor terms,

$$\tau=\mu\left(\nabla\vec{v}+(\nabla\vec{v})^T\right). \tag{2.1.4}$$

For incompressible and isothermic fluids, the density is constant, and eq. (2.1.2) reduces to

$$\nabla \cdot \vec{v} = 0. \tag{2.1.5}$$

Note that the mass conservation equation, eq. (2.1.2), does not explicitly depend on the pressure, while the pressure occurs in the momentum conservation equation, eq. (2.1.1), only in terms of a pressure gradient. This implies that the absolute values of pressure are only known relative to a given reference pressure.

The spatial and temporal discretisation of the solution variables determines the size of small-scale fluctuations of the flow which cannot be resolved directly. However, the kinetic energy transfered to these fluctuations is of particular importance for highly sheared flows like boundary layers and vortices. The fundamental idea of modelling such turbulences, proposed by Osborne Reynolds, is to split a flow quantity ϕ into its statistical mean, $\bar{\phi}$, and a fluctuation about this mean, $\phi\prime$,

$$\phi(x,t) = \bar{\phi}(x,t) + \phi\prime(x,t). \tag{2.1.6}$$

Accordingly, ensemble averaging is done for unsteady problems,

$$\bar{\phi}(x,t) = \lim_{N\to\infty} \frac{1}{N} \sum_{n=1}^{N} \phi(x,t). \tag{2.1.7}$$

When applying Reynolds-averaging to the conservation equations, all linear fluctuation terms vanish. The only remaining term is a quadratic term $\overline{\rho \vec{v}\prime \vec{v}\prime^T}$ in eq. (2.1.1), called the Reynolds stress tensor. The NS equations are now solved for the Reynolds-Averaged flow quantities. Because of the additional Reynolds stresses, new equations have to be introduced for closure of the system of coupled equations. This may be accomplished with turbulence models of varying complexity, depending on the needs of the application at hand, Ferziger and Perić (2002), Wilcox (1998). For most applications in this thesis, the flow is dominated by pressure and viscous effects are of minor interest. In cases where viscosity is accounted for and a turbulence model is needed, standard $k-\varepsilon$ or SST $k-\omega$ models are used, Launder and Sharma (1974), Menter (1993).

2.1.1 Pressure-Velocity Coupling

The mass and momentum conservation equations need to be solved in a coupled manner in order to obtain a consistent solution of pressure and velocity. For this purpose, the conservation equations must be reordered to obtain dedicated equations for the velocity and pressure fields. This is done with projection methods which combine the conservation equations eq. (2.1.1) and eq. (2.1.2) to obtain an explicit equation for the pressure. The most common pressure-velocity coupling approaches based on pressure correction are SIMPLE (Semi-Implicit Method for Pressure-Linked Equations), Patankar and Spalding (1972), and PISO (Pressure-Implicit with Splitting of Operators), Issa (1986), see also Ferziger and Perić (2002).

The SIMPLE algorithm is outlined here for incompressible flow, meaning that the (constant) density is effectively eliminated from eqs. (2.1.1) and (2.1.2). In each time step, outer iterations are performed which involve a sequential update of all solution variables based on the latest available set of solution values (Picard Iteration).

The sequence is outlined here using a semi-discretised form of the equations according to a staggered arrangement where the momentum equation is solved for grid points located in the cell centers, while the pressure correction equation uses a computational mesh based on the cell face centers:

1. The momentum equation is solved for a provisional velocity field based on the previous iteration or time step pressure field, whichever is available (upper index 0 denotes these old values):

$$a_P \vec{v}_P = -H(\vec{v}) - \nabla p^0, \tag{2.1.8}$$

where a_p are the diagonal matrix coefficients corresponding to cell centers (index P) of the linear algebraic system of equations, and

$$H(\vec{v}) = -\sum_{NB} a_{NB} \vec{v}_{NB} + S_{m,P} + \frac{\vec{v}^o}{\Delta t} \tag{2.1.9}$$

consists of the matrix coefficients of the neighbouring cells, index *NB*, multiplied by the respective velocities, the momentum source terms except for the pressure gradient, $S_{m,p}$, and the unsteady term.

2. Next, the cell-centered values are interpolated to obtain the corresponding velocities at cell faces (face values have index f):

$$\vec{v}_f = \left(\frac{H(\vec{v})}{a_p}\right)_f - \frac{(\nabla p)_f}{(a_p)_f} \tag{2.1.10}$$

3. The newly found approximate face velocity field forms the basis for solving the following continuity equation:

$$\nabla \cdot \vec{v} = \sum_f A_f \vec{n}_f \vec{v}_f = 0, \tag{2.1.11}$$

with face areas A_f and face normal vectors $\vec{n}_f$. Now, substituting eq. (2.1.10) into eq. (2.1.11) yields an explicit expression for the pressure:

$$\nabla \cdot \left(\frac{1}{a_p}\nabla p\right) = \nabla \cdot \left(\frac{H(\vec{v})}{a_p}\right) = \sum_f A_f \vec{n}_f \left(\frac{H(\vec{v})}{a_p}\right)_f \tag{2.1.12}$$

4. Solution of eq. (2.1.12) provides a pressure field which is used to correct the mass fluxes and the velocity field (momentum correction).
5. The sequence is repeated until the convergence criteria are satisfied.

Under-relaxation is applied to both the velocity field and the pressure field in order to stabilise the iterative solution. The choice of appropriate under-relaxation factors requires some experience with the problem at hand in order to find the best trade-off between stability and fast convergence.

The PISO algorithm differs from SIMPLE in that iterations are performed over the last steps only instead of a full iteration sequence, so iteration covers only the solution the pressure correction equation and the update of the velocity field[1]. This is to achieve faster convergence within each time step by omitting the multiple solution of the momentum equation, and instead assure a fully consistent solution of pressure and velocity already after the first pass of the sequence. While PISO therefore converges faster within each time step and avoids the need for under-relaxation, it is less stable for larger Courant numbers and requires smaller time steps. Temporal accuracy may also be compromised because corrections for the temporal nonlinearity are made once per time step only. See Weller

[1] The original formulation of Issa (1986) proposes a restriction to two pressure correction steps only.

(2005) for further discussion. The advantage of fast convergence of the PISO algorithm over SIMPLE becomes less interesting for fluid-structure coupling methods, where a certain number of iterations is required anyway to couple the fluid and structure solutions, and where underrelaxation may be beneficial for the stability of the overall solution.

COMET implements the SIMPLE algorithm, whereas *interDyMFOAM* offers PIMPLE, a hybrid combination of PISO and SIMPLE, Weller (2005). PIMPLE aims at faster convergence by combining the implicit solution of the momentum equation with an optional pressure corrector loop. Compared to SIMPLE, the additional pressure correction steps in PIMPLE may help reducing the required number of iterations and mitigate the need for under-relaxation.

Both SIMPLE and PIMPLE based solvers are suited for an iterative coupling with motion solvers since they already rely on an iterative solution in each time step; no additional outer iteration loop has to be imposed, only the number of iterations may increase because of additional constraints arising from the structure solver.

2.1.2 Free Surface Flows

An interface capturing method based on the Volume of Fluid (VoF) approach is used for free-surface flows. An additional transport equation solves for a scalar quantity Γ:

$$\frac{\partial \Gamma}{\partial t} + \nabla \cdot (\Gamma \vec{v}) = 0. \tag{2.1.13}$$

Γ represents the volume fraction of one out of two different fluids, in this case air and water. Fluid properties like density and molecular viscousity are set for each control volume according to the properties of the involved fluids and the volume fraction Γ,

$$\rho_{eff} = \Gamma \rho_{water} + (1-\Gamma)\rho_{air}, \quad \mu_{eff} = \Gamma \mu_{water} + (1-\Gamma)\mu_{air}, \tag{2.1.14}$$

so the NS equations are solved for an effective fluid. Equations (2.1.13) and (2.1.14) can easily be extended to multiphase flows of an arbitrary number of fluids, simply by introducing additional scalar volume fractions. In such cases, an additional constraint equation has to assure that the sum over all phase fractions equals 1.

The VoF approach implicitly accounts for topological changes of the free surface and allows computation of breaking and overturning waves, splash, air entrapment, etc. As a downside, the exact position of the free surface is not explicitly known. Instead, it is implicitly defined by $\Gamma = 0.5$ and has to be reconstructed from the Γ scalar field by interpolation.

For free surface flows of immiscible fluids, the numerical solution scheme has to assure that the fluids involved do not mix. Using interface capturing methods, the discontinuity of the free surface is necessarily replaced by a phase transition over at least one control volume, and the free surface is represented by a set of control volumes with values of $\Gamma\,\varepsilon\,]0,1[$. Avoiding mixing of the fluids is then equivalent to minimizing the number of cells with values of Γ other than 0 or 1.

Therefore, the numerical solution scheme of the scalar transport equation has to meet the following requirements:

- Mass conservation must be assured.
- The scalar field must be bounded, $0 \leq \Gamma \leq 1$, in order not to introduce unphysical fluid properties.
- The number of cells with values of Γ larger than 0 and smaller than 1 must be minimized in order to retain a sharp interface and avoid smearing.

Special numerical schemes for fullfilling above requirements, in particular retaining a sharp fluid interface, are discussed in paragraph 2.1.3.

2.1.3 Finite Volume Discretisation

The solvers use an integral formulation of the above partial differential equations. The solution domain is discretised by cells of finite volume V, and eqs. (2.1.1) and (2.1.2) are rewritten in integral form for each finite volume, (Finite Volume Method, FVM),

$$\frac{\partial}{\partial t}\int_V \rho\vec{v}dV + \int_S \rho\vec{v}(\vec{v}-\vec{v}_S)\cdot\vec{n}dS = \int_S \mathbf{T}dS + \int_V \vec{b}dV \tag{2.1.15}$$

$$\frac{\partial}{\partial t}\int_V \rho dV + \int_S \rho(\vec{v}-\vec{v}_s)\cdot\vec{n}dS = 0. \tag{2.1.16}$$

Here, $\int_V dV$ are volume integrals, $\int_S dS$ surface integrals over the cell's surfaces, and $\vec{n}$ the surface normal vector. $\vec{v}$ is the fluid velocity, while $\vec{v}_S$ is the cell surface

velocity, resulting in a Euler-Lagrangian formulation for arbitrarily moving and deforming control volumes. A finite volume is discretised by a polyhedron which consists of a number of planar polygon faces, whereas each polygon is described through its corner vertices and has a distinct face normal vector.

With the exception of a few terms, eqs. (2.1.15) and (2.1.16) are discretised with second-order approximations; face and volume integrals are approximated using mid-point rule and are based on the polygonal cell face definition; cell center to face center interpolation is done with second-order linear interpolation; gradients are approximated using Gauss theorem and second-order central differencing (CD). The convective fluxes are discretised using central differencing blended with a small amount of first-order upwind differencing (UD) in COMET, and second-order upwind in *interDyMFoam*. The temporal differencing schemes are second-order implicit three-time level (ITTL) Adams-Moulton in COMET, and Crank-Nicolson in *interDyMFoam*. The Crank-Nicolson time marching scheme is formally second-order accurate when used with constant time steps, but usually has to be blended with first-order implicit Euler (IE) to assure numerical stability. The blending deteriorates the second-order accuracy, effectively yielding a first-order accurate time scheme.

COMET uses a special HRIC (High Resolution Interface Capturing) discretisation scheme for the convective fluxes in the scalar transport equation, Muzaferija and Perić (1998). HRIC accounts for the local position and advance direction of the free surface and combines upwind and downwind differencing schemes in order to retain a sharp interface and assure boundedness of the scalar flux. The *interDyMFoam* solver uses central differencing for the convective flux of the phase fraction scalar. An additional compressive convection term is introduced in eq. (2.1.13) which facilitates retaining a sharp interface,

$$\frac{\partial \Gamma}{\partial t} + \nabla \cdot (\Gamma \vec{v}) = \nabla \cdot (\Gamma (\Gamma - 1) \vec{v}_c), \qquad \vec{v}_c = c_\alpha |\vec{v}| \frac{\nabla \Gamma}{|\nabla \Gamma|}, \quad (2.1.17)$$

with a compression coefficient c_α of the order 1, Weller (2008). A special flux limiter based on MULES (Multidimensional Universal Limiter with Explicit Solution) provides a second-order correction of the scalar fluxes while assuring mass conservation and boundedness of Γ, Weller (2006). Two variants of MULES are presently available, one of them being suited for consistent embedding within the PIMPLE framework with an iterative solution algorithm taking advantage of the iterative solution based on outer (SIMPLE) iterations. As a major drawback, this variant is not mass conservative when used in combination

with second-order accurate time integration schemes. The only exception is the Crank-Nicolson scheme.

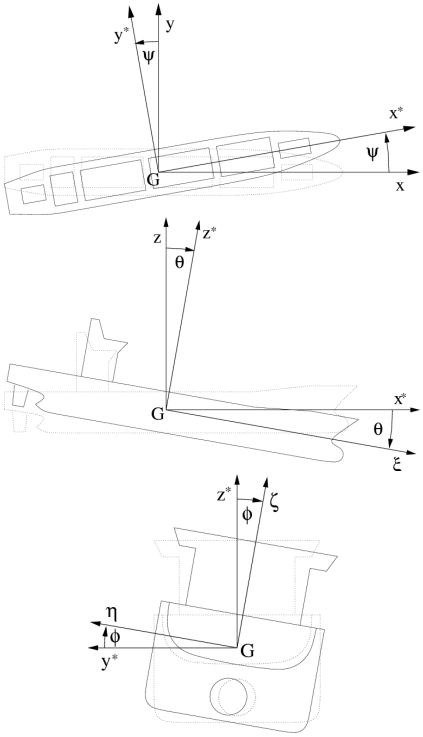

Figure 2.1: Sequence of rotations yaw, pitch and roll (top to bottom); here, (ξ, η, ζ) are local coordinates and (x, y, z) are global coordinates. G denotes $\vec{\xi}_0$, the origin of $\mathbf{O}\prime$. Source: Brunswig (2004)

2.2 Structure Dynamics

This section covers the structure dynamics of rigid and flexible bodies. The nonlinear rigid body motion solver is based on the work of Klemt (2004). Brunswig (2004) presented a motion solver which was the predecessor implementation of

the method discussed here. The solver for linear structural deformations based on a Timoshenko beam formulation was first introduced by Oberhagemann (2006).

2.2.1 Kinematics and Dynamics of Moving Bodies

Let $\mathbf{O}_{(\xi,\eta,\zeta)}$ be an inertial reference frame with the center of gravity of the body located in $\vec{\xi}_0 = (\xi_0, \eta_0, \zeta_0)^T$. A second body-fixed reference frame, $\mathbf{O}\prime_{(x,y,z)}$, is located in $\vec{\xi}$ and performs all translatory and rotary motions of the body in six degrees of freedom (DoFs). The axes of the local system are defined as x (longitudinal, positive to bow), y (transverse, positive to port side), and z (vertical, positive upward). The rotary state of $\mathbf{O}\prime$ corresponds to the rotation $\vec{\Omega} = (\Omega_\xi, \Omega_\eta, \Omega_\zeta)^T$ about the axes of the inertial system.

Instead of expressing rotary motions in terms of rotations about the inertial system axes, rotations in terms of roll, yaw, and pitch are more convenient for ship motion analysis and will be used in what follows according to the definition provided in SNAME (1950). Transforming from the inertial to the local reference frame, these correspond to following sequence of rotations: First about the vertical axis ζ (ψ, yaw motion), next about the new (intermediate) transverse axis y^* (θ, pitch motion) and finally about the resulting longitudinal axis x (φ, roll motion), see Fig. 2.1. The rotations are combined to a vector of generalised coordinates,

$$\vec{\alpha} = \begin{pmatrix} \psi \\ \theta \\ \phi \end{pmatrix}, \tag{2.2.1}$$

and correspond to the Tait-Bryans x-y-z convention of rotations when transforming from the local to the inertial reference frame. This transformation is

represented by the following rotation matrix:

$$\begin{aligned}\mathbf{S}(\vec{\alpha}) =& \mathbf{S}_\psi \cdot \mathbf{S}_\theta \cdot \mathbf{S}_\phi \\ =& \begin{bmatrix} \cos\psi & -\sin\psi & 0 \\ \sin\psi & \cos\psi & 0 \\ 0 & 0 & 1 \end{bmatrix} \\ &\cdot \begin{bmatrix} \cos\theta & 0 & \sin\theta \\ 0 & 1 & 0 \\ -\sin\theta & 0 & \cos\theta \end{bmatrix} \\ &\cdot \begin{bmatrix} 1 & 0 & 0 \\ 0 & \cos\phi & -\sin\phi \\ 0 & \sin\phi & \cos\phi \end{bmatrix}\end{aligned} \tag{2.2.2}$$

The rotation matrix $\mathbf{S}$ is orthonormal for all $\vec{\alpha}$, so $\mathbf{S}$ and its inverse $\mathbf{S}^T$ are always uniquely defined for given $\vec{\alpha}$. On the other hand, $\vec{\alpha}$ for given $\mathbf{S}$ is not always uniquely defined[2].

Equations of Motion in Generalized Coordinates

For the further derivation of the rigid body kinematics, we will transform the state vector of the six degrees of freedom (6DoF),

$$\mathbf{r} = \begin{pmatrix} \vec{\xi}_0 \\ \vec{\Omega} \end{pmatrix} = \begin{pmatrix} \xi_0 & \eta_0 & \zeta_0 & \Omega_\xi & \Omega_\eta & \Omega_\zeta \end{pmatrix}^T, \tag{2.2.3}$$

to a generalised state vector using the Tait-Bryans rotations,

$$\mathbf{y} = \begin{pmatrix} \vec{\xi}_0 \\ \vec{\alpha} \end{pmatrix} = \begin{pmatrix} \xi_0 & \eta_0 & \zeta_0 & \psi & \theta & \phi \end{pmatrix}^T. \tag{2.2.4}$$

[2] A singularity occurs, e. g., when $\theta = \pi/2$. This so-called Gimbal lock is the reason why Euler or Tait-Bryans rotations are frequently labeled inapplicable for motion solvers of large rotary motions - a misconception since the singularities only pose problems if one is to compute the motion state from a given set of local axis orientations, i. e. find $\vec{\alpha}$ for given $\mathbf{S}$.

Both **r** and **y** consist of six degrees of freedom, each three of these are translatory and rotary. They are related through

$$\frac{\partial \mathbf{r}}{\partial \mathbf{y}} = \mathbf{J} = \begin{bmatrix} \mathbf{J_T} & 0 \\ 0 & \mathbf{J_R} \end{bmatrix} = \begin{bmatrix} 1 & 0 & 0 & & & \\ 0 & 1 & 0 & & \mathbf{0} & \\ 0 & 0 & 1 & & & \\ & & & 0 & -sin\psi & cos\psi cos\theta \\ & \mathbf{0} & & 0 & cos\psi & sin\psi cos\theta \\ & & & 1 & 0 & -sin\theta \end{bmatrix}, \tag{2.2.5}$$

with the Jacobian matrix **J**. The submatrices on the diagonal of **J** are the Jacobian of translation, which is the identity matrix, and the Jacobian of rotation,

$$\mathbf{J_R} = \begin{bmatrix} 0 & -sin\psi & cos\psi cos\theta \\ 0 & cos\psi & sin\psi cos\theta \\ 1 & 0 & -sin\theta \end{bmatrix}. \tag{2.2.6}$$

Let $\vec{x}$ now be the location vector of any arbitrary material point of the rigid body, expressed in coordinates of the local reference frame. With the instantaneous position of the local system, $\vec{\xi}_0(t)$, and rotation matrix **S**, $\vec{x}$ can be written in coordinates of the inertial system,

$$\vec{\xi}(t) = \vec{\xi}_0(t) + \mathbf{S}(t)\vec{x}(t). \tag{2.2.7}$$

Momentum $\vec{P}$ and angular momentum $\vec{L}$ of the body with mass m and mass inertia **I**, expressed in inertial coordinates and related to the origin of the inertial reference frame, read

$$\vec{P} = \int_B \rho \dot{\vec{\xi}} dV = m\dot{\vec{\xi}}_0, \tag{2.2.8}$$

$$\vec{L} = \int_B \rho(\vec{\xi} \times \dot{\vec{\xi}}) dV = \mathbf{I}\vec{\omega}. \tag{2.2.9}$$

with $\vec{\omega}$ the vector of angular velocity,

$$\vec{\omega} = \frac{d\Omega}{dt} = \begin{pmatrix} 0 \\ 0 \\ \dot{\psi} \end{pmatrix} + \mathbf{S}_\psi \begin{pmatrix} 0 \\ \dot{\theta} \\ 0 \end{pmatrix} + \mathbf{S}_\psi \mathbf{S}_\theta \begin{pmatrix} \dot{\phi} \\ 0 \\ 0 \end{pmatrix} = \mathbf{J_R}\dot{\vec{\alpha}}. \tag{2.2.10}$$

$\vec{L}$ consists of the orbital angular momentum due to the body's rotation about the origin, and the intrinsic angular momentum of the body about $\vec{\xi}_0$:

$$\vec{L} = m\left(\vec{\xi}_0 \times \dot{\vec{\xi}}_0\right) + \mathbf{I}_0\vec{\omega}, \tag{2.2.11}$$

where $\mathbf{I}_0$ is the intrinsic mass inertia (about $\vec{\xi}_0$). In what follows, the simpler formulations about $\vec{\xi}_0$ will be used:

$$\vec{P}_0 = \int_B \rho\dot{\vec{\xi}}dV = m\dot{\vec{\xi}}_0, \tag{2.2.12}$$

$$\vec{L}_0 = \int_B \rho\left((\vec{\xi} - \vec{\xi}_0) \times \dot{\vec{\xi}}\right)dV = \mathbf{I}_0\vec{\omega}, \tag{2.2.13}$$

where index 0 means the respective quantity is related to $\vec{\xi}_0$; $\int_B dV$ is the volume integral over the whole body.

According to Newton's second law, the changes of momentum and angular momentum in time correspond to the external forces and moments:

$$\frac{d\vec{P}_0}{dt} = \frac{d(m\dot{\vec{\xi}}_0)}{dt} = \vec{F}_0 \tag{2.2.14}$$

$$\frac{d\vec{L}_0}{dt} = \frac{d(\mathbf{I}_0\vec{\omega})}{dt} = \vec{M}_0. \tag{2.2.15}$$

Assuming a constant mass inertia $\mathbf{I}'_0$ about the body's center of gravity and expressed in local coordinates, the mass inertia in inertial coordinates reads:

$$\mathbf{I}_0 = \mathbf{S}\mathbf{I}'_0\mathbf{S}^T. \tag{2.2.16}$$

Further assuming constant mass m, the relations of external forces and moments become:

$$\vec{F}_0 = \frac{d(m\dot{\vec{\xi}}_0)}{dt} = m\ddot{\vec{\xi}}_0, \tag{2.2.17}$$

$$\vec{M}_0 = \frac{d(\mathbf{I}_0\vec{\omega})}{dt} = \dot{\mathbf{S}}\mathbf{I}'_0\mathbf{S}^T\vec{\omega} + \mathbf{S}\mathbf{I}'_0\dot{\mathbf{S}}^T\vec{\omega} + \mathbf{S}\mathbf{I}'_0\mathbf{S}^T\dot{\vec{\omega}}. \tag{2.2.18}$$

Using the skew symmetric tensor $\tilde{\omega}$,

$$\tilde{\omega} = \begin{bmatrix} 0 & -\omega_\zeta & \omega_\eta \\ \omega_\zeta & 0 & -\omega_\xi \\ -\omega_\eta & \omega_\xi & 0 \end{bmatrix} = \dot{\mathbf{S}}\mathbf{S}^T = -\mathbf{S}\dot{\mathbf{S}}^T \tag{2.2.19}$$

where $\tilde{\omega}\vec{v} = \vec{\omega} \times \vec{v}$, and considering that $\vec{\omega} \times \vec{\omega} = 0$, we can reduce eq. (2.2.18) to

$$\vec{M}_0 = \vec{\omega} \times \mathbf{S}\mathbf{I}'_0\mathbf{S}^T\vec{\omega} + \mathbf{S}\mathbf{I}'_0\mathbf{S}^T\dot{\vec{\omega}}. \tag{2.2.20}$$

For the applications considered herein, $\vec{F}_0$ and $\vec{M}_0$ are the total fluid forces and moments acting on the ship plus the action of gravity acceleration. Additional external loads, e. g. due to mooring lines or towing systems, can easily be included as well.

The translatory and rotary velocity of the body in the inertial reference frame is obtained from the generalised state vector by differentiating with respect to time:

$$\dot{\mathbf{r}} = \frac{d\mathbf{r}}{dt} = \frac{\partial \mathbf{r}}{\partial \mathbf{y}}\dot{\mathbf{y}} = \mathbf{J}\dot{\mathbf{y}} \tag{2.2.21}$$

Finally, the acceleration in inertial coordinates is related to that in generalised coordinates by:

$$\ddot{\mathbf{r}} = \frac{d(\mathbf{J}\dot{\mathbf{y}})}{dt} = \mathbf{J}\ddot{\mathbf{y}} + \mathbf{K}\dot{\mathbf{y}}, \tag{2.2.22}$$

where matrix $\mathbf{K}$ is the partial derivative of $\dot{\mathbf{r}}$ with respect to $\mathbf{y}$,

$$\begin{aligned} \mathbf{K} = \frac{\partial(\mathbf{J}\dot{\mathbf{y}})}{\partial \mathbf{y}} &= \begin{bmatrix} \mathbf{0} & \mathbf{0} \\ \mathbf{0} & \mathbf{K_R} \end{bmatrix} \\ &= \begin{bmatrix} \mathbf{0} & & \mathbf{0} \\ & 0 & -\dot{\phi}cos\psi sin\theta & -\dot{\phi}cos\psi sin\theta - \dot{\theta}cos\psi \\ \mathbf{0} & 0 & -\dot{\phi}sin\psi sin\theta & \dot{\phi}sin\psi cos\theta - \dot{\theta}sin\psi \\ & 0 & -\dot{\phi}cos\theta & 0 \end{bmatrix}. \end{aligned} \tag{2.2.23}$$

Combining eqs. (2.2.17), (2.2.18), and (2.2.22) yields a closed-form expression of the rigid body equations of motion,

$$\begin{bmatrix} m\mathbf{J_T} & \mathbf{0} \\ \mathbf{0} & \mathbf{S}\mathbf{I}'_0\mathbf{S}^T\mathbf{J_R} \end{bmatrix}\ddot{\mathbf{y}} + \begin{bmatrix} \mathbf{0} & \mathbf{0} \\ \mathbf{0} & \mathbf{S}\mathbf{I}'_0\mathbf{S}^T\mathbf{K_R} + \dot{\mathbf{S}}\mathbf{S}\mathbf{I}'_0\mathbf{S}^T\mathbf{J_R} \end{bmatrix}\dot{\mathbf{y}} = \begin{pmatrix} \vec{F}_0 \\ \vec{M}_0 \end{pmatrix} = \mathbf{f}. \tag{2.2.24}$$

Constrained Motions

Suppression of generalised degrees of freedom is easily done by removing their rows from $\mathbf{y}$, $\dot{\mathbf{y}}$ and $\ddot{\mathbf{y}}$, and eliminating the corresponding columns of $\mathbf{J}$ and $\mathbf{K}$. Forces and moments acting in the direction of suppressed degrees of freedom have no effect on the motions but need to be considered for internal loads. The load vector $\mathbf{f}$ is therefore split in a vector of applied loads acting in the directions of the degrees of freedom, $\mathbf{f_a}$, and a vector of the constraint loads acting in the directions of suppressed degrees of freedom, $\mathbf{f_c}$:

$$\mathbf{f} = \mathbf{f_a} + \mathbf{f_c} = \begin{pmatrix} \vec{F}_a \\ \vec{M}_a \end{pmatrix} + \begin{pmatrix} \vec{F}_c \\ \vec{M}_c \end{pmatrix} \tag{2.2.25}$$

Since $\mathbf{J}^T\mathbf{f_c} = \mathbf{0}$, left-hand multiplication of eq. (2.2.24) with the transpose of the Jacobian matrix eliminates the constraint forces:

$$\begin{aligned} \mathbf{J}^T\mathbf{f_a} &= \begin{pmatrix} \mathbf{J_T}^T\vec{F} \\ \mathbf{J_R}^T\vec{M} \end{pmatrix} \\ &= \begin{bmatrix} \mathbf{J_T}^T m\mathbf{J_T} & \mathbf{0} \\ \mathbf{0} & \mathbf{J_R}^T\mathbf{S}\mathbf{I}'_0\mathbf{S}^T\mathbf{J_R} \end{bmatrix}\ddot{\mathbf{y}} \\ &\quad + \begin{bmatrix} \mathbf{0} & \mathbf{0} \\ \mathbf{0} & \mathbf{J_R}^T\mathbf{S}\mathbf{I}'_0\mathbf{S}^T\mathbf{K_R} + \mathbf{J_R}^T\dot{\mathbf{S}}\mathbf{S}\mathbf{I}'_0\mathbf{S}^T\mathbf{J_R} \end{bmatrix}\dot{\mathbf{y}}. \end{aligned} \tag{2.2.26}$$

Note that eq. 2.2.26 has terms both proportional to $\dot{\mathbf{y}}$ and to $\ddot{\mathbf{y}}$. Further on, $\mathbf{S}$ and $\mathbf{J}$ depend on $\mathbf{y}$, while $\mathbf{K}$ also depends on $\dot{\mathbf{y}}$. This makes a direct solution impossible. For slowly varying $\ddot{\mathbf{y}}$ or small time steps, it may be sufficient to solve for $\ddot{\mathbf{y}}$ and use $\dot{\mathbf{y}}$ and $\mathbf{y}$ from the previous time step. Explicit formulation, however, does not yield a consistent motion state and may easily suffer from numerical instability. Instead, an iterative implicit solution is recommended. Since the coupled solver is formulated implicitly with outer iterations in each time step, this can be implemented without significant additional costs. Additionally, the present solver implements inner iterations of the rigid-body equations to accelerate the solution and improve consistency of the motion state in each outer iteration.

Constrained loads due to suppression of degrees of freedom are calculated as a post-processing step after updating the motion state:

$$\mathbf{f_c} = \mathbf{f} - \begin{bmatrix} m\mathbf{J_T} & \mathbf{0} \\ \mathbf{0} & \mathbf{S}\mathbf{I}'_0\mathbf{S}^T\mathbf{J_R} \end{bmatrix}\ddot{\mathbf{y}} + \begin{bmatrix} \mathbf{0} & \mathbf{0} \\ \mathbf{0} & \mathbf{S}\mathbf{I}'_0\mathbf{S}^T\mathbf{K_R} + \dot{\mathbf{S}}\mathbf{S}\mathbf{I}'_0\mathbf{S}^T\mathbf{J_R} \end{bmatrix}\dot{\mathbf{y}}. \tag{2.2.27}$$

Internal Loads

Internal loads are the forces and moments acting on a virtual section cut. Integrating the forces and moments on one side of this cut yields the internal loads. Equilibrium of forces requires that the forces on either side of the cut plane have the same magnitude but are opposite in sign [3]:

$$\vec{F}_{I,left}(\tilde{x}_{ref}) = -\vec{F}_{I,right}(\tilde{x}_{ref}) \Leftrightarrow$$
$$\int_{-\infty}^{\tilde{x}_{ref}} \vec{f}(\tilde{x})d\tilde{x} = -\int_{\tilde{x}_{ref}}^{\infty} \vec{f}(\tilde{x})d\tilde{x}. \tag{2.2.28}$$

$\vec{f}(\tilde{x})$ is the force vector per unit length and consists of: a curve integral of hydrodynamic forces (pressure and shear) per unit length along the intersection C of the hull surface with the plane perpendicular to $\tilde{x}$ and denoted $\vec{f}_{hydro}$; the mass inertia forces due to motions, $\vec{f}_{inertia}$; finally, additional external and reaction forces denoted by $\vec{f}_{add}$,

$$\begin{aligned}\vec{f}(\tilde{x}) &= \vec{f}_{hydro} - \vec{f}_{inertia} + \vec{f}_{add} \\ &= \int_C (p\vec{n} + \vec{\tau})ds \Big|_{\tilde{x}} - \mu(\tilde{x})\left[\ddot{\vec{\xi}}_0 + \vec{g} + \dot{\vec{\omega}} \times \vec{\tilde{x}} + \vec{\omega} \times (\vec{\omega} \times \vec{\tilde{x}})\right] + \vec{f}_{add},\end{aligned} \tag{2.2.29}$$

where $\mu(\tilde{x})$ is the mass per unit length at position $\tilde{x}$. Computation of eq. (2.2.28) can be made more efficient when the inertia related terms are evaluated beforehand, i. e. the mass, its moment of inertia and center of gravity left of each section cut are evaluated only once at the start of the transient computation.

Correspondingly, the definition of the moments is

$$\vec{M}_{I,left}(\tilde{x}_{ref}) = \int_{-\infty}^{\tilde{x}_{ref}} \left[(\tilde{x} - \tilde{x}_{ref}) \times \vec{f}(\tilde{x})\right] d\tilde{x}. \tag{2.2.30}$$

[3] For the sake of simplicity, the notation here assumes that $\tilde{x}$ is a coordinate axis normal to the section cut plane, and $\tilde{x}_{ref}$ is the location of the section. Note that, however, resulting forces and moments are expressed in the inertial reference system.

Like the computation of constraint forces, the evaluation of internal loads is a post-processing step of the motion solver and performed at the end of each time step during the simulation.

2.2.2 Extension to Flexible Bodies

The definition of coordinate systems remains as before with rigid bodies. However, $\vec{x}$ now is the location vector of an arbitrary material point of an elastic body. $\vec{x}$ is composed of a rigid (time-invariant) part $\vec{r}$ and an instantaneous deformation $\vec{u}(t)$, see Fig. 2.2:

$$\vec{x}(t) = \vec{r} + \vec{u}(t). \tag{2.2.31}$$

The position of any material point of the ship is then

$$\vec{\xi}(t) = \vec{\xi}_0(t) + \mathbf{S}(t)\,(\vec{r} + \vec{u}(t)). \tag{2.2.32}$$

Differentiation of eq. (2.2.32) with respect to time yields

$$\dot{\vec{\xi}} = \dot{\vec{\xi}}_0 + \dot{\mathbf{S}}(\vec{r} + \vec{u}) + \mathbf{S}\dot{\vec{u}} = \underbrace{\dot{\vec{\xi}}_0 + \vec{\omega} \times \mathbf{S}\vec{r}}_{rigid-body\,part} + \underbrace{\vec{\omega} \times \mathbf{S}\vec{u} + \mathbf{S}\dot{\vec{u}}}_{elastic\,part}, \tag{2.2.33}$$

$$\begin{aligned} \ddot{\vec{\xi}} = &\underbrace{\ddot{\vec{\xi}}_0 + \dot{\vec{\omega}} \times \mathbf{S}\vec{r} + \vec{\omega} \times (\vec{\omega} \times \mathbf{S}\vec{r})}_{rigid-body\,part} \\ &+ \underbrace{\mathbf{S}\ddot{\vec{u}} + \dot{\vec{\omega}} \times \mathbf{S}\vec{u} + \vec{\omega} \times (\vec{\omega} \times \mathbf{S}\vec{u}) + 2\vec{\omega} \times \mathbf{S}\dot{\vec{u}}}_{elastic\,part}. \end{aligned} \tag{2.2.34}$$

The right-hand side terms in eqs. (2.2.33) and (2.2.34) are separated into rigid-body parts and additional contributions due to deformations.

Splitting of large amplitude motions and small elastic deformations is performed in a way that the elastic displacements shall, for all times, neither change the momentum of the body nor its angular momentum, i. e., the motion state of the local reference frame remains unaffected of linear elastic deformations. This is equivalent to assuming that the overall sums of external forces and moments equal the total change of momentum and angular momentum. Then again, local imbalances due to unequal distributions of external and internal forces cause deformations, Söding (2006).

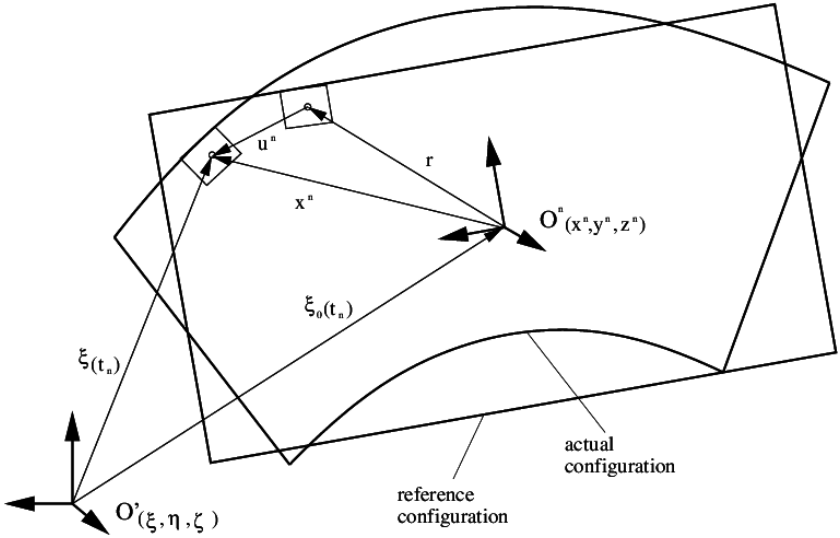

Figure 2.2: Definition of the instantaneous position of a material point of an elastic body; black: undeformed (rigid) body; red: elastically deformed body. Source: Oberhagemann (2006)

A consistent formulation of translatory motions thus requires the following definition of the center of gravity:

$$\frac{1}{m}\int_B \rho\vec{\xi}\,dV = \vec{\xi}_0 \quad \Longrightarrow \quad \frac{1}{m}\int_B \rho\vec{x}\,dV = \frac{1}{m}\int_B \rho\vec{r}\,dV = \vec{0}, \tag{2.2.35}$$

In case of a rigid body or in absence of elastic displacements $\vec{u}$, this definition is trivial. For a deformed body, eq. (2.2.35) implies

$$\frac{1}{m}\int_B \rho\,(\vec{r}+\vec{u})\,dV = \vec{0} \quad \Longrightarrow \quad \frac{1}{m}\int_B \rho\vec{u}\,dV = \vec{0}. \tag{2.2.36}$$

From eq. (2.2.36) follows that $\int_B \rho\dot{\vec{u}}\,dV = \int_B \rho\ddot{\vec{u}}\,dV = \vec{0}$. Combining eqs. (2.2.17), (2.2.35) and (2.2.36), the definition of $\vec{F}_0$ remains the same as for the rigid-body

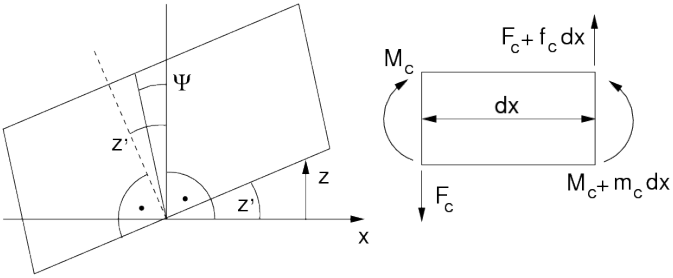

Figure 2.3: Nodal degrees of freedom of the Timoshenko beam (left); equilibrium of forces for an infinite beam cross section (right), f_c and m_c are forces and moments per length, respectively. Source: Oberhagemann (2006)

case:

$$\vec{F}_0 = \frac{d\vec{P}_0}{dt} = \int_B \rho \ddot{\vec{\xi}} dV = m\ddot{\vec{\xi}}_0 \tag{2.2.37}$$

The corresponding derivation of $\vec{M}_0$ is provided in appendix B.

2.2.3 Finite Element Timoshenko Beam

The ship hull, or, generally speaking, the body under investigation is idealized with a straight-line Timoshenko beam with two nodal degrees of freedom, vertical displacement z and horizontal rotation Ψ, Fig. 2.3 (left). The Timoshenko beam formulation allows (linearised) planar shear deformation, so the section rotation is not identical with the derivative of the deflection in beam-wise direction, z', like is the case for a Bernoulli beam. Displacement z and rotation Ψ are linked through a set of differential equations, here given for the unloaded beam,

$$\begin{aligned} \left(EI\Psi'\right)' + GA_S\left(z' - \Psi\right) - \bar{\mu}\ddot{\Psi} &= 0 \\ \left(GA_S\left(z' - \Psi\right)\right)' - \mu\ddot{z} &= 0, \end{aligned} \tag{2.2.38}$$

with Young's modulus E, shear modulus G, area moment of inertia I, effective sectional shear area A_S, mass per length unit μ, and mass inertia per length unit

$\bar{\mu}$. Disregarding the small terms $\bar{\mu}\ddot{\Psi}$ and $\mu\ddot{z}$, z and Ψ are related by

$$z' = \Psi - \frac{EI}{GA_S}\Psi''. \tag{2.2.39}$$

Finite Element Formulation

The numerical calculation of elastic deformations is accomplished with the finite element method (FEM). Elemental properties E, I, G, A_S, μ and $\bar{\mu}$ are assumed constant over the element length l_E. The deformations are approximated for each element by a set of polynomial shape functions which represent elementary deformation modes, and, for any given time t, relate the deformation at a given position s with the deformation of the element's nodes,

$$z(s,t) = \tilde{\mathbf{q}}(s) \cdot \mathbf{u}_j(t), \tag{2.2.40}$$

where s is a local coordinate with $0 < s < 1$, and $\mathbf{u}_j(t)$ is the vector of degrees of freedom of element j,

$$\mathbf{u}_j = \begin{bmatrix} z_{left} \\ \Psi_{left} \\ z_{right} \\ \Psi_{right} \end{bmatrix}. \tag{2.2.41}$$

Vector $\tilde{\mathbf{q}}$ in eq. (2.2.40) is composed from the shape functions. The higher order derivatives in eq. (2.2.38) require third order shape functions based on Hermite polynomials of third order, which in turn results in smooth deformation slopes along the beam axis. Further on, the coupling of the displacements and rotations through eq. (2.2.39) requires two sets of shape functions, $\mathbf{p}$ and $\mathbf{q}$, which read

$$\begin{aligned} \mathbf{q} &= \frac{1}{1+\kappa} \begin{bmatrix} 1+\kappa-\kappa s-3s^2+2s^3 \\ l_E\left(s^3-(2+\frac{\kappa}{2})s^2+(1+\frac{\kappa}{2})s\right) \\ -2s^3+3s^2+\kappa s \\ l_E\left(s^3-(1-\frac{\kappa}{2})s^2-\frac{\kappa}{2}s\right) \end{bmatrix} \\ \mathbf{p} &= \frac{1}{1+\kappa} \begin{bmatrix} \frac{6}{l_E}(s^2-s) \\ 3s^2-(4+\kappa)s+1+\kappa \\ \frac{6}{l_E}(s^2-s) \\ 3s^2-(2-\kappa)s \end{bmatrix}, \end{aligned} \tag{2.2.42}$$

with a non-dimensional coefficient κ relating bending stiffness and shear stiffness,

$$\kappa = \frac{12EI}{GA_S l_E^2}. \tag{2.2.43}$$

According to the Galerkin method, the elemental mass and stiffness matrices are computed by multiplication of the shape functions with the constitutive functional operators for mass and stiffness and integration over the element. For example, the element stiffness matrix reads

$$\mathbf{K}_{kj} = l_E \int_0^1 EI\mathbf{p}_k'(\mathbf{p}_j')^T ds + l_E \int_0^1 GA_S(\mathbf{q}_k' - \mathbf{p}_j)(\mathbf{q}_k' - \mathbf{p}_j)^T ds. \tag{2.2.44}$$

Having established the element matrices, these are assembled to the linear algebraic system of equations

$$\mathbf{M}\ddot{\mathbf{u}} + \mathbf{D}\dot{\mathbf{u}} + \mathbf{K}\mathbf{u} = \mathbf{f}(t), \tag{2.2.45}$$

with the vector of the nodal degrees of freedom $\mathbf{u}$, mass matrix $\mathbf{M}$, damping matrix $\mathbf{D}$, stiffness matrix $\mathbf{K}$, and the forcing vector $\mathbf{f}(t)$. The matrices are symmetric and have band matrix structure with entries only on three subdiagonals. The forcing vector comprises the external fluid forces and moments as well as mass inertia forces and moments due to rigid-body motions. Forces and moments per length are multiplied with the shape functions and integrated over the element.

Structural Damping

For ship structures, no practical procedure exists to establish the functional operators for the damping matrix. However, in order to allow for damping contributions not arising from external forcing[4], a Rayleigh damping approach is implemented where the damping matrix is a linear combination of mass and stiffness matrix,

$$\mathbf{D} = \alpha_R \mathbf{M} + \beta_R \mathbf{K} \tag{2.2.46}$$

[4]For example, this could be material damping or cargo damping

For known damping ratios D_1 and D_2 associated with natural frequencies ω_1 and ω_2, respectively, parameters α_R and β_R are

$$\begin{aligned} \alpha_R &= \frac{2\omega_1\omega_2(D_1\omega_2 - D_2\omega_1)}{\omega_2^2 - \omega_1^2}, \\ \beta_R &= \frac{2(D_2\omega_2 - D_1\omega_1)}{\omega_2^2 - \omega_1^2}. \end{aligned} \tag{2.2.47}$$

Eq. (2.2.47) allows to adjust the damping to match the required damping at two frequencies ω_1 and ω_2 but introduces deviations for other frequencies. The damping coefficients will typically be adjusted to the lowest natural frequencies because these account for the major part of vibration energy. Higher frequencies do not contribute significantly to the overall level of vibration, hence errors introduced at higher frequencies are tolerable.

Internal Loads

Flexural motions contribute to the internal loads in that the corresponding accelerations add to the mass inertia forces. Their computation for a section cut at a reference location $\vec{x}_{ref}$ outlines as follows; for each element j and each elemental degree of freedom k, force $\vec{\mu}_{j,k}$ and moment $\vec{\bar{\mu}}_{j,k}$ per unit acceleration are computed via the associated shape functions q_k and r_k, $k = 1 \ldots 4$ which are multiplied by the mass and mass inertia per length, respectively, and integrated over the element:

$$\begin{aligned} \vec{\mu}_{j,k} &= \int_0^{s_j} \vec{e}_3 q_k \mu_j \, ds \\ \vec{\bar{\mu}}_{j,k} &= \int_0^{s_j} \left[(\vec{r}(s) \times [\vec{e}_3 q_k \mu_j]) - \vec{e}_2 r_k \bar{\mu}_j \right] ds, \end{aligned} \tag{2.2.48}$$

where $\vec{r}_s$ is the vector from the reference location $\vec{x}_{ref}$ (section cut) to the instantaneous integration location, and vectors $\vec{e}$ are the constituting unit vectors of the local coordinate system. The upper integration limit s_j is defined as

$$s_j = max\left(0, min\left(s_{ref}, 1\right)\right), \tag{2.2.49}$$

with s_{ref} being the ordinate of the section cut position relative to the beam element. Next, the contributions of all N_E elements are summed up and combined to a matrix $\mathbf{P}$,

$$\mathbf{P} = \left[\begin{array}{cccccc} \vec{\mu}_{1,1} & \vec{\mu}_{1,2} & \vec{\mu}_{1,3}+\vec{\mu}_{2,1} & \vec{\mu}_{1,4}+\vec{\mu}_{2,2} & \vec{\mu}_{2,3}+\vec{\mu}_{3,1} & \vec{\mu}_{2,4}+\vec{\mu}_{3,2} \\ \vec{\mu}_{1,1} & \vec{\mu}_{1,2} & \vec{\mu}_{1,3}+\vec{\mu}_{2,1} & \vec{\mu}_{1,4}+\vec{\mu}_{2,2} & \vec{\mu}_{2,3}+\vec{\mu}_{3,1} & \vec{\mu}_{2,4}+\vec{\mu}_{3,2} \end{array} \cdots \right.$$
$$\left. \begin{array}{ccc} \vec{\mu}_{N_E-1,4}+\vec{\mu}_{N_E,2} & \vec{\mu}_{N_E,3} & \vec{\mu}_{N_E,4} \\ \vec{\mu}_{N_E-1,4}+\vec{\mu}_{N_E,2} & \vec{\mu}_{N_E,3} & \vec{\mu}_{N_E,4} \end{array} \right], \tag{2.2.50}$$

which is finally multiplied with the vector of nodal accelerations to yield the internal forces and moments,

$$\left(\begin{array}{c} \vec{F}_{I,vib}(\tilde{x}_{ref}) \\ \vec{M}_{I,vib}(\tilde{x}_{ref}) \end{array} \right) = -\mathbf{P} \cdot \ddot{\mathbf{u}}. \tag{2.2.51}$$

2.2.4 Time Integration

The solvers for the nonlinear equations of rigid-body motions and the linear equations of elastic deformations use a common time integration scheme which is an iterative version of the Newmark scheme with underrelaxation. The motion equation at hand is solved for the second time derivative of the state vector $\mathbf{u}$, i. e., the vector of accelerations $\ddot{\mathbf{u}}$. In iteration k of time step i, the vectors of velocity, $\dot{\mathbf{u}}$, and position, $\mathbf{u}$, are then obtained from $\ddot{\mathbf{u}}^{i,k}$ using

$$\dot{\mathbf{u}}^{i,k} = \dot{\mathbf{u}}^{i-1} + \Delta t \left[(1-\gamma)\, \ddot{\mathbf{u}}^{i-1} + \gamma \ddot{\mathbf{u}}^{i,k} \right] \tag{2.2.52}$$

$$\mathbf{u}^{i,k} = \mathbf{u}^{i-1} + \Delta t \dot{\mathbf{u}}^{i-1} + \frac{\Delta t^2}{2} \left[(1-2\beta)\, \ddot{\mathbf{u}}^{i-1} + 2\beta\, \ddot{\mathbf{u}}^{i,k} \right]. \tag{2.2.53}$$

β and γ are integration parameters. The Newmark time marching scheme is unconditionally stable if

$$\begin{aligned} \gamma &\geq 0.5 \\ \beta &\geq 0.25\,(0.5+\gamma)^2\,. \end{aligned} \tag{2.2.54}$$

Setting $\gamma = 0.5$ and $\beta = 0.25$ yields second order accuracy.

For the solution of the linear FE system of equations, eqs. (2.2.45), (2.2.52) and (2.2.53) are combined to

$$\begin{aligned}\left[\mathbf{M}+\gamma\Delta t\mathbf{D}+\beta\Delta t^2\mathbf{K}\right]\ddot{\mathbf{u}}^{i,k} &= \mathbf{f}^{i,k}-\left[\mathbf{D}\tilde{\mathbf{u}}^{i,k}+\mathbf{K}\tilde{\mathbf{u}}^{i,k}\right]\\ \tilde{\mathbf{M}}\ddot{\mathbf{u}}^{i,k} &= \tilde{\mathbf{f}}^{i,k},\end{aligned} \tag{2.2.55}$$

where the right-hand side consists of the force vector and known terms from the old time step,

$$\begin{aligned}\tilde{\dot{\mathbf{u}}}^{i,k} &= \dot{\mathbf{u}}^{i-1}+\Delta t\,(1-\gamma)\,\ddot{\mathbf{u}}^{i-1}\\ \tilde{\mathbf{u}}^{i,k} &= \mathbf{u}^{i-1}+\Delta t\dot{\mathbf{u}}^{i-1}+\frac{\Delta t^2}{2}\,(1-2\beta)\,\ddot{\mathbf{u}}^{i-1}.\end{aligned} \tag{2.2.56}$$

2.3 Solver Coupling and Communication

The coupling scheme between CFD and CSD solvers is an implicit two-way coupling to account for the mutual dependency between fluid and structure. In each time step, the solutions on both fluid and structure domain are found in an iterative way, whereas in each iteration an update of the fluid and structural solution is found alternatingly as well as an update of the nonlinear 6-DoF motion state, see Brunswig and el Moctar (2004) and Oberhagemann (2006). Compared to the solution of the RANS equations, the small-size additional sets of equations of the two motion solvers add only minor computation efforts.

Since the pressure-velocity coupling scheme of the fluid flow solvers is based on the iterative SIMPLE and PIMPLE pressure-velocity coupling schemes, iterative coupling with the structure solvers is easily accomplished by integrating calls to these solvers into the outer iteration sequences of the CFD solvers. To improve numerical stability and convergence, under-relaxation is applied to all solvers.

During the iterative coupling of fluid and structure solvers in each time step, updates of the fluid forces acting on the hull are communicated to the structure solvers, and hull motions and deflections are communicated back to the fluid solver through CFD grid deformations according to the instantaneous position and deflection.

The solution sequence within each time is as follows:

- Update of the nonlinear rigid-body motion state using fluid forces from the previous iteration or time step, whichever is available

- Update of the linear elastic deformation state based on most recent fluid forces and rigid-body inertia forces
- Fluid grid deformation according to the instantaneous total motion state
- Solution sequence of momentum predictor and pressure corrector steps according to the pressure-velocity coupling scheme
- Check for convergence according to applicable convergence criteria
- Advance to new time step in case of convergence, otherwise perform next iteration

In the first iterations of a time step, mass inertia forces due to gravity and ship motions are not balanced with the fluid forces because of under-relaxation and the time lag of fluid forces in the first iteration. This imbalance of fluid and inertia loads may influence the linear elastic deformations significantly and therefore must be eliminated by careful iteration until it has dropped below a small threshold. Otherwise, the deformations will show undesired drift with time due to unbalanced forces and moments. Further on, imbalance of forces also affects the evaluated internal loads.

2.3.1 Mesh Morphing

The motions and deformations of the body correspond to displacements of the fluid grid boundary nodes representing its surface. In order to maintain fluid mesh quality, this boundary displacement due to rigid and flexural motions has to be propagated into the fluid domain while maintaining the quality of the volume mesh.

Following criteria need to be considered; cells must have positive volume; cells must not penetrate each other; face edges must have positive length; control volumes must not be stretched excessively; face edge angles must not become too small or large. In addition, the grid node density distribution shall be maintained as far as possible.

The first three of these criteria must be strictly adhered to, otherwise the algebraic systems of the linearised NS equations become singular. Violation of the other criteria is less critical, however, may still cause divergence of the solution or at least lead to useless results.

A variety of grid morphing approaches exists, e. g., Laplacian based methods that diffuse the boundary displacements into the interiour of the solution domain,

and stiffness based approaches that deform the grid in analogy to solids or systems of springs.

While such methods are applicable to a variety of boundary displacements in a generical sense, they come at a relatively high computational expense. In case of the present structure solvers, specialised grid morphers can take advantage of the limited number of degrees of freedom. Moreover, the simplicity of the structural representation offers an efficient and unambiguous allocation of the grid node displacements to a given structural deformation.

Finite element nodal displacements are transformed to fluid grid node displacements via an analytical scheme that computes the displacement of the grid nodes from displacements at reference locations on the beam axis. Deflection z and rotation Ψ are known for any position along the longitudinal axis of the body from the linear deformation state $\mathbf{u}$. Each fluid grid node is now assigned to a reference point $\vec{x}_r$ on the beam axis. Deflection z_r and rotation Ψ_r at position $\vec{x}_r$ are then evaluated from the element node deformations of the corresponding element using the element shape functions. The instantaneous displacement of the grid node is

$$\Delta\vec{x} = \begin{bmatrix} \cos\psi_r & 0 & -\sin\psi_r \\ 0 & 1 & 0 \\ \sin\psi_r & 0 & \cos\psi_r \end{bmatrix} (\vec{x}-\vec{x}_r) + \begin{pmatrix} 0 \\ 0 \\ z_r \end{pmatrix}, \tag{2.3.1}$$

where $\vec{x}$ is the undisplaced position of the grid node. See also Fig. 2.4. For grid nodes beyond the ends of the beam, the displacements and rotations are extrapolated. In order to avoid excessive grid deformations far off the body, all grid node displacements are multiplied with a factor that exponentially decreases with increasing distance away from the body.

Grid node displacements due to rigid-body motions are performed in a similar way. The displacement for each grid node is obtained from eq. (2.2.7) using the translation and rotation of the body, and is then scaled with the same exponential decay function.

This grid morphing approach is fast and scalable since it requires only a few (and fixed) number of operations per grid node. It is easily parallelized because the transformations are performed independently for each grid node. On the other hand, none of the criteria on grid quality put up in the beginning of this paragraph is explicitly enforced, therefore, this morphing approach has no inherent mechanism to preserve grid quality. Fig. 2.5 shows a fluid grid

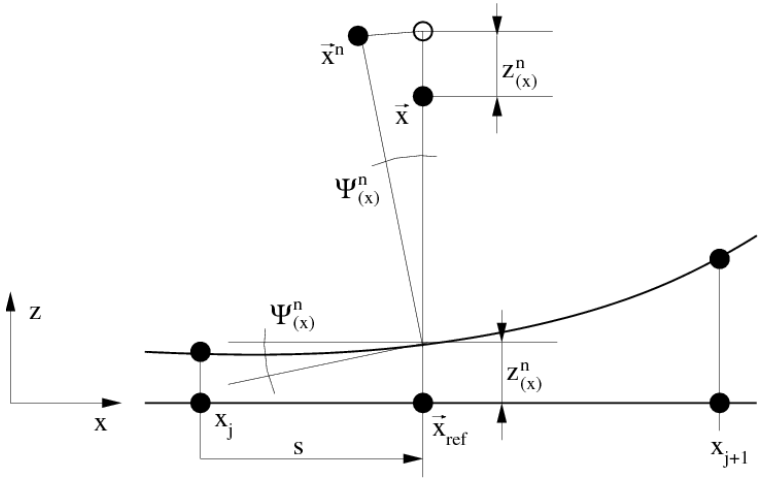

Figure 2.4: Fluid grid node displacement according to beam deformation. Source: Oberhagemann and el Moctar (2007)

with strong deformations due to large amplitude roll motion. Although large motion amplitudes including roll angles of more than 60^o could be realised in the simulation without producing degenerated volumes, grid quality became poor already for smaller amplitudes.

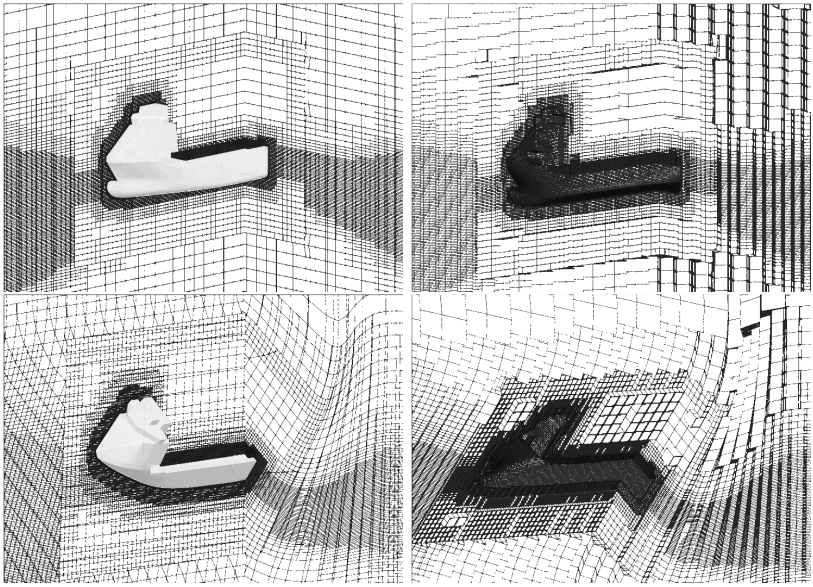

Figure 2.5: Grid deformation with analytical morphing for simulation of large amplitude roll motions; undeformed (top) and deformed grid (bottom)

3 Wave Load Statistics

This chapter introduces probabilistic methods to describe wave load processes and corresponding loads on ships. The chapter starts with fundamentals of the statistical description of wind generated ocean waves. Next, concepts of short- and long-term statistical analysis of ship responses (reactions) to waves are introduced. Starting point is the standard closed-form analysis based on spectral moments of a linear response with narrow-banded response spectrum. It is based on assuming a linear correlation of the ship response amplitude with wave amplitude, and is usually employed in combination with linear frequency domain seakeeping theory. Nonlinear reactions, however, often require statistical approaches based on time-domain simulations. Several concepts based on transient computations are introduced here which will later be applied in case studies.

3.1 Statistical Description of Waves

Ocean waves are excited by wind forces which continuously vary in space and time. For short time intervals, however, the wind conditions (velocity and direction) at a given location can be regarded stationary. The wind generated waves corresponding to a given stationary wind condition also form a stochastic process with certain stationary characteristics, called a sea state. Sea states are usually described by their significant wave height H_S and the zero-upcrossing period T_z. The significant wave height is defined as the mean height of the one third largest waves. It corresponds to the traditional and rather intuitive visual observation characterisation system of seamen. T_z is the mean period between upcrossings of the water surface through the mean level at any given location.

When wind blows over an undisturbed water surface, the friction forces at the water-air interface generate small waves starting with capillary waves dominated by the surface tension. Interaction of these waves soon transfers energy towards lower frequencies (dispersion of these waves is now governed by gravity), while the continuous energy transfer from air to water increases the height of the waves.

Depending on the duration of the wind action and the fetch[1], the wave energy increases and the frequency distribution of waves changes, until asymptotically reaching a fully developed condition.

In addition to the spectral distribution of wave energy, atmospheric turbulences cause a scatter of wave propagation directions around the mean wind direction which is called directional spreading.

Once generated, the wave energy disperses for large distances almost without loosing energy. Hence, at any given location, the present wave system can be divided into waves due to the prevailing wind (wind sea) and waves due to wave generation at other locations (swell). Due to interaction of waves, swell typically becomes dominated by a very narrow band of wave frequencies and has only small directional spreading.

3.1.1 Spectral Wave Energy Distribution

For short periods, the wave elevation, ζ_W, can be described as a stationary zero-mean ergodic Gaussian process. The Joint North Sea Wave Project (JONSWAP), Hasselmann et al. (1973), investigated the spectral distribution of wind sea wave energy for fetch limited situations. The spectral energy density distribution, S, as a function of wave frequency ω is defined by wind speed (measured $10\,m$ above sea level), fetch and wind duration.

$$S_\zeta(\omega) = \frac{\alpha_J g^2}{\omega^5} exp\left[-\beta_J \left(\frac{\omega_p}{\omega}\right)^4\right] \cdot \gamma^{exp\left(\frac{-(\omega-\omega_p)^2}{2\sigma_J^2\omega_p^2}\right)}. \tag{3.1.1}$$

with the spectral peak frequency ω_p and constant parameters $\beta_J = 1.25$,

$$\sigma_J = \begin{cases} 0.07 & : \quad \omega < \omega_p \\ 0.09 & : \quad \omega \geq \omega_p \end{cases}, \tag{3.1.2}$$

and the spectral shape parameter

$$\alpha_J = 5.061 \frac{H_S^2}{T_p^4} \left(1 - 0.287 \ln(\gamma)\right). \tag{3.1.3}$$

[1] The effective length of constant wind action

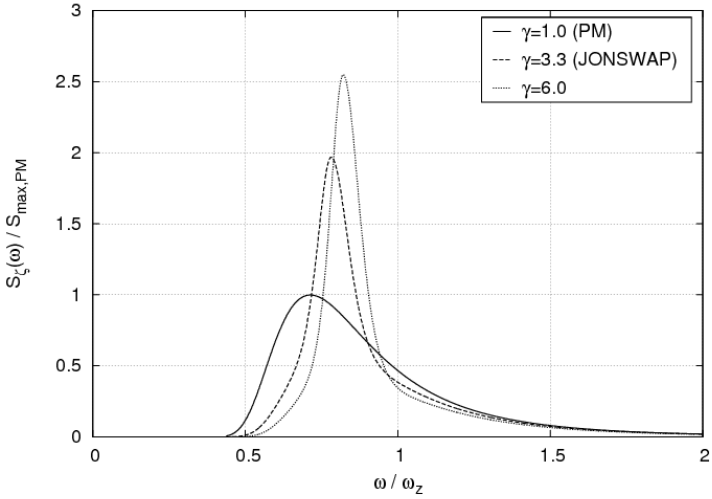

Figure 3.1: Spectral density distributions for selected values of γ

$T_p = 2\pi/\omega_p$ is the peak period, γ the spectral peakedness parameter. Wave observations indicate that γ typically ranges from 1 to 6. $\gamma = 3.3$ was proposed as an observed average value for developing, fetch-limited seas. $\gamma = 1$ corresponds to the Pierson-Moskowitz (PM) wave spectrum for fully developed wind seas, Pierson and Moskowitz (1964), see also IACS (2001).

For wind sea, the directional energy distribution of wave dispersion is assumed normal distributed around the mean wind direction, μ_0. It is common practice in engineering to approximate the distribution density by a cosine power function, with a cosine squared distribution as the widely accepted standard, IACS (2001),

$$S_\zeta(\omega,\mu) = \begin{cases} S_\zeta(\omega)\frac{2}{\pi}cos^2(\mu-\mu_0) & : \quad |\mu-\mu_0| < 90^o \\ 0 & : \quad otherwise \end{cases} \tag{3.1.4}$$

The visual characteristics of a sea state mentioned above can be derived conveniently from the spectral energy density distribution using spectral moments,

$$m_{j,\zeta} = \int_0^\infty (\omega)^j S_\zeta(\omega)\, d\omega, \tag{3.1.5}$$

where $m_{j,\zeta}$ is called the j-th spectral moment of S_ζ. The significant wave height reads

$$H_S = 4\sqrt{m_0}, \tag{3.1.6}$$

while the zero upcrossing period T_z and defined as

$$T_z = \frac{1}{2\pi}\sqrt{\frac{m_2}{m_0}}. \tag{3.1.7}$$

3.1.2 Discretised Wave Elevation Process

At a given location $\vec{\xi}$, the free surface wave elevation ζ_W is a function of time and has the representation

$$\zeta(t) = \int_0^\infty \left[\cos(\omega t)\, dU(\omega) + \sin(\omega t)\, dV(\omega)\right], \tag{3.1.8}$$

with zero-mean independent normal random variables $U(\omega)$ and $V(\omega)$,

$$E\left[dU^2(\omega)\right] = E\left[dV^2(\omega)\right] = S_\zeta(\omega) d\omega. \tag{3.1.9}$$

An equivalent formulation directly expresses ζ in terms of the spectral energy density distribution $S_\zeta(\omega)$,

$$\zeta(t) = \int_0^\infty \sqrt{\frac{S_\zeta(\omega)}{2\omega}} \cos\left(\omega t + \Theta(\omega)\right) d\omega, \tag{3.1.10}$$

where $\Theta(\omega)$ is a uniformly distributed random phase angle, $0 \leq \Theta \leq 2\pi$. Additional alternatives exist, e.g. a complex formulation commonly used in frequency domain ship response analyses. Discretising eq. 3.1.8 or eq. 3.1.10 allows to generate random realisations (samples) of $\zeta(t)$. The wave elevation process is then approximated by a superposition of a finite number of sinusoidal harmonic components. Using eq. 3.1.10, the wave process discretised by n components reads

$$\zeta(t) = \sum_{i=0}^{n} a_{\zeta,i} \cos(\omega_i t + \Theta_i) \tag{3.1.11}$$

where the component's amplitudes are defined by the spectral energy distribution of the sea state,

$$a_{\zeta,i} = \sqrt{2 S_\zeta(\omega_i)\Delta\omega}. \tag{3.1.12}$$

The Θ_i are again uniformly distributed random variables, and also the frequencies ω_i are randomly chosen from the respective frequency bands of width $\Delta\omega$ centered around the mean frequencies ω_i. Random variation of the ω_i increases the maximum sample time before repetition of the process.

For a coordinate system $\mathbf{O}_{(\xi,\eta,\zeta)}$ with its origin located at the mean free surface level $\zeta_0 = 0$ and moving with the average ship forward speed v, the wave elevation process $\zeta(\vec{\xi},t)$ at the origin $\vec{\xi} = [0,0,0]^T$ and time t is represented by

$$\zeta(t) = \sum_{i=1}^{n} a_{\zeta,i}\left(\cos(\omega_i^e t + \Theta_i)\right). \tag{3.1.13}$$

Here, the Doppler effect requires the wave frequency ω to be replaced by the the wave encounter frequency, ω_e, defined as

$$\omega_i^e = \omega_i - k_i v \cos(\mu_i), \tag{3.1.14}$$

with the and the gravity acceleration g and wave numbers for deep-water waves k, $k_i = \omega_i^2/g$. Wave encounter angles $\mu = 0^\circ$ and $\mu = 90^\circ$ correspond to following waves and waves from starboard, respectively.

The surface elevation for any location $\vec{\xi} = [\xi, \eta, \zeta]^T$ is

$$\zeta(\vec{\xi},t) = \sum_{i=1}^{n} a_{\zeta,i}\left[\cos(\omega_i t - k_i \tilde{x})\right], \qquad \tilde{x} = (\xi + vt, \eta, \zeta)\cdot\begin{pmatrix}\cos\mu\\ \sin\mu\\ 0\end{pmatrix}. \tag{3.1.15}$$

3.1.3 Wave Climate

Large scale atmospheric processes cause an inhomogeneous global distribution of prevailing winds and, as a consequence, a spatial distribution of different wave climates. The west wind drift zones of the North Atlantic (NA), the North Pacific and the Southern Ocean are characterised by harsh wave environments due to the

Hs/Tz	1.5	2.5	3.5	4.5	5.5	6.5	7.5	8.5	9.5	10.5	11.5	12.5	13.5	14.5	15.5	16.5	17.5	18.5	SUM
0.5	0.0	0.0	1.3	133.7	865.6	1186.0	634.2	186.3	38.9	5.6	0.7	0.1	0.0	0.0	0.0	0.0	0.0	0.0	3060
1.5	0.0	0.0	0.0	29.3	986.0	4586.0	7738.0	5648.7	2375.7	703.5	160.7	30.5	5.1	0.8	0.1	0.0	0.0	0.0	22575
2.5	0.0	0.0	0.0	2.2	197.5	2169.8	6230.0	7449.5	4880.4	2068.0	644.5	180.2	33.7	6.3	1.1	0.2	0.0	0.0	23810
3.5	0.0	0.0	0.0	0.2	34.9	696.5	3226.5	6676.0	5099.1	2838.0	1114.1	337.7	84.3	18.2	3.5	0.6	0.1	0.0	19128
4.5	0.0	0.0	0.0	0.0	6.0	198.1	1364.3	3288.5	3857.5	2685.5	1276.2	455.1	130.9	31.9	6.9	1.3	0.2	0.0	13389
5.5	0.0	0.0	0.0	0.0	1.0	51.0	498.4	1602.9	2372.7	2008.3	1126.0	463.6	160.9	41.0	9.7	2.1	0.4	0.1	9328
6.5	0.0	0.0	0.0	0.0	0.2	12.6	167.0	690.3	1257.9	1268.6	825.9	386.8	140.8	42.2	10.9	2.5	0.5	0.1	4806
7.5	0.0	0.0	0.0	0.0	0.0	3.0	52.1	270.1	594.4	703.2	524.9	276.7	111.7	36.7	10.2	2.5	0.6	0.1	2586
8.5	0.0	0.0	0.0	0.0	0.0	0.7	15.4	97.9	255.9	350.6	296.9	174.6	77.6	27.7	8.4	2.2	0.5	0.1	1309
9.5	0.0	0.0	0.0	0.0	0.0	0.2	4.3	33.2	101.9	159.9	162.2	99.2	48.3	18.7	6.1	1.7	0.4	0.1	626
10.5	0.0	0.0	0.0	0.0	0.0	0.0	1.2	10.7	37.9	67.5	71.7	51.5	27.3	11.4	4.0	1.2	0.3	0.1	285
11.5	0.0	0.0	0.0	0.0	0.0	0.0	0.3	3.3	13.3	26.6	31.4	24.7	14.2	6.4	2.4	0.7	0.2	0.1	124
12.5	0.0	0.0	0.0	0.0	0.0	0.0	0.1	1.0	4.4	9.9	12.8	11.0	6.8	3.3	1.3	0.4	0.1	0.0	51
13.5	0.0	0.0	0.0	0.0	0.0	0.0	0.0	0.3	1.4	3.5	5.0	4.6	3.1	1.6	0.7	0.2	0.1	0.0	21
14.5	0.0	0.0	0.0	0.0	0.0	0.0	0.0	0.1	0.4	1.2	1.8	1.8	1.3	0.7	0.3	0.1	0.0	0.0	8
15.5	0.0	0.0	0.0	0.0	0.0	0.0	0.0	0.0	0.1	0.4	0.6	0.7	0.5	0.3	0.1	0.1	0.0	0.0	3
16.5	0.0	0.0	0.0	0.0	0.0	0.0	0.0	0.0	0.0	0.1	0.2	0.2	0.2	0.1	0.1	0.0	0.0	0.0	1
SUM:	0	0	1	166	2091	9280	19922	24879	20870	12898	6245	2479	837	247	66	16	3	1	100000

Figure 3.2: Cumulative joint probability distributions of H_S and T_z as recommended by the IACS for ship structural load assessments; source: IACS (2001)

Table 3.1: Coefficients for joint distribution functions of H_S and T_z for the North Atlantic and the DNV GL wave climate for world-wide trade

	α_{Hs}	β_{Hs}	γ_{Hs}	a_0	a_1	a_2	b_0	b_1	b_2
NA	3.04	1.48	0.66	0.70	1.27	0.13	0.13	0.03	−0.19
WW	1.80	1.21	0.86	−1.01	2.85	0.08	0.16	0.15	−0.68

frequent passages of cyclones, whereas the equatorial regions of the innertropical convergence zone, for instance, have comparatively constant weather conditions with low to moderate winds and hence much milder wave climates. Yet, these regions suffer from the occurrence of tropical storms. Further on, the wave climate of sheltered coastal areas is different from that of open ocean areas with longer fetch.

Visual observations, wave buoy and satellite measurement data provide statistical information about the long-term probability distributions of significant wave height and wave period. Metocean service providers collect these data and distribute them in form of joint probability tables of H_S, T_z and wind directions for specific sea areas, so-called wave scatter tables, see e.g. BMT (1986). Some scatter tables also include seasonal information.

Scatter tables give, for specific sea areas, the joint probabilities $p(T_z, H_S)$ of encountering, at an arbitrary time instant, a sea state condition with significant wave height and zero-upcrossing period within small ranges around their characteristic values of H_S and T_z, respectively; a typical resolution is $\Delta H_S = 1\,m$

and $\Delta T_z = 1\,s$. Alternatively, wave environment models may specify $p(T_z, H_S)$ through distribution functions which allow for any desired degree of refined resolution. Joint distribution functions are established in terms of a marginal distribution function of one quantitiy and conditional density functions of the respective other quantity. DNV (2010) recommends a 3-parameter Weibull distribution for the significant wave height,

$$f_{H_S}(h) = \frac{\beta_{Hs}}{\alpha_{Hs}} \left(\frac{h - \gamma_{Hs}}{\alpha_{Hs}} \right)^{\beta_{Hs}-1} exp \left[- \left(\frac{h - \gamma_{Hs}}{\alpha_{Hs}} \right)^{\beta_{Hs}} \right], \tag{3.1.16}$$

and a lognormal distribution for the conditional probability distribution of the zero-upcrossing period,

$$f_{T_z|H_S}(t\,|\,h) = \frac{1}{\sigma_t\, t\, \sqrt{2\pi}}\, exp \left[- \frac{(\ln t - \mu_t)^2}{2\sigma_t^2} \right]. \tag{3.1.17}$$

Parameters μ_t and σ_t are functions of wave height h,

$$\begin{aligned} \mu_t &= E\left[\ln T_z\right] = a_0 + a_1 h^{a_2} \\ \sigma_t^2 &= VAR\left[\ln T_z\right] = b_0 + b_1 e^{b_2 h}. \end{aligned} \tag{3.1.18}$$

Table 3.1 lists the coefficients fitted to measured probability distributions of the North Atlantic wave climate and a combined wave climate recommended by DNV GL for fatigue assessments of ships in world-wide service. The latter corresponds to a trade route covering crossings of the North Atlantic and the North Pacific as well as a route from Europe to East Asia around Africa. The parametrized scatter tables are the result of regression fits to the BMT data and corrections based on ocean wave measurements, Bitner-Gregersen (2005).

3.2 Linear Ship Responses to Waves

Assuming a linear dependency of a ship reaction r on the wave amplitude, the reaction to a harmonic wave of frequency ω is

$$r(\omega, t) = Y(\omega) a_\zeta(\omega) cos(\omega t + \theta(\omega)), \tag{3.2.1}$$

where the amplitudes of wave and response are related through $Y(\omega)$, the response amplitude operator (RAO), and $\theta(\omega)$ which is the phase lag between

these two. $Y(\omega)$ (denoted Y_ω in the following) and $\theta(\omega)$ (denoted θ_ω) are independent of $a_\zeta(\omega)$ and can be obtained from frequency-domain seakeeping analysis. It follows that the linear (index l) response process associated with a wave process according to eq. 3.1.11 is

$$r_l(t) = \sum_{i=1}^{n} Y_{\omega_i} a_{\zeta,i} [U_i \cos(\omega_i^e t + \theta_{\omega_i}) + V_i \sin(\omega_i^e t + \theta_{\omega_i})]. \tag{3.2.2}$$

Loads on the ship structure depend on many variables; as a minimum, consider the average forward speed of the ship v, the angle between the ship course and the mean wave direction μ, and the loading condition LC in addition to the sea state parameters H_S and T_z. It was discussed above that a ship experiences continuously varying sea state conditions during its service life at sea. Further on, operational parameters such as forward speed and heading with respect to wave direction vary continuously, and for typical merchant ships the loading condition also varies although at a much lower frequency. However, at least for short time intervals, all variables can be assumed statistically stationary. That allows to divide the parameter space of operational and environmental conditions into short time intervals of constant conditions, and assign each cell a probability. The statistical properties of ship responses are then conveniently computed for each set of constant service parameters individually, yielding short-term distribution functions of ship responses conditional on the respective service parameters.

Assume a transfer function Y for a specific loading condition and ship speed and for all wave headings. For a given (stationary) sea state condition with significant wave height H_S and zero upcrossing period T_z, the ship responses spectral energy density, $S_r(\omega,\mu)$, is readily obtained by multiplication of Y with the wave energy spectral density,

$$S_r(\omega,\mu) = [Y_\omega(\omega,\mu)]^2 \, S_\zeta(\omega,\mu). \tag{3.2.3}$$

$S_r(\omega,\mu)$ allows computing the short-term upcrossing rates with relatively small effort using spectral moments. For a wave spectrum with small bandwidth $\delta \ll 1$,

$$\delta = \sqrt{1 - \frac{m_2^2}{m_0 m_4}}, \quad 0 \le \delta \le 1, \tag{3.2.4}$$

and a correspondingly narrow ship response spectrum, the resulting ship response is well approximated by a Gaussian process with zero mean for which the probability density function of response amplitudes follows the Rayleigh distribution. The probability of any random amplitude r exceeding a certain level R is

$$P(r > R) = \exp\left(-\frac{R^2}{2m_{0r}}\right). \tag{3.2.5}$$

Let now T_{zr} be the the zero upcrossing period of the process, i. e. the mean period in between two successive upcrossings of the mean level. It is defined as

$$T_{zr} = 2\pi\sqrt{\frac{m_{0r}}{m_{2r}}}. \tag{3.2.6}$$

Further assume that T_{zr} is also the mean period of positive peaks of the process[2]. Then, the mean frequency χ with which the response has an amplitude in excess of R becomes

$$\chi(r > R) = \frac{P(r > R)}{T_{zr}} = \frac{1}{2\pi}\sqrt{\frac{m_{2r}}{m_{0r}}} \cdot \exp\left(-\frac{R^2}{2m_{0r}}\right) = \chi_R. \tag{3.2.7}$$

χ_R is called the upcrossing rate of R and has the unit $[s^{-1}]$. Sometimes the upcrossing rate is also referred to as exceedance rate or upcrossing intensity. χ_R is the inverse of the short-term return period $T_R(r > R)$ which is the mean time in between two successive upcrossings of level R for a given stationary condition. Further, χ_R is closely linked to the expected number N of amplitudes larger than R per time interval T:

$$N(r > R) = T \cdot \chi_R. \tag{3.2.8}$$

That means, χ_R is the expected number of upcrossings of level R per time unit. In return, the expected maximum value R of r during a time interval T corresponds to

$$N(r > R) = 1 \iff R = \sqrt{2m_{0r}\ln(T\chi_R)}. \tag{3.2.9}$$

[2]The error of this approximation is compensated largely by the error of the assumption of a narrow-banded process, Rice (1944).

Calculation of life-cycle distributions of ship reactions requires establishing conditional probability distributions of all variables mentioned above. Wave statistics provide information about the probability distributions of sea state parameters for the intended areas of operation. Probability distributions of loading conditions and operational parameters need to be established based on theoretical considerations or real life observations, if available. The expected number of upcrossings of a target response level R, denoted $N_{T_D}(r > R)$, during the total service life at sea, T_D, becomes

$$N_{T_D}(r > R) = T_D \sum_{T_z} \sum_{H_S} \sum_{v} \sum_{\mu} \sum_{LC} [\chi\,(r > R \,|\, T_z, H_S, v, \mu, LC) \cdot p(T_z, H_S) p(v, \mu \,|\, LC, T_z, H_S) p_{LC}] \tag{3.2.10}$$

where the sea state probability $p(T_z, H_S)$ follows eqs. 3.1.16 and 3.1.17, and $p(v, \mu \,|\, LC, T_z, H_S)$ is the probability of sailing with forward speed and wave encounter angle within small ranges around values v and μ, respectively, conditional on the loading condition, wave zero-upcrossing period and significant wave height. For brevity, the combination $[T_z, H_S, v, \mu]$ will be referred to as service parameters. $\chi(r > R \,|\, T_z, H_S, v, \mu, LC)$ is the short-term upcrossing rate of R conditional on T_z, H_S, v, μ and LC, see eq. 3.2.7.

The expected maximum value R of r during T_D, i. e. the value with one expected upcrossing during T_D, will be assigned with R^* and called the long-term extreme value.

3.3 Nonlinear Response Statistics

The previous sections provided the basic concepts of short- and long-term statistical analyses of ship responses based on frequency domain hydrodynamic computations and the narrow-band assumption. The linearisations made in such analyses make the correlation between response amplitudes and their probability distributions readily available from the properties of the response spectra. Spectral analysis, however, requires the excitation and its response to have the same frequencies. In the context of wave-induced vibration, whipping and nonlinear resonant vibration are examples of responses that are not amenable to spectral analysis because they take place at natural frequency, irrespective of the excitation frequency.

Time domain simulations allow to include all nonlinearities of interest and are an obvious choice to circumvent the limitations of spectral analysis. A straightforward approach to determine the short-term or long-term load distributions with a time domain method is to perform Monte-Carlo simulations covering the time interval of interest, T_D. Preferably, the simulated time interval, T_S, should cover several times T_D to increase statistical confidence. The maximum expected value is then simply obtained as the load with a return period of T_D. While being very intuitive, Monte-Carlo simulations are in principle also a very reliable statistical approach.

However, a major drawback of direct long-term simulations is the associated computational effort. Calculation of the long-term probability of exceeding a certain load level R requires averaging over all possible short-term sea states, as well as all ship speeds, wave encounter angles and loading conditions. A straightforward approach would be to carry out Monte-Carlo simulations for a sufficiently large number of service parameter combinations, discretising the entire service parameter space with a sufficient resolution. In addition to the large number of service parameter combinations to be considered, many long random realisations are required for each of these combinations to obtain reliable statistical estimates; the overall duration of such simulations would need to be a multiple of the ship's service life. Methods are required which are several orders of magnitude faster than real time to allow such analyses with reasonable computation times. Even for short-term analyses, T_S easily becomes prohibitively large when rarely occurring events are sought.

This renders the use of direct simulations unfeasible for the particular case of a field method solving the NS equations. Although the numerical method offers a high degree of accuracy and physical modelling, hence is well suited for simulation of extreme events, the associated computational expenses simply prohibit simulations of long time intervals. As a rough figure, a single second simulation time with the present numerical method takes about half an hour of computation time when executed in parallel on a recent processor. This can be scaled with the use of large modern cluster computers which allow parallel execution of several computations, thus reducing the total wall time for a given simulation duration. However, not every potential user will have access to such computing facilities or be able and willing to bear the related costs.

A practical long-term extreme value procedure therefore necessitates simplifications that allow a reduction of the required simulation time by several orders of magnitude.

An obvious concept of reducing the computation time is to restrict simulations to small sequences of interest. This can be accomplished by using a faster but less accurate method – called *predictor method* in the following – to identify one or several simulation scenarios in a way that these correspond to given probabilities of exceedance. These pre-selected scenarios are then simulated with a more complex method that will be denoted *corrector method* here. For brevity, the term *linear* will refer to predictor methods and corresponding results in the following, although predictor methods may already account for certain nonlinear effects. Nonlinear, in turn, will refer to corrector methods and corresponding results.

The following describes several approaches based on predictor and corrector methods. Applications and case studies will be presented later on in chapter 5.

While pre-selection reduces the simulation time, it introduces uncertainty because results of the predictor method inevitably differ to some extent from the corrector method results. Basically, pre-selection requires to establish response probability distributions with the predictor method. During the process of selection, assumptions on corresponding probability distributions of the corrector method need to be made.

In a first and rather naïve approach, simulations with the corrector method can be used to simply calculate a nonlinear equivalent of the linear response. A load process leading to a linear response of amplitude R_l is used in the simulation with the corrector method to obtain a nonlinear response amplitude R. No additional probability information about the nonlinear response will be sampled from the simulation. This is tantamount to assuming that the associated nonlinear upcrossing probability is equal to that defined by the predictor method,

$$P(r > R) = P(r_l > R_l). \tag{3.3.1}$$

Any approach relying on this assumption will be denoted *response-corrective approach* (RCA). Such approach allows to restrict to a single simulation with the corrector method for each R_l.

This section discusses two approaches that establish one or several wave sequences of short duration designed to cause a response peak associated with a pre-defined probability of exceedance according to the predictor method: the well established equivalent design wave method, and a theoretically more consistent technique to generate transient wave sequences. In either case, the obtained nonlinear response is assumed to have the same probability of exceedance as

the response obtained by the predictor method. The impossibility to improve this probability estimation is a fundamental limitation of response-corrective approaches.

Approaches which overcome this shortcoming by improving the linear probability distributions are expected to be of higher informational value, albeit at the price of increased computational effort. Such *probability-corrective approaches* (PCA) will inevitably require a larger number of computations in order to allow establishing nonlinear response probability distributions.

3.3.1 Equivalent Regular Design Waves

The concept of the Equivalent Regular Design Wave (ERDW) is a simple way of adding nonlinear effects to a linear response value. The design wave is a regular harmonic wave constructed such that the associated ship response amplitude corresponds to a target design value R_l, obtained by the predictor method. R_l is chosen to match a targeted probability level which could be defined by the expected number of upcrossings during a certain time interval, or by an associated return period, e.g., $N(r_l > R_l) = 0.01$ or $T_R(r_l > R_l) = 1\,y$, for example. The result of the simulation in this wave using the corrector method is regarded as a correction of the linear response. For a given wave frequency ω_d, the amplitude of the equivalent regular design wave is

$$a_\zeta(\omega_d, R_l) = \frac{R_l}{Y(\omega_d)}. \tag{3.3.2}$$

In principle, a regular wave of any frequency can be used as ERDW by choosing the wave amplitude a_ζ according to eq. (3.3.2). Often, the wave frequency of the ERDW is selected as the frequency corresponding to the peak of the transfer function over all μ and v for selected loading conditions. Experience-based corrections are used sometimes, or responses to multiple ERDWs are computed and compared [3]. Still, the resulting nonlinear response is strongly related to the selection criteria and hence arbitrary.

[3] The CSR for bulker and tanker establish ERDWs based on fixed ratios of wave length to ship length. These ratios are, however, based on experience and intend to match the peak of transfer functions.

3.3.2 Response-Conditioned Wave Sequences

Instead of using a single RAO, the whole information included in the transfer function for a given combination of [μ,v,LC] and a given sea state [H_S,T_z] could be used to establish a wave excitation corresponding to R_l. Dietz (2004) proposed, based on previous work of Tromans et al. (1991), Friis-Hansen and Nielsen (1995), Adegeest et al. (1998) and Pastoor (2002), a concept of conditioning wave sequences to a response peak of specific amplitude. The basic idea is to choose amplitudes and phases of wave components of a certain sea state in such a way that the ship response at a given time instant t_0 exactly corresponds to a certain target value R_l according to, as for example in this case, linear theory. Simulations with a higher order method in these wave sequences allow a correction of the linear response, accounting for nonlinearities covered by the respective method. Nonlinear simulations can either be performed for a single wave sequence (i. e. in the sense of an RCA), or for multiple wave sequences which allows to obtain the probability distribution of nonlinear reactions conditional on the linear reaction. The formulation here is that of Dietz (2004) for long-crested waves, with a slightly modified terminology. The terminology has been presented in Drummen et al. (2009), where the authors investigated the performance of conditioned wave sequences in terms of accuracy and required resources, compared with short-term probability distributions derived from simulations in random long-crested irregular head waves using a time domain hydroelasticity method.

The random coefficients $\mathbf{V} = [U_i, V_i]$ of the response process eq. 3.2.2 are transformed to establish wave sequences which are conditioned on the target response amplitude at target time, $r_l(t_0) = R_l$, $\dot{r}_l(t_0) = 0$, and have an instantaneous frequency $\Omega_r = \hat{\dot{r}}_l(t_0)/r_l(t_0) = \omega_r$. Here, $\hat{[\cdot]}$ denotes the Hilbert transform, and $\dot{[\cdot]}$ the first time derivative. For this purpose, $\mathbf{V}$ is used to formulate a random

vector process $\mathbf{A} = [A_1, A_2, A_3, A_4]$, where

$$\begin{aligned}
A_1 &= \sum_{i=1}^{n} a_{r,i}^e \left[U_i \cos(\theta_{\omega_i}) + V_i \sin(\theta_{\omega_i})\right] - r_l(t_0) \\
A_2 &= \sum_{i=1}^{n} a_{r,i}^e \omega_i^e \left[U_i \sin(\theta_{\omega_i}) - V_i \cos(\theta_{\omega_i})\right] - \dot{r}_l(t_0) \\
A_3 &= \sum_{i=1}^{n} a_{r,i}^e \left[-U_i \sin(\theta_{\omega_i}) + V_i \cos(\theta_{\omega_i})\right] - \hat{r}_l(t_0) \\
A_4 &= \sum_{i=1}^{n} a_{r,i}^e \omega_i^e \left[U_i \cos(\theta_{\omega_i}) + V_i \sin(\theta_{\omega_i})\right] - \hat{\dot{r}}_l(t_0)
\end{aligned} \tag{3.3.3}$$

with $a_{r,i}^e = Y_{\omega,i} a_{\zeta,i}^e$. The random variables U_i and V_i shall now be replaced by random constrained coefficients,

$$\begin{aligned}
(U_{c,i}, V_{c,i}) &= \{\mathbf{V} \,|\, \mathbf{A} = (0,0,0,0)\} \\
&= \mathbf{V} - Cov\left[\mathbf{V}, \mathbf{A}^T\right] Cov\left[\mathbf{V}, \mathbf{A}^T\right]^{-1} \mathbf{A}.
\end{aligned} \tag{3.3.4}$$

Replacing the U_i and V_i in eq. 3.2.2 with constrained coefficients $U_{c,i}$ and $V_{c,i}$ yields a response process that satisfies $r_l(t_0) = R_l$ and $\dot{r}_l(t_0) = 0$ but at other times resembles a rather random sequence. The corresponding wave process is denoted *Conditioned Random Response Wave* (CRRW). Of all such processes, the *Most Likely Response Wave* (MLRW) is defined now as their mean, $\bar{E}[\cdot]$.

If the instantaneous frequency ω_r of the response at t_0 is set equal to the mean frequency of the response process,

$$\omega_r = \frac{m_{1r}}{m_{0r}}, \tag{3.3.5}$$

this corresponds to the Most Likely Extreme Response (MLER) method developed by Adegeest et al. (1998). The mean constrained coefficients $\overline{U}_{c,i}$ and $\overline{V}_{c,i}$ can efficiently be calculated using spectral moments of the response process by solving equations

$$\begin{aligned}
\overline{U}_{c,i} &= E\left[U_i \,|\, \mathbf{A} = (0,0,0,0)\right] \\
\overline{V}_{c,i} &= E\left[V_i \,|\, \mathbf{A} = (0,0,0,0)\right],
\end{aligned} \tag{3.3.6}$$

see Dietz (2004) for further details.

MLRW sequences are directly associated with a short-term probability according to the predictor method through R_l and eq. 3.2.5. This allows to remove some of the arbitrariness of the ERDW concept, and links the resulting nonlinear response to a given short-term condition. Further, this allows for a very fast estimation of nonlinear response distributions. Only a single simulation per probability level is required to approximate the nonlinear response distribution, i. e. each MLRW simulation provides a nonlinear correction for the selected linear response amplitude, while assuming the nonlinear response to have the same probability of being exceeded. This corresponds to a response-corrective approach.

Multiple simulations in CRRW sequences, in contrast, allow establishing corrected probability distributions. The procedure outlines as follows, see also Dietz (2004). A statistically representative number of CRRW simulations is performed for each response level, and this is repeated for the range of probability levels of interest. The results are probability density functions (PDF) of the nonlinear response peaks conditional on the linear responses for each of these levels, i.e. $f(R \,|\, r_l = R_l, T_z, H_S, v, \mu, LC)$. Finally, unconditioning with respect to the probability density function of the corresponding linear response, $f(R_l \,|\, T_z, H_S, v, \mu, LC)$, yields the cumulative probability distribution of the nonlinear response:

$$F(r < R \,|\, T_z, H_S) = \int_0^\infty F(r < R \,|\, r_l = R_l, T_z, H_S) f(r_l \,|\, T_z, H_S)\, dr_l, \quad (3.3.7)$$

where $f(r_l)$ is the probability density function of r_l. This approach implies a significantly larger computational effort because a large number of simulations need to be carried out for each response level, compared to a single computation using the MLRW approach, see Drummen et al. (2009) for a qualitative comparison.

3.3.3 Monte-Carlo Simulations

Modern computing resources allow direct simulations using Monte-Carlo techniques at least for limited time intervals. Random realisations of wave processes according to eq. 3.1.11 are drawn and used as input for simulations of sufficiently long duration in order to derive statistical properties of the nonlinear response, Oberhagemann et al. (2012). Statistical evaluation of peak distributions from

time records of Monte-Carlo simulations is straightforward for rigid-body responses which are narrow-banded processes. Peaks are then defined as the maximum and minimum response values between consecutive zero up-crossings of the response process.

However, evaluation becomes difficult when one is interested in the amplification of response peaks due to wave-induced vibration. The response process resulting from a superposition of low-frequency and high-frequency responses may have additional zero up-crossings. These deteriorate the direct comparability of peaks from simulations for rigid bodies and flexible bodies. An option to preserve comparability of individual peaks is to perform simulations for the rigid and the flexible case simultaneously in identical wave processes. The time instants of zero up-crossings found for the rigid case may then be used for evaluating the flexible case as well. Alternatively, eliminating vibrations through low-pass filtering yields a response process which can be assumed a good approximation of the rigid-body case, thus avoiding the need for two simultaneous simulations.

Rainflow counting techniques, Rychlik (1987), Matsuishi and Endo (1968), are an alternative to peak evaluations. The fundamental idea is to extract upward and downward ranges between all local maxima and minima, and combine them to pairs of closed cycles. Further information about mean levels and bandwidth of the response process can be obtained when storing the maxima and minima in a matrix format. Rainflow counting is commonly used in time record analyses for fatigue assessment.

3.3.4 Extrapolation of Upcrossing Rates

From eqs. (3.1.5), (3.1.6) and (3.2.3) follows that the variance of the linear response process, m_{0r}, is directly proportional to H_S^2 for a given stationary service condition $[T_z, v, \mu, LC]^T$. As a consequence, the logarithm of the return period of a certain linear response is inversely proportional to the significant wave height squared,

$$-ln(\chi) \propto \frac{1}{m_{0r}} \propto \frac{1}{H_s^2}. \tag{3.3.8}$$

This dependency is violated for broad-banded and nonlinear responses; however, Söding and Tonguć (1986) showed that a linear dependency of $-\ln\chi$ on $1/H_S^2$

can be assumed if, first, χ is sufficiently low, i.e. upcrossing events are rare, and, second, the characteristics of the response process (such as the failure mode) do not change with changing the significant wave height. Therefore, when the response mode does not change with H_S, it should be possible to estimate upcrossing rates for one significant wave height $H_{S,1}$ from upcrossing rates obtained for a different significant wave height $H_{S,2}$. Söding and Tonguć (1986) proposed this approach for assessing excessive roll motions. Assuming that rare events happen with some unknown probability P when encountering a wave group of n (n unknown) waves that exceed a certain unknown threshold wave height H; the upcrossing rate $\chi(R)$ can be approximated in this case as

$$\chi(R) \approx P \cdot f(H, n \,|\, H_S), \tag{3.3.9}$$

where f is the frequency of encountering rare wave groups which are approximately Rayleigh distributed:

$$f(H, n \,|\, H_S) = \frac{1}{T_z} \exp\left(\frac{-2nH^2}{H_S^2}\right). \tag{3.3.10}$$

Combining eqs. (3.3.9) and (3.3.10) gives

$$-H_S^2 \cdot \ln\left(\frac{\chi T_z}{P}\right) = 2nH^2 \tag{3.3.11}$$

Finally, substituting $A = ln(T_z/P)$ and $B = 2nH^2$ yields

$$-ln(\chi(R)) = A + \frac{B}{H_S^2}. \tag{3.3.12}$$

Derivation of eq. (3.3.12) does not require any assumptions about the response process, except for assuming that rare events happen when encountering specific rare wave groups. It should also be noted that A and B are not expressed in terms of the unknown quantities P, n and H. These only motivate the functional relation eq. (3.3.12), while A and B are determined from simulations instead, see example applications in Shigunov et al. (2010), Söding and Tonguć (1986).

If we now assume that T_z/P corresponds to a characteristic period of the response and provisionally set

$$T_{zr} = T_z/P = exp(A), \tag{3.3.13}$$

we can transform eq. (3.3.12) to obtain

$$\chi(R) = \exp(-A)\exp\left(-\frac{B}{H_S^2}\right) = \frac{1}{T_{zr}}\exp\left(-\frac{B}{H_S^2}\right). \tag{3.3.14}$$

Note that $A = ln(T_{zr})$ is assumed constant for all response levels R, so eq. (3.3.12) becomes

$$-\ln\left[\chi(R)\,T_{zr}\right] = B/H_S^2. \tag{3.3.15}$$

That means, the mean zero upcrossing period of the response process will also be interpreted as the return period of any response level R at the limit of infinite significant wave height. $\left[\chi(R)\,T_{zr}\right]^{-1} = T_R(R)/T_{zr}$ asymptotically equals the mean number of response peaks in between consecutive upcrossings of R for large return periods. The expression

$$\Lambda(R) = -\ln\left[\chi(R)\,T_{zr}\right] \tag{3.3.16}$$

will therefore be denoted the logarithmic number of periods to exceedance (LNPE) of response level R.

Eq. (3.3.12) will later be used to establish functional relationships between upcrossing rates and significant wave height for nonlinear hull girder loads including wave-induced vibration. Coefficients A and B will be determined through simulations in random irregular waves.

An alternative to the above formulation is based on the reliability index β, which is commonly used in reliability theory, see e. g. der Kiureghian (2000), Ditlevsen and Madsen (2005). Interpreted in the present context, β is the ratio of the target response level R divided by the standard deviation of the response process,

$$\beta = \frac{R}{\sqrt{m_{0r}}}. \tag{3.3.17}$$

Reliability index and upcrossing rate of R are linked through eq. (3.2.7):

$$\chi_R = \frac{1}{T_{zr}}\cdot\exp\left(-\frac{R^2}{2m_{0r}}\right) = \frac{1}{T_{zr}}\cdot\exp\left(-\frac{\beta^2}{2}\right) \tag{3.3.18}$$

Further on, eq. (3.3.17) suggests to exploit the proportionality of m_{0r} and H_S again, so that the reliability index may be defined as

$$\beta = \frac{B'}{H_S} \tag{3.3.19}$$

with a constant B'. Jensen (2010) and Jensen (2011) suggested to assume the inverse proportionality between β and H_S irrespectively of the nonlinearity of the response, extending eq. (3.3.17) in a more general way as

$$\beta = A' + \frac{B'}{H_S}, \tag{3.3.20}$$

and demonstrated that this equation fits well to simulation results of hull girder loads, obtained with a nonlinear time-domain strip method and including slamming and hull girder elasticity effects. Derbanne et al. (2012) tested the extrapolation of peak upcrossing rates based on eq. (3.3.19) and reported good agreement with simulations for a larger range of wave height variations even with this simpler formulation. They used a 3D boundary element method coupled in the time domain with a 3D solver for the structural deflection modes, also accounting for slamming effects with a Generalized Wagner method.

Λ is closely linked to the reliability index β: for a linear narrow-banded process, the LNPE is proportional to the reliability index squared. Since eq. (3.3.12) is also asymptotically equivalent to eq. (3.3.20) for low upcrossing rates, both formulations basically reflect the same dependency of the upcrossing rate on H_S, see further discussion in Jensen (2011).

3.3.5 Coefficient of Contribution

Above simulation strategies basically provide short-term distributions of nonlinear responses conditional on service parameters and sea state conditions [4]. The long-term cumulative distribution of the response is, in analogy to section 3.2, then calculated as a sum of the conditional distributions times the joint probabilities of service parameters and sea state conditions. This sum is typically dominated by a few terms which allows a significant reduction of the parameter combinations to be considered. A statistical analysis using results of a predictor method can be used to identify the combinations of the service parameters which contribute most to the upcrossing rate of a given linear long-term reaction R_l^*. Baarholm and Moan (2000) proposed a quantitative measure for the selection of such dominating parameter combinations, denoted *coefficient of contribution* (C_C). It is equal to the expected number of upcrossings for a particular combination of short-term parameters, divided by the long-term total expected number

[4] With the exception of the ERDW approach which is not directly linked to any sea state condition.

of upcrossings:

$$C_C(R_l^*;T_z,H_S,v,\mu) = \frac{T_D\,\chi\left\{r_l > R_l^* \,|\, T_z,H_S,v,\mu\right\}\, p_{T_zH_S}\, p_{\mu v}}{T_D \sum_{T_zH_S v\mu} \chi\left\{r_l > R_l^* \,|\, T_z,H_S,v,\mu\right\}\, p_{T_zH_S} p_{\mu v}}. \quad (3.3.21)$$

The denominator in eq. (3.3.21) becomes 1 when C_C is calculated for the linear long-term extreme response R_l^*.

Baarholm and Moan (2000) demonstrated that only few parameter combinations significantly contribute to the extreme value distribution, and these typically correspond to sea states with low probabilities of occurrence. Restricting Monte-Carlo simulations to such subsets of parameter combinations significantly reduces the required computational effort. However, two issues need to be considered when disregarding all other parameter combinations in the long-term cumulative summation.

First, the service parameter combinations most relevant for the linear extreme reaction R_l^* may not necessarily lead to the nonlinear reaction with the same probability of exceedance because of nonlinearities not accounted for by the predictor method. This is tantamount to different distributions of the significance of the parameter combinations with respect to R_l^* and R^*. Baarholm and Moan (2000) addressed this issue using contour lines of C_C in the space of service parameter combinations. Nonlinear simulations used the combination with the largest C_C as a starting point; iteratively, more parameter combinations were included, until the estimate of the nonlinear long-term extreme converged.

Second, the duration of the simulations for the selected service parameter combination needs to be prolonged. If it were simply taken equal to the expected duration of this combination over the operational life, the expected number of upcrossings of a linear long-term response would become $N(r_l > R_l^*) = C_C < 1$. This is equivalent to underpredicting the linear response R_l^* and, as a consequence, also the nonlinear value R^*. The iterative procedure converges towards a certain nonlinear response as the set of selected parameter combinations is iteratively increased. However, the estimate of the long-term extreme value in any iteration is non-conservative in that the long-term extreme response R^* always remains the upper bound of the calculated extreme. If O is the total number of service parameter combinations in the discretised space of service parameters and $O_{s,k}$ is the subset of parameter combinations selected for nonlinear simulations in the present iteration, then

$$\sum_{O_{s,k}} C_C < \sum_{O} C_C = 1 \quad (3.3.22)$$

This issue can be resolved, consistently with the C_C approach, when the total duration associated with the selected service parameter combinations is prolonged. The duration time of each individual parameter combination has to be scaled by the ratio of the C_C sum over all possible parameter combinations (which is 1 for the case of the value exceeded on the average once per service time at sea R_l^*) to the C_C sum over the reduced set of parameter combinations selected for nonlinear simulations. Such scaling assures that the expected linear extreme, computed over the selected subset, equals the original linear extreme, computed over all possible parameter combinations.

4 Validation

> *A much better approach is to retain validation as a scientific (or engineering science) activity by not specifying validation as a pass / fail activity but just as a comparison activity (between modeling and experiment) and in which the level of validation is reported with pertinent recognition of the uncertainties of both the computations and the experiments.*
>
> P. J. Roache

This chapter addresses the validation of the numerical method with respect to the intended applications. The overarching idea is to start with isolated problems before addressing combined problems and more complex applications. All validation work presented is based on model scale experimental data. The experimental data originate from model test campaigns at KRISO, CEHIPAR and MARIN. Ship and model particulars are listed in appendix A.

Full scale data measured on board of ships may be regarded less biased by scale effects and model uncertainty. They are, however, not well suited for the purpose of validating numerical methods as they bear large uncertainties related to the environmental conditions present during measurements. Model tests provide a better means for validation; they take place in a controlled environment, and they offer the possibility for repetitions. Although validation is made against model scale experimental data, results are presented in full scale using Froude scaling. Scale effects due to insufficient Reynolds similitude are not considered significant for wave-induced and pressure-dominated loads. Therefore, validation is regarded representative also for full scale.

The accuracy of numerical results is, of course, sensitive to the discretisation of the governing equations at hand. Grid generation and simulation set-up therefore need to follow established strategies that assure sufficiently accurate results. Section 4.1 introduces and discusses concepts of error estimation based on systematic grid refinement. Although basically all numerical results contain discretisation errors, the relative error and hence the relevance of the error will

be larger in certain cases depending on the physical phenomenon addressed. In this chapter on validation, refinement studies will be performed for several problems where the grid sensitivity is large. Such cases require a fine resolution which can impose tremendous computational efforts for practical application examples.

The free decay of vibrations of ship hull girders is studied in calm water at zero and forward speed. Hydrodynamic damping, mainly due to radiation of waves, causes the vibrations to decay with time. It is demonstrated that the numerical solution is strongly dependent on the grid resolution in space and time. A strategy for extrapolating grid independent damping values is developed based on treating the hydrodynamic damping as a function of grid resolution. Further, these studies validate the ability of the numerical method to replicate the frequencies of free vibrations of floating structures which are a coupled fluid and structure dynamics problem.

The second part of the validation covers simulations in waves. Regular harmonic waves of small and large amplitude are investigated to explore the method's ability with respect to nonlinear effects on loads. Next, simulations in irregular waves are addressed. Such simulations are a straightforward approach to determine short-term load distributions, yet the effort to converge short-term probability distributions is tremendous, particularly when addressing rare and extreme events.

Further on, grid resolution becomes of particular importance when trying to compute short-term probability distributions of ship response in severe and extreme sea state conditions using RANS methods. For these purposes, fine grid and time step resolution is prohibitive and grid refinement studies become the only viable strategy to achieve sufficiently accurate results in reasonable computing time. The work documented herein addresses the grid dependency of short-term response distributions and strategies to estimate grid independent solutions. However, the scope is limited and it is therefore recommended to gain further experience about sufficient and efficient spatial and temporal discretisations through similiar grid sensitivity studies.

For comparison, results of simulations in regular and irregular waves are, in selected cases, presented along with results of a potential theory sea-keeping solver *GL Rankine*, Söding et al. (2012). *GL Rankine* solves the linearized boundary problems of wave radiation and diffraction in the frequency domain using a Rankine source-patch formulation. The formulation takes into account the steady flow around the ship including dynamic trim and sinkage. The

diffraction and radiation problems are linearized about the free surface, deformed by the steady ship wave system.

4.1 Assessment of Numerical Errors and Uncertainties

Numerical results of field methods are sensitive to both spatial and temporal discretisation. Insufficient grid resolution or bad quality grids may lead to inaccurate results or give wrong tendencies. Even with very fine discretisations, one may still not obtain sufficiently converged, i. e. grid independent, results, mainly due to the asymptotic accuracy when discretising differential equations. Keeping this in mind, one may arrive at two contrary conclusions:

a) Since the solution may significantly depend on the discretisation in space and time, field methods are sometimes judged as inaccurate, or even producing unreliable or random results. Additionally, these methods may be regarded excessively computational time-consuming since very fine grids are required to minimise the discretisation errors.

b) For many problems, coarse discretisations give results of sufficient accuracy, or at least indicate a trend towards accurate results which could be obtained on finer grids. Grid studies then allow to estimate grid-independent solutions. Provided that governing parameters are identified, one may even transfer the error estimates to similar problems. Doing so indeed affects the accuracy of the results to a certain extent, but the savings in computation time can often outweigh this loss of accuracy. For instance, in transient 3D computations, the number of unknowns is a function of the grid spacing to the power of four, while the error is typically a function of the grid spacing to the power of one or two, depending on the order of the approximation schemes. Beyond a certain refinement level, further reduction of the discretisation error will not be worth the additional computational effort in such cases.

Adopting the more optimistic point of view (b), the asymptotic accuracy can be regarded as a chance to determine the error of the numerical result with a given uncertainty, Roache (1997), Roache (1998). In the context of this thesis, this is a potential advantage when assessing the reliability of a marine structure against failure due to hydrodynamic loading. Wave dispersion of high-frequency wave components, local pressure distributions due to slamming, and radiated waves due to ship motions are examples of flow features that require a fine

grid resolution in space and time. Numerical damping and underestimation of local peaks are typical consequences of insufficient refinement. Discretisation requirements in the context of ship responses to wave excitation will be addressed later on in this chapter.

The underlying idea of error estimation from grid refinement studies is to approximate the numerical solution by a power series expansion of the grid spacing Δx. With decreasing grid spacing, the discretisation error, δ, is reduced, and the solution values asymptotically approach the grid-independent solution. Still, extrapolation is in principle required because of the impossibility to achieve zero grid spacing. For sufficiently small characteristic grid spacings, the discretisation error becomes dominated by the leading error term of the approximation scheme, and one may reduce the functional relation of the error on grid spacing to a suitable power of the grid spacing. This is done in Richardson extrapolation, where the discretisation error δ_{RE} is calculated from a set of solution values ϕ_i on successively refined grid representations indexed by i. The discretisation error is

$$\delta_{RE} = \phi_i - \phi_\infty = \alpha \Delta x_i^p, \tag{4.1.1}$$

with the grid-independent solution ϕ_∞, coefficient α and exponent p. p is the observed order of convergence. Solution of eq. 4.1.1 requires a minimum of three grid representations in order to determine α, p and ϕ_∞, unless p is assumed to equal a theoretical value corresponding to the order of the approximation scheme.

Richardson extrapolation is widely accepted for uncertainty and error estimation of steady or quasi-steady problems and has been applied to solutions of periodic problems, see for instance Simonsen et al. (2013), Hänninen et al. (2012) for application to ships in regular waves. It also has been adopted by the ITTC guideline for uncertainty analysis in CFD, see ITTC (2002). Eça and Hoekstra (2002) attempt to generalize the concept of Richardson extrapolation and propose uncertainty estimators based on truncated power series expansion formulations and least squares fitting to allow for large flexibility and data scatter in grid refinement studies. In Eça and Hoekstra (2014), the same authors present a comprehensive study on various error estimators, applied to standard two-dimensional test cases but also resistance and wake predictions of the KVLCC2 tanker. Yet, published error estimators are limited to discretisation errors formulated as functions of a single scalar characteristic grid spacing. In contrast, transient problems involve discretisation in space and time, so the

discretisation error is a function of at least two independent variables, Δx and Δt, and more general formulations are required. However, Δx and Δt are linked through the Courant number as will be discussed in more detail later on.

This chapter discusses the extension of existing error estimators to scalar results of transient computations, introduced by discretisation errors in both space and time. The transient nature of any solution variable makes it more challenging to define a quantifiable measure of the error, and to relate it to a discretisation in a given dimension. Later on, the presented concept will be transferred and applied also to response distributions resulting from statistical assessment of transient simulations of ships in random irregular waves.

To some extent, the approach discussed here contradicts guidelines of the ITTC on uncertainty analysis. Therefore, the next paragraph will briefly discuss the ITTC guideline and justify the presently proposed approach by contrasting it against the guideline.

4.1.1 Grid Refinement for Transient Problems

The guideline of the ITTC on CFD uncertainty analysis, ITTC (2002), provides general advice on uncertainty estimation of numerical simulation results. The total numerical error is assumed to consist of contributions from incomplete iteration convergence, δ_I, numerical grid density, δ_G, time step size, δ_T, and other parameters, δ_P. These other parameters are not explicitly specified, but presumably shall include potential round-off errors. While the error is typically unknown, all error contributions are also associated with corresponding uncertainties that can be estimated from simulation results. The uncertainties are assumed to add to the total numerical uncertainty:

$$U_{SN}^2 = U_I^2 + U_G^2 + U_T^2 + U_P^2. \tag{4.1.2}$$

Systematic parameter sensitivity studies are suggested for all input parameters (grid size, time step, etc.) while the other parameters are fixed, i.e., grid size or time step shall be varied individually, ITTC (2002). Richardson extrapolation is suggested to estimate the uncertainties and errors related to each parameter. Apparently, the definition of total numerical uncertainty, eq. (4.1.2), and the proposed sensitivity studies assume the uncertainties arising from grid spacing and time step are non-correlated. Giving eq. (4.1.2) a geometrical interpretation, the uncertainty contributions are assumed independent and corresponding to

orthogonal dimensions constituting the space of uncertainty. This viewpoint does not allow for any interaction between uncertainty contributions.

In what follows, a different view will be discussed. It is agreed that, for a transient problem, both the grid spacing and the time step are relevant. Given a sensible resolution in all dimensions, in space and in time, it is therefore recommended that exactly the same refinement factors should be applied to all dimensions and that refinement in space and time should be done simultaneously. This contradicts the ITTC approach, and will be justified by considering the opposite situation, i.e., a non-uniform refinement: in this case, continued refinement will negatively affect the solution values on finer grids because characteristic measures for grid quality, such as the Courant number or cell aspect ratios, tend to zero or infinity, depending on the refinement factors. In order to avoid this, refinement needs to be uniform in all directions and has to be applied simultaneously.

Consider a set of refined grids where index i denotes the level of refinement. For transient problems, uniform refinement in all directions (space and time) corresponds to keeping constant the Courant number, which appears particularly reasonable for convection-dominated flows:

$$\Delta x_{i+1}/\Delta x_i = \Delta t_{i+1}/\Delta t_i \qquad \Rightarrow \qquad CFL = \frac{u\Delta t}{\Delta x} = const \tag{4.1.3}$$

To further elaborate on the above; assume a numerical analysis for a problem in two dimensions, x and y. Further assume three sets of refined grid representations, all starting from a reference grid with grid node spacings Δx_1 and Δy_1. Let each of these grid sets use constant refinement factors defined as the ratio of reference values of two grids,

$$\begin{aligned} c_x &= \frac{\Delta x_i}{\Delta x_{i+1}} \\ c_y &= \frac{\Delta y_i}{\Delta y_{i+1}}. \end{aligned} \tag{4.1.4}$$

The first set uses refinement only in Δy and keeps the original grid spacing in x ($c_x = 1$), while the second set uses refinements in both directions x and y, but with different refinement factors ($c_x < c_y$). Finally, a third set uses the same refinement factors for both dimensions x and y ($c_x = c_y$). The sets of grid representations are illustrated in Fig. 4.1.

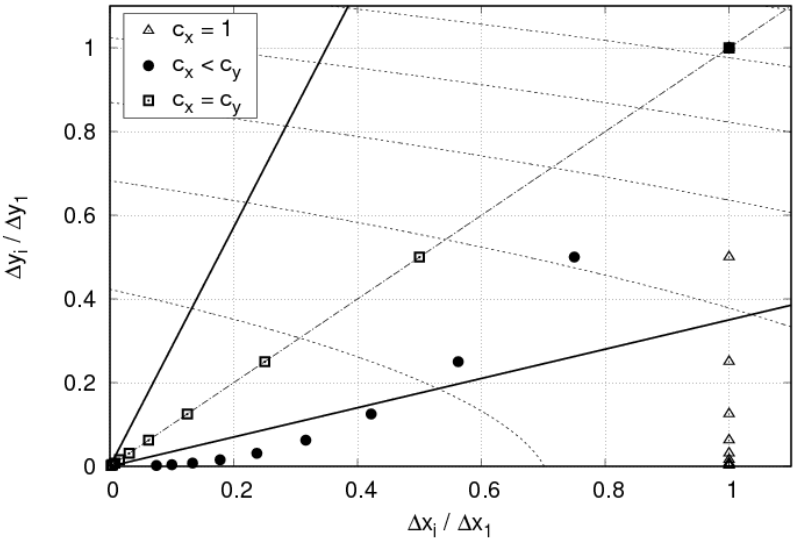

Figure 4.1: Illustrative example for refinement strategies: uniform refinement (squares), non-uniform refinement (circles), and refinement in one dimension only (triangles); solid lines symbolize the lower and upper bounds of a region of valid solutions

By definition, the grid-independent solution is found for $\Delta x = 0$ and $\Delta y = 0$, so the discretisation error is typically zero only for this point. For sufficiently small Δx and Δy, we may, without loss of generality, assume in addition that the discretisation error is monotonically increasing with increasing Δx and Δy. The dashed lines in Fig. 4.1 represent example isolines of a monotonically increasing discretisation error.

From the definition of the discretisation error follows that the first example refinement study, using only refinement in one dimension, is not producing a grid-independent solution at all, because all obtained solution values depend on Δx_1.

The other two refinement strategies asymptotically approach the grid independent solution, $\lim_{i\to\infty}(\Delta x_i) = 0$ and $\lim_{i\to\infty}(\Delta y_i) = 0$. However, practical limitations

exist for numerical methods in terms of lower and upper bounds of ratios $\Delta x/\Delta y$ beyond which the methods yield wrong solutions or become unstable due to badly conditioned systems of equations. Such bounds are sketched in Fig. 4.1 with solid lines [1]. Hence, the second refinement strategy will fail to produce a good estimate of the grid independent solution because it exceeds one of the fictitious bounds. Even if no numerical grid representations were used in the study that violated the bounds, it is still likely that the solution values on representations close to the limits will be of poor quality and result in wrong predictions of the grid-independent solution.

In contrast to the other two grid studies, the third refinement strategy, using uniform refinement factors in x and y, will produce reasonable solution values for all refinement ratios irrespective of the grid spacings, and will asymptotically arrive at the grid independent solution. Hence, this approach of uniform refinement in all dimensions is the only viable grid refinement strategy that allows extrapolating grid-independent solutions. Salas (2006) and Roache (2006) discuss non-uniform refinement strategies and recommend the application of uniform refinement factors to preserve the theoretical order of convergence. Yet, they do not generally reject application of non-uniform refinement factors. A reason for this may be that numerical stability is not addressed in these studies.

For any refinement strategy, the necessity remains to extrapolate the grid-independent solution because of the finite discretisation. Provided that all grid representations used in a refinement study are sufficiently close to the grid-independent solution, the discretisation error, δ_D, can be approximated by a Taylor series expansion of the grid spacings, here Δx and Δy,

$$\delta_D = \mathfrak{a}_{01}\Delta x + \mathfrak{a}_{10}\Delta y + \mathfrak{a}_{11}\Delta x\Delta y + \mathfrak{a}_{02}\Delta x^2 + \mathfrak{a}_{20}\Delta y^2 + \mathfrak{a}_{12}\Delta x^2\Delta y + \mathfrak{a}_{21}\Delta x\Delta y^2 + \ldots, \tag{4.1.5}$$

in analogy to the truncated power series approximations suggested by Eça and Hoekstra (2014) for grid refinement studies in a single discretisation dimension. If the same refinement factors are used for both dimensions, Δx can be substituted by Δy and vice versa. For instance, eq. (4.1.5) can be rewritten, substituting

[1] If, for example, x and y represent space dimensions, $\Delta x/\Delta y$ correspond to cell aspect ratios. In another example, x may represent time and y a space dimension. Then, $\Delta x/\Delta y$ is proportional to the local Courant numbers, and the bounds are lower and upper Courant number stability limits.

$\Delta y = \kappa \Delta x$,

$$\begin{aligned}\delta_D =& (\mathfrak{a}_{01} + \kappa \mathfrak{a}_{10}) \Delta x + \left(\mathfrak{a}_{02} + \kappa \mathfrak{a}_{11} + \kappa^2 \mathfrak{a}_{20}\right) \Delta x^2 + \ldots, \\ =& \tilde{\mathfrak{a}}_1 \Delta x + \tilde{\mathfrak{a}}_2 \Delta x^2 + \ldots.\end{aligned} \tag{4.1.6}$$

Referring to Fig. 4.1, eq. (4.1.6) approximates the discretisation error for any set of grid representations located on a straight line through the origin. Hence, eq. (4.1.6) can be established for any value of κ, provided the reference grid representation lies within the bounds of valid discretisations[2].

In order to be able to compare grid sets with different reference values (or initial grids), a non-dimensional scalar grid refinement ratio, Υ, is proposed as a measure for the relative grid resolution,

$$\begin{aligned}\Upsilon_i =& \sqrt{\frac{1}{2}\left[\left(\frac{\Delta x_i}{\Delta x_1}\right)^2 + \left(\frac{\Delta y_i}{\Delta y_1}\right)^2\right]} \\ =& \sqrt{\frac{1}{2}\left[\left(\frac{1}{c_x}\right)^{2i} + \left(\frac{1}{c_y}\right)^{2i}\right]},\end{aligned} \tag{4.1.7}$$

with arbitrarily chosen reference grid node spacings Δx_1 and Δy_1. According to this approach, $\Upsilon_\infty = 0$ corresponds to a grid representation with infinitely small grid spacing in all directions which is associated with the grid-independent solution. A geometrical interpretation of Υ is the relative distance to the origin in a two-dimensional space spanned by Δx and Δy, where the point $(\Delta x_1, \Delta y_1)$ has distance 1.

In analogy to eq. (4.1.6), the grid-dependent solution value may now be established as a function of Υ,

$$\begin{aligned}\delta_D(\Upsilon) =& \phi(\Upsilon) - \phi_\infty \\ \phi(\Upsilon) =& \phi_\infty + \mathfrak{a}_1 \Upsilon + \mathfrak{a}_2 \Upsilon^2 + \ldots\end{aligned} \tag{4.1.8}$$

The order of this polynomial should be chosen so that the expected order of grid convergence can be replicated. Then, the required minimum number of solution values on different grid representations is defined from the number of

[2] In this respect, non-uniform refinement sensitivity studies are justified because they may help to identify these bounds.

coefficients, i.e., for a second-oder approximation a minimum of solution values on three grids is required to determine the coefficients $(\phi_\infty, \mathfrak{a}_1, \mathfrak{a}_2)$.

For practical engineering applications, solution values usually show a considerable degree of scatter. One of the sources of scatter is the virtual impossibility to use systematically refined grids on which the solution values can be obtained for identical grid nodes. Interpolation and, more important, not geometrically identical grid representations introduce scatter. Eça and Hoekstra (2002) suggested to use more than the minimum required number of grid representations to level out the effect of data scatter. The grid-independent solution is then determined from least-squares fitting of the available solution values. In case of the original Richardson extrapolation and a number of n_g grid representations, the proposed least-squares formulation is to minimise

$$S_{RE}(\phi_\infty, \alpha, p) = \sqrt{\sum_{i=1}^{n_g} \left(\phi_i - \left(\phi_\infty + \alpha \Delta x_i^p\right)\right)^2}. \tag{4.1.9}$$

Consistently, least-squares minimisation can also be applied to eq. (4.1.8), here given for the cases of first and second order polynomial formulations of δ_D:

$$S_1(\phi_\infty, \mathfrak{a}_1) = \sqrt{\sum_{i=1}^{n_g} \left(\phi_i - (\phi_\infty + \mathfrak{a}_1 \Upsilon)\right)^2} \tag{4.1.10}$$

$$S_2(\phi_\infty, \mathfrak{a}_1, \mathfrak{a}_2) = \sqrt{\sum_{i=1}^{n_g} \left(\phi_i - (\phi_\infty + \mathfrak{a}_1 \Upsilon + \mathfrak{a}_2 \Upsilon^2)\right)^2}. \tag{4.1.11}$$

Several reasons for scattered solution values exist which are not related to the discretisation error. For example, one source of scatter is the need for post-processing to obtain the quantity of interest from the computation results, e. g. the extraction of motion amplitudes from transient simulations. This source of scatter is particularly difficult to address but has to be kept in mind when estimating the required minimum number of solution values for extrapolation of grid independent solutions.

4.2 Free Vibration Decay Simulations

Vibration damping is of primary importance to predict vibration magnitudes excited by resonance, since the maximum amplitudes in resonance conditions

are directly linked to the overall damping. The range of relevant frequencies to cause springing excitation depends on the damping as well; the higher the damping ratio, the smaller the response amplitude in resonance, but the broader the range of frequencies of interest.

The damping ratio is also of importance for vibration excited by slamming because it defines the decay rate of the free vibration after the initial impact. Although the typically small damping does not affect the initial maximum response amplitude, it determines the number of vibration cycles until the response amplitude has decayed below a certain threshold, as well as the residual vibration level that is still present in case of a consecutive impact.

Despite its significant influence on the total vibration levels, vibration damping of ships is related to large uncertainty. Generally speaking, there exists no accurate method to determine structural damping experimentally or numerically. Only estimates of structural damping exist based on full scale measurements of freely decaying vibrations, but these need to rely on an estimate of the hydrodynamic damping. The damping of welded ship structures is negligible due to a very low material damping of steel. Paint, cargo (in particular bulk cargo and cars), as well as outfitting and gear (e. g. hatch covers) may contribute to damping.

On the other hand, hydrodynamic damping of vibrations has several sources and probably is the major contribution to overall vibration damping. According to Söding (2009), the most important contributions are wave radiation at sections with inclination in the waterline, and momentum transfer from the oscillating transom stern to the wake flow at forward speed. Other hydrodynamic contributions are viscous damping from flow separation at bilge keels and lifting forces of the propeller. For a large containership at $20\,kts$ forward speed, Table 4.1 lists the estimates of the damping contributions given in Söding (2009).

A simple and straightforward approach to determine the total damping numerically or experimentally is a free vibration decay test. Fig. 4.2 shows the vertical bending moment measured during a free vibration decay experiment in model scale and corresponding computed results [3]. The floating flexible ship model was excited to vibrate by a hammer stroke. The measured time series is typical in that vibrations are clearly dominated by the fundamental vertical two-node vibration mode, while higher frequency modes contribute in the initial phase

[3] All time series of vibration decay are normalized with the initial amplitude to allow for easy comparison.

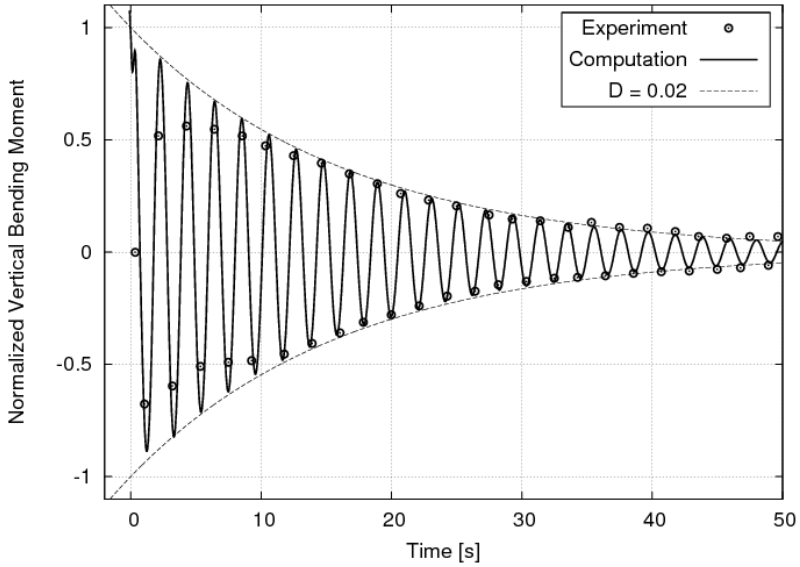

Figure 4.2: Example of normalized vertical bending moment in vibration decay experiment and corresponding computation

only. After this short initial phase, the time series can well be approximated by a two-node vibration with exponentially decaying amplitude,

$$\Phi(t) = \Phi_0 \, cos(\omega_n t + \Psi) \, \exp(-D\omega_n t), \tag{4.2.1}$$

where Φ_0 is the initial amplitude at $t = 0\,s$, ω_n the natural frequency of the fundamental two-node bending mode, and D the damping ratio of actual damping, C, to critical damping, C_{crit}. A phase angle Ψ accounts for the phase shift between exposure to the initial shock and the maximum response. Eq. (4.2.1) is valid for linear damping only, i.e. the damping ratio is assumed independent of the vibration magnitude. Apart from the initial phase of the free vibration where transients and higher frequencies contribute to the stresses, this is a reasonable approximation.

A major shortcoming of experiments is the difficulty to separate hydrodynamic and structural damping. Here, free vibration damping simulations using the

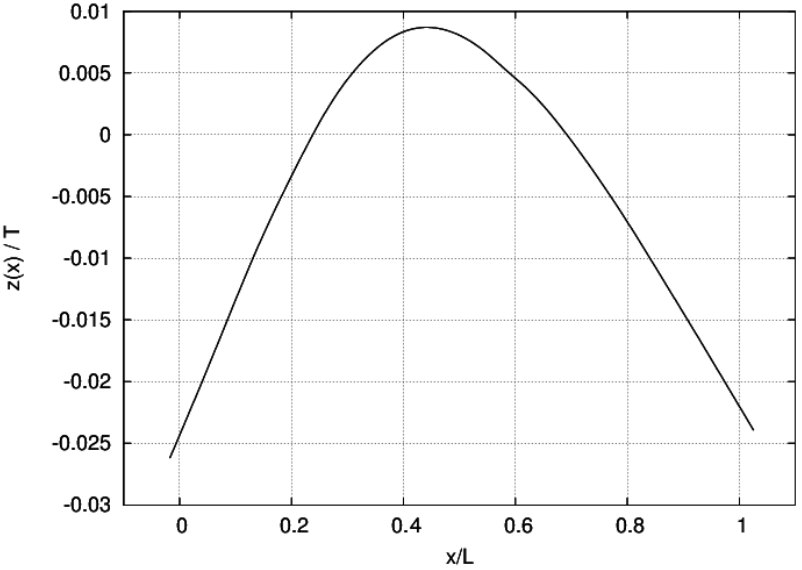

Figure 4.3: Example of static hull deflection in hogging (normalized with ship draught) at the end of a free vibration decay simulation

coupled numerical methods can be beneficial in explicitly addressing the hydrodynamic damping. However, flow features with relatively small time or length scales require a fine grid and time step resolution; otherwise, numerical damping will impose artificially high damping.

In the following, free vibration decay simulations are introduced for determining the hydrodynamic damping. Grid refinement studies help to quantify the influence of the discretisation and to estimate the grid-independent hydrodynamic damping. The procedure outlines as follows. The ship is simulated in still water at the forward speed of interest. After a short initial time, the ship is released to move and deflect freely, so that the load imbalance due to inequal longitudinal distribution of buoyancy and weight acts as an impulsive loading and the hull girder is excited to free vibrations around the final hogging or sagging deflection. Fig. 4.3 exemplifies the static deflection of a large containership at the end of such a simulation, emphasizing that the load imbalance in still water mainly

Table 4.1: Estimates of hydrodynamic and structural damping ratios in percent for vertical vibration according to Söding (2009)

nodes	transom	wave radiation	bilge keels	propeller	hatch cover	Sum
2	1.850	0.400	0.080	0.030	0.006	2.366
3	0.910	0.075	0.034	0.022	0.003	1.044

excites the vertical two-node bending mode. Setting structural damping to zero, only the numerical and the hydrodynamic damping cause the vibrations to decay with time. Since numerical damping is a discretisation error, it will approach zero when the grid spacing becomes infinitely small. Systematic grid refinement allows to formulate the computed damping ratio, D, as a function of grid refinement, Υ, in analogy to eq. (4.1.8),

$$D(\Upsilon) = D_\infty + \mathfrak{a}_1 \Upsilon, \tag{4.2.2}$$

where index ∞ denotes the limit of an infinitely refined grid (zero grid spacing). The hydrodynamic damping is now interpreted as the total damping for the limit of zero grid spacing,

$$D_{hyd} = D(\Upsilon = 0) = D_\infty. \tag{4.2.3}$$

RoPax ferry

Results of a vibration decay simulation study for the ferry are discussed in the following, particulars listed in appendix A. Model test results with a segmented model were available, but unfortunately no time series data of experimental vibration decay tests. All results provided here are valid for the ship at zero speed, and given in full scale.

The hull girder structural model replicated the segmented model used in experiments. It consisted of 15 uniform beam elements representing the aluminium backbone, and two stiff elements at the bow and stern extending beyond the backbone ends. Bending stiffness contributions from the wooden hull segments were disregarded because the experimental model was assembled in a way

Table 4.2: Dry and wet natural frequencies of RoPax passenger ferry

mode	$\omega_{n,dry}$	ω_n	$\omega_{n,exp}$
2-node	$7.17\,rad/s$	$5.36\,rad/s$	$5.10\,rad/s$
3-node	$20.86\,rad/s$	$13.80\,rad/s$	$11.80\,rad/s$
4-node	$38.77\,rad/s$	$27.00\,rad/s$	

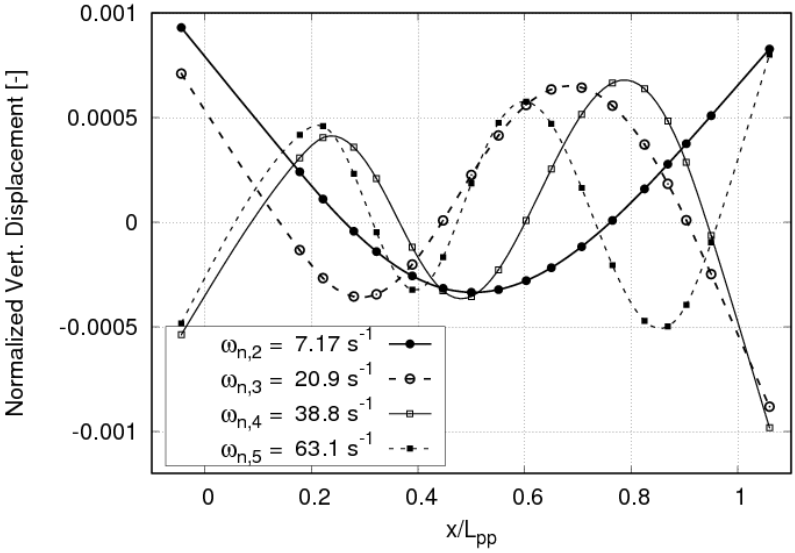

Figure 4.4: Dry natural modes of the RoPax ferry beam model and corresponding frequencies

that bending deflections of the hull segments were not transferred to the backbone. Fig. 4.4 shows the lowest dry natural mode shapes and associated natural frequencies of the beam model.

Fourier analysis of simulated vibratory accelerations, Figs. 4.5 and 4.6, determined the natural vibration frequencies of the wetted numerical model. The two-node vibration mode in this case had a frequency in water of $5.36\,rad/s$, while the three- and four-node modes had frequencies of approximately $13.8\,rad/s$

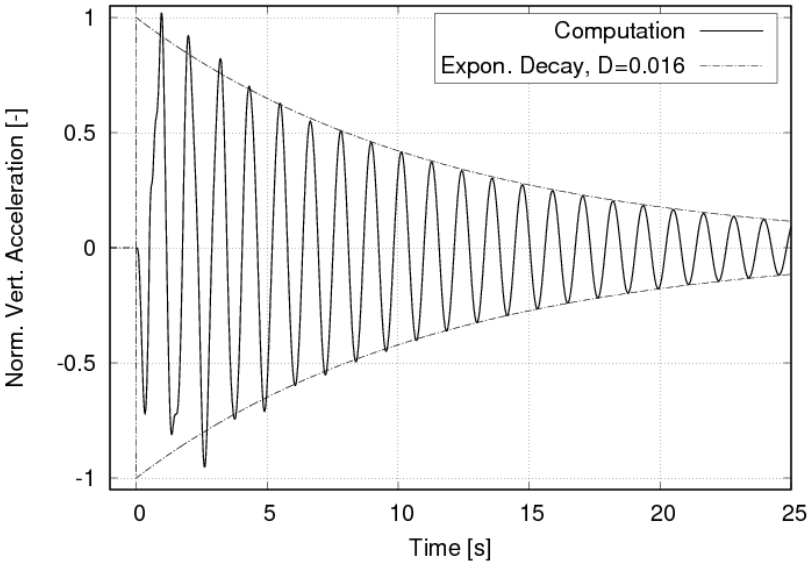

Figure 4.5: Exemplary time series of normalized vertical vibration acceleration from free vibration decay simulation of the RoPax ferry at zero speed

and 27 rad/s, respectively. The latter are difficult to determine due to the small amplitudes and the unpronounced peaks. These figures reasonably match the frequencies measured in the experiments, see Table 4.2 (index *exp* refers to the experiments). The spectral analysis reveals a secondary peak at 10.8 rad/s, twice the two-node frequency which is caused by small peak-trough asymmetries, and probably due to changes in waterline breadth.

Fig. 4.5 shows that only in the initial phase of vibration there is a contribution from the higher vibration modes, but with time the signal becomes more and more dominated by the two-node frequency. The relevance of individual vibratory modes can also be assessed from the amplitude spectrum, Fig. 4.6, here given in logarithmic scale. The amplitude spectrum clearly indicates the insignificance of vibration modes other than the fundamental two-node vertical mode.

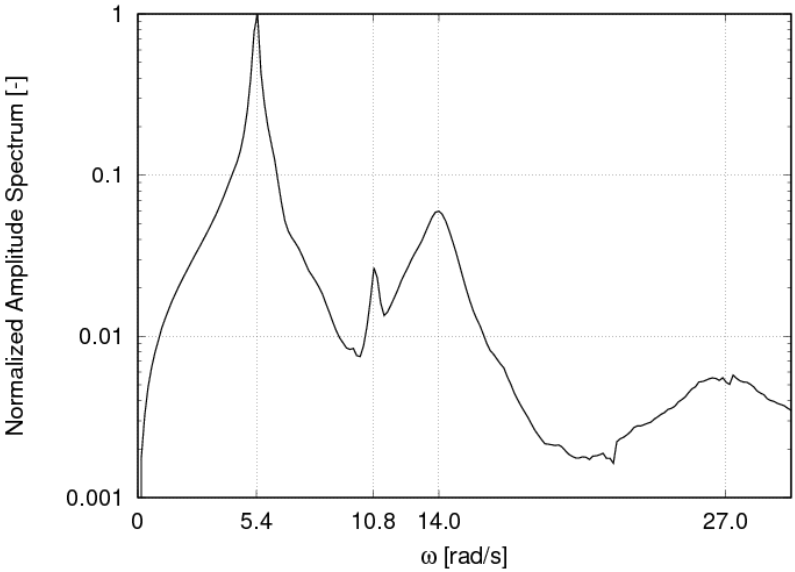

Figure 4.6: Amplitude spectrum of vibratory accelerations corresponding to Fig. 4.5

The measured damping ratio in the experiments was $D = 0.8\%$ of the critical damping. This included a structural damping of approximately 0.2%, Drummen and Holtmann (2014). The structural damping estimate, however, should be handled with care due to a large uncertainty arising from the difficulty to measure the structural damping in model experiments.

To investigate the influence of spatial and temporal resolution on the total damping, vibration decay simulations were performed with *COMET* on four different grids using six different time step sizes. The unstructured grids consisted of mainly hexahedral cells with polyhedral cells in the vicinity of the hull and prism layers on the hull boundary, and were generated with an automatic meshing strategy. This does not allow systematic refinements in a strict sense because of the unstructured grid point distributions of the polynomial and prismatic cells. However, the grid node allocation of the hexahedral cells basically followed the criteria of systematic refinement, and the ratio of numbers of cell between

consecutive grids fairly well matched $2/1$. This was achieved by setting the spatial grid refinement factor to $c_x = \sqrt[3]{2}$ uniformly for all directions, resulting in $560,000$ control volumes on the coarsest grid up to the finest grid with $4,100,000$ control volumes. The refinement factor for the time step was $c_t = \sqrt[3]{2}$ as well, with time steps $\Delta t_1 = 0.01\,s$ down to $\Delta t_6 = 0.00315\,s$.

Natural frequencies were not sensitive with respect to grid resolution. Throughout all computations, there was no change of natural frequencies. This finding is important since the computed natural frequencies are a result of the fluid-structure interaction; the vibrating structure accelerates the surrounding fluid, thus virtually increasing the vibrating mass (added mass). Inaccurately captured added masses would change the natural frequencies. Therefore, all investigated combinations of grid spacing and time step size were sufficient to capture the hydrodynamic radiation forces driven by acceleration.

Table 4.3: Extrapolated hydrodynamic damping ratios from computations in percent of the critical damping

	set A	set B	set C	set D	Experiment
D_{hyd}	0.52	0.53	0.50	0.44	0.6
$\tilde{\mathfrak{a}}_1$	1.12	0.98	0.86	0.84	n/a

The vibration decay simulations were assigned to five sets, A through E, of uniformly refined grid representations, see Fig. 4.7 (top). For each of these sets, least-squares minimisation according to eq. (4.1.10) yielded the damping ratio, D, as functions of Υ for each set of grid representations,

$$S_1(D_{hyd}, \mathfrak{a}_1) = \sqrt{\sum_{i=1}^{n_g} \left(D_i - \left(D_{hyd} + \mathfrak{a}_1 \Upsilon\right)\right)^2}, \tag{4.2.4}$$

with $D_{hyd} = D_\infty$ according to eq. (4.2.3). Fig. 4.7 (bottom) shows the fitted curves along with the solution values. The resulting D_{hyd} for each grid set are listed in Table 4.3.

All extrapolated hydrodynamic damping ratios are comparable in magnitude and, except for grid set D, are very close to each other. The discrepancy between the extrapolated value found from grid set D can at least partly be explained with the reduced number of only three grid representations in this set, but considering the amount of scatter found for all grid sets, the very good matching may as

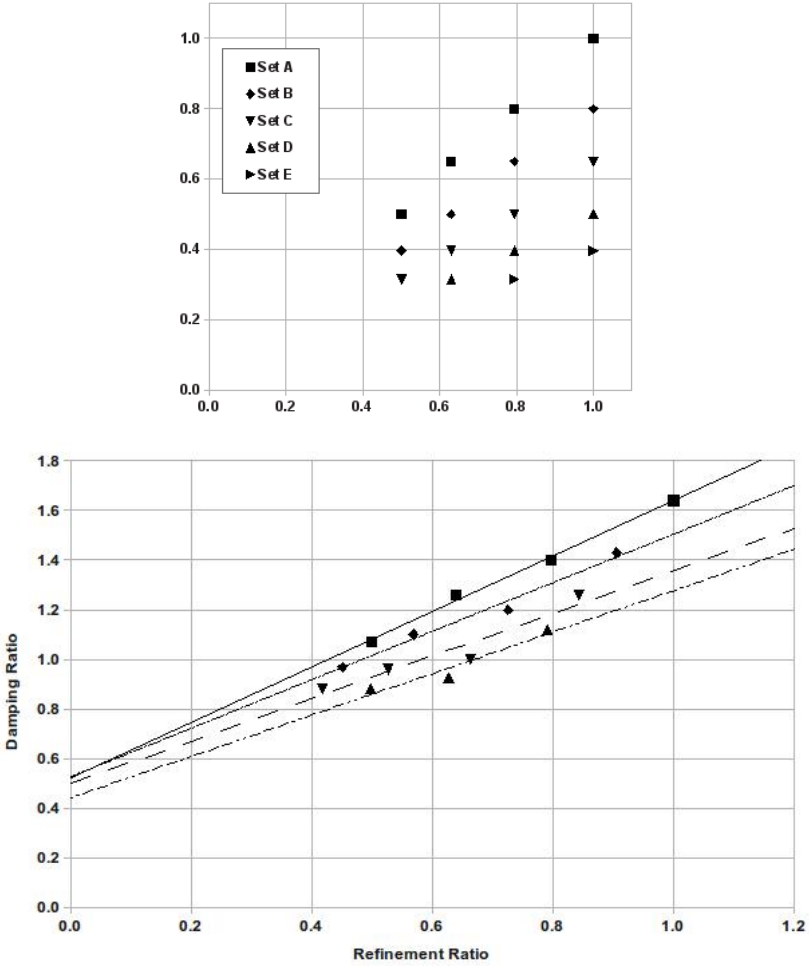

Figure 4.7: Top: relative spacings $\Delta x_i/\Delta x_{ref}$ (horizontal axis) and $\Delta t_i/\Delta t_{ref}$ (vertical axis) of the grid sets; bottom: damping ratio as a functions of combined spatial and temporal grid refinement ratio for different grid sets

well be a coincidence. However, the computed hydrodynamic damping ratios also agree reasonably well with the experimental hydrodynamic damping ratio of $D_{hyd} = 0.6\%$ of the critical damping according to Drummen and Holtmann (2014).

In an earlier published evaluation of the above computational results, el Moctar et al. (2011), a different extrapolation approach was applied based on a linear regression fit over all numerical solution values. A different definition of the grid refinement ratio was used that corresponds to Υ^2, so the regression effectively assumed a second-order convergence, and the hydrodynamic damping ratio estimate was 0.75%. However, comparing the goodness of fit of the earlier evaluation with the present results given in Table 4.3, indicates that first-order regression actually gives a better overall fit to the data.

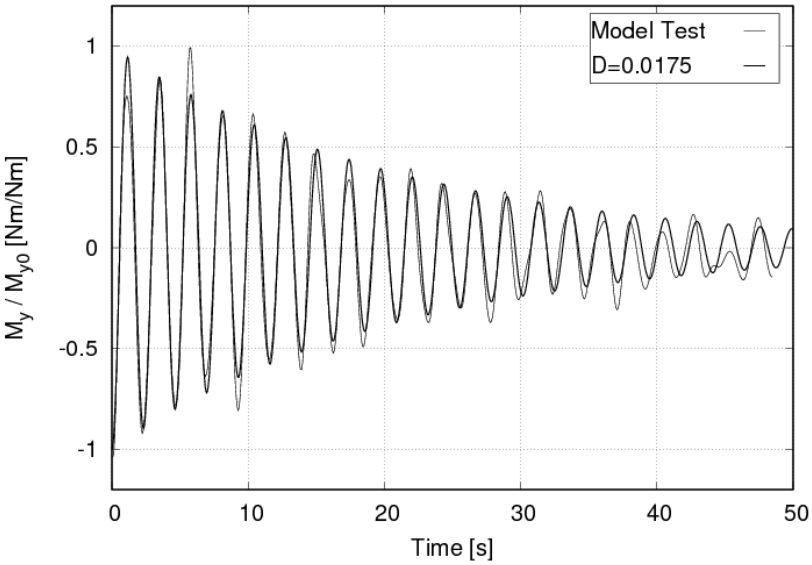

Figure 4.8: Normalized vertical bending moment in experimental free vibration decay test for 10,000 TEU containership

10,000 TEU Containership

A second vibration decay study is presented for the 10,000 TEU containership. Experimental data were available for vibration decay tests at forward speeds ranging from $0\,kts$ to $20\,kts$ in increments of $5\,kts$. In experiments, vibrations were initiated by hammer strokes on the bow of the model; simulations, instead, used the initial imbalance of mass and floatation distribution to excite vibrations, see Figs. 4.8 and 4.9 for example time series. Computations were performed, for each forward speed, on three grid representations with refinement ratios $c_x = c_t = \sqrt[3]{2}$ and using both solvers *COMET* and *interDyMFoam*. Fig. 4.10 shows the time series from Figs. 4.8 and 4.9 on a logarithmic scale. Although the signal from experiments becomes distorted by random irregularities after the vibration amplitudes have decayed below 0.25 of the initial amplitudes, both time series indicate that the damping can well be described by a linear damping function according to eq. (4.2.1). The reason for the irregular disturbances in

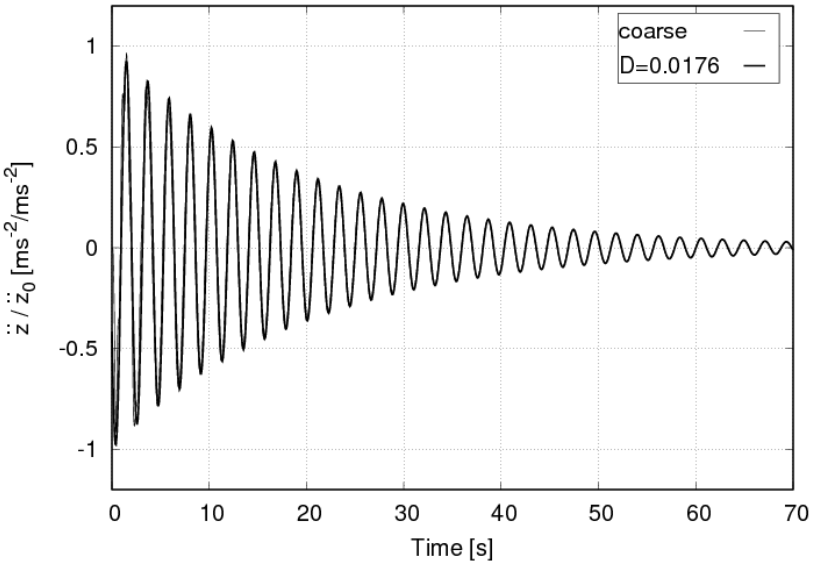

Figure 4.9: Normalized vertical vibration acceleration in free vibration decay computation with *COMET* for 10,000 TEU containership

experiments is not known, yet these are believed to be caused by undesired external forcing; residual waves in the test basin or vibratory excitation from the model carriage may be potential sources of the disturbances.

Damping values D_i were assigned to each computation by visually fitting the time series with a decay function according to eq. (4.2.1) and manually adjusting the parameters ω_n, Ψ and D_i. It can be observed from Fig. 4.9 that this results in a good replication of the time series. The obtained damping ratios consistently decrease with grid refinement for both solvers and all speeds considered. For each speed, linear regression over the damping ratios computed on three grids established the damping as functions of the grid refinement and allowed to extrapolate the damping towards $\Upsilon = 0$, again assuming the grid-independent solution value D_∞ to equal the hydrodynamic damping D_{hyd}, Fig. 4.11.Fig. 4.12 shows the grid-independent damping ratios found from this regression, plotted over forward speed, along with the total damping found from the experimental

vibration decay tests. The computed damping ratios generally replicate the trend of increasing damping with increasing forward speed as observed from experiments. Note that the damping ratios from experiments are associated with some uncertainty due to the observed irregularities in the time series, particularly for the lower speeds. Except for the case of $5\,kts$ forward speed, the computed damping ratios D_∞ have an offset towards the experiments which is almost constant. This offset is different for the two solvers, with a smaller offset found from the *interDyMFoam* results. Structural damping was disregarded in the computations and may account for part of the constant offsets between computational results and experiments. However, the difference between the results obtained with *COMET* and *interDyMFoam* cannot be explained with structural damping. Instead, this difference may be attributed to differences of the solution algorithms, but numerical uncertainty and scatter introduced through data analysis and processing may also contribute.

Additional computations with *interDyMFoam* were performed to confirm that the regression fits established for the initial grid set could be used to extrapolate the damping ratio towards more refinened representations. These computations used further refined grids with up to $25,000,000$ cells. Fig. 4.11 compares the regression fits obtained on the initial set of grids with those obtained on the amended set of up to six grids. Generally, the trends were confirmed although the finer grids tended to give lower damping and the regression over the larger grid sets resulted in lower extrapolated damping ratios D_∞. Nevertheless, the differences were of the order of 0.1% of the critical damping only. Considering the significant increase in computational effort, it may be sufficient for practical applications to omit computations on very fine grids and extrapolate the D_∞ based on a set of relatively coarse grids.

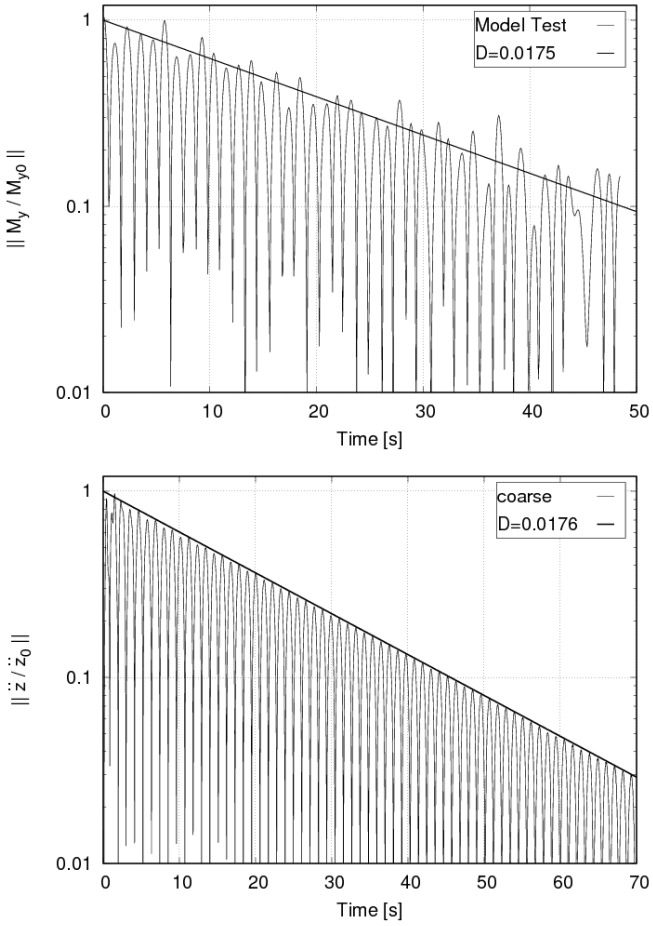

Figure 4.10: Logarithmic plots of free vibration decay time series from Fig. 4.8 (top) and Fig. 4.9 (bottom) along with the envelopes of the fitted decay functions

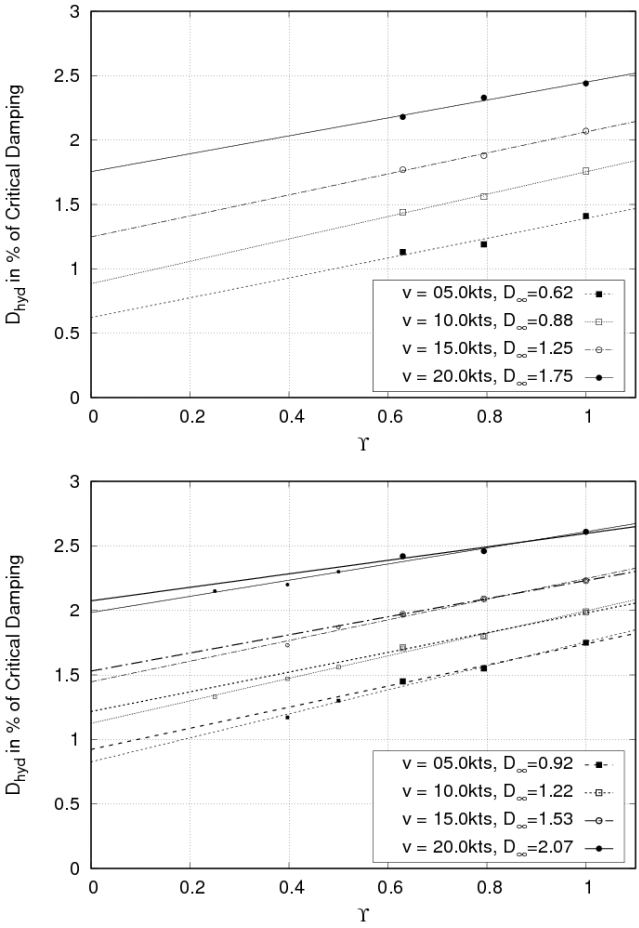

Figure 4.11: Hydrodynamic damping of 10,000 TEU containership as function of grid refinement ratio for different forward speeds using *COMET* (top) and *interDyMFoam* (bottom); initial set of three grids (large symbols and thick lines), amended set of up to six grids (small symbols and thin lines); values of D_∞ displayed are for the initial set

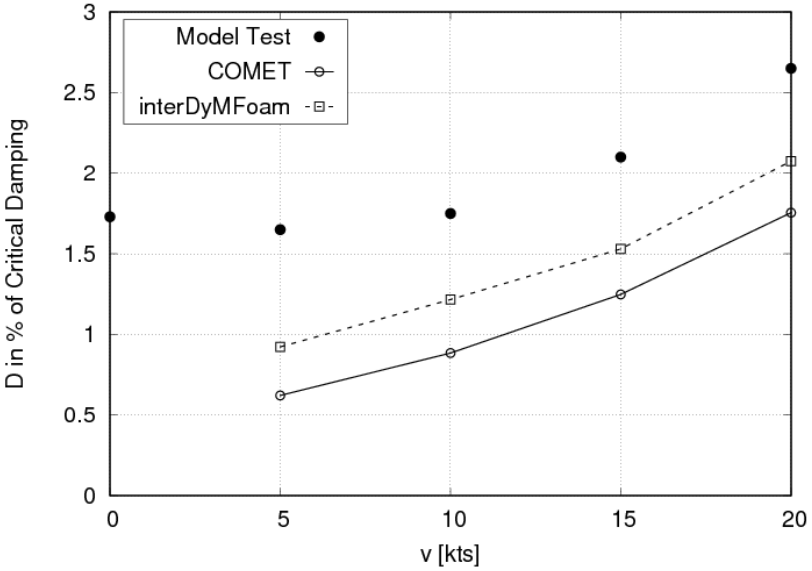

Figure 4.12: Damping of 10,000 TEU containership as a function of forward speed; experimental values are the total damping, computed values include only the extrapolated grid-independent hydrodynamic damping D_∞

4.3 Motions and Loads in Waves

The previous sections dealt with hydrodynamic impact loads and ship hull girder vibration for calm water conditions. Now, systematic investigations of motions and related loads in waves are presented, starting with regular harmonic waves of low to moderate steepness and various lengths. The loads and ship reactions of interest are hydrodynamic impact loads and global internal loads, with the latter being consequences of the external forcing by waves and the mass inertia forces due to rigid-body and flexural motions of the ship. Systematic comparisons are presented with test series of a flexible ship model, confirming the applicability of the numerical method to problems related to wave loads and flexural responses of ships. Computations in irregular waves are discussed next, with emphasis on the short-term statistical properties of the ship reactions. Again, comparisons with model tests show reasonable agreement of the numerical method with experiments. It is demonstrated that the upcrossing rate of a ship response of a given magnitude is a function of the fluid grid resolution. Based on this finding, strategies are discussed to estimate grid independent upcrossing rate distributions of the vertical bending moment.

The ship reaction of particular interest is the vertical bending moment (VBM). In the following, all VBM are normalised using water density ρ, gravitational acceleration g, ship's breadth B and length L, and wave amplitude A_W. In case of irregular waves, $H_S/2$ will be used instead of A_W.

4.3.1 Regular Waves

Linear potential theory captures many ship reactions in regular waves of small steepness with sufficient accuracy[4], so comparisons are made first with model tests and linear frequency domain computations using *GL Rankine* for waves of small amplitude. Next, slamming impacts and nonlinearities of the ship reaction are studied in regular waves of larger amplitude.

For small amplitude waves, the response becomes a linear function of the wave amplitude and basically takes place at encounter frequency. Simulations and computations in single regular waves allow to identify the ship reactions to the excitation at the particular wave encounter frequency. The amplitudes of ship

[4] In particular, this holds for the reactions of interest here: the heave and pitch motions as well as the VBM

reaction per wave amplitude as a function of frequency are conveniently found from Fourier analysis of the time series data. Assuming linear correlation in small waves between wave amplitude and ship response amplitude, the results are interpreted as transfer functions of the ship response. In case of larger wave amplitudes, time series analyses of ship responses in regular waves of same frequency but varied amplitude allow to assess quadratic or higher-order dependencies of the ship response on the wave height.

10,000 TEU Containership

Model scale experimental data are available for the 10,000 TEU post-panamax containership, appendix A, running in regular head waves of systematically varied length. These data are used here for validating the numerical method's ability of replicating the ship reaction in terms of motions and internal loads including vibratory effects. Experiments and computations used a flexible representation of the hull girder, allowing to address resonant vibrations caused by harmonic wave excitation. Hammering tests of the floating segmented model provided the fundamental natural frequency of the vertical 2-node bending mode at $20\,kts$ forward speed, $\omega_n = 2.702\,rad/s$ (full scale), see also section 4.2. The hammering tests also provided the total damping which was used to tune the numerical models in a way that these have the same total damping.

Two types of ship response were obtained from the Fourier decomposed time series data:

- Responses at a frequency equal to wave encounter frequency ω_e; these correspond to conventional transfer functions.
- Responses at a frequency equal to the two-node vertical bending natural frequency ω_n; these secondary responses correspond to resonant vibration.

Resonant vibration is excited when the wave encounter frequency matches a natural frequency of the hull girder, typically the natural frequency of the fundamental two-node vertical bending mode. Hence, for a given ship speed v and wave encounter angle μ, waves with frequency ω are in resonance with the hull girder if

$$\omega_n = \omega_e = \omega - kv\cos(\mu). \tag{4.3.1}$$

Higher order resonance occurs if the natural frequency of the response is a multiple of the frequency of excitation:

$$\omega_n = m \cdot \omega_e, \quad m = 2,3,4,... \tag{4.3.2}$$

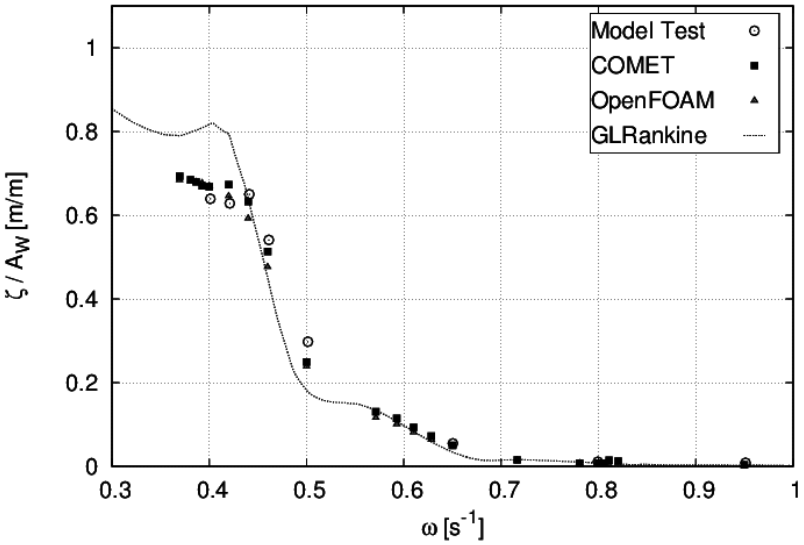

Figure 4.13: RAOs of heave motion in head waves at $20\,kts$ ship speed

Starting point for comparisons are heave and pitch motions in head waves at a ship forward speed of $20\,kts$, along with corresponding accelerations. Wave lengths varied from $\lambda = 34.0\,m$ to $\lambda = 450.0\,m$ with clustering around resonance frequencies. Wave heights were limited by a maximum steepness of $H_W/\lambda_W = 1/40$ and a maximum wave height $H_W = 3.0\,m$. Computations were performed with solvers *COMET* and *interDyMFoam*, both using identical time steps sizes and the same grid which was relatively coarse with about $250,000$ cells. Fourier transformations of numerical and experimental time series provided response amplitudes at wave encounter frequency. The time interval for the evaluation was, for each regular wave computation, set to a multiple of the wave encounter period to avoid aliasing effects. The initial phases of at least $50\,s$ were excluded from evaluation to minimize effects of initial transients on the results and to assure periodicity of the analysed time signal.

Figs. 4.13 and 4.14 show transfer functions of heave and pitch motions from the Fourier analysed computed and measured time series data, amended with

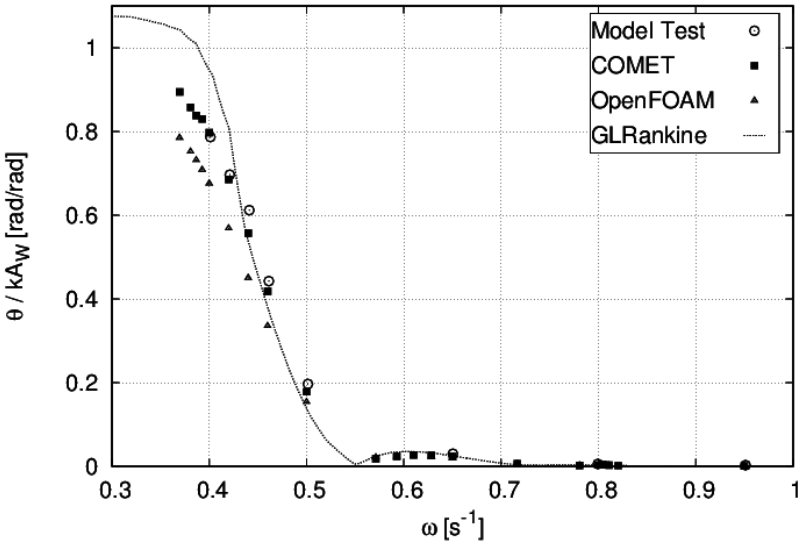

Figure 4.14: RAOs of pitch motion in head waves at $20\,kts$ ship speed

additional results of *GL Rankine* for reference. Generally good agreement with experiments is found for all numerical results. However, the *interDyMFoam* solutions tend to underpredict motion amplitudes, particularly pitch at frequencies around $\omega_e = 0.5\,s^{-1}$. The underprediction is the result of significant numerical dissipation of wave energy. The main source of numerical diffusion arises from the actually first-order accurate discretisation in time of the conservation equations, particularly the momentum transport equation. While *COMET* uses a second-order accurate Adams-Moulton scheme, the restrictions of MULES in *OpenFOAM* only allow the use of the Crank-Nicolson scheme which requires blending with implicit Euler. As a result, waves generated at the inlet boundary have already lost a significant amount of energy when they approach the ship.

Fig. 4.15 shows, for the same set of computations and experiments, the transfer functions of vertical bending moments at the sensing locations 2 and 3 ($x/L = 0.33$ and $x/L = 0.50$, respectively) as functions of wave frequency. Again, result of *COMET* are closer to experiments than those of *interDyMFoam* as a

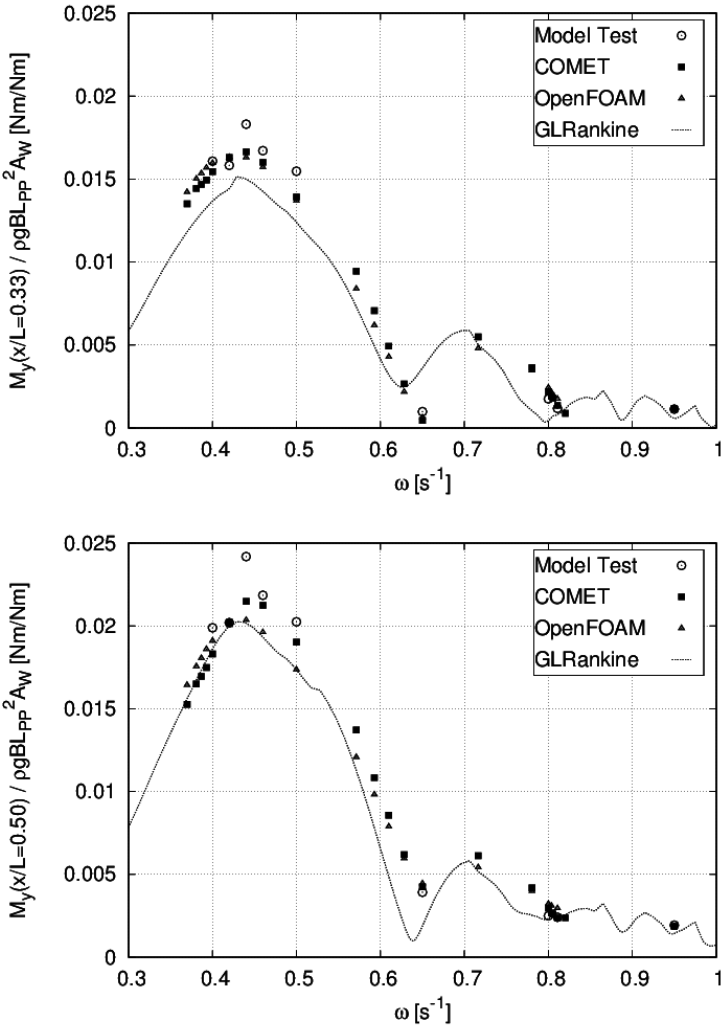

Figure 4.15: RAOs of VBM at station 2 ($x/L = 0.33$) and stations 3 ($x/L = 0.50$)

consequence of the observed wave energy diffusion with *interDyMFoam* and associated deviations in motion amplitudes.

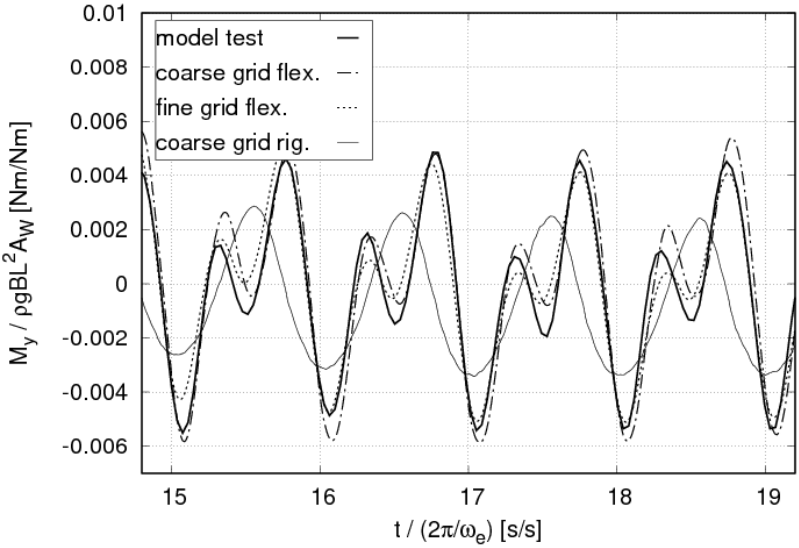

Figure 4.16: Time series of vertical bending moment at station 4 ($x/L = 0.67$) in run **#211**

In a next step, a similar evaluation yielded response amplitudes at ω_n. The time intervals for evaluation were modified and set to multiples of the natural period. The data analysis procedure is exemplified for the model test series with ID **#211**. The test run used a regular wave with $\omega_e = 1.50\,rad/s$, which is close to second order resonance, $2\,\omega_e = \omega_n$, and a wave height of $H_W = 3.0\,m$. Fig. 4.16 shows a comparison of the vertical bending moment (VBM) at station 4 ($x/L = 0.667$), from the model test with *COMET* computations using the initial coarse grid, denoted *A1*, and a refined grid with $1,800,000$ cells, denoted *A2*. Additional numerical results on grid *A1* for the rigid ship are included, revealing significant differences between rigid and elastic hull girder. Computations for the elastic hull girder on both grids replicate the experiments well. However, the model test has a slightly larger dynamic amplification due to vibration.

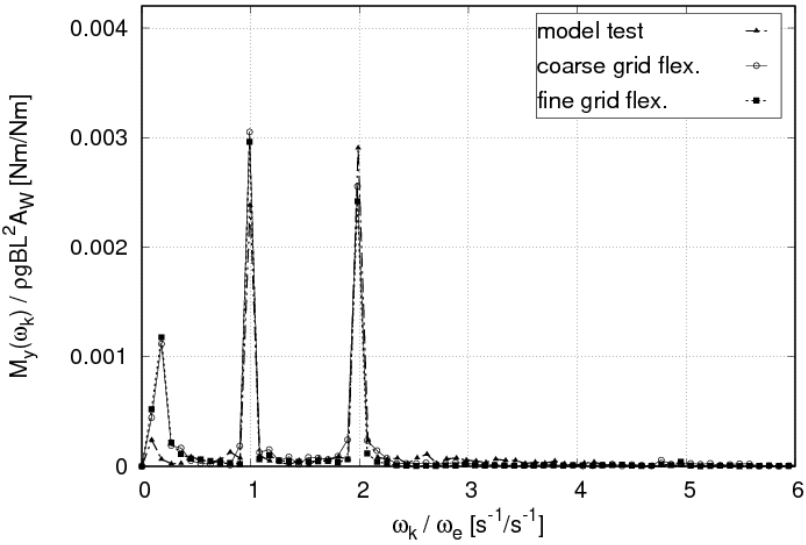

Figure 4.17: Normalised Fourier components of VBM corresponding to Fig. 4.16 (run **#211**)

Fourier decomposition of the time series determines the response contributions at frequencies ω_e and ω_n, Fig. 4.17. The constituent Fourier components ω_k are normalized here by the wave encounter frequency to highlight excitation and response mechanisms. Two distinct peaks are observed in both experimental and numerical results. The response peak at ω_e ($\omega_k/\omega_e = 1$) is the conventional reaction at wave frequency and is used to define the response amplitude operator. The second peak is caused by vibratory resonance, in this case of second order ($\omega_k = 2\omega_e = \omega_n$).

Figs. 4.18 shows amplitudes of VBM at the midship section (sensing station 3) for various wave encounter frequencies, each decomposed into wave encounter ($\omega_k = \omega_e$) and resonance ($\omega_k = \omega_e$) components according to the Fourier analyses. The graphs represent wave encounter (top) and vibratory (bottom) VBM amplitudes for various ω_e. The abscissa uses a non-dimensional encounter frequency ω_e/ω_n to emphasize resonance excitation mechanisms.

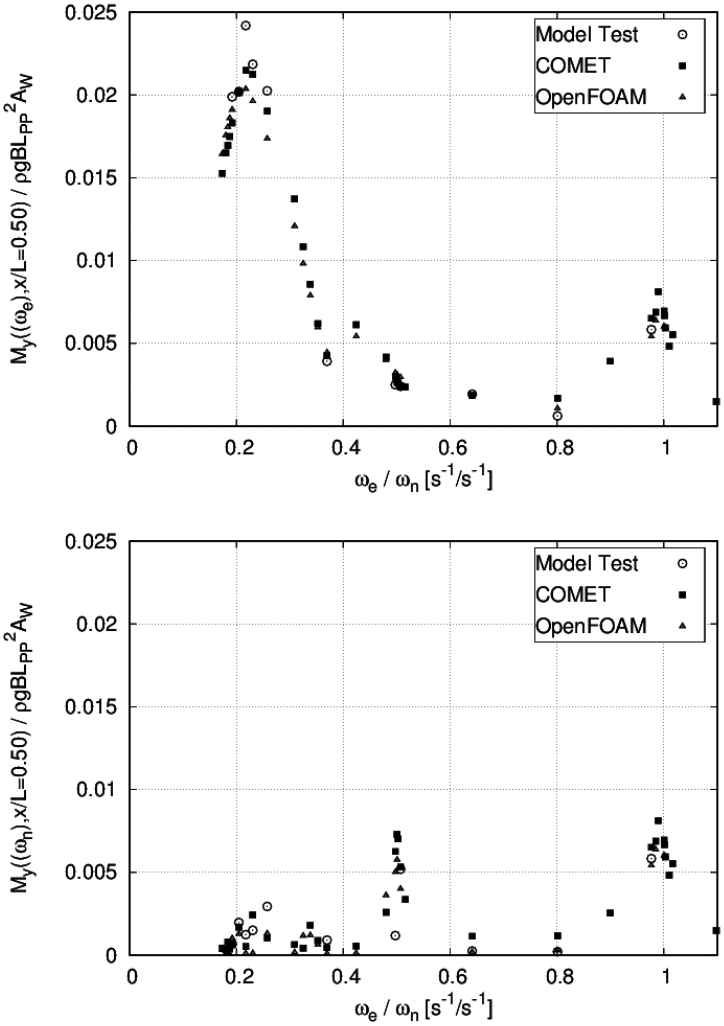

Figure 4.18: VBM at station 3 ($x/L = 0.50$) as functions of normalised wave encounter frequency; responses with frequency ω_e (top) and ω_n (bottom)

Two distinct peaks are observed in the vibratory components, the first of these at pure resonance ($\omega_e/\omega_n = 1$) and a second peak at second order excitation ($\omega_e/\omega_n = 0.5$). The latter even exceeds the corresponding response amplitudes at wave encounter frequency.

Due to the wave steepness limit, wave heights decrease for $\omega_e/\omega_n > 0.42$ with increasing ω_e. Since there is a nonlinear correlation between vibration response and wave height, one should be careful not to draw conclusions on the relevance of first and second order resonance only based on the presented figures. Nevertheless, comparisons showed a fair agreement of the numerical method with experiments.

The nonlinear dependency of resonant vibration on wave amplitude is an additional higher-order effect. It is exemplified for run **#211** and a run **#212** which has the same wave frequency but an increased wave amplitude, $H_W = 5.0\,m$. Figs. 4.17 and 4.19 show amplitudes of VBM normalised by wave amplitude for each discrete component k of the Fourier transformed time series data of runs **#211** and **#212**, respectively. The numerical and experimental coefficients for $\omega_k/\omega_e = 1$ indicate an almost linear dependency of VBM at wave encounter frequency on wave amplitude, although computations yield higher peaks. In contrast, vibration responses at $\omega_k/\omega_e = 2$, here corresponding to ω_n, increase more than proportionally with wave amplitude due to the nonlinear dependency of vibrations on wave amplitude. In addition to a good agreement of computational and experimental results, the numerical data consistently replicate the experimental trend.

Simulations and experiments presented so far for wave height $H_W = 3.0\,m$ did not show significant vibration responses at higher order resonance conditions, e.g., at $\omega_e/\omega_n = 0.33$, $\omega_e/\omega_n = 0.25$ or $\omega_e/\omega_n = 0.20$. Comparative computations in higher waves of $H_W = 9.0\,m$, Figs. 4.20 through 4.23, instead revealed an increase of vibration responses for such encounter frequencies. These computations use a reduced speed $v = 15\,kts$. Experimental data are available for waves with $\omega_e/\omega_n = 0.25$ and $\omega_e/\omega_n = 0.20$ corresponding to fourth and fifth order resonance, respectively. The wave lengths ($\lambda_W \approx 250\,m$ in case of $\omega_e/\omega_n = 0.25$, and $\lambda_W \approx 300\,m$ in case of $\omega_e/\omega_n = 0.20$) in conjunction with the wave height suggest the occurence of slamming events and consecutive vibration. Measured and computed time series of vertical bending moment and accelerations for both wave lengths show only modest characteristics of slamming impacts, see Figs. 4.24 and 4.25; high frequency oscillations, typically observed in severe impacts, are not present. The same finding holds for section loads and accel-

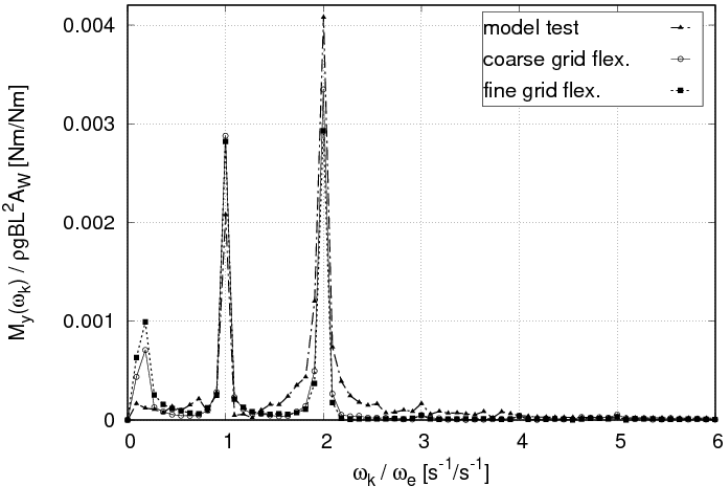

Figure 4.19: Normalised Fourier components of VBM at station 4 ($x/L = 0.67$) from run **#212**

erations at other section cuts. This suggests that the magnitude of observed vibration is not only determined by the severity of slamming impacts but also by the addition or extinction of vibration from a previous wave encounter. The peaks of the vibration responses in Figs. 4.20 through 4.23 (bottom figures) are hence related to resonant vibration which is initiated by small but periodic impacts.

The comparisons between computations and experiments presented above do not cover systematic grid refinement studies. However, results indicate that good qualitative agreement may already be achieved on coarse grids; computations on finer grids did not consistently provide improved results. This observation should not be interpreted as a deficiency of the numerical method. Instead, this indicates that the solutions, at least on the coarse grid, may be outside of the asymptotic range for the tested wave frequencies $\omega_e/\omega_n = 0.50$ and above, and therefore should be used with care when estimating grid independent solutions.

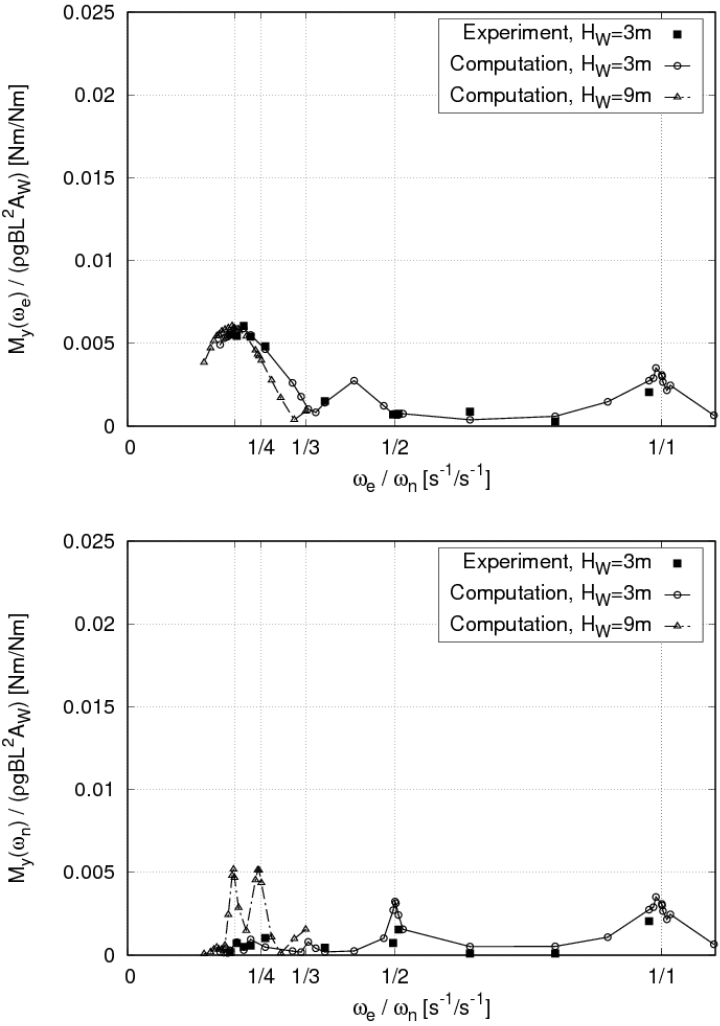

Figure 4.20: VBM at station 1 ($x/L = 0.17$) as functions of normalised wave encounter frequency; responses with frequency ω_e (top) and ω_n (bottom) for wave heights $H_W = 3.0m$ and $H_W = 9.0m$

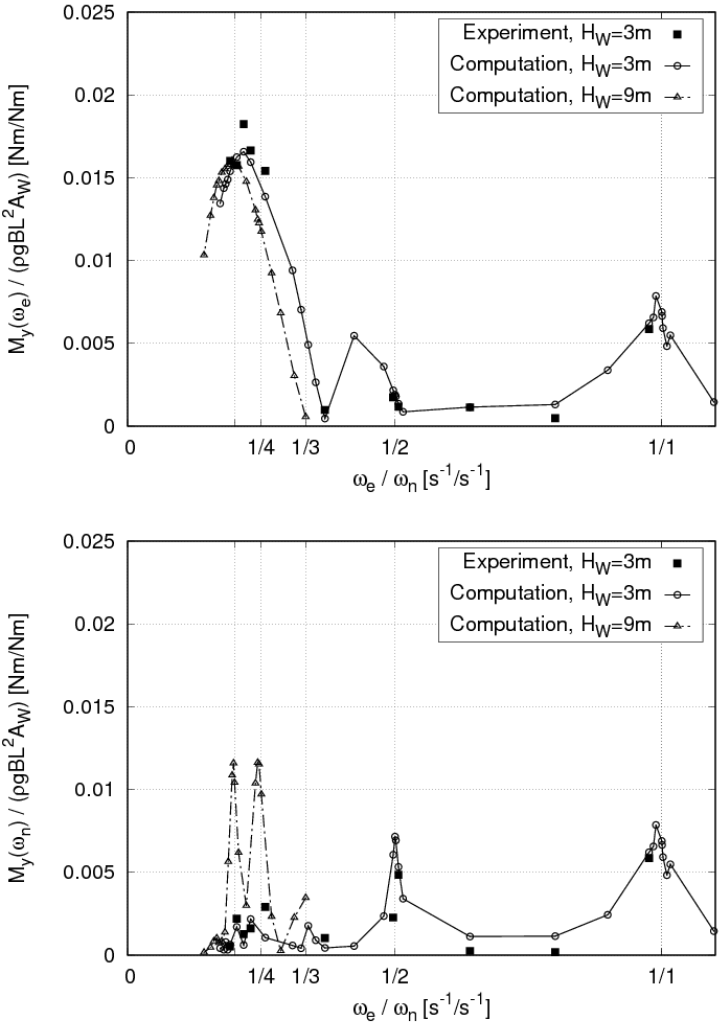

Figure 4.21: VBM at station 2 ($x/L = 0.33$) as functions of normalised wave encounter frequency; responses with frequency ω_e (top) and ω_n (bottom) for wave heights $H_W = 3.0\,m$ and $H_W = 9.0\,m$

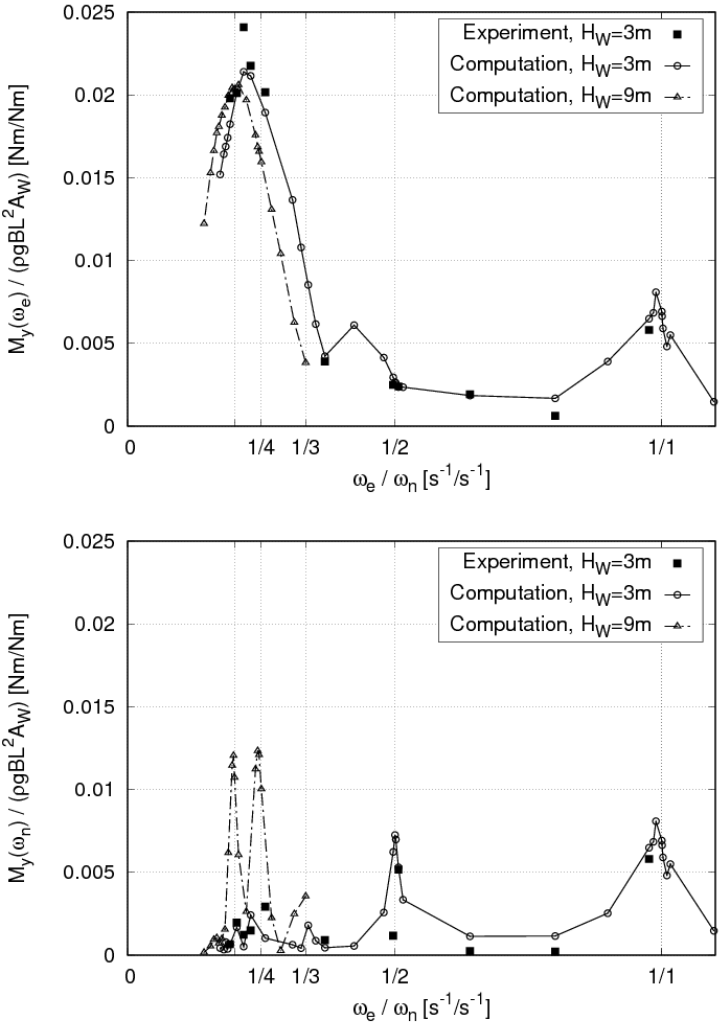

Figure 4.22: VBM at station 3 ($x/L = 0.50$) as functions of normalised wave encounter frequency; responses with frequency ω_e (top) and ω_n (bottom) for wave heights $H_W = 3.0m$ and $H_W = 9.0m$

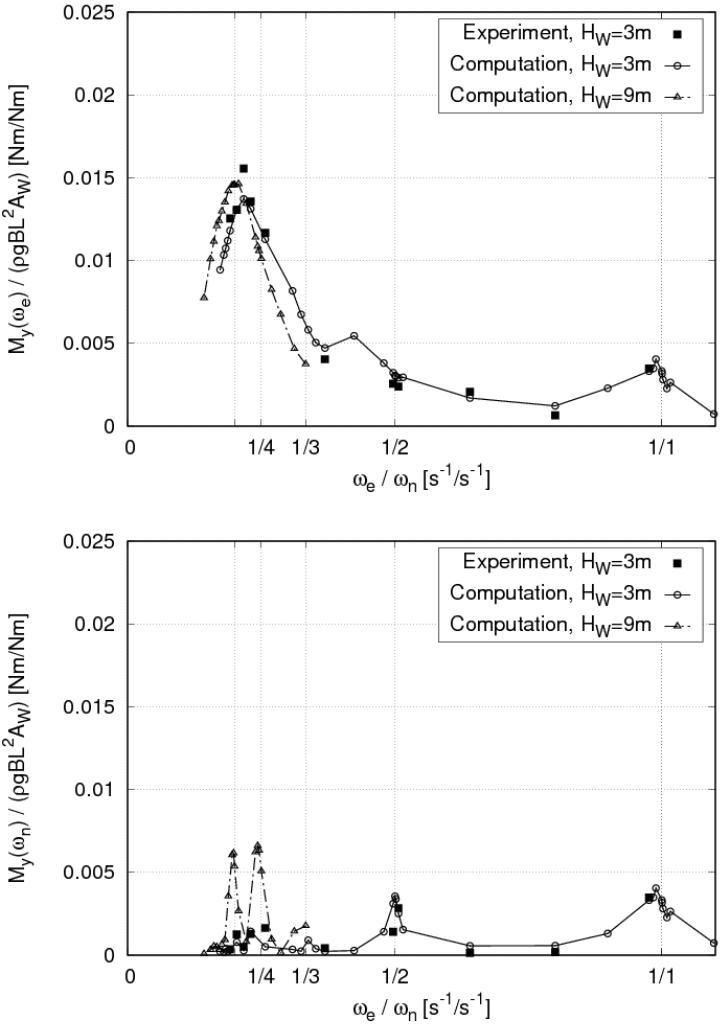

Figure 4.23: VBM at station 4 ($x/L = 0.67$) as functions of normalised wave encounter frequency; responses with frequency ω_e (top) and ω_n (bottom) for wave heights $H_W = 3.0\,m$ and $H_W = 9.0\,m$

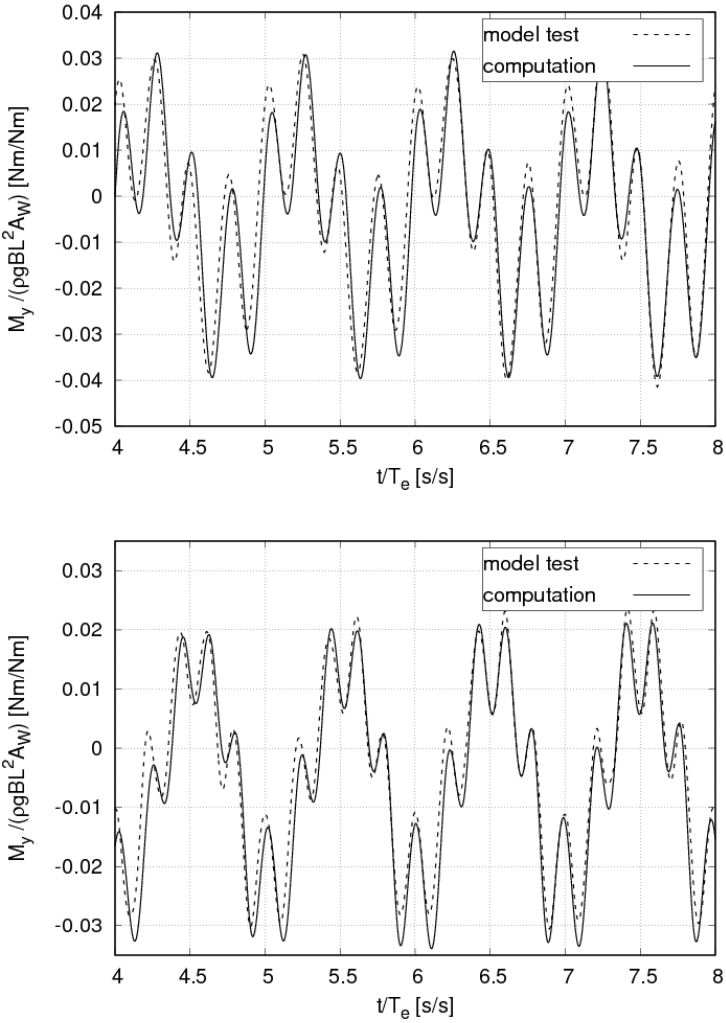

Figure 4.24: Time series of midships VBM in regular wave runs with fourth order ($\omega_e/\omega_n = 0.25$, top) and fifth order ($\omega_e/\omega_n = 0.20$, bottom) resonant excitation

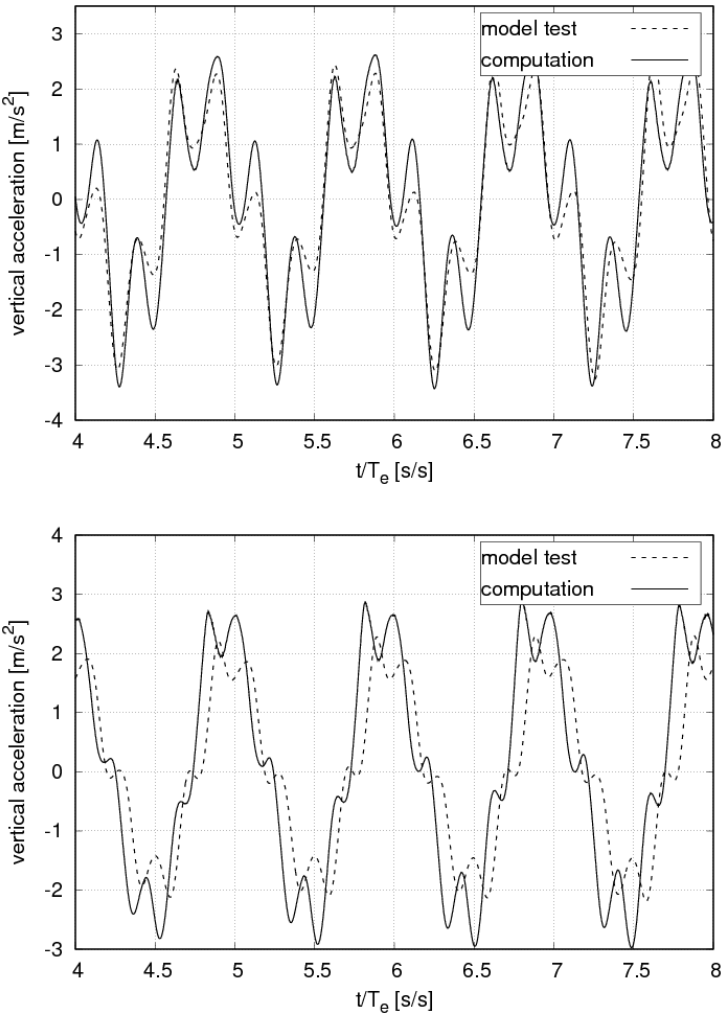

Figure 4.25: Time series of vertical accelerations at the bow in regular wave runs with fourth order ($\omega_e/\omega_n = 0.25$, top) and fifth order ($\omega_e/\omega_n = 0.20$, bottom) resonant excitation

RoPax Ferry

This section will further discuss nonlinear loads in regular waves and assess the grid dependency of the numerical solution more systematically. Bow slamming impacts are shown here for the RoPax ferry running in a regular head wave. Model test data are available for a wave length of $\lambda_W = 204.0\,m$ with wave height $H_W = 5.7\,m$, and a ship forward speed of $25\,kts$, Drummen and Holtmann (2014).

Computations were performed using *COMET* on three hexahedral dominant unstructured grids with identical topology and systematically varied reference lengths. The spatial refinement factor was $c_x = \sqrt[3]{2}$, resulting in grid sizes of approximately $500,000$, $1,000,000$ and $2,000,000$ cells. Time step refinement used the same factor, $c_t = c_x$.

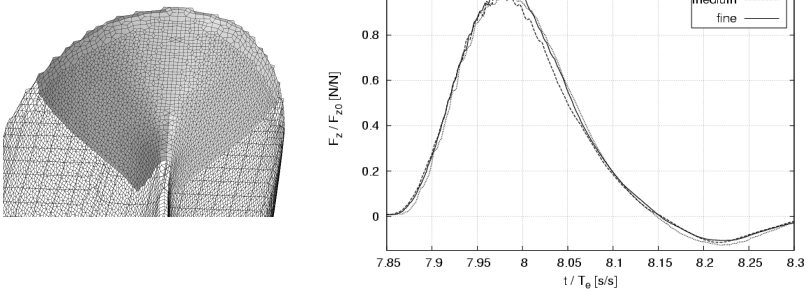

Figure 4.26: Coarse surface grid on the bow segment of the ferry (left); time series of impact force on the bow segment, computed on three refined grids

Hydrodynamic bow impacts occurred in each wave encounter. The impact forces were integrated over the bow door region, see Fig. 4.26 (left, grey shaded area) and Fig. A.1 (appendix A). The impact forces computed on the refined grids show only small differences in peak magnitude, Fig. 4.26 (right), but generally agree well in shape and amplitude. Integrating the forces over time yields the hydrodynamic impules which are here the most contributing excitation of structural vibration. The computations are in favourable agreement with the experiments, Fig. 4.27.

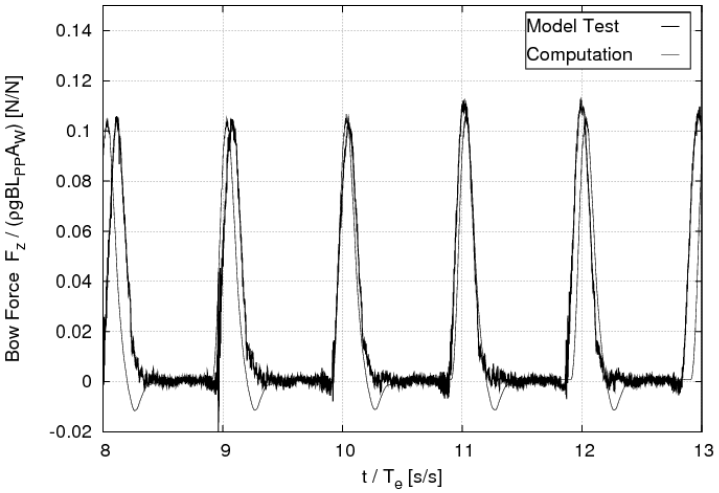

Figure 4.27: Time series of bow impact force; model test data courtesy CRS

Vertical accelerations at the bow comprise contributions from rigid-body heave and pitch accelerations, as well as vibratory accelerations. Computed accelerations match the model tests, Fig. 4.28. Measured internal loads at the foremost section cut could also be replicated numerically, Fig. 4.29. Differences are only observed for the VBM at midship section, Fig. 4.30, where the computations predict significantly smaller peaks from bow slamming impacts. However, only the pronounced peaks are underpredicted and the overall qualitative agreement is good. Given the fine agreement of bow forces, accelerations and VBM in the foreship, the deviation of the impact peaks at the midship section cut is somewhat surprising and lacks a satisfactory explanation.

Fig. 4.31 shows the hull girder deflection for various time instants (time increment $\Delta t = 0.4\,s$) during a slamming impact. The 3-node vibration mode significantly contributes to the deflection in addition to the 2-node mode.

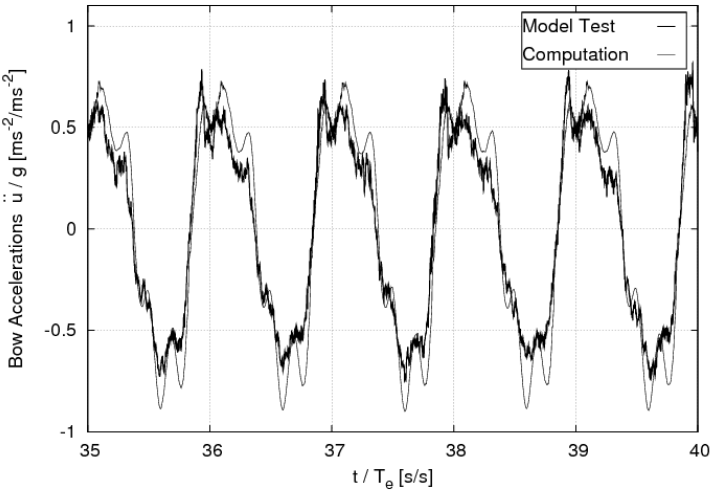

Figure 4.28: Time series of vertical acceleration at the bow; model test data courtesy CRS

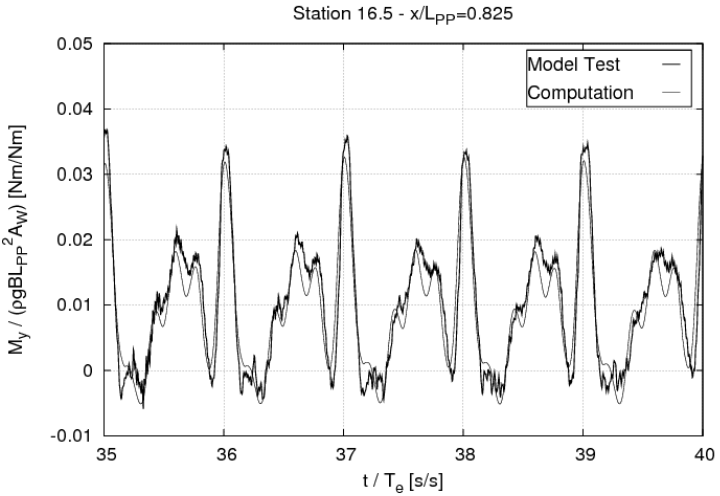

Figure 4.29: Time series of VBM at $x/L = 0.825$; model test data courtesy CRS

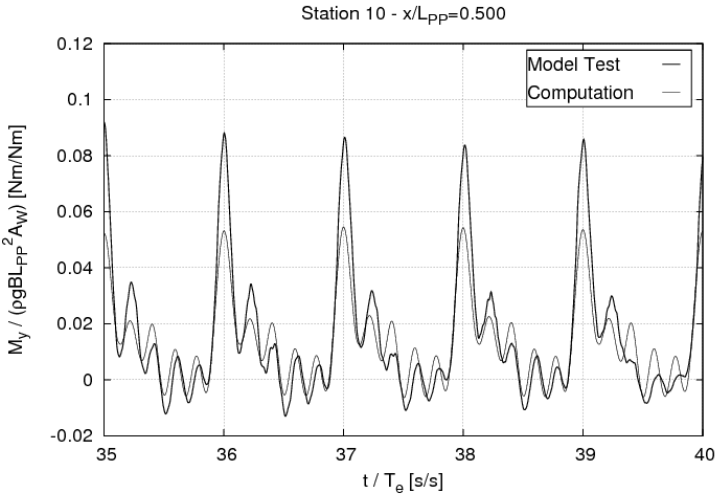

Figure 4.30: Time series of VBM at $x/L = 0.50$; model test data courtesy CRS

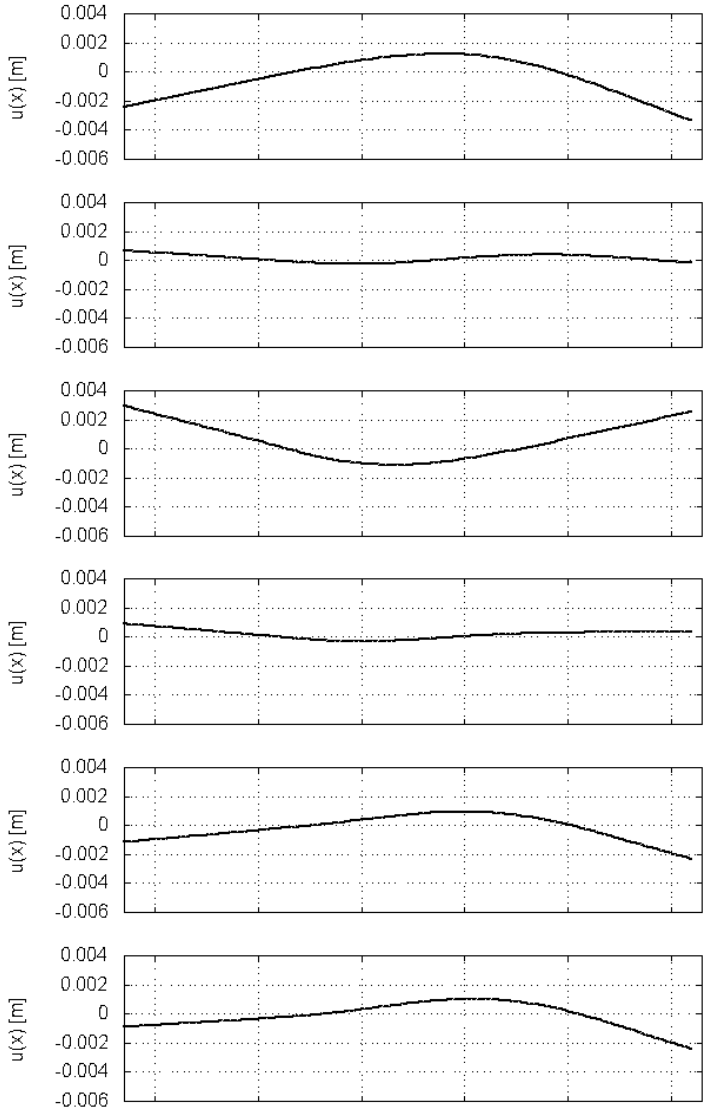

Figure 4.31: Hull girder deflection (model scale) plotted over ship length at various time instants in increments of $\Delta t = 0.4\,s$; top to bottom

4.3.2 Irregular Waves

This section covers validation of the numerical method for motions and loads in irregular waves. Comparisons with model tests focus on the cruise ship and the 10,000 TEU containership in long-crested stationary head seas. Statistical information derived from computed and measured time series are discussed. While direct comparisons of time series data are difficult to interpret, comparisons of statistical quantities are demonstrated to provide more insight since these are found valuable for estimating discretisation errors and their influence on ship response probability distributions for short- and long-term statistical load analysis.

This section will also address the grid dependency of ship reactions in irregular waves. Ley et al. (2011) and Oberhagemann et al. (2012) investigated numerical dissipation of wave energy for irregular free-surface gravity waves in the fluid solution domain; the dissipation was demonstrated to depend on spatial and temporal discretisation. On any given grid representation, numerical diffusion of wave energy is a function of wave frequency since shorter waves are subject to larger numerical diffusion due to their relatively coarse resolution. Rigid-body ship reactions to waves typically are most relevant at wave lengths in the order of the ship length. It can be expected that grid density requirements for such responses are less demanding compared to high frequency vibratory responses excited by short waves. Vibration initiated by local hydrodynamic impacts (slamming) may also impose additional requirements on the numerical grid representation in order to accurately capture the local flow.

Statistical Evaluation of Ship Response Time Series

Typically, only the maxima and minima of response processes are of relevance. This is particularly the case with loads for structural consequence analysis. Linear ship response processes are well approximated using the narrow-band assumption, see also section 3.2; for such processes, a zero level upcrossing is typically followed by each one positive and one negative peak. That is, the number of positive and negative peaks approximately equals the number of response cycles. Further on, such linear processes have a zero mean and are symmetric (no skewness). Dynamic trim and the static deflection of the hull may cause a shift of the mean level. Nonlinearities, on the other hand, may cause skewed distributions with a shift of the median level. Relevant

nonlinearities with respect to internal loads are, e. g., the hogging / sagging asymmetry due to nonlinear Froude-Krylov forces. Finally, the presence of vibration deteriorates the correlation of zero upcrossings and peaks because of the vibratory response modulation; the response process becomes broad-banded and typically has multiple local minima and maxima in between zero upcrossings. With increasing significance of vibration, the local maxima and minima even create additional upcrossings of the mean level.

Rainflow counting techniques, Matsuishi and Endo (1968), Rychlik (1987), are well suited to identify all response cycles and thus account for temporal maxima and minima of broad-banded response processes. Fatigue analyses of ship structures commonly use rainflow counting to obtain stress range distributions from measured time series of stresses. The effect of mean stresses is often disregarded, and only the cycle magnitudes (ranges) are processed for damage sum calculations based on Miner's rule, see e. g. Kahl and Menzel (2008), Mao et al. (2010). Rainflow evaluation is therefore preferred for fatigue analysis of nonlinear loads including vibration. If consistency and comparability of response distributions of flexible and rigid bodies are required, an evaluation procedure is better suited that identifies each a single maximum and minimum in between consecutive zero upcrossings. Following procedure is proposed and used in the following:

- Low-pass filter the original time series to remove the vibratory contributions. The cut-off frequency is chosen slightly lower than the two-node vertical bending natural frequency.
- Split the response process into individual cycles by identifying zero upcrossings from the low-pass filtered time series.
- Use the same time instants of zero upcrossings to split the unfiltered original time series to response cycles as well.
- Determine response peaks as the absolute maxima and minima per response cycle.
- Sort the peaks by magnitude in descending order.
- Assign each peak value R an upcrossing rate, defined as the number of peak values equal to or larger than R divided by the total evaluated time T_S: $\chi(r \geq R) = N(r \geq R)/T_S$.

This peak evaluation procedure is better suited for extreme value analyses than rainflow counting because it disregards local maxima and minima caused by

vibratory modulation; only the largest response value per cycle is of interest. Moreover, the proposed peak evaluation procedure preserves the absolute values of extremes and is able to account for peak-to-trough asymmetries. On the other hand, it does not account for additional vibratory load cycles and is therefore not suited for fatigue analyses.

Fig. 4.32 exemplifies the evaluation for a short sequence from a simulation of duration $T_S = 1500\,s$ for the 10,000 TEU containership. The ship is sailing at $20\,kts$ in long-crested head seas with $H_S = 5.0\,m$ and $T_z = 9.5\,s$. The original *COMET* time series, including vibrations of the flexible hull girder, is shown together with a corresponding low-pass filtered time series. Peaks identified from the total and the filtered signal are marked with dots, as well as the zero upcrossings found for the filtered data. It is apparent that the vibration increases the number of maxima and minima (empty dots), and that these also cause additional upcrossings of the zero level.

A reference time series based on linear rigid-body results of *GL Rankine* is added based on inverse Fourier transformation of the wave components multiplied by the linear VBM transfer function. The filtered time series deviates significantly from the linear time series. Nonetheless, both processes fairly agree in the number and time instants of peaks and zero upcrossings, and visually have more commonalities with each other than the filtered signal shares with the original time series.

Fig. 4.33 compares rates of VBM cycle ranges resulting from rainflow (range-pair) counting with upcrossing rates from evaluation of hogging and sagging peaks[5]. The distributions are similar for large values of VBM, and the results from rainflow counting resemble the mean between the sagging and hogging peak distributions except for the largest observed responses. However, significant deviations are observed towards low response magnitudes for the unfiltered data. The distributions from peak evaluation have by definition the same zero upcrossing rate as the filtered data, which corresponds well to the zero upcrossing frequencies found from the linear results. Also rainflow counting of the filtered time series yields a similar frequency for cycles ranges of vanishing magnitude, indicating the validity of the narrow-band assumption for the wave frequency load process, Fig. 4.33 (top).

On the other hand, the rainflow evaluation for the total unfiltered time series yields increased rates of small cycle ranges due to the additional cycles caused

[5]The cycle ranges are divided by two to allow comparison with the positive and negative peaks

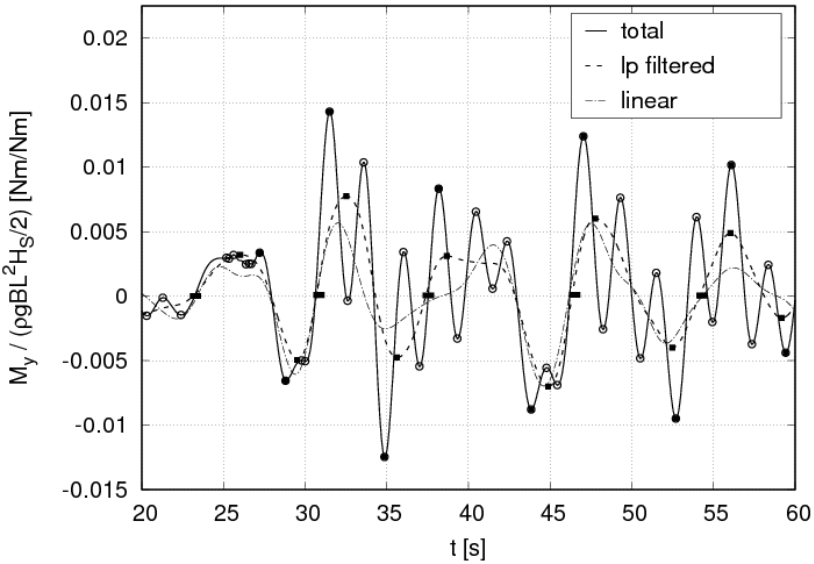

Figure 4.32: Time series of midship VBM; total (solid line) and low-pass filtered (dashed line) VBM from *COMET* computation, linear rigid-body results for reference (dotted line)

by vibratory contributions to the response process, Fig. 4.33 (bottom). These small cycles usually do not correspond to upcrossings of the zero level, but modulate the wave frequency response process and each have their individual mean value. Therefore, a direct correlation of cycle range exceedance rates from rainflow counting with the upcrossing rates from peak evaluation does not make sense for practical purposes and is done here only for illustrating the differences.

Both types of time series evaluation provide discrete distributions that consist of the sampled peaks (or cycle ranges) and their associated upcrossing frequencies. Further statistical assessment often requires a continuous representation instead, so the discrete distributions have to be approximated by analytical distribution functions. In case of peak distributions, this is done here with regression fits based on the following generic relation of upcrossing rate χ and response level

R:

$$\chi(R) = \frac{1}{T_{zr}} \exp\left(-\frac{B(R)}{H_S^2}\right). \tag{4.3.3}$$

The term $B(R)$ could in principle be established as a power series expansion of arbitrary order to fit any sampled distribution. However, only two functional expressions will be used in this thesis based on polynomials of low order. The first of these is a single power term expression,

$$B_w(R) = aR^k, \tag{4.3.4}$$

and corresponds the two-parameter Weibull distribution. Exponent k is typically of the order 1 to 2, with $k = 2$ corresponding to the Rayleigh distribution; see also Ochi (1978) for a more generalised formulation. For a linear narrow-banded response process, $a = 8\frac{m_0}{m_{0r}}$, see eq. (3.2.7). $k < 2$ is equivalent to a departure from a narrow-banded Gaussian process with Rayleigh distributed peaks; $k = 1$ corresponds to the exponential distribution, and $k \approx 1$ is observed for amplitude distributions of purely vibratory random processes.

The second variant of $B(R)$ is a second-order polynomial,

$$B_p(R) = b_1 R + b_2 R^2, \tag{4.3.5}$$

which prove to fit well to the sampled distributions. Extending the original Rayleigh formulation by introducing b_1, eq. (4.3.5) establishes a semi-empirical relation between B and R. The motivation for introducing the linear term is justified as follows. A response process including structural vibration can be considered a combination of two random processes, a basically Gaussian process in response to Gaussian wave excitation, and transient vibrations. Amplitudes of the former are well approximated by a Rayleigh distribution and the vibration amplitudes follow an exponential distribution. The peak distribution of a combination of both processes may therefore be well approximated by eq. (4.3.3) with B based on eq. (4.3.5).

This fitting of B to sampled VBM distributions is exemplified in Fig. 4.34 for the hogging and sagging VBM of the 14,000 TEU containership in long-crested irregular head waves of $H_S = 14.0\,m$ and $T_z = 11.5\,s$. The regressions are based on weighted fits with weights corresponding to the square root of the upcrossing rate, thus assigning largest weights on the data corresponding to large

upcrossing rates and corresponding higher statistical confidence. The second-order polynomial formulation of B apparently fits the data better. Although none of the formulations fully captures the trend of the tail distributions, the polynomial formulation resembles the slope of the sampled distribution of upcrossing rates over a larger range, compared to the Weibull formulation. Similar observations are made also for other distributions of hogging and sagging VBM peaks including wave-induced vibration. The second-order polynomial formulation B_p, eq. (4.3.5), is given preference over the single power term formulation B_w according to eq. (4.3.4) because it results in improved fits to the available data.

Rigid Hull Girder

Validation of the numerical method using the coupled solver in irregular waves is first demonstrated for a rigid ship. Experimental data were available for the segmented model of the cruise ship equipped with a backbone, see appendix A. The backbone was designed very stiff to assure the model could be considered rigid. Results will lend on an evaluation of simulation results presented in Ley (2012). Experimental data were available for a time interval covering $1,700\,s$ (full scale). The inlet boundary in the computations was positioned in a way that the experimental wave probe data ahead of the model could be used to define the wave elevation. Wave orbital velocities were imposed according to the wave elevation and superposition of linear Airy wave components. Fig. 4.35 (top) shows time series of midship VBM for the ship at speed $6.0\,kts$ in severe irregular long-crested head waves with sea state parameters $H_S = 16.5\,m$ and $T_z = 11.5\,s$. The wave spectral energy distribution followed the JONSWAP spectrum with peak enhancement factor $\gamma = 3.3$. Although the computation used a relatively coarse grid with $350,000$ cells, visually good agreement is achieved with the experiment. A comparison of cycle range exceedance rates from rainflow counting, Fig. 4.35 (bottom), confirms the fine agreement between computation and experiment.

Hogging and sagging peak upcrossing rates from computation and experiment, Fig. 4.36 (top), reveal a significant asymmetry with hogging peaks (negative sign) being smaller than sagging peaks (positive sign) of same upcrossing rate. Furthermore, the slope of the sagging peak distribution is less curved. Computational results are in good agreement with the experiment except for the largest hogging peaks where the computed peaks underpredict those from

experiments.

The data are used to further assess the agreement by directly correlating response peaks evaluated from the numerical and experimental data, Fig. 4.36 (bottom). The plot shows the relative deviation $\left(M_{y_{Num}} - M_{y_{Exp}}\right) / M_{y_{Exp}}$ of computed VBM peaks from their corresponding experimental counterparts as a function of the experimental peak value. Corresponding peaks were identified by coincidence of response zero upcrossings within a small tolerance time. Therefore, not all peaks were used for this analysis. The direct correlation of individual response magnitudes indicates a significant scatter between numerically determined response peaks and corresponding experimental results. As a trend, the scatter of the relative deviation decreases with increasing response magnitude. Therefore, the scatter can be considered a random variation between computational and experimental results. For large hogging amplitudes, however, there is a bias with computed hogging peaks being smaller in magnitude than the experimental values. This finding is in line with the above observations from the comparison of peak upcrossing rates. Considering the limited number of sampled events, the disagreement at low upcrossing rates may be attributed to random variation.

Generally, good agreement with experiments was demonstrated for rigid-body loads in a severe sea state computed with the numerical method on a relatively coarse fluid grid representation. Oberhagemann et al. (2012) presented similar comparisons, combined with studies into grid requirements for free surface wave propagation with a finite volume method. Ley (2012) documented and discussed further variations of sea state conditions for this ship. These comparisons also showed good agreement with model experiments.

Flexible Hull Girder

Validation of the numerical method for short-term response statistics of a flexible hull girder is given here for the 10,000 TEU containership. The experimental data was generated as part of the WILS JIP series, Hong (2010), Hong (2013). The segmented model was studied in the wave basin at KRISO and represents a typical modern post-panamax containership, see appendix A.

Computations used Fourier transformations of the wave surface elevation measured ahead of the ship in the experiments to define the waves at the inlet to the fluid domain. Wave elevation and wave orbital velocities were computed based on a superposition of the wave components according to eq. (3.1.11).

Computations for different sea state conditions are compared with model test data, Table 4.4. Time series of both experiments and computations are composed of short sequences of a few minutes duration which were combined to a longer time series. The wave component phases were shifted according to the dispersion relation, resulting in a virtual continuous wave process realisation. Each two consecutive runs had an overlapping interval which allowed removing the initial phase of each computation. This composition technique made computations more efficient because several runs could be performed in parallel on a computer cluster. Experiments had to use the same technique because the wave basin size limited the maximum length of test runs. Further, the time intervals used in computations and experiments were the same for consistency. The finite volume

Table 4.4: Sea states tested with 10,000 TEU segmented model

Model Test ID	H_S	T_z	μ	v	T_S
403	$5.0\,m$	$9.0\,s$	180°	$20.0\,kts$	$0.3\,hrs$
501	$9.0\,m$	$9.5\,s$	180°	$10.0\,kts$	$3.0\,hrs$

grid for the test condition **403** computations consisted of 1,400,000 cells with refinements around the free surface and the hull. Cell stretching towards the aft and the side boundaries dampened out the incident and radiated waves. Figs. 4.37 through 4.40 exemplarily show time series of midship VBM of the 10,000 TEU containership. Model test and computation agree well, particularly for the low-frequency wave responses. The vibratory part differs more. However, peak upcrossing rate distributions show differences for both the unfiltered and the low-pass filtered VBM, Fig. 4.41. Comparisons with linear BEM seakeeping results and peak upcrossing rates according to eq. (3.2.7) reveal the significance of nonlinear effects on the rigid-body VBM, most obvious being the asymmetry between hogging and sagging peak upcrossing rates.

Similar observations are made for the more severe sea state with test ID **501**, Fig. 4.42. Despite a fine agreement of the cycle exceedance rates and peak upcrossing rates of the total unfiltered VBM, differences are observed in the low-pass filtered ship reactions. This affects both the peak upcrossing rates and the cycle exceedance rates. Still, the overall agreement is fair and the computation replicates the hogging / sagging asymmetry as well as the significant amplification due to vibration.

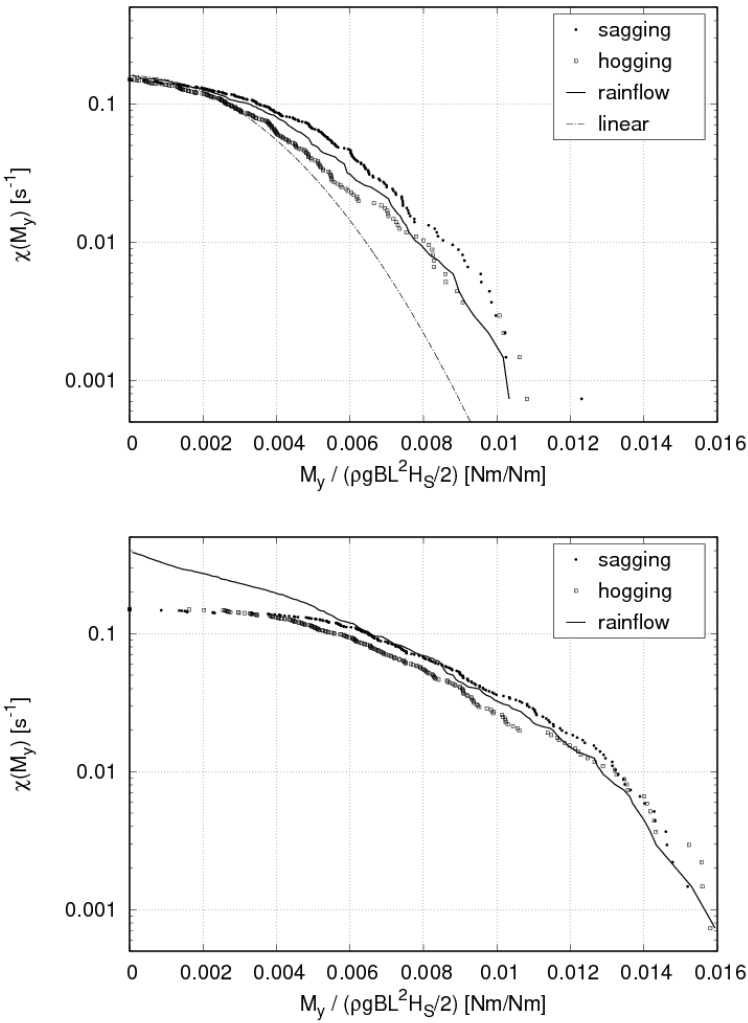

Figure 4.33: Examples of short-term VBM upcrossing rates from rainflow counting (solid line, half-ranges) and evaluations of hogging and sagging peak magnitudes (dots), based on low-pass filtered (top) and total (bottom) time series; linear Rayleigh distribution for reference

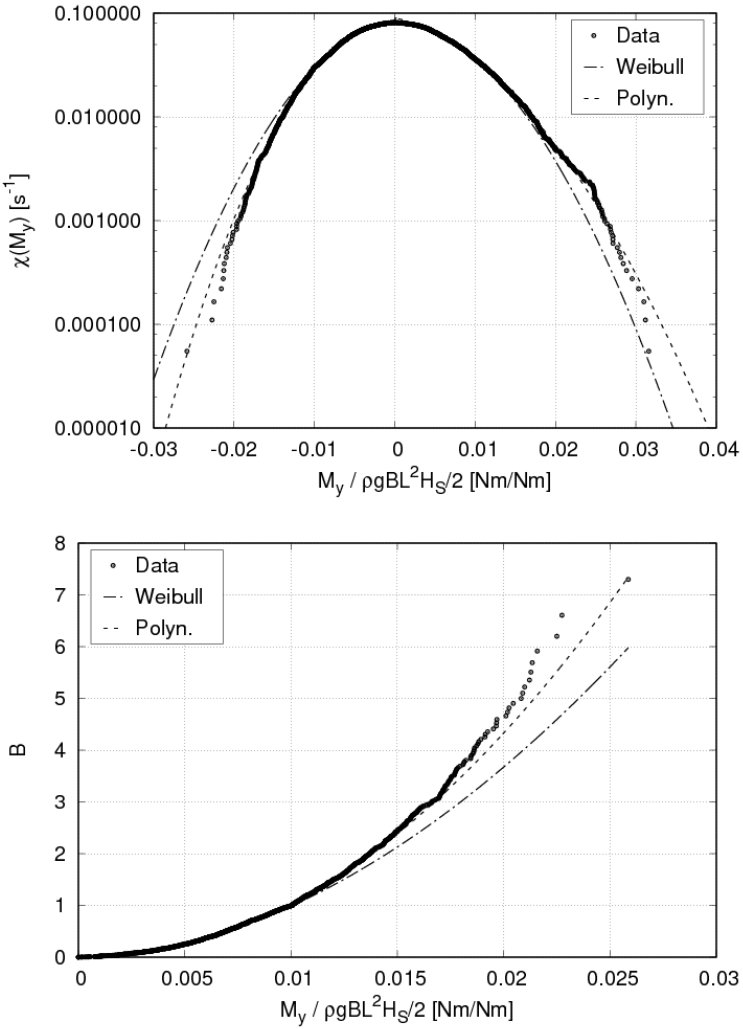

Figure 4.34: VBM peak upcrossing rates for the 14,000 TEU (top); corresponding B as a function of nondimensional hogging VBM peaks (bottom); regressions based on expressions eqs. (4.3.4) and (4.3.5) to fit the data from simulation (symbols)

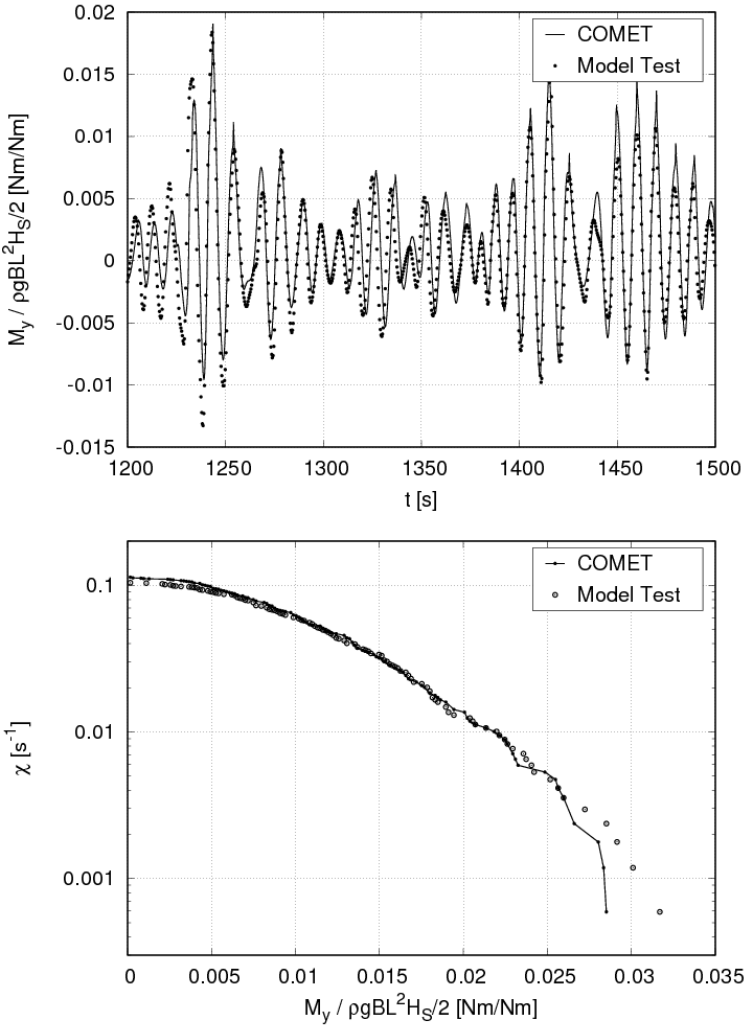

Figure 4.35: Time series of VBM for the cruise ship in irregular head waves with $H_S = 16.5\,m$ and $T_z = 11.5\,s$ (top); cycle range exceedance rates from rainflow counting (bottom)

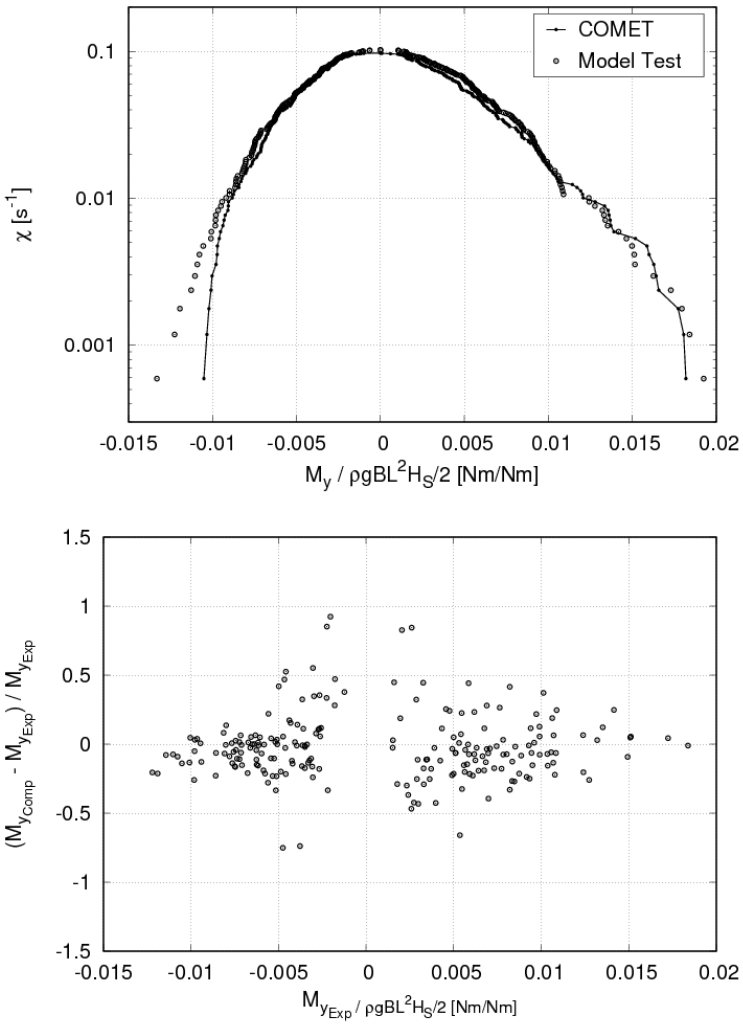

Figure 4.36: VBM peak upcrossing rates for cruise ship in irregular head waves with $H_S = 16.5\,m$ and $T_z = 11.5\,s$ (top); relative deviation of computed VBM peaks from corresponding experimental VBM peaks (bottom)

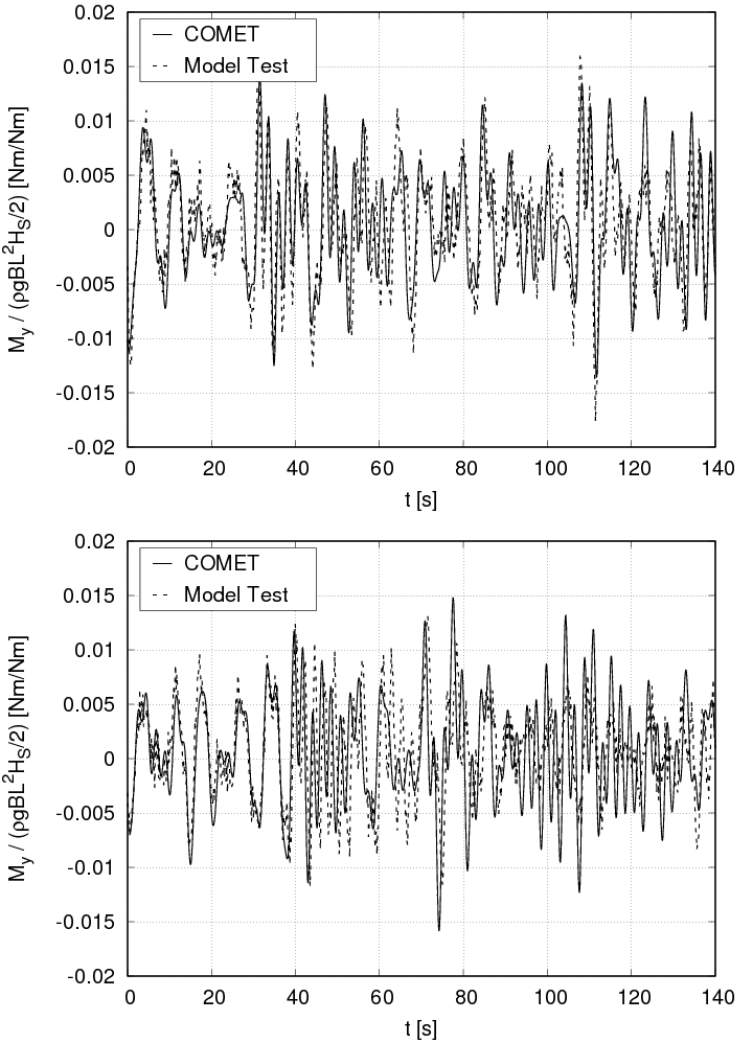

Figure 4.37: Time series of midship VBM of the 10,000 TEU containership in sea state with $H_S = 5.0\,m$ and $T_z = 9.5\,s$; computation (solid lines) and model test (dashed lines)

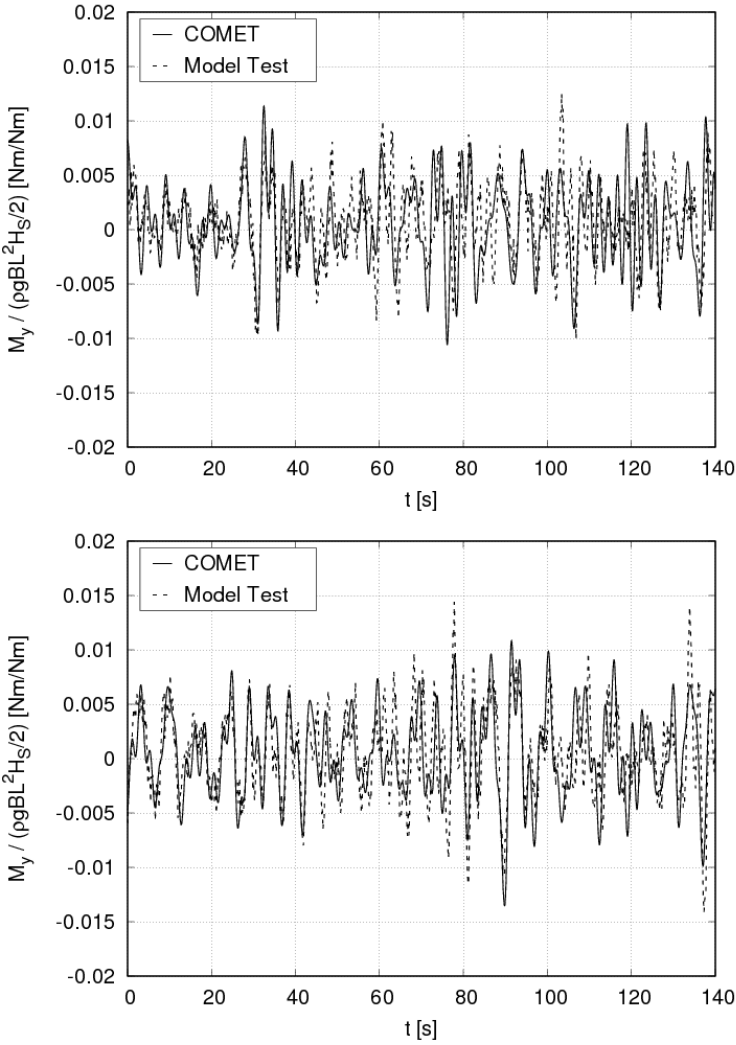

Figure 4.38: Time series of midship VBM of the 10,000 TEU containership in sea state with $H_S = 5.0\,m$ and $T_z = 9.5\,s$; computation (solid lines) and model test (dashed lines)

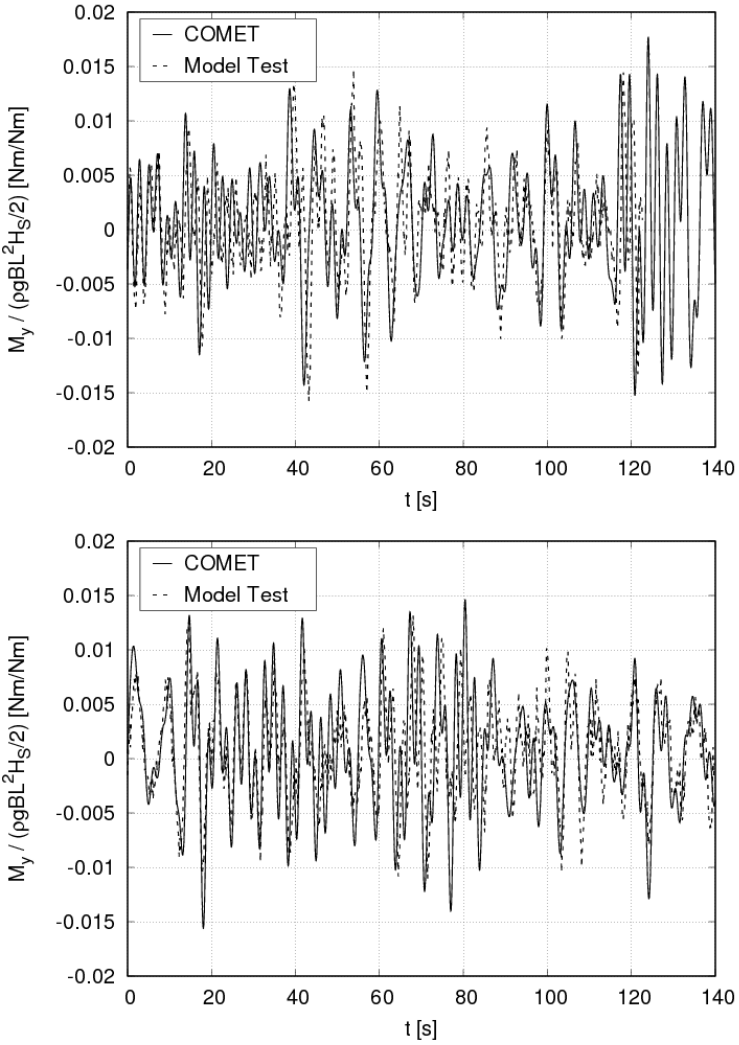

Figure 4.39: Time series of midship VBM of the 10,000 TEU containership in sea state with $H_S = 5.0\,m$ and $T_z = 9.5\,s$; computation (solid lines) and model test (dashed lines)

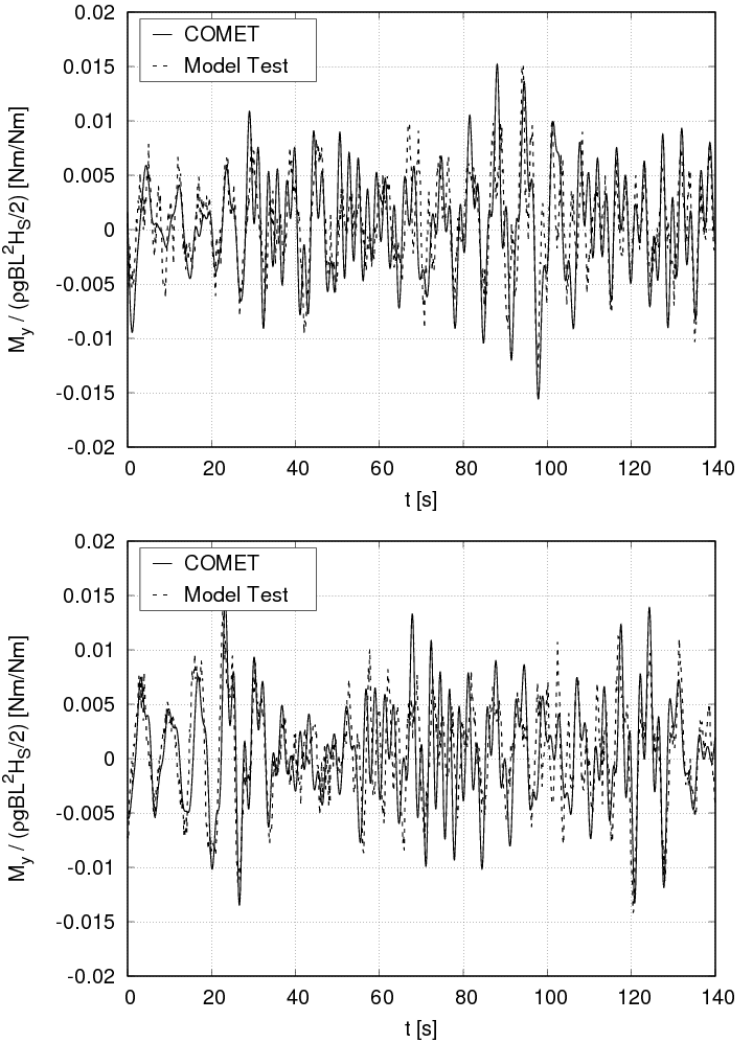

Figure 4.40: Time series of midship VBM of the 10,000 TEU containership in sea state with $H_S = 5.0\,m$ and $T_z = 9.5\,s$; computation (solid lines) and model test (dashed lines)

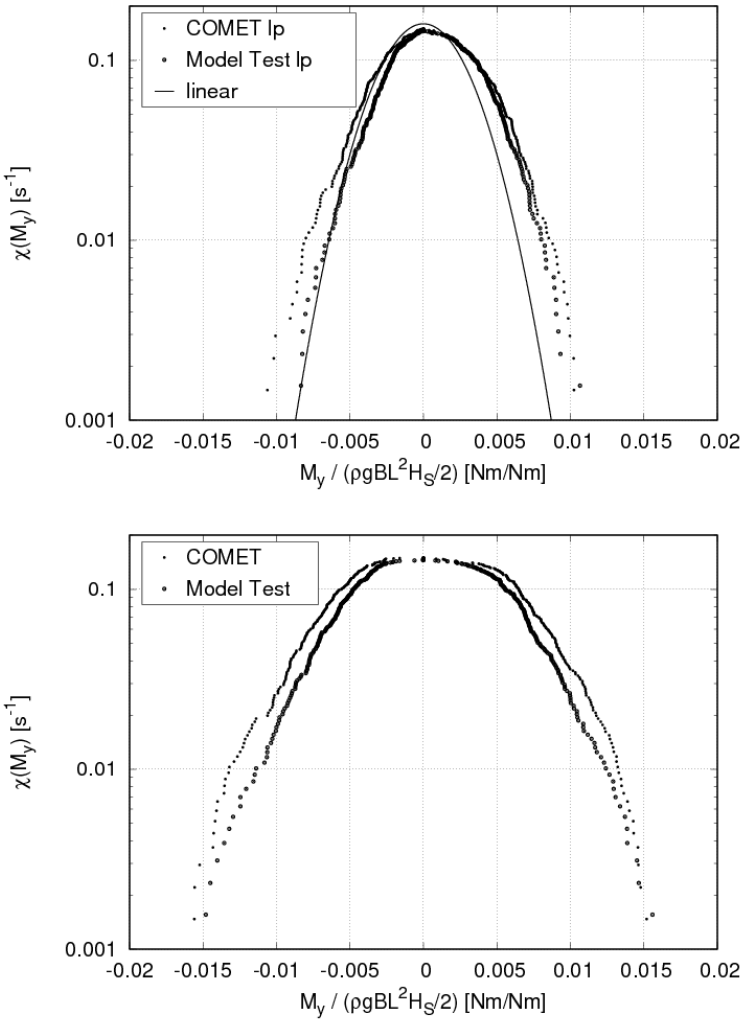

Figure 4.41: VBM upcrossing rates from low-pass filtered (top) and unfiltered (bottom) time series of the 10,000 TEU containership in sea state with $H_S = 5.0\,m$ and $T_z = 9.5\,s$

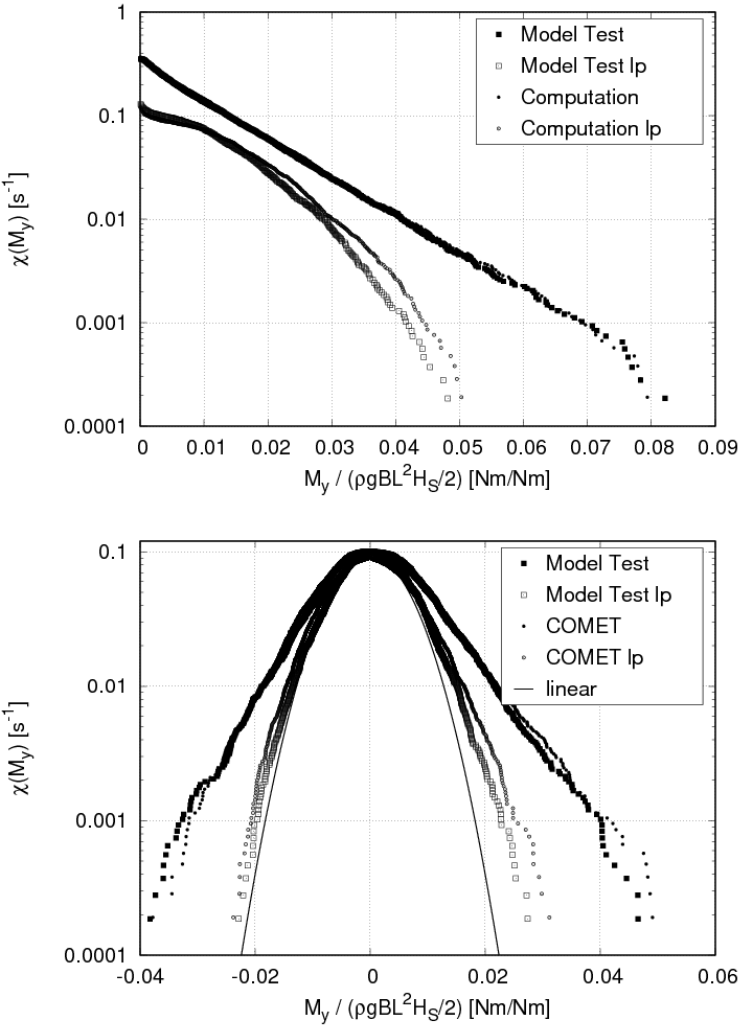

Figure 4.42: VBM cycle range exceedance rates (top) and VBM upcrossing rates (bottom) of the 10,000 TEU containership in sea state with $H_S = 9.0\,m$ and $T_z = 9.5\,s$

Grid Sensitivity Studies

Insufficient grid resolution negatively affects the numerical prediction of ship vibration responses in several aspects. Structural vibrations are subject to overpredicted damping through large time steps and the numerical damping of radiated waves on coarse grids. Such radiated waves are comparatively high in frequency and small in amplitude. Fine discretisation is also of importance to capture local hydrodynamic excitation. Pressure impulses (slamming) as a main source of transient vibrations are very sensitive to the local flow and require high resolution in space and time. Coarse grids and large time steps cause a broadening of the hydrodynamic impact in space and time while decreasing the peak, i. e. local pressure pulses are diffused in space and time and less pronounced, Oberhagemann et al. (2012), el Moctar et al. (2011). Finally, insufficient resolution causes an increased loss of wave energy, particularly of high frequency components of the wave spectrum which then diffuse on their way from the inlet boundaries to the ship, see discussions in Ley et al. (2011) and Oberhagemann et al. (2012). These short waves are a potential source of vibration due to resonance of wave encounter frequency with the hull girder natural frequency.

On the other hand, comparisons in section 4.3.1 demonstrated that the more global responses, such as motions or the internal forces and moments in rigid ships, can be calculated with sufficient accuracy even on coarse grid representations of the fluid domain, of the order $300,000$ control volumes. This is because the low frequency wave components dominate the reponse process and these are, for a given grid, less affected by discretisation errors than the higher frequency components due to their smaller spatial and temporal gradients.

To exemplify the influence of grid resolution, computations of midship VBM of the $10,000$ TEU containership in waves with $H_S = 9.0\,m$, $T_p = 14.3\,s$ and $\gamma = 3.3$ are discussed. Computations covered a time interval of $250\,s$ and were performed on three refined grids with $c_x = c_t = \sqrt[3]{2}$, resulting in finite volume grids with $300,000$, $580,000$ and $1,060,000$ cells, respectively. A time record from model tests was available for comparisons, see Fig. 4.43 (top).

The grid density of the coarsest grid was characterized by 10 cells per significant wave height, 100 cells per peak wave length and 800 time steps per peak period. Ley et al. (2011) reported significant wave energy loss on grids of corresponding density in simulations on large fluid domains. Despite, the time series of VBM are in overall good agreement with experiments on all grids.

A correlation was now established between computed and measured peaks in a way that minima and maxima between two consecutive zero up-crossings were paired when the corresponding zero up-crossings in experiments and computation coincided within a tolerance of $\pm 1\,s$, see Fig. 4.43 (top, matched peaks marked with dots). The initial $50\,s$ were not evaluated to avoid effects of the initial transients on the results. The response peaks generally correlate fairly well on all grids, Fig. 4.43 (bottom), despite significant scatter of individual points. Trend lines from linear regression confirm the good agreement; moreover, the lines indicate a trend of improved matching with increasing grid resolution.

Fig. 4.44 shows, for the same grids, computed upcrossing rates in irregular head seas with $T_z = 11.5\,s$ and $H_S = 14.5\,m$. Simulations covered a longer interval of $T_S = 2700\,s$ in this case. The influence of the grid density on the upcrossing rates of low-pass filtered (rigid-body) response peaks, Fig. 4.44 (top), is small and only becomes relevant for the larger response levels. The upcrossing rates of response peaks including wave-induced vibration, Fig. 4.44 (bottom), instead, reveal significant differences between the grid representations also for the smaller response levels. The upcrossing rates for given response levels increase with grid and time step refinement, particularly for large values. Still, the general characteristics of the response processes and the upcrossing rate distributions are the same for all grid representations.

Similar observations are made with simulations using a smaller significant wave height, $H_S = 8.5\,m$, and a shorter time interval $T_S = 1800\,s$, Fig. 4.45. Upcrossing rates of low-pass filtered nondimensional VBM again do not indicate a significant grid dependency. The differences between filtered and unfiltered upcrossing reates are less pronounced for the lower wave height, and also the differences between the results on refined grids are smaller, compared with the larger wave height. Hence, the influence of grid resolution is most relevant for the vibratory contributions to the response, and it increases with the magnitude of the response.

Section 4.1 introduced an approach to finding grid-independent scalar solution values from transient computations. This approach has been successfully applied to the hydrodynamic damping coefficient from vibration decay simulations in section 4.2. The following will extend this approach to allow extrapolation of upcrossing rate distributions towards grid-independent solutions. This is done by establishing the grid-dependent upcrossing rate as a function of the magnitude of the solution value on the reference grid.

The observations so far indicate that low resolution may suffice to detect the

occurrence of vibratory excitation such as slamming events, although accurate resolution of vibratory responses requires finer resolution in space and time. Global effects of hydrodynamic impulses are captured qualitatively even on coarse grids, but are associated with an inaccuracy which depends on grid resolution. In the examples presented here, coarse resolution tended to give underpredicted response peaks and, as a consequence, too low response upcrossing rates for given response magnitudes. It follows that the number of upcrossings, N, of a response level R is grid dependent, and that the ratio of N_i (computed on a grid of refinement level i) to N_1 (computed on the initial coarsest grid) can be expressed as a function of the refinement ratio Υ_i and will be denoted Ξ in the following,

$$\frac{N_i(R)}{N_1(R)} = \Xi(R, \Upsilon_i). \tag{4.3.6}$$

The following cubic function was found to give reasonable approximations to the existing data and prove to be robust:

$$\Xi(R, \Upsilon_i) = 1 + a_1(\Upsilon_i)R^3. \tag{4.3.7}$$

a_1 is first defined for each refined grid individually. That means, individual $a_{1,i} = a_1(\Upsilon_i)$ are fit to the $\Xi(R)$ found for each grid representation according to eq. (4.3.7). Next, a_1 is established as a function of grid refinement ratio,

$$a_1(\Upsilon) = a_1(\Upsilon_\infty) + \mathfrak{a}(\Upsilon). \tag{4.3.8}$$

In what follows, $a_1(\Upsilon_\infty) = a_\infty$ will be substituted. Regression over all available $a_{1,i}$ in analogy to eq. (4.1.10),

$$S_1(a_\infty, \mathfrak{a}) = \sqrt{\sum_{i=1}^{n_g} \left(a_{1,i} - (a_\infty + \mathfrak{a}\Upsilon)\right)^2} \tag{4.3.9}$$

yields the value of a_1 for zero grid spacing. The scaling function for the extrapolated grid-independent solution finally reads

$$\Xi(R, \Upsilon_\infty) = 1 + a_\infty R^3. \tag{4.3.10}$$

Figure 4.46 illustrates examples of fitting eq. (4.3.7) to VBM upcrossing rates of the 10,000 TEU containership, calculated on three different grids. Simulations

comprised 2700 s simulation time on each grid using the same wave process realisations. Although there is scatter, particularly for large R, the fit agrees fairly well with the data. In order to compare grid-dependency studies at different significant wave heights, VBM responses were non-dimensionalised with respect to $\rho g B L^2 H_S$, where ρ is water density, g gravity acceleration, B ship breadth and L the ship length. Fig. 4.47 shows the corresponding fitted functions for a_1. Apparently, the grid refinement ratios used in this study implied the need to extrapolate over a large range. Besides introducing a corresponding large uncertainty in the extrapolated grid independent solution, further uncertainty relates to the choice of appropriate functional relations for $\Xi(R, \Upsilon_i)$ and the regression model eq. (4.3.8) which here assumed a first-order grid convergence.

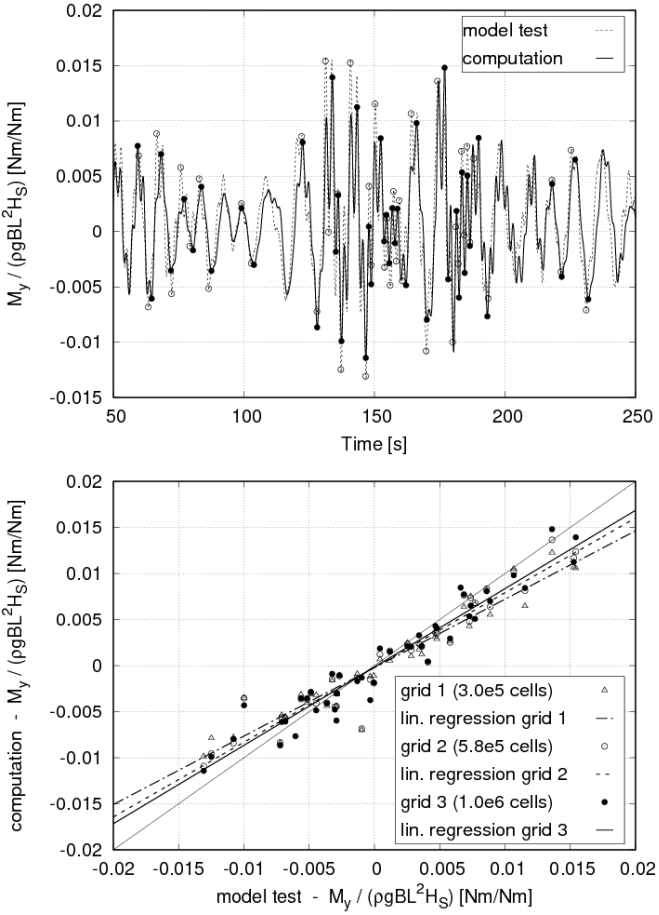

Figure 4.43: Time series of VBM (top), correlation of computed peaks on three refined grids with model tests (bottom)

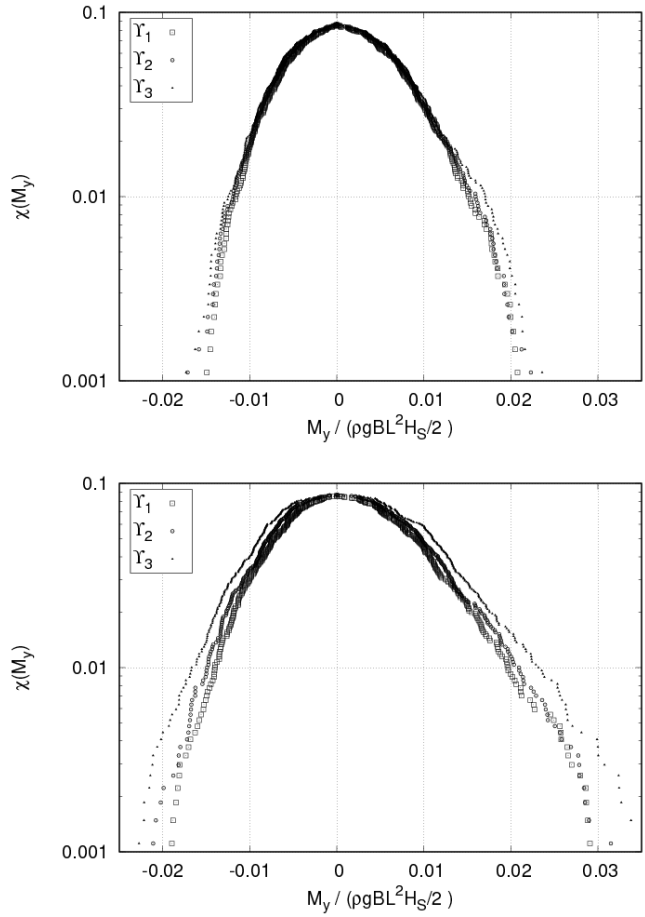

Figure 4.44: Upcrossing rates of VBM of 10,000 TEU containership in sea state with $T_z = 11.5\,s$ and $H_S = 14.5\,m$ computed on refined grids; low-pass filtered (top) and total time series (bottom)

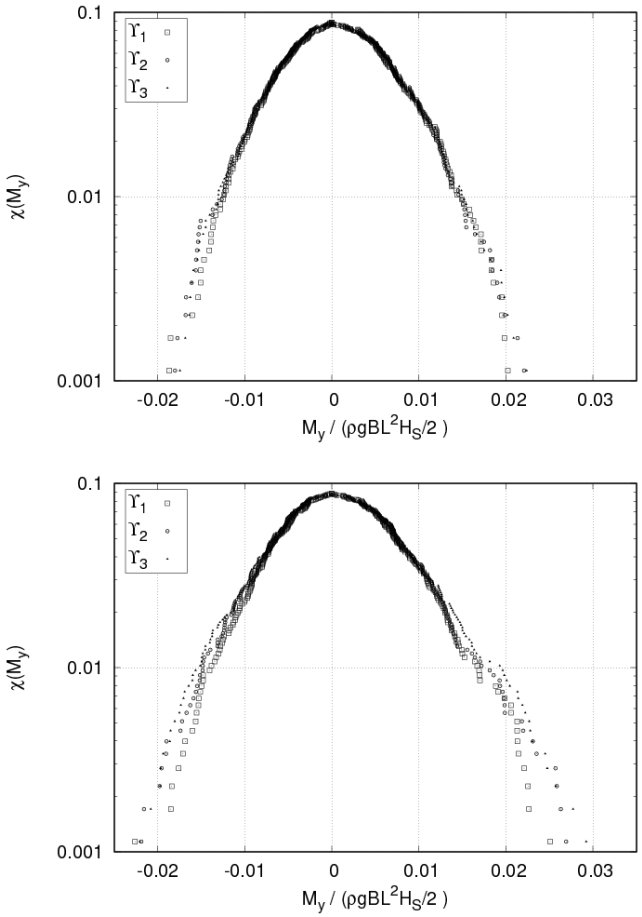

Figure 4.45: Upcrossing rates of low-pass filtered (top) and total (bottom) VBM of 10,000 TEU containership in sea state with $T_z = 11.5\,s$ and $H_S = 8.5\,m$ computed on refined grids

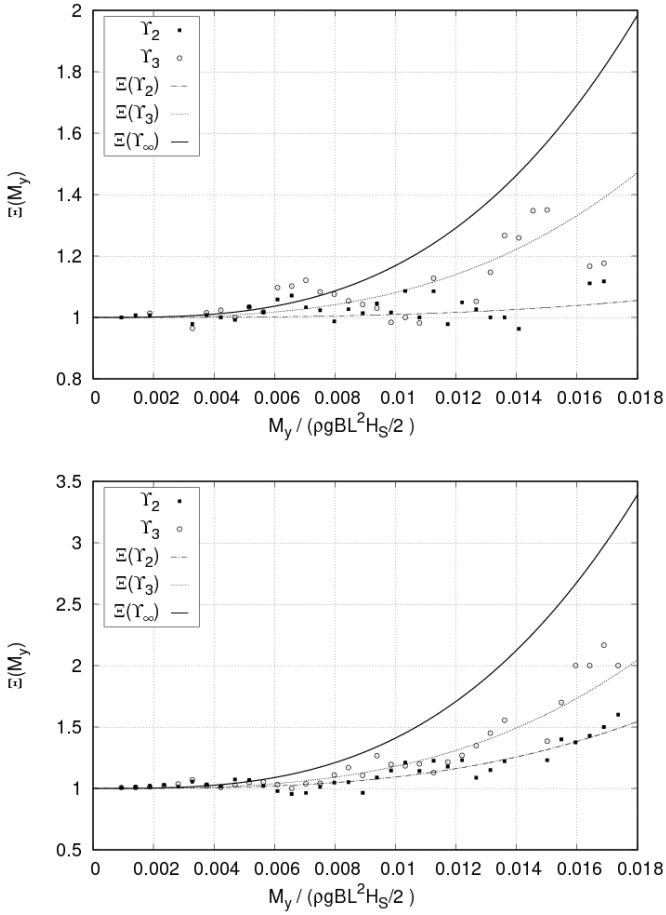

Figure 4.46: Increase in number of upcrossing events of peaks on refined grids, N_i/N_1, as a function of response level in hogging (top) and sagging (bottom); 10,000 TEU containership, $H_S = 8.5\,m$, $T_z = 11.5\,s$, $v = 10\,kts$, $\mu = 180^\circ$

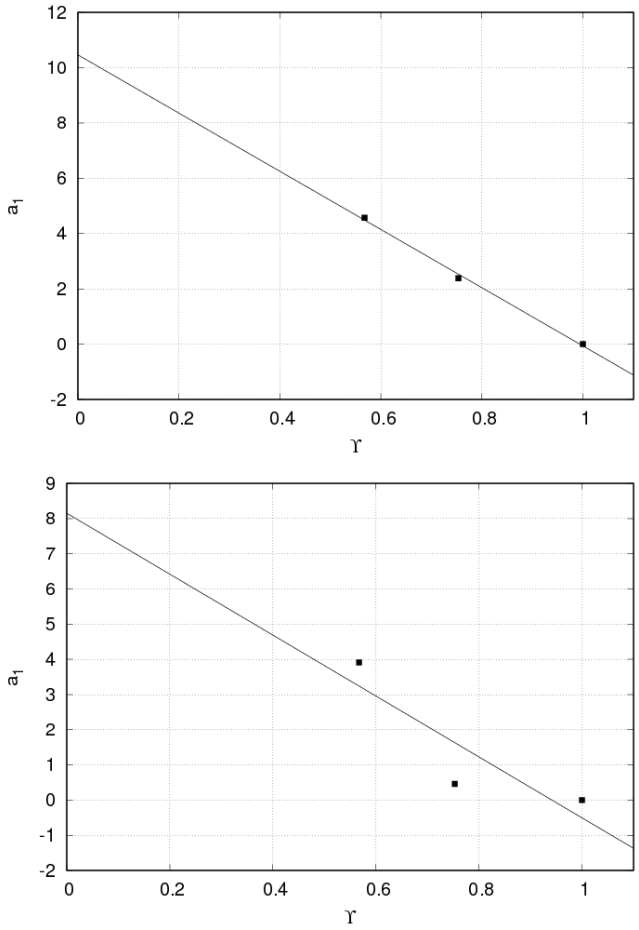

Figure 4.47: Definition of a_1 from regression over Υ; hogging (top) and sagging (bottom); 10,000 TEU containership, $H_S = 8.5\,m$, $T_z = 11.5\,s$, $v = 10\,kts$, $\mu = 180^\circ$

5 Method Application

It has been discussed in the previous chapters that the associated large computational resource requirements impose significant constraints on the use of the numerical method in practical applications. Direct long-term simulations will not become feasible within the foreseeable future. Instead, appropriate statistical procedures are needed to reduce the the required overall simulation time by several orders of magnitude.

Chapter 3 and in particular section 3.3 discussed available concepts to reduce the required simulation time based on the use of simpler and faster predictor methods for selecting sets of simulation scenarios. These scenarios may range from short wave sequences to sets of environmental parameters for truncated long-term statistical analysis.

The use of short wave sequences, such as harmonic design waves or conditioned wave sequences, is appealing because of the potentially large reductions in simulation time. The predictor method is used to establish such a sequence, and, at the same time, assigns this sequence response magnitude and a short- or long-term probability of exceeding this response. A simulation with the nonlinear corrector method in this sequence will then simply provide a nonlinear correction to the response of the predictor method, but will not provide additional information on the probability of this corrected response. In other words, such wave sequences are response-corrective.

Due to their simplicity, regular harmonic waves have been predominantly used as wave scenarios for CFD, and numerous applications have correspondingly been reported in the literature, see for example el Moctar et al. (2005), Oberhagemann et al. (2008), Paik et al. (2009), Kim (2010), Robert et al. (2015). The concept of response-conditioned wave sequences has attracted attention in recent years with Seng and Jensen (2012) and Oberhagemann et al. (2012) who used coupled CFD-CSD methods in conditioned wave sequences for improving short-term distributions of VBM from potential theory methods in a response-corrective manner. Oberhagemann et al. (2012) also tested to use wave sequences based on the CRRW formulation in a probability-corrective way. Instead of deriving the nonlinear cumulative probability distribution of nonlinear VBM according

to eq. (3.3.7), however, they used a simplified approach based on averaging over all CRRW response corrections for each linearly predicted response probability level. Observed deviations from a short-term cumulative distribution of VBM response obtained from direct simulations in random irregular waves may be explained with this simplification.

Oberhagemann et al. (2012) also computed short-term cumulative distributions of VBM for several sea states with largest linearly predicted *coefficient of contribution* C_C. They did not report significant differences between the linear and nonlinear C_C. The resulting nonlinear extreme value turned out to be relatively robust with respect to the evaluated simulation duration, and also using an even smaller subset of sea states had only small influence on the resulting long-term extreme value. Fig. 5.1 shows the extrapolated non-dimensional long-term extreme values from subsets of the total available simulation data. They are plotted over the simulation duration associated with this subset, divided by the expected sojourn time of the ships in these sea state ensembles. Although this study was limited to relatively small sets of sea state conditions, the associated computational effort was orders of magnitude too large for routine applications in structural design assessments. Furthermore, the investigated sea states were associated with high probabilities of exceeding the linear long-term extreme value and at the same time very short expected durations according to the underlying wave scatter diagrams. Expanding the range of investigated sea states towards lower wave heights would further increase the required computation times by orders of magnitude.

Oberhagemann et al. (2015) circumvented the need to compute short-term upcrossing rate distributions of VBM from simulations in random waves by using conditioned wave sequences for selected short-term upcrossing rates. They documented a comprehensive application of conditioned wave sequences in a long-term statistical analysis of wave loads including wave-induced vibration, based on the *coefficient of contribution* approach. Simulations were performed in several wave sequences for each sea state of the scatter table, resulting in response-corrected short-term distributions. These short-term distributions, in turn, were summed to obtain an approximate long-term cumulative distribution of fully nonlinear ship responses, this second analysis step being of probability-corrective type. The authors observed a shift of each sea state's relevance with respect to the long-term extreme value when compared to the linear prediction. This was in line with the original study of Baarholm and Moan (2000) who observed a similar trend. Oberhagemann et al. (2015) defined individual speeds

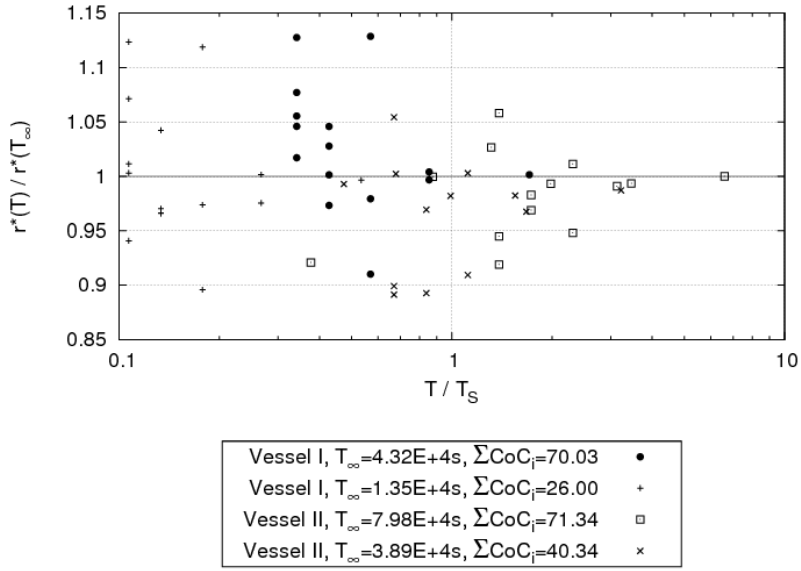

Figure 5.1: Extrapolated non-dimensional long-term extreme value as a function of simulation time divided by the total expected sojourn time in the investigated sea states; vessel I is the 10,000 TEU and vessel II the 14,000 TEU containership; T_∞ is the total available simulation time and $\sum CoC$ denotes the sum of the sea state set's contributions to the linear long-term extreme value in percent; source: Oberhagemann et al. (2012)

for each sea state based on the maximum achievable ship forward speed in waves, resulting in significant wave-induced vibration in less severe and more moderate sea states with associated higher ship speeds. The contributions of these sea states to the long-term extreme value distribution significantly increased and, as a consequence, the most contributing sea states turned out to be different from those as resulting from linear analysis. Due to the approximate definition of the short-term upcrossing rate distributions from conditioned wave sequences, the nonlinear distribution of C_C was related to uncertainty to an unknown extent. However, it can be assumed that the observed changes of C_C from linear to nonlinear correspond to what would have been obtained from direct simulations,

at least qualitatively.

The latter findings fundamentally question the feasibility of single design sea state approaches as these fully rely on a correct identification of the most relevant sea state condition from linear theory. They further contradict the conclusions from Oberhagemann et al. (2012) who did not observe significant changes of individual sea state's relevance with respect to the long-term extreme value. Their study, however, was based on a constant ship speed and restricted to a limited set of sea states which were chosen based on the linear analysis results.

When combined, the lessons learned from the two studies above result in a dilemma. Apparantly, large uncertainty has to be accepted either because short-term upcrossing rate distributions are only computed in an approximate way (but the analysis covers all short-term conditions), or the nonlinear analysis needs to be restricted to a very limited number of short-term conditions.

It appears, on the one hand, not feasible to restrict the set of sea state conditions to be investigated a-priori to a small subset, although a number of sea states can be excluded with relatively high confidence. Still, computations are necessary for a large number of short-term sea state conditions, and most of these are associated with very long expected durations. That means, short-term upcrossing rates are required corresponding to return periods of several hundred or thousands of hours which are practically impossible to obtain directly from simulations using the coupled numerical method. This makes short wave episodes attractive because they can be used to estimate a nonlinear response correction for a pre-defined short-term upcrossing probability with limited computational effort.

On the other hand, the use of response conditioned wave sequences bears a risk of disregarding important contributions to the nonlinear response. The sequences are necessarily established from simpler theory and therefore likely to introduce large uncertainty or even a systematic bias to the response correction. This is apparently an inherent issue with response-corrective approaches which easily leads to over- or underestimated long-term extremes and also gives rise to wrong conclusions about individual service parameter's relevance with respect to the long-term extreme value distribution.

To resolve the dilemma, alternatives are sought which allow for mitigating the need to define short-term upcrossing rate distributions from very long simulations in random irregular waves. The scaling law of LNPE over H_S presented in section 3.3 can help here as an approach to accelerate the required simulation time through an artificial increase of the load spectrum.

This chapter documents numerical investigations that aim at appraising the feasibility of using this approach for accelerated predictions of short-term upcrossing rate distributions. The judgement is based on a qualitative level since the scope of investigations cannot be regarded comprehensive. Studies for the 10,000 and 14,000 TEU containerships are presented, see appendix A. Parts of these results have already been published in Oberhagemann et al. (2013).

5.1 Extrapolation of Upcrossing Rates in Stationary Sea States

It was demonstrated in chapter 3 that, for a linear narrow-banded response process and a stationary service condition $[\, T_z, v, \mu, LC \,]$, the logarithm of the upcrossing rate of a response level R is inversely proportional to H_S^2. This was extended to nonlinear responses based on assuming that the excitation and response mechanisms to cause a reaction of magnitude R remain unaffected of the significant wave height. The following will elaborate on the resulting generic relation of $\chi(R)$ and H_S,

$$-ln\left(\chi(R)\right) = A + \frac{B}{H_S^2}. \tag{5.1.1}$$

The formulation suggests that it should be possible to derive upcrossing rates for one significant wave height $H_{S,1}$ from upcrossing rates obtained for a different significant wave height $H_{S,2}$. Choosing a reasonably large $H_{S,2}$ is then an effective means to significantly decrease the simulation time required for determining the return period of the response for $H_{S,1}$. Such artificial increase of the significant wave height should be done with caution since nonlinearities of the wave and response processes may violate the inverse proportionality assumed in eq. (5.1.1). Yet, it helps to give at least an estimate of response magnitudes at upcrossing rates which are not amenable to direct simulation.

Table 5.1: Simulation durations for 10,000 TEU containership and different H_S

$H_S\,[m]$	**8.5**	9.5	12.5	13.5	**14.5**	15.5
$T_S \cdot 10^{-4}\,[s]$	**1.0**	0.3	0.3	0.3	**1.8**	0.3

Applications are now presented for midship hogging and sagging VBM of the 10,000 and 14,000 TEU containerships. Simulation data are available for

Table 5.2: Simulation durations for 14,000 TEU containership and different H_S

$H_S\,[m]$	**8.0**	9.0	11.0	12.0	13.0	**14.0**
$T_S \cdot 10^{-4}\,[s]$	**2.2**	0.8	0.5	0.8	1.0	**1.8**

simulation durations $T_S = 1.0 \cdot 10^4\,s$ to $2.2 \cdot 10^4\,s$ in irregular sea state realisations of significant wave heights $H_S = 8.0\,m$ and $14.0\,m$ (14,000 TEU) as well as $8.5\,m$ and $14.5\,m$ (10,000 TEU). Further simulation results in intermediate significant wave heights are available for shorter T_S and will be used for plausibility checks only. Tables 5.1 and 5.2 list all available simulation results. Both ships were sailing at a forward speed $v = 10.0\,kts$. All simulations used long-crested head seas ($\mu = 180°$) and Pierson-Moskowitz wave spectra with $T_z = 11.5\,s$. The realisations consisted of each 500 random wave components which is sufficient to avoid repetition of the wave process for the durations considered.

In what follows, all results will refer to non-dimensional vertical bending moments $\tilde{R}$. For the present purpose, the factor $\rho g B L^2 H_S/2$ used in previous chapters for making the VBM non-dimensional is not convenient because it depends on H_S which is not constant. Instead, the VBM will be made non-dimensional based on

$$\tilde{R} = \frac{R}{R_{rule}}, \tag{5.1.2}$$

where R_{rule} refers to the IACS rule wave bending moment in hogging or sagging, see IACS (2010). R_{rule} for the midship section is defined for both containerships as

$$R_{rule} = \begin{cases} R < 0 & : \quad 2042.5 \cdot B L^2 C_B \\ R > 0 & : \quad 1182.5 \cdot B L^2\,(0.7 + C_B) \end{cases} \tag{5.1.3}$$

since their lengths are in the range $300\,m < L < 350\,m$ and $C_B > 0.6$.

The approach used here to establish a functional relationship between upcrossing rates of response levels and significant wave height outlines as follows. Peak evaluations from simulations in two different significant wave heights provide peak upcrossing rates for selected response levels $\tilde{R}_k$; coefficients A_k and B_k are determined for each $\tilde{R}_k$ individually from the relation

$$-ln\left(\chi(\tilde{R}_k)\right) = A_k + \frac{B_k}{H_S^2}; \tag{5.1.4}$$

Table 5.3: Upper response level limits for fitting coefficients A and B

	10,000 TEU		14,000 TEU	
	Hog	Sag	Hog	Sag
$\tilde{R}_{max}$	0.64	0.64	0.57	0.49
$N\left(\tilde{R} > \tilde{R}_{max} \vert H_{S,1}\right)$	404	448	393	534
$N\left(\tilde{R} > \tilde{R}_{max} \vert H_{S,2}\right)$	16	27	29	36

A is taken as the average over all A_k; least squares regression over the B_k based on the second-order polynomial formulation eq. (4.3.5) proposed in section 4.3.2 defines $B(\tilde{R})$ from the relation $B(\tilde{R}) = -H_S^2\left[A + ln\left(\chi(\tilde{R})\right)\right]$; finally, A and $B(\tilde{R})$ establish the upcrossing rate χ as a function of $\tilde{R}$ and significant wave height H_S,

$$\chi(\tilde{R}, H_S) = exp\,(-A)\; exp\left(-\frac{b_1\tilde{R} + b_2\tilde{R}^2}{H_S^2}\right). \tag{5.1.5}$$

The approach is exemplified based on hogging VBM of the 10,000 TEU containership. Observations and conclusions, however, hold for the sagging data as well as for hogging and sagging peaks of the 14,000 TEU containership. Corresponding tables and figures are found at the end of this section.

Fig. 5.2 shows the upcrossing rates of VBM peaks in hogging, determined from the simulations, that are the starting point for the further evaluations. The upcrossing rates are sample mean values. For low response levels with many sampled upcrossing events, (or for long evaluated time records) the upcrossing rates approach the statistical mean. On the other hand, small samples of upcrossings will show large random scatter. The upper limits of response levels for establishing A and $B(\tilde{R})$ assure that the available time series comprise at least 16 relevant peak events in order not to introduce too large scatter, see Table 5.3.

First, A_k and B_k are individually adjusted to peak upcrossing rates of selected $\tilde{R}$, Fig. 5.3. The resulting curves support the assumption of a constant A since the $ln\left[\chi(\tilde{R})\right]$ become independent from $\tilde{R}$ when H_S^{-2} approaches zero [1]. It appears therefore reasonable to define a constant A as the average over the A_k for all $\tilde{R}_k$.

[1] The A_k are the y-intercepts of the lines in Fig. 5.3, while the B_k are the corresponding slopes

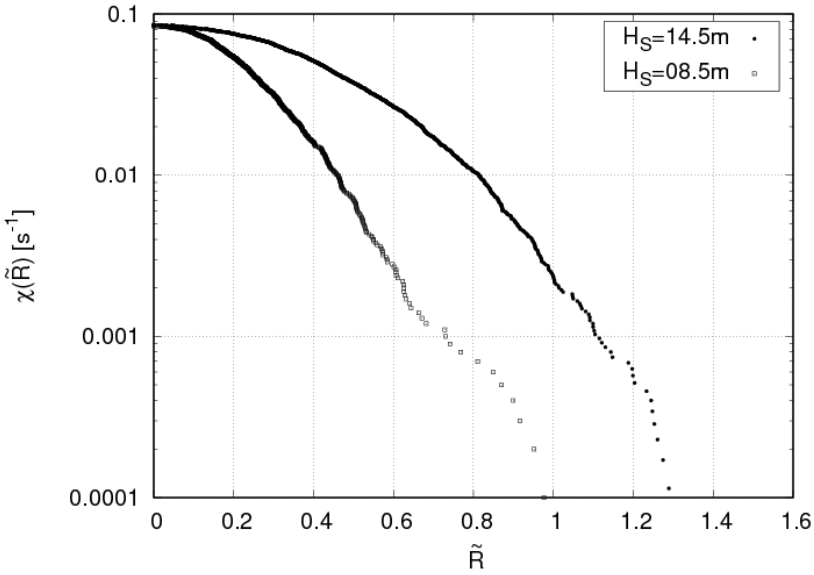

Figure 5.2: Upcrossing rates of hogging VBM peaks for the 10,000 TEU containership

Next, second-order polynomial regression according to eq. (5.1.5) determines the $B(\tilde{R})$, see Fig. 5.4. For reference, $B_{lin} = R^2/(2m_{0r})$ is added with m_{0r} based on linear BEM seakeeping analysis. The polynomial resulting from regression favourably agrees with simulation data for both H_S for small to moderate $\tilde{R}$, $0 < \tilde{R} < \tilde{R}_{max}$, but deviates for larger $\tilde{R}$. Considering that simulation data for $H_S = 14.5\,m$ comprises approximately 100 hogging peaks in exceedance of $\tilde{R} = 0.9$, the corresponding shape of B may be expected to have only small statistical variability at least up to this level. Nevertheless, the simulation data starts to have a less smooth shape already at a significantly lower response level, indicating that there is at least some statistical uncertainty. The discrepancy between the regression model and the simulation data for larger $\tilde{R}$ will be further discussed later.

Fig. 5.5 shows the LNPE as functions of H_S^{-2} for hogging VBM peaks and a range of response levels $\tilde{R} < 1.0$. Lines representing the results of the regression

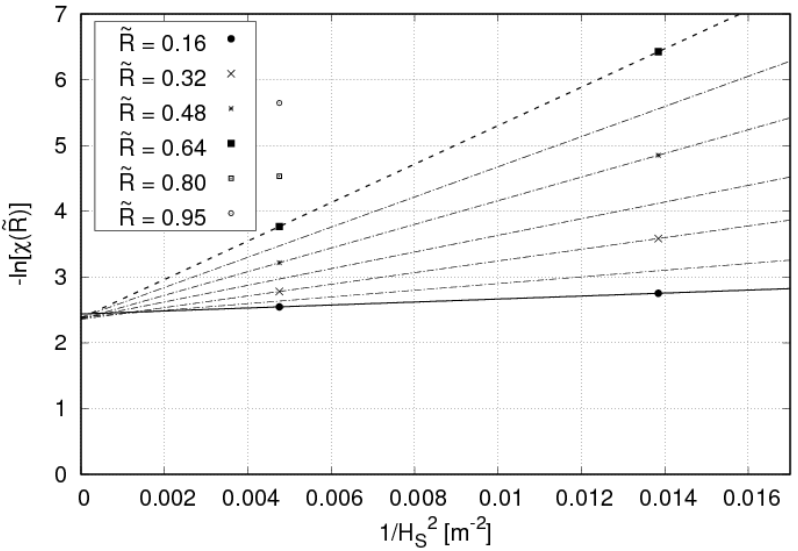

Figure 5.3: $-ln\left[\chi(\tilde{R})\right]$ as a function of H_S^{-2} for selected levels of $\tilde{R}$ in hogging for the 10,000 TEU containership

model eq. (5.1.5) are plotted along with the data points from simulation. In addition to the simulation data used for establishing the functional relations, data for intermediate significant wave heights are included to indicate the goodness of fit. Although using eq. (5.1.4) with coefficients A_k and B_k individually adjusted to each response level produced better matching with the data points, Fig. 5.3, the results in Fig. 5.5 indicate good overall agreement of the approximation eq. (3.3.15) with the simulation data. At least for the investigated H_S, B as the slope parameter of the LNPE can be regarded a function of $\tilde{R}$, but independent from H_S. Further on, the results support the assumption of a characteristic period $T_{zr} = exp(A)$, see eq. (3.3.13), which is independent from both $\tilde{R}$ and H_S.

The above approach for establishing the upcrossing rates as functions of H_S is just one of several conceivable options. Söding and Tonguć (1986) originally proposed to use an estimated T_{zr} and simulation data for only one significant wave height in order to extrapolate the LNPE for the targeted H_S. Using a

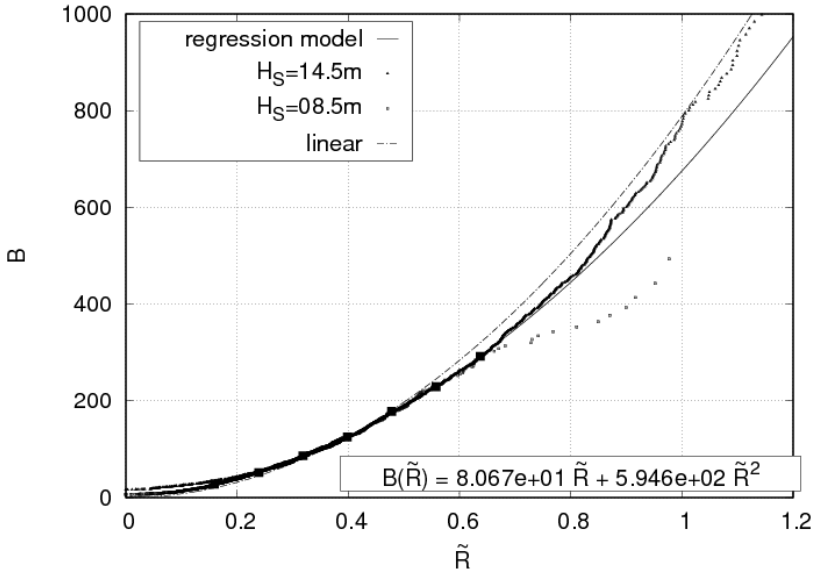

Figure 5.4: 10,000 TEU: $B(\tilde{R})$ resulting from regression over B_k from hogging VBM peaks; filled squares mark the data points for regression; linear BEM results added for comparison

sufficiently large H_S, this can be an effective means to drastically reduce the required simulation time. This is tested next using the simulation data from $H_S = 14.5\,m$. Instead of the above regression model, $B(\tilde{R})$ is now fit to the simulation data directly using all hogging peak values with at least a hundred sampled exceedances. T_{zr} is set equal to the response zero upcrossing period found from eq. (3.2.6) based on a linear frequency domain BEM computation. Fig. 5.6 compares B resulting from both approaches with the simulation data and indicates good overall agreement. The model based on a single simulation matches slightly better with the corresponding simulation data for larger $\tilde{R}$ as expected, yet the tail of the distribution is not matched by any of the models. This is attributed to scatter in the data since statistical uncertainty is largest for large response levels with a limited number of upcrossings.

Extrapolation of the LNPE towards lower significant wave heights according

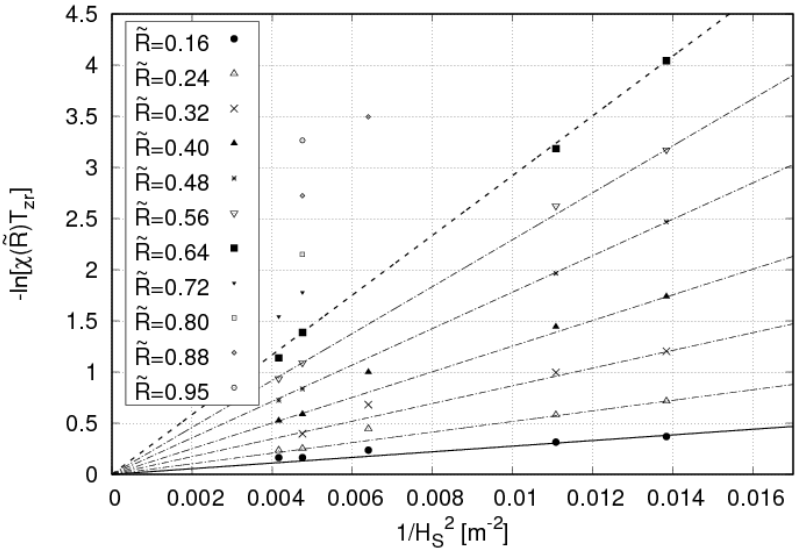

Figure 5.5: 10,000 TEU containership: LNPE of hogging VBM peaks, simulation data (symbols) and regression results (lines)

to eq. (5.1.5), Fig. 5.7, confirms the overall agreement of both data fitting approaches with each other; moreover, the LNPE as functions of $\tilde{R}$ and H_S established from simulation in a single H_S are also in good agreement with the simulation results for all simulated H_S for the response levels tested here. The inaccuracy associated with both approaches when scaling upcrossing rates from simulation data towards different significant wave heights is acceptable, considering the savings in computation time that can be achieved. Particularly the extrapolation according to eq. (5.1.5) based on simulation data for one single sea state can significantly reduce the required simulation time when choosing a large H_S.

The potential savings in simulation time can easily be illustrated with the following example based on the above findings. The rule bending moment in hogging, $\tilde{R} = 1$, was exceeded 41 times in the simulation with $H_S = 14.5\,m$. This corresponds to a return period of approximately 8 minutes. Fig. 5.8 illustrates

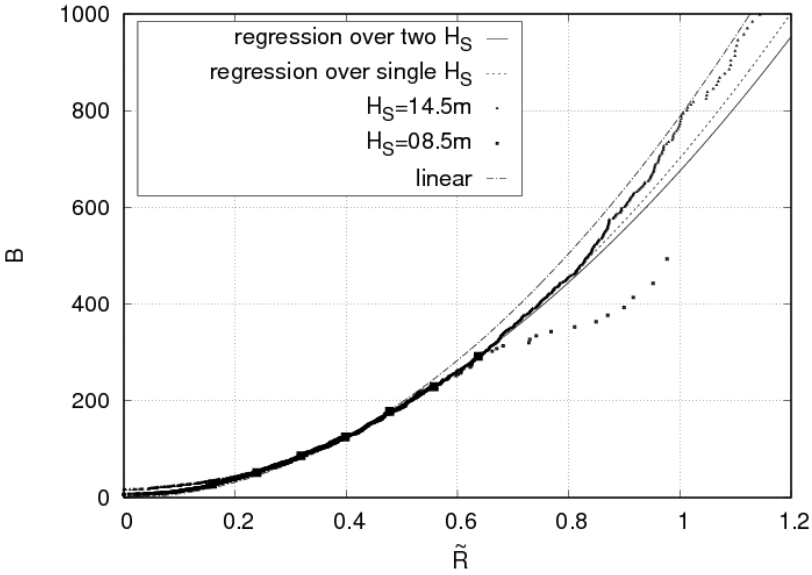

Figure 5.6: 10,000 TEU: $B(\tilde{R})$ resulting from regression over B_k from hogging VBM peaks (solid line) versus $B(\tilde{R})$ fitted to a single simulation with $H_S = 14.5\,m$; filled squares mark the data points for regression; linear BEM results added for comparison

the increase of the return period when decreasing the significant wave height, resulting in return periods of several days already for $H_S = 8.5\,m$, and further exceeding hundred years for significant wave heights less than $H_S = 6\,m$. At the same time, the relative reduction of the return period, when compared against linear results, is becoming more significant with decreasing wave height. The reduction of the return period is, in this example, somewhat less in the case of using data from a single H_S for extrapolation.

A fundamental restriction of both approaches discussed so far is the assumption of T_{zr} and $B(\tilde{R})$ being constant over H_S. At least for very large H_S, a change of slope is expected since, in this case, events that cause exceedances of $\tilde{R}$ are not rare anymore. Shigunov et al. (2010) discussed this issue. Jensen (2011) documented deviations from linear also for a larger range of H_S. This nonlinear

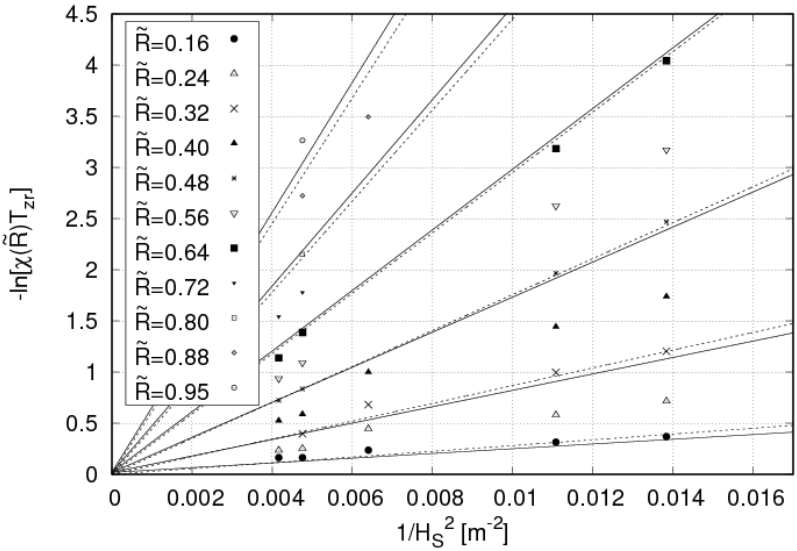

Figure 5.7: 10,000 TEU containership: LNPE of hogging VBM peaks, simulation data (symbols) and regression results based on single H_S (solid lines) and two H_S (dashed lines)

trend could well be replicated using a SORM approach instead of FORM, which indicates a nonlinear dependency of the reliability index on H_S while the scenario leading to exceedance of $\tilde{R}$ basically remains the same.

Results presented here so far could not confirm a significant change in slope although the data for establishing the LNPE largely relied on frequent events at least for the large H_S. Oberhagemann et al. (2012) addressed the dependency of B on H_S using simulation data obtained with the present numerical method. They suggested approaches to establish T_{zr}, b_1 and b_2 as functions of H_S, depending on the number of short-term upcrossing rate distributions available. Considering the significant increases in computation times when more simulation data are required, the additional costs will only be justified when the LNPE have to be extrapolated towards much smaller significant wave heights.

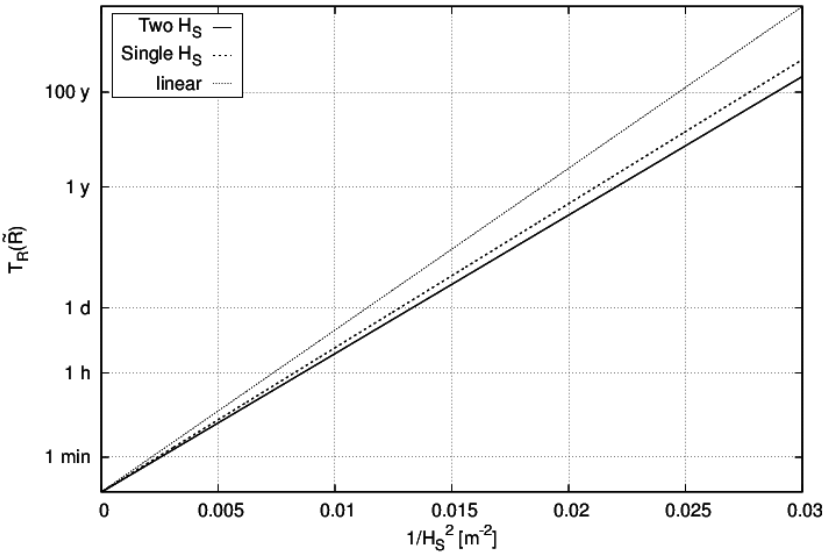

Figure 5.8: 10,000 TEU: extrapolated return periods of $\tilde{R} = 1$ according to regression models based on two H_S (solid line) and a single H_S (dashed line), respectively; linear BEM results added for comparison (dotted line)

5.2 Extrapolation of Grid Independent Solutions

The results discussed in the previous section relied on simulation data obtained on relatively coarse grids. The associated discretisation errors particularly affect the vibratory contribution to the responses. This will be addressed now by estimating these errors and using the scaling function Ξ to correct the LNPE. Strategies discussed in sections 4.1 and 4.3.2 will be applied in grid studies for the lower and upper H_S.

The underlying idea is to generalize eq. (4.3.10) and establish Ξ as a function of H_S,

$$\Xi\left(\tilde{R}, H_S\right) = 1 + a_\infty(H_S)\tilde{R}^3, \tag{5.2.1}$$

with a_∞ assumed to linearly depend on H_S:

$$a_\infty(H_S) = a_{10} + a_{11}H_S. \tag{5.2.2}$$

The coefficients a_{10} and a_{11} require data from simulations in at least two different H_S. Starting point is there $\Xi(\tilde{R}\,|\,H_{S,1})$ and $\Xi(\tilde{R}\,|\,H_{S,2})$

Grid refinement studies for the 10,000 TEU containership and two different H_S had already been presented in chapter 4. Figs. 5.9 and 5.10 show the resulting scaled short-term upcrossing rate distributions. To highlight the contribution of vibration, an additional evaluation yielded upcrossing rate distributions from low-pass filtered response time series. They can be considered representative of the rigid hull, although effects of low-frequency deflections in waves are still present. These cause a slight underprediction of responses compared to computations for the rigid hull. Further on, short-term response statistics data from linear BEM computations and corresponding nonlinearly corrected results are shown for comparison.

Additional grid refinement studies for the 14,000 TEU containership are given now in long-crested irregular waves with $T_z = 11.5\,s$, $v = 10\,kts$ and $\mu = 180^\circ$ and two different significant waves heights $H_S = 14.0\,m$ and $H_S = 8.0\,m$. Corresponding short-term distributions of hogging and sagging peaks, obtained on the coarsest grid, are shown in Figs. 5.11.

The $\Xi(\tilde{R})$ were computed on a total of five refined grid representations for the larger H_S and three for the lower, Figs. 5.12 and 5.13. Despite some scatter for the coarsest grids, the results for $H_S = 14.0\,m$ clearly support the assumption

of a linear dependency of a_∞ on grid refinement ratio, i. e. a first-order grid convergence. The uncertainty related to extrapolation will again be large. The range of extrapolation is even larger than in the previous example for the 10,000 TEU containership.

However, the changes of a_∞ with grid refinement ratio are significant and emphasize the necessity to account for the grid dependent error. The suggested extrapolation of grid independent upcrossing rates is therefore meaningful despite the large associated uncertainty.

Another observation from Figs. 5.12 and 5.13 as well as Figs. 4.46 and 4.47 is that $\Xi(\tilde{R}, \Upsilon)$ changes with H_S. If short-term upcrossing rate distributions are computed for more than one significant wave height, grid dependency studies should be carried out at least for a representative subset of wave heights in order to define the coefficients a_∞ as functions of H_S. $\Xi(\tilde{R}, \Upsilon_i, H_S)$ can then be applied to extrapolate grid independent upcrossing rate distributions in sea states with other H_S. Fig. 5.14 illustrates the resulting VBM upcrossing rate distributions when applying the extrapolation approach to the results of the reference grid representation. Function Ξ is also expected to depend on other service parameters, therefore, grid-dependency studies are recommended for at least a representative number of parameter combinations T_z, v, μ and LC.

Figs. 5.15 and 5.16 show the LNPE as functions of H_S^{-2} including the corrections based on $\Xi(R, H_S)$. The figures indicate that the applied scaling towards grid-independent solutions is inconsistent with the scaling law of the LNPE. While resulting curves of LNPE for given $\tilde{R}$ approach a linear slope for small H_S, they increasingly depart from linear dependency at large H_S. Since Ξ has been established based on only two H_S, its shape beyond these limits is unknown. The suggested extrapolation function Ξ should be regarded an approximation, and its use should be limited to a small range of H_S.

On the other hand, extrapolation of upcrossing rates towards lower significant wave heights appears practical and not affected by excessive uncertainty for the range of wave heights tested, considering the resulting reduction in required simulation times.

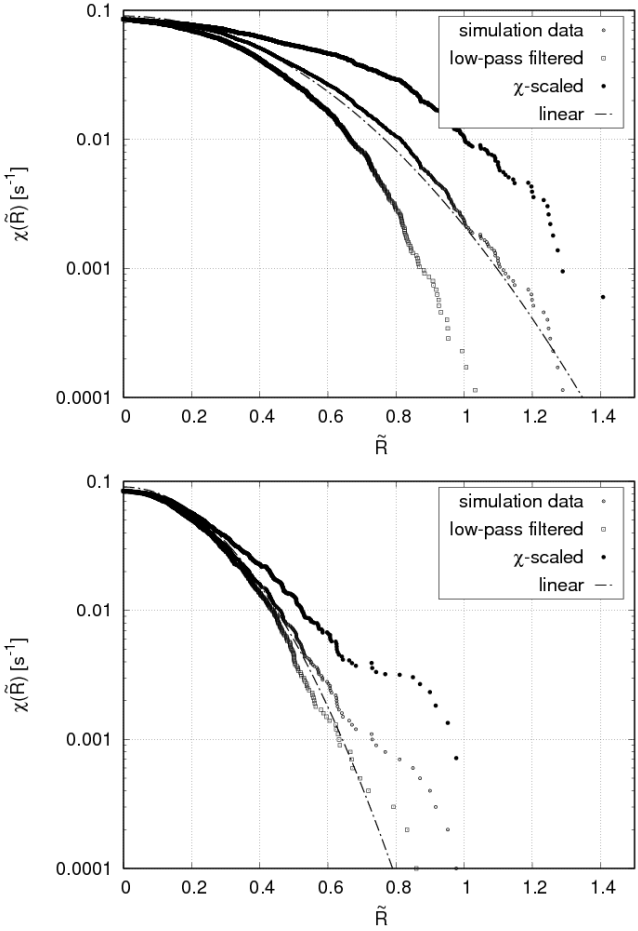

Figure 5.9: 10,000 TEU containership: upcrossing rates of hogging VBM peaks for $H_S = 14.5\,m$ (top) and $H_S = 8.5\,m$ (bottom); low-pass filtered simulation data (squares), original data (empty dots) and scaled data (filled dots); linear BEM results for comparison

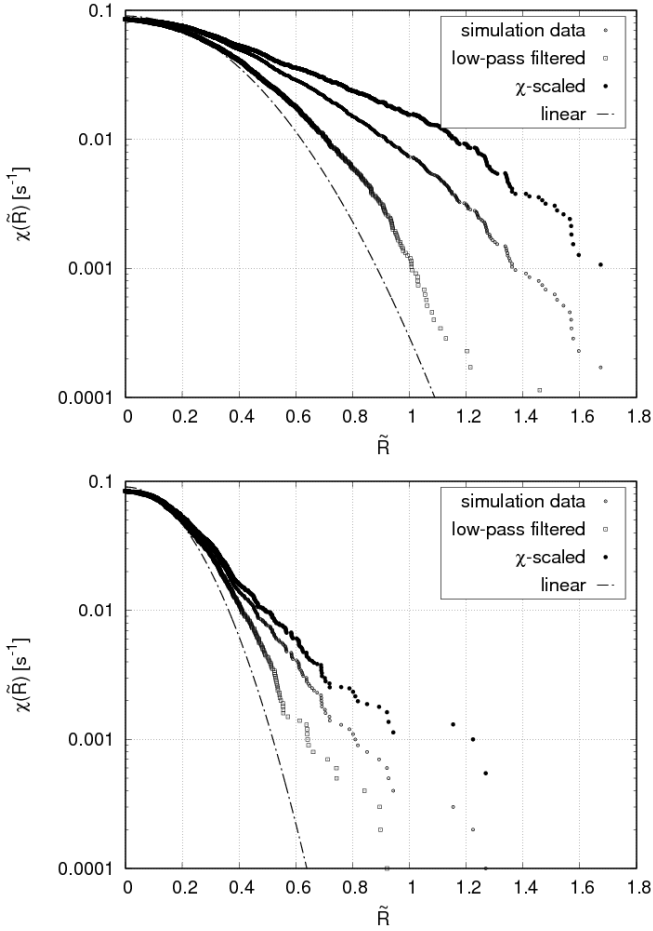

Figure 5.10: 10,000 TEU containership: upcrossing rates of sagging VBM peaks for $H_S = 14.5\,m$ (top) and $H_S = 8.5\,m$ (bottom); low-pass filtered simulation data (squares), original data (empty dots) and scaled data (filled dots); linear BEM results for comparison

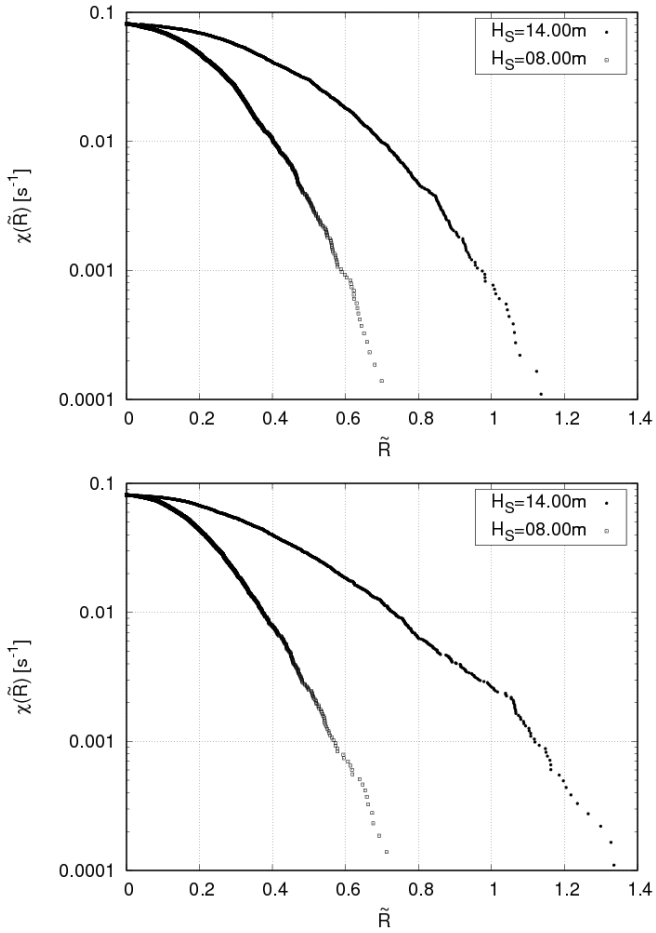

Figure 5.11: Upcrossing rates of hogging (top) and sagging (bottom) VBM peaks for the 14,000 TEU containership in sea states with $H_S = 14.0\,m$ and $H_S = 8.0\,m$

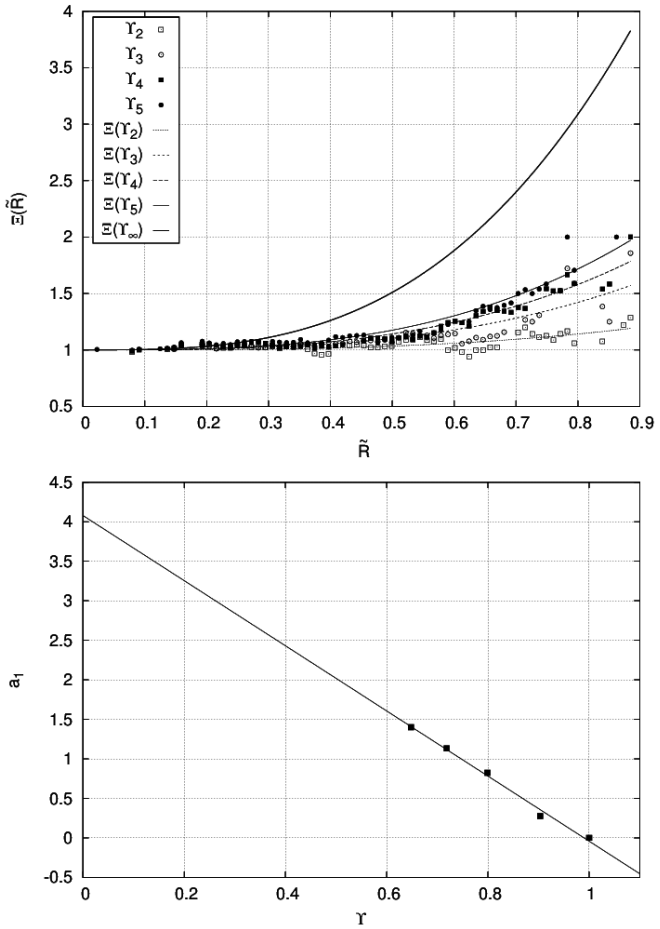

Figure 5.12: Fits of Ξ and extrapolated scaling function for Υ_∞ of 14,000 TEU containership, $H_S = 14.0\,m$, $T_z = 11.5\,s$, $v = 10\,kts$, $\mu = 180°$, hogging (top); coefficient a_1 of extrapolation function Ξ as a function of Υ (bottom)

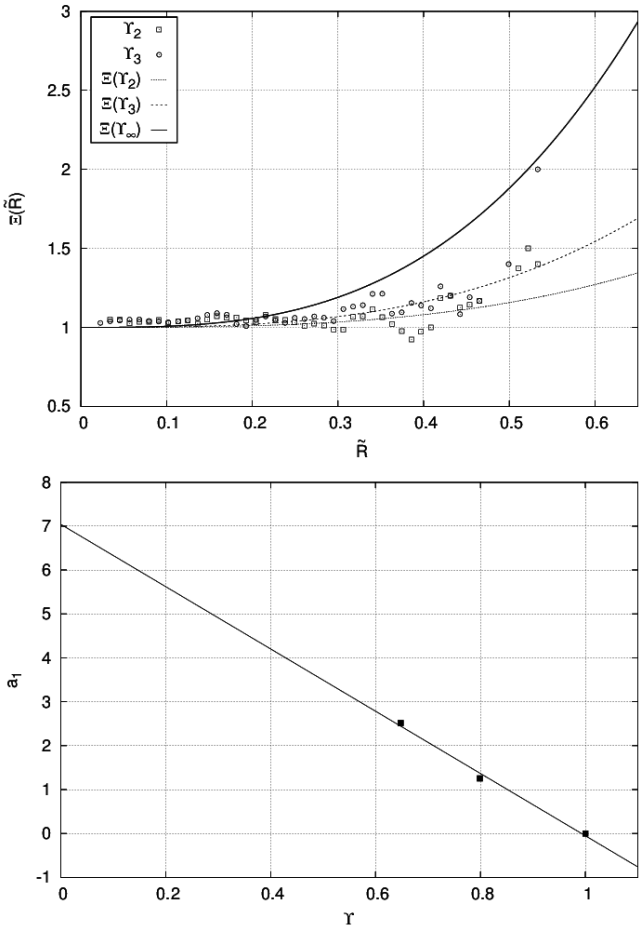

Figure 5.13: Fits of Ξ and extrapolated scaling function for Υ_∞ of 14,000 TEU containership, $H_S = 8.0m$, $T_z = 11.5s$, $v = 10kts$, $\mu = 180°$, hogging (top); coefficient a_1 of extrapolation function Ξ as a function of Υ (bottom)

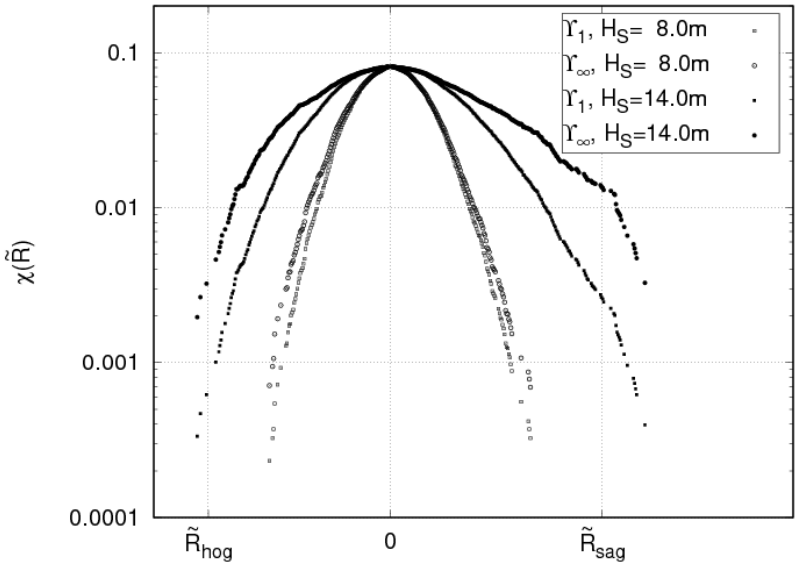

Figure 5.14: VBM upcrossing rate distributions of 14,000 TEU containership in two different significant wave heights, computed on reference grid representation and extrapolated grid independent solution

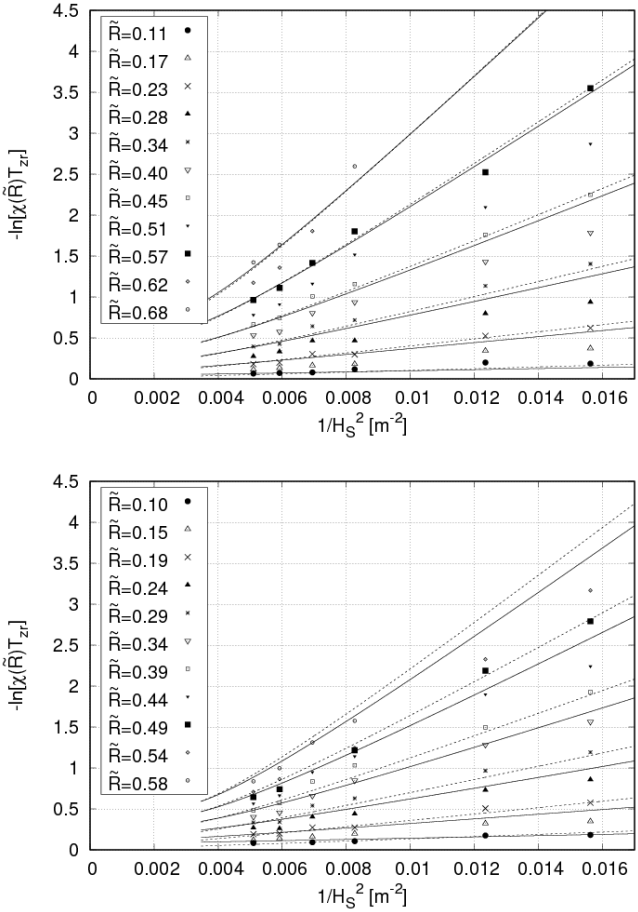

Figure 5.15: 14,000 TEU containership: LNPE of hogging (top) and sagging (bottom) peaks, found from one (solid lines) and two H_S (dashed lines), respectively, and extrapolated towards grid independent solution

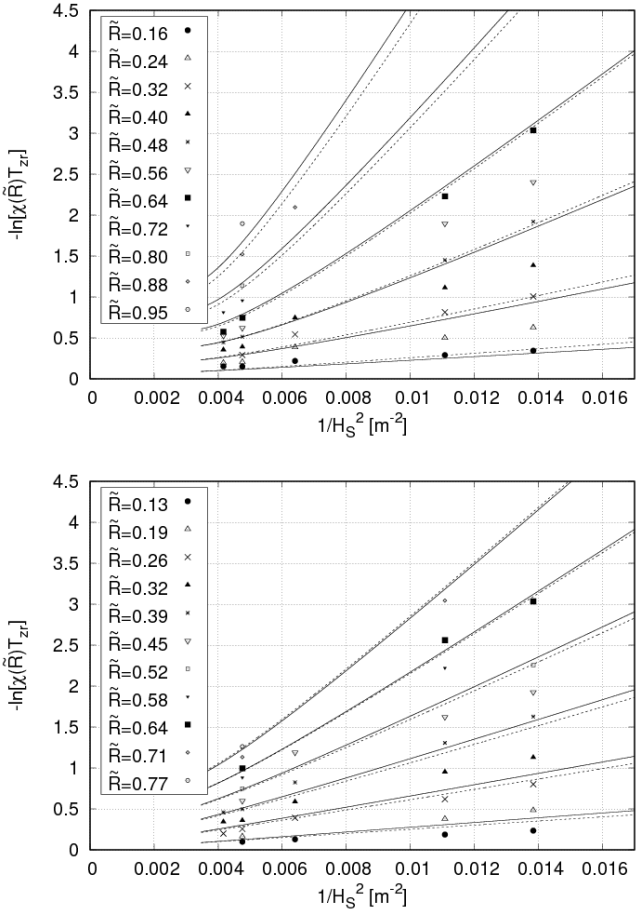

Figure 5.16: 10,000 TEU containership: LNPE of hogging (top) and sagging (bottom) peaks, found from one (solid lines) and two H_S (dashed lines), respectively, and extrapolated towards grid independent solution

6 Discussion

The work documented in this thesis covers the description of a numerical method for coupled transient computations of fluid and structural dynamics, including flexural deformations, with a focus on suitability for statistical analyses of wave loads on ships. The method has been validated against model scale experimental data. Application of the method was presented for computing probability distributions of internal hull girder loads in stationary sea states.

The fluid dynamics method implements a transient solution of the conservation equations of momentum and mass in a three-dimensional finite volume formulation. An additional scalar transport equation is used for a Volume of Fluid type interface capturing method. This is a suitable way to capture non-linear flow features relevant for ship responses in severe or extreme wave conditions, since wave-wave interaction and wave non-linearities including breaking are implicitly accounted for.

The structural dynamics solver consists of two distinct parts. A nonlinear solver for the six degrees of rigid-body motions is capable of large motion amplitudes which may for ships, e. g., occur in terms of excessive roll. Structural deformations, on the other hand, are treated linearly. This is sufficient for ship structures as long as yielding, buckling and collapse do not need to be modelled in the simulation explicitly. Further on, the structural deformation solver used throughout this thesis models the ship hull girder as a simple Timoshenko beam. Only global hull girder deformations can thus be accounted for with a further restriction to planar vertical vibration and deformation.

The coupled method accounts for non-linearities of wave-structure interaction, which is essential for realistic simulations of slamming and green water effects on the structural response. Validation method was presented for several aspects related to transient wave load and ship response analysis, albeit with emphasis on wave-induced vibration. Generally good agreement with model scale experiments could be achieved despite observed discrepancies for a few cases.

Of all conceivable sources of error and uncertainty, only numerical grid resolution in space and time was investigated. One reason for doing so is the

importance of appropriate grid generation for practical application purposes. Awareness of the grid sensitivity of a certain flow problem is a prerequisite for producing reasonable numerical solutions. Another reason is the dominance of grid dependent errors, observed from practical application. Attempt was made here to quantify the discretisation error related to a given grid resolution and establish a procedure for estimating the grid independent solution to transient problems.

The validations started with isolated yet complex flow problems. Applications of the numerical method to hydrodynamic impacts were rather academic in that 2D problems of local flows allow a fine grid resolution that can not be afforded for computational domains covering a whole ship and the surrounding flow in simulations covering long time intervals. Computations were in fine agreement with the experiments and showed that the coupled numerical method is able to compute the transient impacts and corresponding test specimen decelerations accurately and consistently.

The later validation example of the RoPax ferry slamming in regular head waves demonstrated that impulses from slamming can be reproduced despite a coarser grid with insufficient resolution to capture local pressure peaks. In other words, lack of accuracy in computed local pressures does not necessarily impair the prediction of the overall response. Comparing integral values is of higher relevance for the latter and leads to more optimistic conclusions: variations of time-integrated pressures are small, and numerical and experimental results are in good agreement. Of importance for global structural responses are force impulses acting on the whole impact area. el Moctar et al. (2004), el Moctar et al. (2005) and Oberhagemann et al. (2008) presented further studies that demonstrated the feasibility of computing integral quantities of hydrodynamic impact loads in waves sufficiently accurate on grids with relatively coarse local resolution, compared to the resolution used in the 2D impact studies. Another well-known but important observation is that even in regular waves the peak pressures strongly vary, in both experiments and simulation, while integrated impulses show significantly less variability.

Studies of free vibration decay for two ships were performed to check the numerical method's ability of determining the hydrodynamic damping associated with the fundamental vertical bending vibration mode. It was demonstrated that the computed damping is sensitive to the grid resolution in space and time because of numerical damping. Grid refinement studies are thus required to determine the damping contributions from numerical damping. The concept

of grid extrapolation introduced in section 4.1 was successfully applied here and allowed a distinction between numerical and hydrodynamic damping. This made a quantification of the hydrodynamic damping possible. Comparisons with experimental data showed reasonable agreement of the computed damping ratios. Although numerical and experimental results were subject to uncertainty, the magnitude of damping observed in experiments was reasonably well predicted by the computations, and the dependency of damping on the ship forward speed was replicated as well.

A comprehensive study of ship motions and internal loads of the 10,000 TEU containership in regular head waves compared solutions of the coupled solvers based on *COMET* and *interDyMFoam* with experimental data. While fine agreement was observed for the *COMET* solution, results from *interDyMFoam* revealed larger differences owing to a lack of a second-order accurate discretisation in time. As this can only be compensated by using smaller time steps, results of comparable accuracy are significantly more computationally expensive when using *interDyMFoam*. For this reason, *interDyMFoam* was not used for all following investigations.

It was demonstrated for wave frequency responses in low amplitude regular waves that coarse grid resolutions provided sufficiently accurate results. Further, the numerical method's ability to predict periodically excited wave-induced vibration was demonstrated and qualitatively validated against experimental data. First-order and higher-order resonance could be well replicated, highlighting the benefits of a first-principle approach to the fluid dynamic problem.

Grid refinement did not improve the wave frequency response predictions and basically only modified predictions of higher frequency wave-induced vibrations. Disturbingly, the refined grid did not improve the agreement with the experimental results. Since only solutions on two grid resolutions were available for this case, it is difficult to estimate grid-independent solutions. Moreover, it can not be assessed whether at least the coarse grid was out of the asymptotic range and therefore not suited for extrapolating grid independent solutions.

Computational results based on systematically refined grid representations were presented for a RoPax ferry advancing in a regular head wave. Bow impact forces did not indicate a significant influence of grid resolution, with the coarsest of the grids already providing satisfactory results. Favourable agreement with experiments could be achieved with some smaller deviations of the midship vertical bending moment. Hull girder vibration in this particular case was

composed of the 2-node and 3-node vertical vibration modes which is rather unusual.

Short-term upcrossing rate distributions of vertical bending moment of the 10,000 TEU containership were computed from long simulations of the ship sailing in long-crested irregular head waves. Simulation durations of up to three hours were compared with available model scale experimental data. The computations used the experimental wave probe data for generating the input wave processes. Comparisons showed a reasonable agreement between computations and model tests despite some differences. Although visual inspection of the time series indicates a good qualitative agreement of the computations with the experiments, the differences become clearer when looking at the evaluated upcrossing rate distributions. Surprisingly, the computations tend to over-predict the model test data. However, best agreement was observed for a three hour simulation in a significant wave height $H_S = 9.0m$. Here, evaluations of response cycles from rainflow counting as well as peak upcrossing rate distributions showed that computations very well reproduced the experimental results. Differences were found for evaluations of low-pass filtered time series, corresponding to rigid-body responses, where the computations again over-predicted the experimental results.

Extreme value predictions of ships or other marine structures require appropriate hydrodynamic methods capable of modelling all relevant nonlinearities. Procedures involving simulations with field methods could be advantageous because of the higher degree of nonlinearities implicitly included, but suffer from the high computational cost they involve. Parallelisation in space and parallel execution of several simulation parts is an obvious means to speed up the required wall time for simulations. Nevertheless, the total time required for comprehensive statistical analyses remains large even with medium size cluster computers[1].

Embedding such computationally expensive methods in sensible computational procedures to define loads for further structural reliability assessments is therefore an important but challenging task. The vast computing resource requirements motivate, or even necessitate, efforts for reducing the overall turnaround times for a numerical analysis. Simplifications are inevitable in this respect. These simplifications should, however, be based on conservative assumptions

[1] Aside from that, such cluster computers have high capital investment and operational costs. On the other hand, comparable model test campaigns also take their time at significantly higher daily costs.

and not be overly simplistic. Disregarding important load effects or using too crude assumptions will result in over- or under-estimated design loads, which in turn deteriorates the usefullness of a computionally intensive method.

Closely linked to the large computational requirements, the asymptotic accuracy of finite volume methods is a major drawback when performing simulations in waves for long time intervals. Computational results presented in chapters 4 and 5 revealed a relevant dependency of upcrossing rate distributions of VBM of flexible ships on the grid resolution. Insufficient discretisation in space and time was found to result in inaccurate and potentially non-conservative solutions. Fine discretisation, on the other hand, strongly increases the computational expenses. Therefore, a reasonable compromise between accuracy and efficiency has to be found particularly when calculating responses of a flexible ship in irregular waves.

The use of systematically refined grids is a good alternative to improve confidence in the results while avoiding the computational burden of very fine grid resolution in space and time. While the results on each of the used grids are subject to discretisation errors, grid extrapolation allows the estimation of grid independent solutions. Grid extrapolation was performed here not only for scalar solution values, but for upcrossing rate distributions resulting from transient simulations in irregular waves.

In the examples presented, extrapolation towards grid-independent solutions yields a significant decrease of return periods, therefore fundamentally influences the results. Using coarse grids in the simulations, although essential to allow reasonable computation times, introduces large inaccuracy. The presented extrapolation function $\Xi(R)$ is based on experience gathered so far and requires further investigation and improvement. One can, however, conclude that estimating a grid-independent solution is meaningful and improves the results.

A further option to accelerate the computation of short-term response distributions is an artificial increase of the significant wave height and assume an inverse proportionality of the LNPE on the significant wave height squared. This can be motivated from linear reliability theory based on FORM, or, alternatively, on fundamental phenomenological considerations initially proposed by Söding and Tonguć (1986). Based on the original formulation of Söding and Tonguć (1986), a scaling law of the LNPE according to eq. (3.3.16) was presented that establishes a semi-empirical relation of the coefficient B on the response R, with a second-order regression model fitting best to the available simulation

data. Its motivation was to account for a combined response process including vibrations. The proposed scaling law was tested for the 10,000 TEU and 14,000 TEU containerships and showed good agreement with the available simulation data.

Application of the scaling law may result in remarkable savings of computation times of several orders of magnitude, depending on the case at hand. Observed uncertainties and errors were reasonably small, so the scaling law is expected to produce good results when the extrapolation over H_S is within the bounds of the tested H_S. However, extrapolation from large H_S towards much smaller significant wave heights will not be necessary in extreme value analyses because service conditions with small H_S only contribute little to the extreme value distribution. Furthermore, instead of simulating for a number of different significant wave heights, a single simulation set for each combination of T_z, v, μ and LC can be used to cover a range of significant wave heights.

A proposed generalized formulation $\Xi(\tilde{R}, H_S)$ appears to be not consistent with the scaling law of the LNPE versus significant wave height. However, the inconsistency turned out to mainly affect the upcrossing rates towards infinite significant wave height and therefore is irrelevant for practical purposes; one would not want to extrapolate towards larger significant wave heights. In conclusion, combined extrapolation of upcrossing rates towards grid-independent solutions and towards sea states with lower significant wave height appears practicable and not affected by large uncertainties for the range of wave heights tested.

6.1 Concluding Remarks

Wave-induced vibration is an important contribution to the loads exerted on ship structures in waves. The presented coupled numerical method was intended to enable accurate predictions of wave loads in severe and extreme conditions to allow improved extreme value assessments of wave loads including effects of wave-induced vibration. The presented validation showed a good agreement with experiments, despite some differences. Further validation, especially for long duration computations in irregular waves, may improve confidence in the method.

The use of CFD for marine applications, and in particular wave load analyses of ships, is increasingly becoming popular. Despite the apparently straight-forward

formulation of the hydrodynamic problem, practical problems are likely due to the complex requirements on grid generation and solver settings. Inappropriate use of this type of computational methods in turn easily results in wrongly predicted ship responses and, as a consequence, potentially unsafe designs. The thesis hopefully contributes to improve knowledge on appropriate and informed use of CFD for wave load analyses of ships.

The thesis further presented and discussed options to improve the efficient use of the coupled numerical method. These options necessarily require assumptions and introduce simplifications, and, as a consequence, introduce uncertainty and scatter of results. The scope of the documented work does not allow for general conclusions on expected uncertainties or achievable accuracies; however, it could be exemplified that such techniques for reducing the computation time are meaningful and do not deteriorate the analysis results.

The most suitable role of CFD and coupled CFD-CSD methods needs further clarification but could in principle cover three different aspects: First, such methods can be used to calibrate or validate simpler methods; second, application of CFD methods can provide loads for improving assumptions in prescriptive rules; third, CFD simulations can be included in procedures settled in the rules. The third options probably being the most ambitious. Guidance for decisions on these options must not only be based on capabilities and deficiencies of the numerical method itself, but, at least in case of options two and three, also take into consideration the practicality of developing appropriate embedding procedures. Fundamental tasks of the work presented here were therefore the improvement and validation of existing methods; investigation of required computational accuracy and estimations of numerical uncertainties; finally, application of the method in case studies to determine the achievable accuracy.

The work documented herein can not be regarded complemented or exhaustive. Various aspects open up for further studies. Below is a list of suggested topics for further research which are considered most interesting.

6.2 Suggestions for Future Work

Increase the Empirical Data Base

Two important aspects of the work relied on extrapolation; namely, the extrapolation of grid-independent solutions and the scaling of LNPE over H_S. Both

concepts are meaningful in that they allow significant savings in computation time and results indicated the plausibility of the approaches. Nevertheless, more experience from further application is needed to achieve more confidence in these approaches. Furthermore, validation with experiments is still pending.

Additionally, the formulations may require adjustment based on larger sets of available data. This is particularly the case for the scaling function $\Xi(R, \Upsilon)$ and its dependency on H_S. The present formulation reasonably fits to simulation data but lacks a theoretical justification. However, further experience from application could help to derive an improved formulation from a larger empirical data base. It might also be worthwhile to not establish Ξ as a function of H_S but to combine data from all available H_S, assuming that the grid-dependent error is only depending on R.

Validation of Ξ with experimental data is also urgently recommended. Parts of the experimental data presented in this thesis are well suited for corresponding studies. Unfortunately, the experiments were made at a time when it was not possible anymore to perform grid sensitivity studies.

Oblique Waves and Complex Vibration Modes

All computations presented were performed in long-crested head waves. This is a strong simplification which is presumably conservative. Experience from computations so far indicates that vertical vibration is less excited in bow oblique or beam waves. Following waves are known to increase the risk of slamming in the flared stern region, but overall stern slamming has a smaller contribution to wave-induced vibration than bow slamming.

However, wave-induced vibration in more complex torsional and transverse vibration modes has been observed in full-scale measurements although their contributions to the largest observed loads were small. However, replacing the simplistic Timoshenko beam solver with a more sophisticated solver for three-dimensional flexural motions based on a modal structural representation will allow to include them in the analysis efficiently, see Dilba (2008), Cabos et al. (2011), Oberhagemann et al. (2012).

Bibliography

Adegeest, L., A. Braathen, and R. Løseth (1998). Use of Nonlinear Sea Loads Simulations in Design of Ships. In *Proc. 7th Int. Symp. on Practical Design of Ships and Other Floating Offshore Structures*, The Hague, pp. 53–58.

Andersen, I. M. V. (2014). *Full Scale Measurements of the Hydro-Elastic Response of Large Container Ships for Decision Support*. Ph. D. thesis, Technical University of Denmark, Lyngby.

Baarholm, G. S. and T. Moan (2000). Estimation of Nonlinear Long-Term Extremes of Hull Girder Loads in Ships. *Marine Structures 13(6)*, 495–516.

Bishop, R. E. D. and W. G. Price (1979). *Hydroelasticity of Ships*. Cambridge University Press.

Bitner-Gregersen, E. M. (2005). Joint Probabilistic Description for Combined Seas. In *Proc. 24th Int. Conf. Offshore Mechanics and Arctic Engineering*, Halkidiki. OMAE2005-67382.

British Marine Technology (BMT) (1986). *Global Wave Statistics*. London: Unwin Brs. Ltd.

Brunswig, J. (2004). Prediction of Ship Motions in Waves using RANSE. Master's thesis, Technische Universität Hamburg-Harburg, Hamburg.

Brunswig, J. and O. el Moctar (2004). Prediction of Ship Motions in Waves using RANSE. In *Proc. 7th Numerical Towing Tank Symposium*, Hamburg, pp. 9–13.

Cabos, C., B. Dilba, M. Krömer, and A. Schwenkenberg (2011). Modal Approach to Fluid Structure Interaction Applied to a Ship in Waves. In G. Soares and Fricke (Eds.), *Advances in Marine Structures*, pp. 9–17. London: Taylor and Francis.

Craig, M., D. Piro, L. Schambach, J. Mesa, D. Kring, and K. Maki (2015). A Comparison of Fully-Coupled Hydroelastic Simulation Methods to Predict

Slam-Induced Whipping. In *Proc. 7th Int. Conf. on Hydroelasticity in Marine Technology*, Split.

der Kiureghian, A. (2000). The Geometry of Random Vibrations and Solutions by FORM and SORM. *Probabilistic Engineering Mechanics 15(1)*, 81–90.

Derbanne, Q., F. Bigot, and G. de Hauteclocque (2012). Comparison of Design Wave Approach and Short Term Approach with Increased Wave Height in the Evaluation of Whipping Induced Bending Moment. In *Proc. 31st Int. Conf. on Ocean, Offshore and Arctic Engineering*, Rio de Janeiro. OMAE2012-83562.

Det Norske Veritas (DNV) (2010). Recommended Practices; Environmental Conditions and Environmental Loads. `exchange.dnv.com/publishing/Codes/ToC_edition.asp` (accessed 2014-01-03).

Dietz, J. S. (2004). *Application of Conditional Waves as Critical Wave Episodes for Extreme Loads on Marine Structures*. Ph. D. thesis, Technical University of Denmark, Lyngby.

Dilba, B. (2008). Ein Verfahren zur Simulation von dreidimensionalen Strukturverformungen im Seegang mithilfe modaler Reduktion. Master's thesis, Technische Universität Hamburg-Harburg, Hamburg. In German.

Ditlevsen, O. and H. O. Madsen (2005). *Structural Reliability Methods* (2nd ed.). Chichester: Wiley. ISBN 0471960861.

Drummen, I. and M. Holtmann (2014). Benchmark Study of Slamming and Whipping. *Ocean Engineering 86*, 3–10.

Drummen, I., M. K. Wu, and T. Moan (2009). Numerical and Experimental Investigations into the Application of Response-Conditioned Waves for Long-Term Nonlinear Analyses. *Marine Structures 22(3)*, 576–593. doi:10.1016/j.marstruc.2008.12.002.

Eça, L. and M. Hoekstra (2002). An Evaluation of Verification Procedures for CFD Algorithms. In *Proc. 24th Symp. Naval Hydrodynamics*, Fukuoka.

Eça, L. and M. Hoekstra (2014). A Procedure for the Estimation of the Numerical Uncertainty of CFD Calculations based on Grid Refinement Studies. *J. Computational Physics 262*, 104–130. doi:10.1016/j.jcp.2014.01.006.

el Moctar, O., A. Brehm, and T. E. Schellin (2004). Prediction of Slamming Loads for Ship Structural Design using Potential Flow and RANSE Codes. In *Proc. 25th Symp. Naval Hydrodynamics*, St. Johns.

el Moctar, O., J. Brunswig, A. Brehm, and T. E. Schellin (2005). Computations of Ship Motions in Waves and Slamming Loads for Fast Ships Using RANS. In *Proc. International Conference on Fast Sea Transportation*, St. Petersburg.

el Moctar, O., J. Oberhagemann, and T. E. Schellin (2011). Free-Surface RANS Method for Hull Girder Springing and Whipping. *SNAME Transactions 119*, 48–66.

el Moctar, O., T. E. Schellin, and T. Priebe (2006). CFD and FE Methods to Predict Wave Loads and Ship Structural Response. In *Proc. 26th Symp. Naval Hydrodynamics*, Rome, pp. 219–234.

Ferziger, J. H. and M. Perić (2002). *Computational Methods for Fluid Dynamics* (3rd ed.). Berlin Heidelberg New York: Springer Verlag.

Friis-Hansen, P. and L. P. Nielsen (1995). On the New Wave Model for the Kinematics of Large Ocean Waves. In *Proc. 14th Int. Conf. on Offshore Mechanics and Arctic Engineering*, Copenhagen, pp. 17–24.

Hanke, M. (2003). *Eine Numerische Methode zur Bestimmung Erweiterter Flugdynamischer Derivativa durch Aerostrukturdynamische Simulation*. Ph. D. thesis, Rheinisch-Westfälische Technische Hochschule Aachen, Aachen. In German.

Hänninen, S. K., T. Mikkola, and J. Matusiak (2012). On the Numerical Accuracy of the Wave Load Distribution on a Ship Advancing in Short and Steep Waves. *J. Marine Science and Technology 17*, 125–138. doi: 10.1007/s00773-011-0156-8.

Hasselmann, K., T. P. Barnett, E. Bouws, H. Carlson, D. E. Cartwright, K. Enke, J. A. Ewing, H. Gienapp, D. E. Hasselmann, P. Kruseman, A. Meerburg, P. Müller, D. J. Olbers, K. Richter, W. Sell, and H. Walden (1973). Measurements of wind-wave growth and swell decay during the Joint North Sea Wave Project (JONSWAP). Ergänzungsheft zur Deutschen Hydrographischen Zeitschrift A(8)12.

Heggelund, S. E., G. Storhaug, and B. K. Choi (2011). Full Scale Measurements of Fatigue and Extreme Loading Including Whipping on an 8600 TEU Post Panamax Container Vessel in the Asia to Europe Trade. In *Proc. 30th Int. Conf. on Ocean, Offshore and Arctic Engineering*, Rotterdam. OMAE2011-49378.

Hong, S. Y. (2009). Wave Induced Loads on Ships Joint Industry Project - II, First Year Model Test Report. Technical Report No. BSPIS503 A-2112-2 (confidential), MOERI, Daejeon.

Hong, S. Y. (2010). Wave Induced Loads on Ships Joint Industry Project - II. Technical Report No. BSPIS503 A-2207-2 (confidential), MOERI, Daejeon.

Hong, S. Y. (2013). Wave Induced Loads on Ships Joint Industry Project III. Technical Report No. BSPIS7230-10306-6, MOERI, Daejeon.

Hong, S. Y., B. W. Kim, and B. W. Nam (2012). Experimental Study on Torsion Springing and Whipping of a Large Container Ship. *Int. J. Offshore and Polar Engineering 22(2)*, 97–107.

International Association of Classification Societies (IACS) (2001). Recommendation No. 34 Standard Wave Data. `http://www.iacs.org.uk/document/public/Publications/Guidelines_and_recommendations/PDF/REC_34_pdf186.pdf` (accessed 2014-01-03).

International Association of Classification Societies (IACS) (2010). Unified Requirement S - Longitudinal Strength Standard. `http://www.iacs.org.uk/document/public/Publications/Unified_requirements/PDF/UR_S_pdf158.pdf` (accessed 2014-01-03).

International Ship Structures Committee (ISSC) (2012). Report of Committee II.2 - Dynamic Response. In *18th Int. Ship and Offshore Structures Congress*, Volume I, Hamburg, pp. 213–283. Schiffbautechnische Gesellschaft.

International Towing Tank Conference (ITTC) (2002). Recommended Procedures and Guidelines 7.5-03 - CFD General - Uncertainty Analysis in CFD - Verification and Validation Methodology and Procedures. `http://ittc.sname.org/2006_recomm_proc/7.5-03-01-01.pdf` (accessed 2014-10-20).

Issa, R. I. (1986). Solution of the Implicitly Discretized Fluid-Flow Equations by Operator-Splitting. *J. Computational Physics 62(1)*, 40–65.

Jensen, J. J. (2009). Stochastic Procedures for Extreme Wave Load Predictions - Wave Bending Moments in Ships. *Marine Structures 22*, 194–208. doi:10.1016/j.marstruc.2008.08.001.

Jensen, J. J. (2010). Extreme Value Predictions using Monte Carlo Simulations with Artificially Increased Wave Height. In *Proc. 11th PRADS Conference*, Rio de Janeiro, pp. 1169–1172.

Jensen, J. J. (2011). Extreme Value Predictions using Monte Carlo Simulations with Artificially Increased Load Spectrum. *Probabilistic Engineering Mechanics 26*, 399–404.

Kahl, A. and W. Menzel (2008). Full-Scale Measurements on a PanMax Containership. In *Ship Repair Technology Symposium Proceedings*, Newcastle upon Tyne, pp. 59–66.

Kim, D. H. and A. W. Troesch (2010). An Application of Design Load Generator to Predict Extreme Dynamic Bending Moments. In *Proc. 29th Int. Conf. on Ocean, Offshore and Arctic Engineering*, Shanghai. OMAE2010-20378.

Kim, S. (2010). Something about simulating ship in waves with CCM. In *ITTC proceedings*, Seoul.

Klein, M. and A. Maron (2012a). ExtremeSeas Deliverable 5.3 - Specification of Models to be Constructed. Technical Report D5.3-TUB, Technical University of Berlin, CEHIPAR, Berlin.

Klein, M. and A. Maron (2012b). ExtremeSeas Deliverable 5.4 - Specification of Model Tests. Technical Report D5.4-TUB, Technical University of Berlin, CEHIPAR, Berlin.

Klemt, M. (2004). *Bewegungssimulation schwimmender Körper in viskoser Strömung*. Ph. D. thesis, Technische Universität Hamburg-Harburg, Hamburg. In German.

Lakshmynarayanana, P. A., P. Temarel, and Z. Chen (2015). Coupled Fluid-Structure Interaction to Model Three-Dimensional Dynamic Behaviour of Ship in Waves. In *Proc. 7th Int. Conf. on Hydroelasticity in Marine Technology*, Split.

Launder, B. E. and B. I. Sharma (1974). Application of the Energy Dissipation Model of Turbulence to the Calculation of Flow Near a Spinning Disc. *Letters in Heat and Mass Transfer 1(2)*, 131–138.

Ley, J. (2012). ExtremeSeas Deliverable 4.7 - Report with Validation of the New Time Domain Seakeeping Codes by Systematic Comparisons with Experimental Data obtained in the Project. Technical Report D4.7-UDE, University of Duisburg-Essen, Duisburg.

Ley, J., M. Onorato, J. Oberhagemann, and O. el Moctar (2011). Simulation of Ships in Severe and Extreme Sea Conditions. In *Proc. 14th Numerical Towing Tank Symposium*, Poole.

Mao, W., I. Rychlik, and G. Storhaug (2010). Safety Index of Fatigue Failure for Ship Structure Details. *J. Ship Research 54(3)*, 197–208.

Maritime Accident Investigation Branch (MAIB) (2008). Report on the Investigation of the Structural Failure of MSC Napoli. Technical Report 09/2008, Maritime Accident Investigation Branch (MAIB). `http://www.maib.gov.uk/publications/investigation_reports/2008/msc_napoli.cfm` (accessed 2014-01-03).

Matsuishi, M. and T. Endo (1968). Fatigue of Metals Subjected to Varying Stress. In *Proc. Kyushu Branch of Japan Society of Mechanics Engineering*, Fukuoka, pp. 37–40.

Menter, F. R. (1993). Zonal Two Equation k-ω Turbulence Models for Aerodynamic Flows. In *Proc. 23rd AIAA Fluid Dynamics, Plasma Dynamics, and Lasers Conference*, Orlando. Paper No. 93-2906.

Muzaferija, S. and M. Perić (1998). Computation of Free-Surface Flows Using Interface-Tracking and Interface-Capturing Methods. In O. Mahrenholz and M. Markiewicz (Eds.), *Nonlinear Water Wave Interaction*, Chapter 2, pp. 59–100. Southampton: WIT Press.

Muzaferija, S., M. Perić, P. C. Sames, and T. E. Schellin (1998). A Two-Fluid Navier-Stokes Solver to Simulate Water Entry. In *Proc. 22nd Symp. Naval Hydrodynamics*, Washington, D.C., pp. 638–651.

Oberhagemann, J. (2006). A Numerical Method to Assess Effects of Whipping on Global Loads of Ships. Master's thesis, Technische Universität Hamburg-Harburg, Hamburg.

Oberhagemann, J. and O. el Moctar (2007). A Simplified Approach to Investigate Fluid-Structure Coupling Effects on Slamming Loads of Ships. In *Proc. 10th Numerical Towing Tank Symposium*, Hamburg, pp. 150–155.

Oberhagemann, J., O. el Moctar, and T. E. Schellin (2008). Fluid-Structure Coupling to Assess Whipping Effects on Global Loads of a Large Container Vessel. In *Proc. 27th Symposium on Naval Hydrodynamics*, Seoul, pp. 296–314.

Oberhagemann, J., M. Krömer, C. Cabos, and O. el Moctar (2012). A Fluid-Structure Coupling Method Based on Field Methods and a Structural Mode Decomposition. In *Proc. 6th Int. Conf. on Hydroelasticity in Marine Technology*, Tokyo.

Oberhagemann, J., J. Ley, and O. el Moctar (2012). Prediction of Ship Response Statistics in Severe Sea Conditions using RANS. In *Proc. 31st Int. Conf. on Ocean, Offshore and Arctic Engineering*, Rio de Janeiro, pp. 461–468. Paper No. OMAE2012-83955.

Oberhagemann, J., J. Ley, V. Shigunov, and O. el Moctar (2012). Efficient Approaches for Ship Response Statistics using RANS. In *Proc. 22nd ISOPE Conference*, Rhodes, pp. 1133–1140.

Oberhagemann, J., V. Shigunov, and O. el Moctar (2012). Application of CFD in Long-Term Extreme Value Analyses of Wave Loads. *Ship Technology Research 59(3)*, 4–22.

Oberhagemann, J., V. Shigunov, and O. el Moctar (2013). First Order Reliability Analogies of Nonlinear Bending Moments in Ships. In *Proc. 32nd Int. Conf. on Ocean, Offshore and Arctic Engineering*, Nantes. Paper No. OMAE2013-10547.

Oberhagemann, J., V. Shigunov, M. Radon, H. Mumm, and S. I. Won (2015). Hydrodynamic Load Analysis and Ultimate Strength Check of an 18000 TEU Containership. In *Proc. 7th Int. Conf. on Hydroelasticity in Marine Technology*, Split.

Ochi, M. K. (1978). Generalization of the Rayleigh Probability Distribution and its Application. *J. Ship Research 22(4)*, 259–265.

Paik, K. J., P. M. Carrica, D. Lee, and K. Maki (2009). Strongly Coupled Fluid-Structure Interaction Method for Structural Loads on Surface Ships. *J. Ocean Engineering 36*, 1346–1357.

Pastoor, L. W. (2002). *On the Assessment of Nonlinear Ship Motions and Loads*. Ph. D. thesis, Technische Universiteit Delft, Delft.

Patankar, S. V. and D. B. Spalding (1972). A calculation procedure for heat, mass and momentum transfer in three-dimensional parabolic flows. *Int. J. Heat and Mass Transfer 15(10)*, 1787–1806.

Pierson, W. J. and L. A. Moskowitz (1964). Proposed Spectral Form for Fully Developed Wind Seas Based on the Similarity Theory of S. A. Kitaigorodskii. *J. Geophysical Research 69*, 5181–5190.

Rathje, H., A. Kahl, and T. E. Schellin (2012). High-Frequency Ship Response Assessment of Large Containerships. *Int. J. Offshore and Polar Engineering 22(2)*, 115–122.

Rice, S. O. (1944). Mathematical Analysis of Random Noise. *Bell System Technical Journal 23(4);24(1)*, 282–332;46–156.

Roache, P. J. (1997). Quantification of Uncertainty in Computational Fluid Dynamics. *Annual Review of Fluid Mechanics 29*, 123–160.

Roache, P. J. (1998). *Verification and Validation in Computational Science an Engineering*. Albuquerque: Hermosa Publishers.

Roache, P. J. (2006). Recent Developments in Verification and Validation. In *Proc. 2nd Workshop on CFD Uncertainty Analysis*, Lisbon.

Robert, M., C. Monroy, G. Reliquet, A. Drouet, A. Ducoin, P. E. Guillerm, and P. Ferrant (2015). Hydroelastic Response of a Flexible Barge Investigated with a Viscous Flow Solver. In *Proc. 7th Int. Conf. on Hydroelasticity in Marine Technology*, Split.

Rychlik, I. (1987). A New Definition of the Rainflow Counting Method. *Int. J. Fatigue 9(2)*, 119–121.

Salas, M. D. (2006). Some Observations on Grid Convergence. *J. Computers & Fluids 35(7)*, 688–692. DOI: 10.1016/j.compfluid.2006.01.003.

Sames, P. C., T. E. Schellin, S. Muzaferija, and M. Perić (1999). Application of a Two-Fluid Finite Volume Method to Ship Slamming. *J. Offshore Mechanics and Arctic Engineering 121(1)*, 47–52.

Schellin, T. E., V. Shigunov, A. Troesch, D. H. Kim, and K. Maki (2013). Prediction of Loads for Ship Structural Design. Ship Structures Symposium, ASNE Day 2013.

Seng, S. and J. J. Jensen (2012). Slamming Simulations in a Conditional Wave. In *Proc. 31st Int. Conf. on Ocean, Offshore and Arctic Engineering*, Rio de Janeiro. OMAE2012-83310.

Shigunov, V., O. el Moctar, and H. Rathje (2010). Operational Guidance for Prevention of Cargo Loss and Damage on Container Ships. *Ship Technology Research 57(1)*, 6–23.

Simonsen, C. D., J. F. Otzen, S. Joncquez, and F. Stern (2013). EFD and CFD for KCS Heaving and Pitching in Regular Head Waves. *J. Maritime Science and Technology 18*, 435–459. doi:10.1007/s00773-013-0219-0.

Society of Naval Architects and Marine Engineers (SNAME) (1950). Nomenclature for Treating the Motion of a Submerged Body Through a Fluid. *Technical and Research Bulleting 1-5*, 1–15.

Söding, H. (1975). Springing of Ships - Considerations and Computations for the Development of a Forecasting Procedure. Technical Report Publications of the Sonderforschungsbereich 98, Technical University of Hannover, Hannover.

Söding, H. (2006). Berechnungen der Schwingungen von Timoshenko-Balken, die gleichzeitig grosse Starrkörperbewegungen ausführen. unpublished.

Söding, H. (2009). Computation of Springing Transfer Functions. *J. Engineering for the Maritime Environment 223(M)*, 291–304. doi:10.1243/14750902JEME158.

Söding, H. and E. Tonguć (1986). Computing Capsizing Frequencies of Ships in a Seaway. In *Proc. 3rd Int. Conf. on Stability of Ships and Ocean Vehicles*, Gdansk, pp. 51–60.

Söding, H., A. von Graefe, O. el Moctar, and V. Shigunov (2012). Rankine Source Method for Seakeeping Predictions. In *Proc. 31st Int. Conf. on Ocean, Offshore and Arctic Engineering*, Rio de Janeiro. Paper No. OMAE2012-83450.

Storhaug, G. (2007). *Experimental Investigation of Wave Induced Vibrations and their Effect on the Fatigue Loading of Ships*. Ph. D. thesis, Norwegian University of Science and Technology, Oslo.

Storhaug, G., J. Vidic-Perunovic, F. Rüdinger, G. Holtsmark, J. B. Helmers, and X. Gu (2003). Springing / Whipping Response of a Large Ocean Going Vessel - A Comparison between Numerical Simulations an Full-Scale Measurements. In *Proc. 3rd Int. Conf. on Hydroelasticity in Marine Technology*, Oxford, pp. 117–131.

The Investigative Panel on Large Container Ship Safety, Nippon Kaiji Kyokai (ClassNK) (2014). Investigation Report on Structural Safety of Large Container Ships. `www.classnk.or.jp/hp/en/hp_news.aspx?id=1100&type=press_release&layout=1` (accessed 2014-11-14).

Tromans, P. S., A. R. Anaturk, and P. Hagemeijer (1991). A New Model for the Kinematics of Large Ocean Waves. In *Proc. 1st Int. Offshore and Polar Engineering Conference*, Edinburgh, pp. 64–71.

Weller, H. G. (2005). Pressure-Velocity Solution Algorithms for Transient Flows. Technical report, OpenCFD, Reading.

Weller, H. G. (2006). Bounded Explicit and Implicit Second-Order Schemes for Scalar Transport. Technical report, OpenCFD, Reading.

Weller, H. G. (2008). A New Approach to VOF-Based Interface Capturing Methods for Incompressible and Compressible Flow. Technical report, OpenCFD, Reading.

Wilcox, D. C. (1998). *Turbulence Modeling for CFD*. Anaheim: D W C Industries.

A Ship Particulars

Investigations cover two containerships and a RoPax ferry, see Tables A.1 and A.2 for the main particulars. Three-dimensional surface descriptions of the hull forms were available in electronic format for all ships and were the basis to generate the finite volume fluid grids.

Table A.1: Ship particulars of the containerships

		10,000 TEU	14,000 TEU
length btw. perp.	L	$321.0\,m$	$352.0\,m$
waterline breadth	$\mathbf{B}$	$48.4\,m$	$51.2\,m$
draught	$\mathbf{T}$	$15.0\,m$	$13.7\,m$
block coefficient	c_B	0.62	0.69
displacement	Δ	$143,742\,t$	$180,000\,t$
long. center of gravity	x_{CG}	$151.5\,m$	$167.6\,m$
vert. center of gravity	z_{CG}	$21.3\,m$	$25.3\,m$
radius of gyration	r_{yy}	$77.2\,m$	$88.6\,m$
experimental scale		$1/60$	–

Draught $\mathbf{T}$ refers to the actual loading condition used in the investigations, which is not the design loading condition in case of the 14,000 TEU vessel.

The RoPax ferry was studied at MARIN in model tests with a segmented model. The tests were funded through the CRS consortium. The model at scale $1/36$ consisted of five segments connected with an aluminium circular tube backbone. The bow segment was further divided above the still water line so that loads on the bow door could be measured, see Fig. A.1 (top). The mass distribution was available as lumped mass data of each segment. Stiffness properties of the backbone were given in terms of geometric properties of the alumium tube. Material properties such as density, Youngs modulus and Poisson ratio were set to standard values. Part of the test data were used in an ISSC benchmark study, International Ship Structures Committee (ISSC) (2012), Drummen and Holtmann (2014).

Table A.2: Ship particulars of the passenger ships

		RoPax	Cruise
length btw. perp.	L	$173.2\,m$	$216.8\,m$
waterline breadth	$\mathbf{B}$	$25.9\,m$	$32.2\,m$
draught	$\mathbf{T}$	$6.3\,m$	$7.2\,m$
block coefficient	c_B	0.53	0.65
displacement	Δ	$14,964\,t$	$34,087\,t$
long. center of gravity	x_{CG}	$78.3\,m$	$99.6\,m$
vert. center of gravity	z_{CG}	$12.2\,m$	$15.3\,m$
radius of gyration	r_{yy}	$45.49\,m$	$81.3\,m$
experimental scale		$1/36$	$1/50$

The 10,000 TEU containership is a generic design. Experimental data exist which were generated during the joint industry project WILS organised by Korea's Research Institute for Ships and Ocean Engineering (KRISO, former MOERI), who performed extensive model tests with a segmented ship model, Hong et al. (2012), see Fig. A.1 (bottom). The model of the hull at scale $1/60$ was equipped with a backbone manufactured as a welded steel profile. The hull form was designed for the purpose of the project, and the backbone stiffness properties were chosen to match typical fundamental hull girder natural frequencies for this type and size of ship. Strain sensing locations for sectional loads were located at five equidistant segment cuts of the model, see Table A.3. The backbone strain sensing position 3 corresponded to midship section. Hong (2009), Hong (2010), Hong (2013) provide further details of the model test specifications.

The 14,000 TEU containership is a modern design with two-island configuration. The ship was build in 2010 and is operating in the East Asia to Europe trade. Numerical investigations used a loading condition that frequently occurs during the actual ship operation, according to the loading computer logs. There is no further rational for using this loading condition, and its frequency of occurrence may alter when the vessel is operated on a different trade route. The hull girder beam model was generated based on cross sectional properties of a 3D FE model of the ship and fine-tuned to accurately replicate mode shapes and natural frequencies of the FE model two-node and 3-node vertical vibration modes.

The cruise vessel is a generic design produced for the EU project ExtremeSeas.

It was based on an earlier design by Meyer Werft, Germany. Experiments at the Spanish model test basin CEHIPAR were conducted as part of the ExtremeSeas project. The model tests used a segmented model with a dummy superstructure. The backbone of the segmented model consisted of relatively stiff steel profiles interconnected with force transducers, and was intended to represent a rigid hull girder, see Klein and Maron (2012b), Klein and Maron (2012a).

Table A.3: Strain sensing locations of the 10,000 TEU segmented model

	station 1	station 2	station 3	station 4	station 5
x/L	0.167	0.333	0.500	0.667	0.833

Figure A.1: Segmented models of the RoPax ferry (top), the 10,000 TEU containership (center) and the cruise vessel (bottom); photos courtesy MARIN, KRISO and CEHIPAR

B Angular Momentum of Flexible Bodies

Elastic deformations do not affect the momentum of a flexible body, since the total mass remains constant. However, flexibility introduces new terms in the angular momentum equation which will be discussed here.

To improve legibility, $\vec{\zeta} = \mathbf{S}\vec{r}$ and $\vec{v} = \mathbf{S}\vec{u}$ are introduced. The angular momentum of the elastic body in analogy to eq. (2.2.9) reads:

$$
\begin{aligned}
\vec{L} &= \int_B \left(\vec{\xi} \times \dot{\vec{\xi}}\right) \rho dV \\
&= \int_B \left(\left(\vec{\xi}_0 + \vec{\zeta} + \vec{v}\right) \times \left(\dot{\vec{\xi}}_0 + \frac{d(\vec{\zeta} + \vec{v})}{dt} \right) \right) \rho dV \\
&= \left(\vec{\xi}_0 \times \dot{\vec{\xi}}_0\right) \cdot \int_B \rho dV + \int_B \left(\vec{\xi}_0 \times \frac{d(\vec{\zeta} + \vec{v})}{dt} \right) \rho dV \\
&\quad + \int_B \left((\vec{\zeta} + \vec{v}) \times \frac{d(\vec{\xi}_0 + \vec{\zeta} + \vec{v})}{dt} \right) \rho dV \\
&= m\left(\vec{\xi}_0 \times \dot{\vec{\xi}}_0\right) + \underbrace{\vec{\xi}_0 \times \int_B \dot{\vec{v}} \rho dV}_{=0\,(due\,to\,eq.\ 2.2.36)} + \underbrace{\vec{\xi}_0 \times \left(\vec{\omega} \times \left(\int_B \left(\vec{\zeta} + \vec{v}\right) \rho dV \right) \right)}_{=0\,(due\,to\,eq.\ 2.2.36)} \\
&\quad \underbrace{-\dot{\vec{\xi}}_0 \times \int_B \left(\vec{\zeta} + \vec{v}\right) \rho dV}_{=0\,(due\,to\,eq.\ 2.2.36)} + \int_B \left(\left(\vec{\zeta} + \vec{v}\right) \times \dot{\vec{v}} \right) \rho dV \\
&\quad + \int_B \left(\left(\vec{\zeta} + \vec{v}\right) \times \left(\vec{\omega} \times \left(\vec{\zeta} + \vec{v}\right) \right) \right) \rho dV.
\end{aligned}
\tag{B.0.1}
$$

Removing all vanishing terms, eq. (B.0.1) reduces to:

$$\begin{aligned}\vec{L} =& m\left(\vec{\xi}_0 \times \dot{\vec{\xi}}_0\right) + \int_B \left(\left(\vec{\zeta} + \vec{v}\right) \times \dot{\vec{v}}\right) \rho dV \\ &+ \int_B \left(\left(\vec{\zeta} + \vec{v}\right) \times \left(\vec{\omega} \times \left(\vec{\zeta} + \vec{v}\right)\right)\right) \rho dV.\end{aligned} \tag{B.0.2}$$

Introducing $\vec{\varsigma} = \vec{\zeta} + \vec{v}$, the last term on the right-hand side can be transformed,

$$\begin{aligned}\int_B (\vec{\varsigma} \times (\vec{\omega} \times \vec{\varsigma}))\, \rho dV &= \int_B ((\vec{\varsigma} \times \vec{\omega}) \times \vec{\varsigma})\, \rho dV \\ &= \int_B (\vec{\omega} \cdot [\vec{\varsigma} \cdot \vec{\varsigma}] - \vec{\varsigma} \cdot [\vec{\varsigma} \cdot \vec{\omega}])\, \rho dV \\ &= \int_B \left([\vec{\varsigma} \cdot \vec{\varsigma}] \cdot \vec{\omega} - \left[\vec{\varsigma}\vec{\varsigma}^T\right] \vec{\omega}\right) \rho dV \\ &= \left(\int_B \left(\mathbf{E}\,(\vec{\varsigma} \cdot \vec{\varsigma}) - \vec{\varsigma}\vec{\varsigma}^T\right) \rho dV\right) \vec{\omega} \\ &= \mathbf{S}\left(\int_B \left(\mathbf{E}\,(\vec{x} \cdot \vec{x}) - \vec{x}\vec{x}^T\right) \rho dV\right) \mathbf{S}^T \vec{\omega} \\ &= \mathbf{S}\mathbf{I}_0' \mathbf{S}^T \vec{\omega}\end{aligned} \tag{B.0.3}$$

After rearranging the terms, the resulting equation for the angular momentum reads,

$$\vec{L} = m\left(\vec{\xi}_0 \times \dot{\vec{\xi}}_0\right) + \mathbf{S}\mathbf{I}_0' \mathbf{S}^T \vec{\omega} + \mathbf{S} \int_B \left(\vec{r} \times \dot{\vec{u}}\right) \rho dV. \tag{B.0.4}$$

This formulation resembles eq. (2.2.9). The first term on the right-hand side is the orbital angular momentum with respect to the origin of the inertial system. It only depends on the motion of the body's center of gravity, thus is independent of any elastic deformations. The second term is the intrinsic angular momentum of the body which depends on the inertia tensor. The last term of eq. (B.0.4),

finally, is the angular momentum due to deformation velocities. It gives rise to an additional constraint for the rotary state of the local coordinate system:

$$\mathbf{S} \int_B \left(\vec{x} \times \dot{\vec{u}}\right) \rho dV = \vec{0}. \tag{B.0.5}$$

Using this constraint, the calculation of the angular momentum does not require explicit inclusion of deformations or their time derivatives in the constituting equation for the angular acceleration, Hanke (2003).

Finally, the equation for $\vec{M}_0$ becomes

$$\begin{aligned} \vec{M}_0 =& \frac{d\vec{L}_0}{dt} \\ =& \vec{\omega} \times \mathbf{S}\mathbf{I}'_0\mathbf{S}^T\vec{\omega} + \mathbf{S}\dot{\mathbf{I}}'_0\mathbf{S}\vec{\omega} + \mathbf{S}\mathbf{I}'_0\mathbf{S}^T\dot{\vec{\omega}}. \end{aligned} \tag{B.0.6}$$

$\mathbf{I}'_0$ is not constant for elastic bodies. However, the relatively small deformations expected for ships cause only negligible changes of $\mathbf{I}'_0$. It is omitted to save computation time, so the implemented motion solver effectively assumes a constant mass inertia.

C Example of Dynamic Response Amplification

The following will present a closer inspection of the dynamic amplification through vibration caused by slamming impacts. Fig. C.1 (top) shows a time series of vertical accelerations at the bow taken from a longer simulation of the 10,000 TEU containership in long-crested irregular head waves of $H_S = 9.0\,m$ and $T_z = 10.1\,s$. The time series represents typical whipping excitation. It comprises three bow slamming events experienced in a group of larger waves. The first of the slamming impacts is easily identified to occur at around $t = 55\,s$ when vibration is initiated, while the time instants of the second and third impact are less obvious. A decomposition of the acceleration into a purely vibratory part and a rigid-body part, Fig. C.1 (bottom), provides more insight. The rigid-body acceleration is obtained from a reference computation for the rigid hull girder. A spike in the rigid-body acceleration is observed at around $t = 55\,s$. It reflects the acceleration caused by the slamming impact and coincides with the initiation of flexural vibrations. Similar spikes are observed at around $t = 64\,s$ and $t = 73\,s$. These correspond to the second and third impact, respectively, but do not significantly increase the level of vibration. Instead, the vibratory accelerations continuously increase after the initial impact until approximately $t = 70\,s$, then remain on a more or less constant level, and finally start to decay at around $t = 80\,s$. The continuous increase of vibration after the initial impact is caused by wave frequency hydrodynamic loads in sagging and hogging that constitute an increase of modal excitation of the fundamental two-node vibration mode.

Corresponding time series of internal loads (VBM, VSF) at different section cuts along the hull, Figs. C.2 through C.6, further illustrate the excitation of vibrations. Reactions of the rigid hull are plotted along with those of the flexible hull. Additional linear results emphasize the effect of nonlinearities which are most pronounced in the forward section cuts. The responses of the rigid ship show significant effects of slamming, particularly the vertical shear force at the foremost station. The slamming impacts cause distinct spikes of the vertical shear force at $x/L = 0.83$, with the second impact being most prominent. Such spikes are also observed in the time series of the vertical bending moment at this

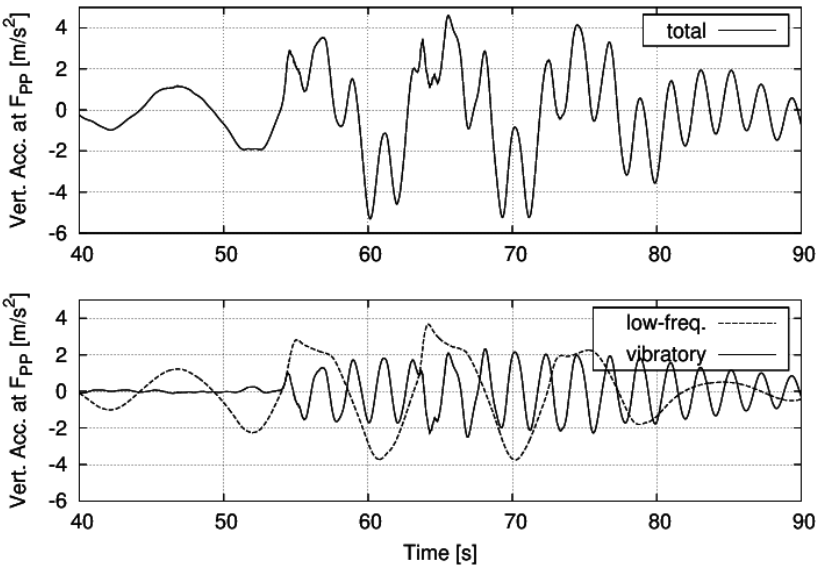

Figure C.1: Time series of vertical accelerations at the bow; total (top) and decomposed signal (bottom)

section cut, causing the nonlinear rigid-body VBM to significantly deviate from the linear VBM. The relative importance of the slamming impacts decreases for the aft section cuts, yet the spikes are clearly visible at all stations. The slamming impacts occur immediately before the maxima in sagging, hence they further contribute to the hogging / sagging asymmetry.

The time series including vibration for the foremost section cut show only a minor increase of the maxima due to vibrations, compared to the rigid-body case. Vibratory amplification becomes effective only after the impact when vibrations modulate the time signal. This relatively large influence of the slamming peak on rigid-body internal loads decreases for the aft section cuts and becomes negligible at the aftmost section cut. However, dynamic amplifications due to vibration significantly contribute to the internal loads at all section cuts and are relevant for sagging as well as hogging loads. The amplitudes of vibration are of the same magnitude as the linear and nonlinear rigid-body wave frequency

responses for all section cuts with the exception of the midship vertical shear force which is small anyway.

The hogging and sagging peaks of rigid-body vertical bending moment coincide with vibratory troughs and peaks, respectively. This means that the maxima of wave frequency excitation of the two-node bending mode are in phase with the vibratory deflections in this mode, hence the wave frequency loads contribute to vibratory excitation in addition to the impulsive loading by bow slamming impacts.

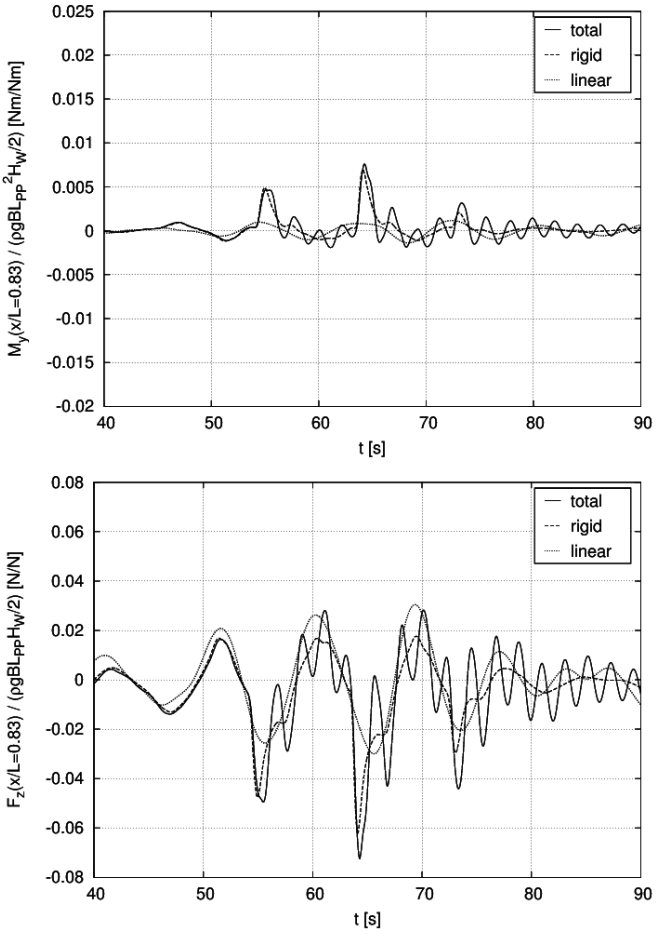

Figure C.2: Time series of VBM (top) and VSF (bottom) of rigid and flexible ship at longitudinal section cut $x/L = 0.833$

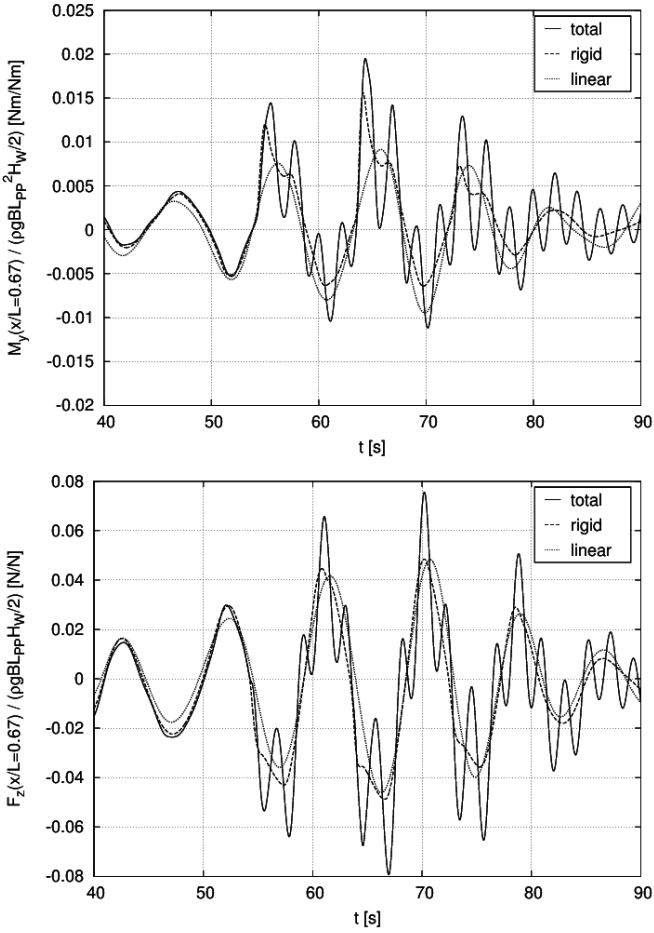

Figure C.3: Time series of VBM (top) and VSF (bottom) of rigid and flexible ship at longitudinal section cut $x/L = 0.667$

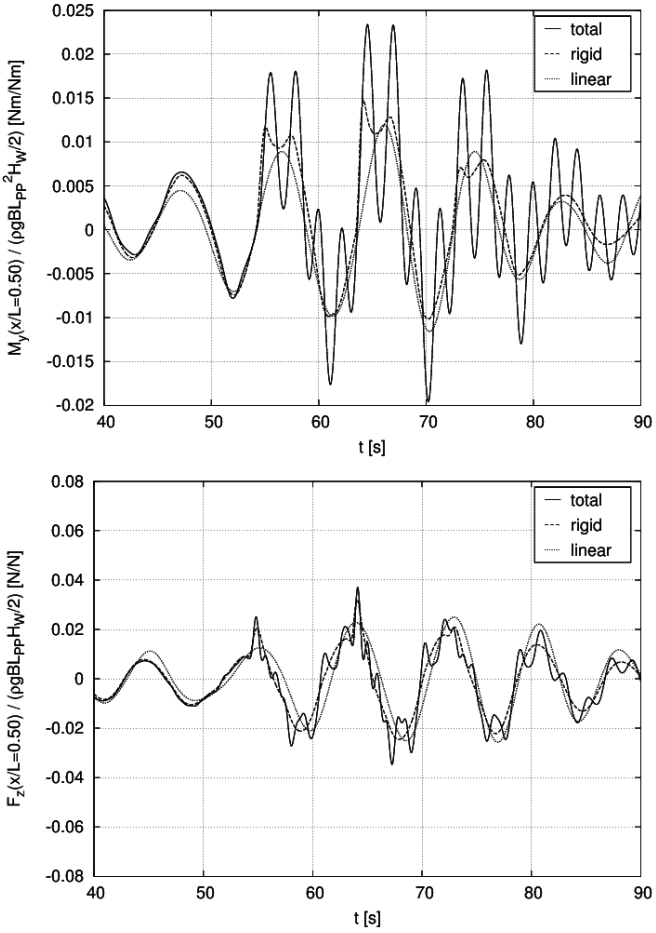

Figure C.4: Time series of VBM (top) and VSF (bottom) of rigid and flexible ship at longitudinal section cut $x/L = 0.500$

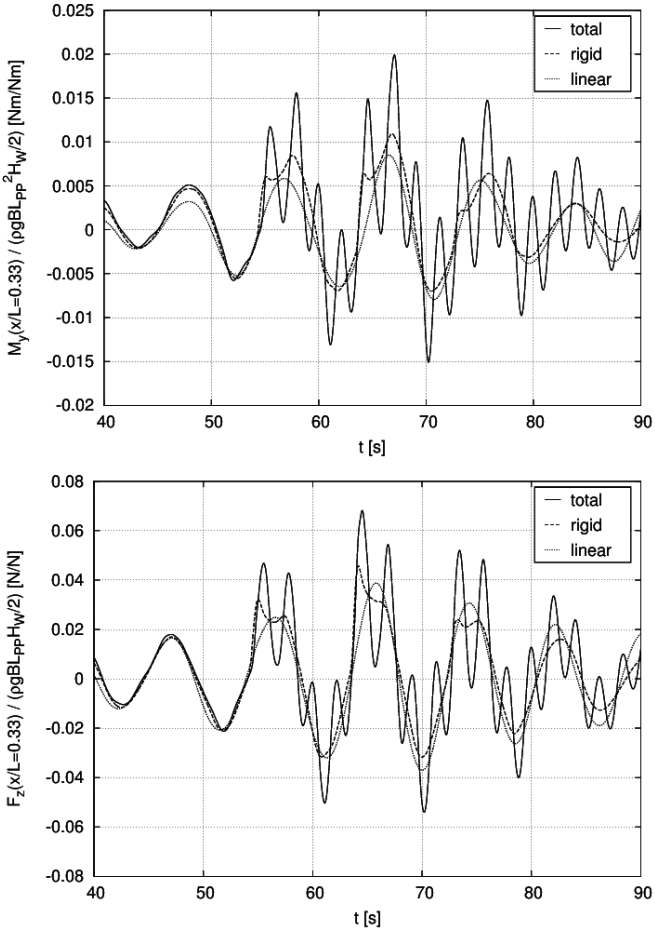

Figure C.5: Time series of VBM (top) and VSF (bottom) of rigid and flexible ship at longitudinal section cut $x/L = 0.333$

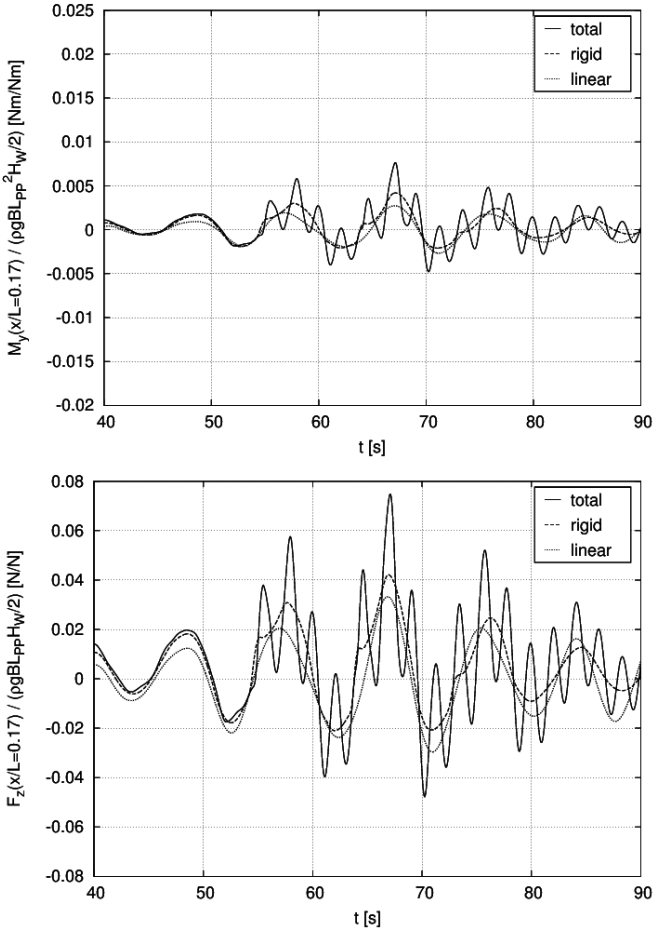

Figure C.6: Time series of VBM (top) and VSF (bottom) of rigid and flexible ship at longitudinal section cut $x/L = 0.167$

D Additional Figures

Section 5.1 exemplified the definition of LNPE as functions of the significant wave height with hogging bending moments of the 10,000 TEU containership. The very same evaluation has been performed for the sagging bending moment as well, and also for the 14,000 TEU containership. The additional evaluations did not change the findings but instead support the feasibility of converting upcrossing rates from one significant wave height to another. For the sake of completeness, all corresponding figures are given below.

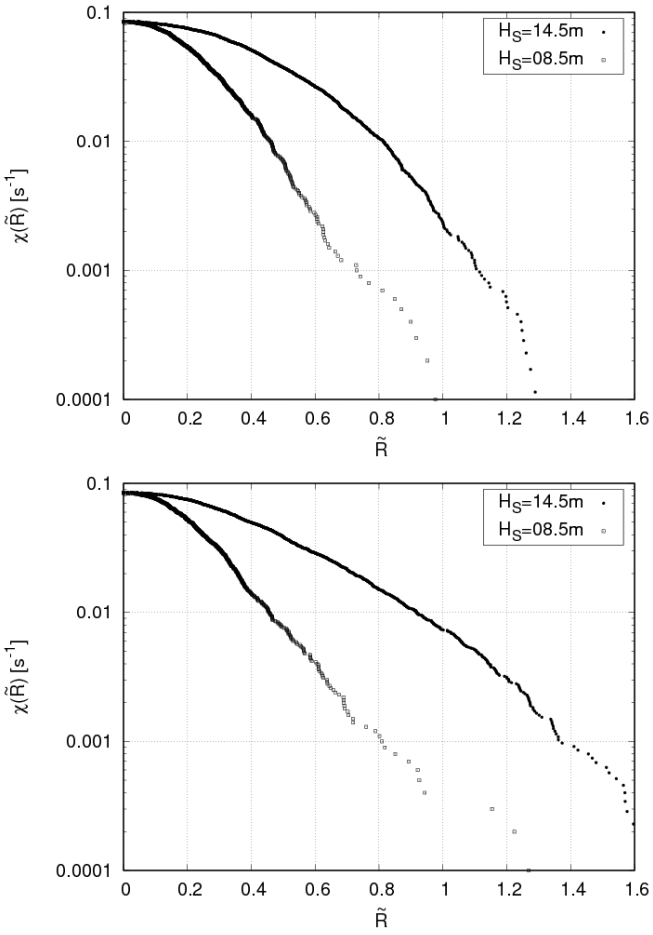

Figure D.1: Upcrossing rates of hogging (top) and sagging (bottom) VBM peaks for the 10,000 TEU containership

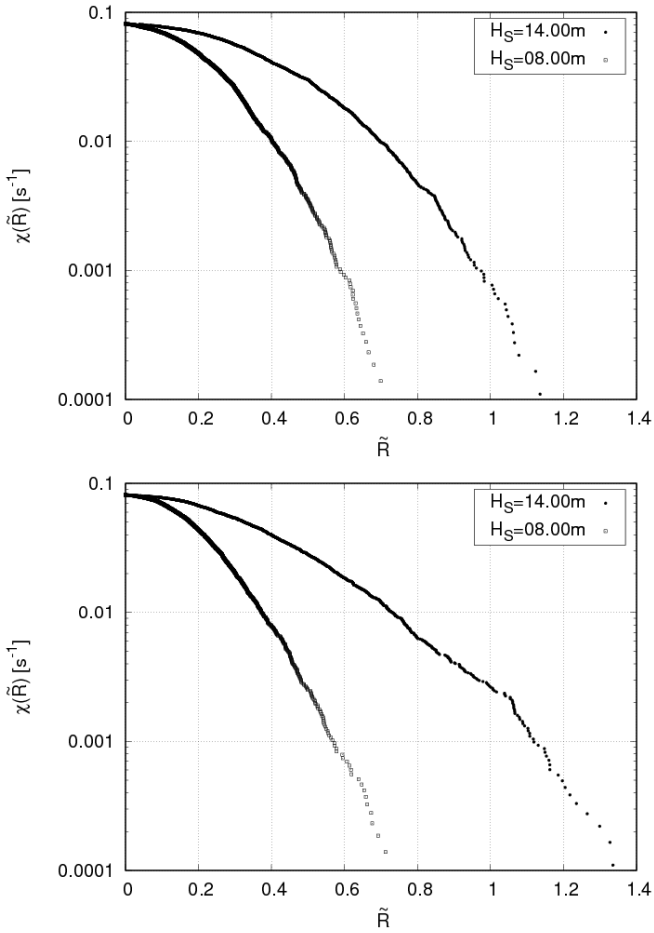

Figure D.2: Upcrossing rates of hogging (top) and sagging (bottom) VBM peaks for the 14,000 TEU containership

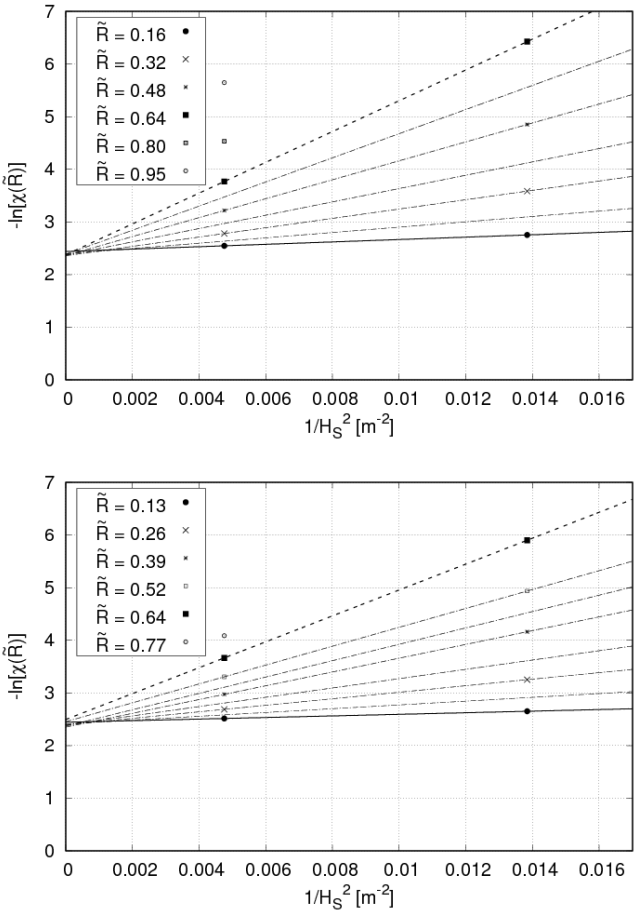

Figure D.3: $-ln\left[\chi(\tilde{R})\right]$ as a function of H_S^{-2} for selected levels of $\tilde{R}$ in hogging (top) and sagging (bottom) for the 10,000 TEU containership

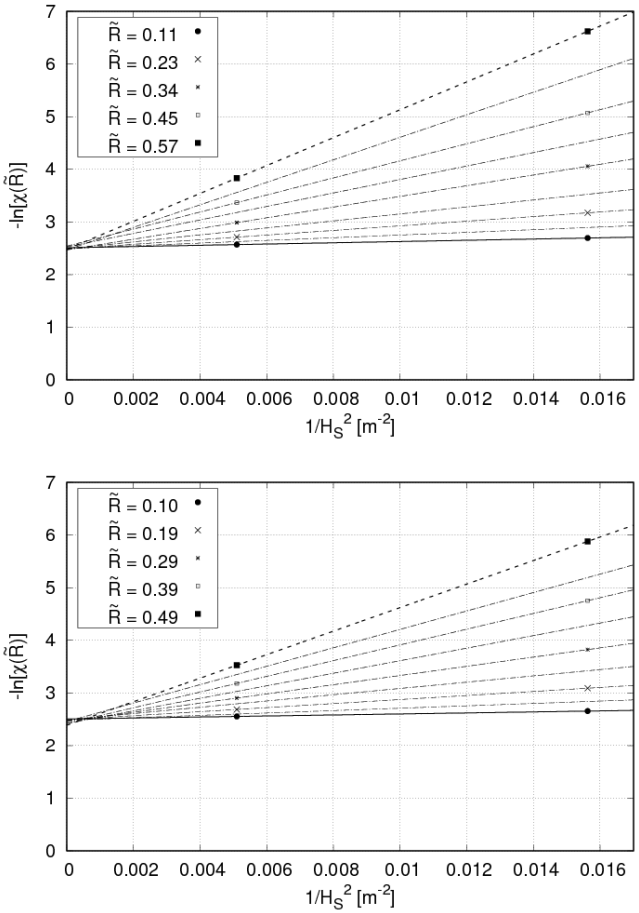

Figure D.4: $-ln\left[\chi(\tilde{R})\right]$ as a function of H_S^{-2} for selected levels of $\tilde{R}$ in hogging (top) and sagging (bottom) for the 14,000 TEU containership

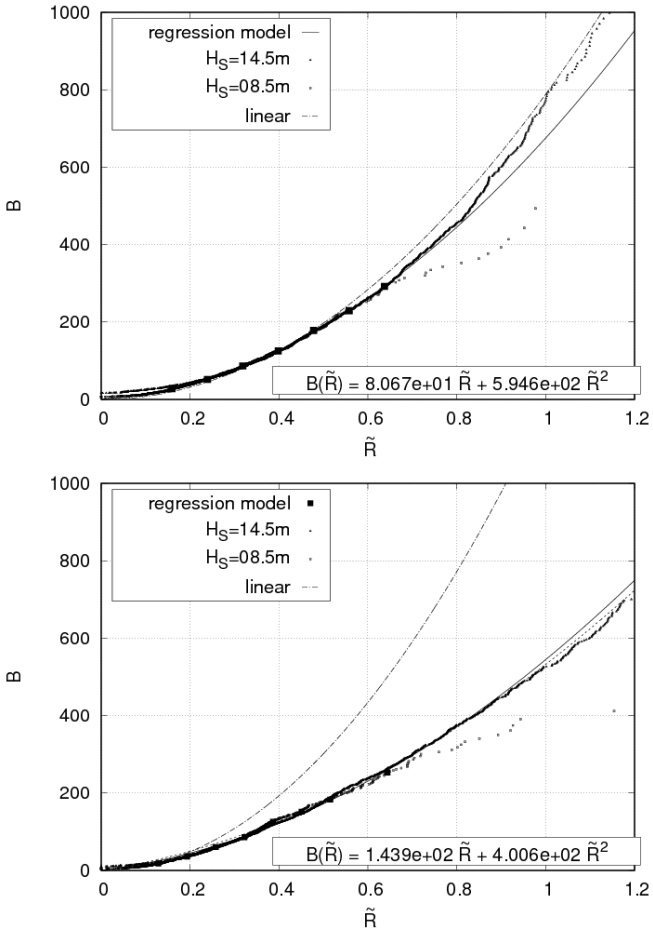

Figure D.5: $B(\tilde{R})$ resulting from regression over B_k from hogging (top) and sagging VBM peaks (bottom) for the 10,000 TEU containership

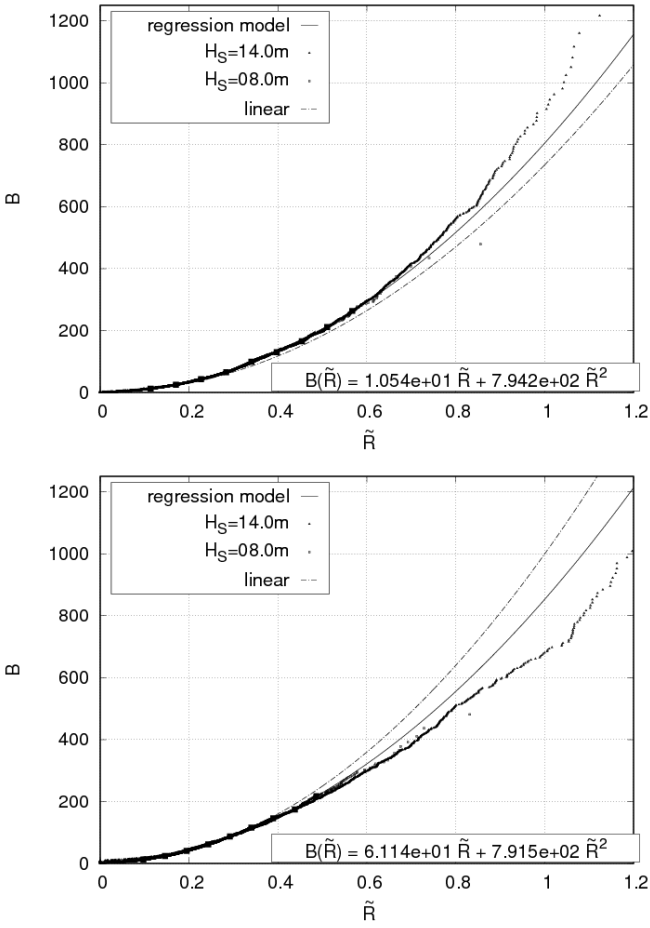

Figure D.6: $B(\tilde{R})$ resulting from regression over B_k from hogging (top) and sagging VBM peaks (bottom) for the 14,000 TEU containership

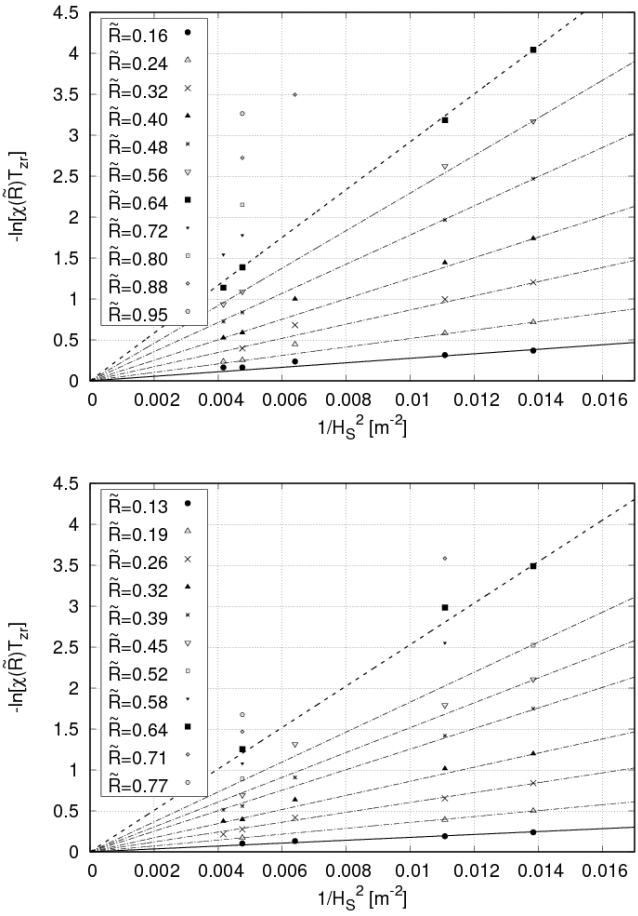

Figure D.7: LNPE of hogging (top) and sagging peaks (bottom), simulation data (symbols) and regression results (lines) for the 10,000 TEU containership

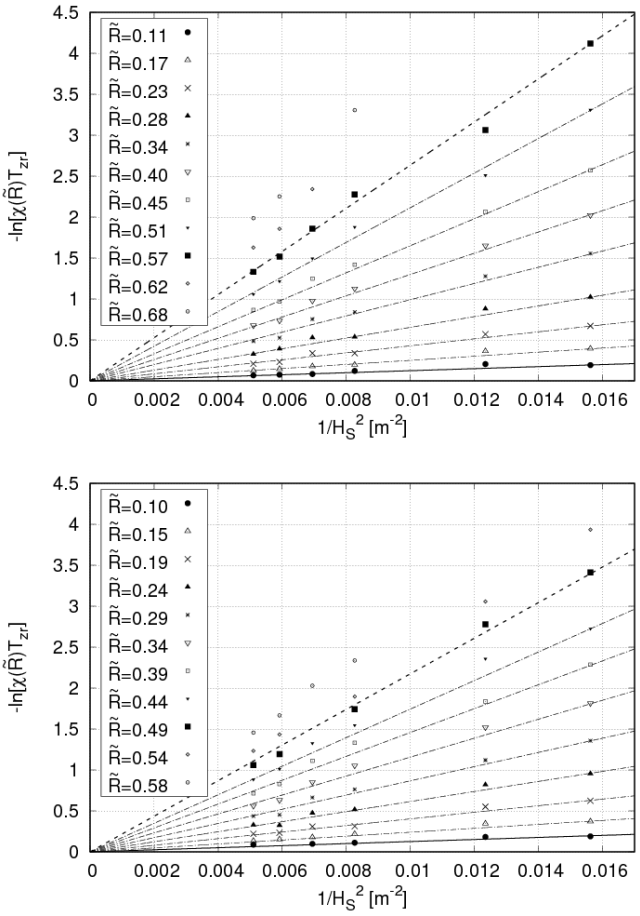

Figure D.8: LNPE of hogging (top) and sagging peaks (bottom), simulation data (symbols) and regression results (lines) for the 14,000 TEU containership

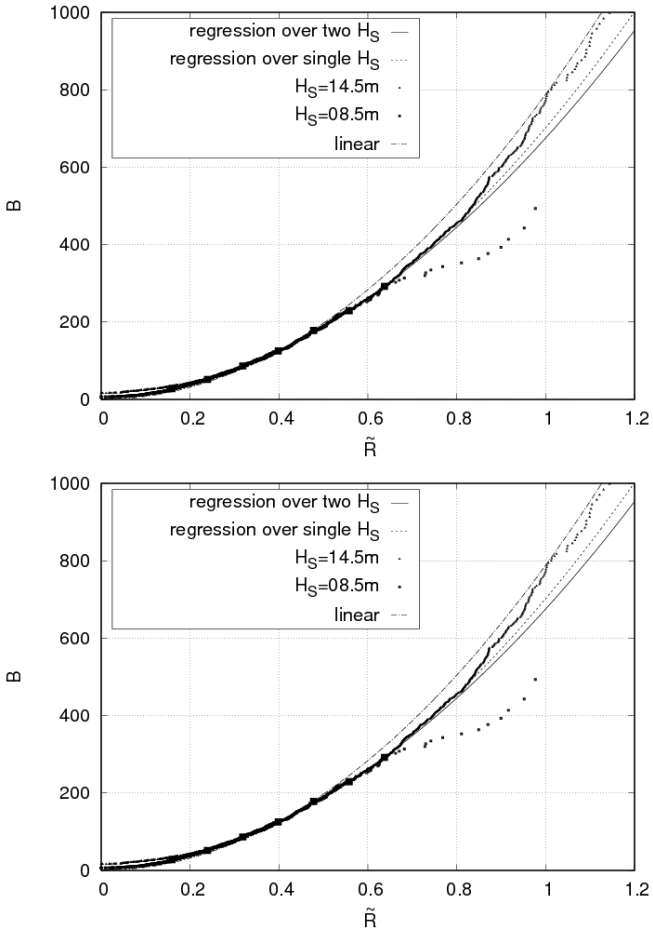

Figure D.9: $B(\tilde{R})$ from regression over B_k (solid line) versus $B(\tilde{R})$ fitted to a single simulation for the 10,000 TEU; hogging (top) and sagging (bottom); filled squares mark the data points for regression

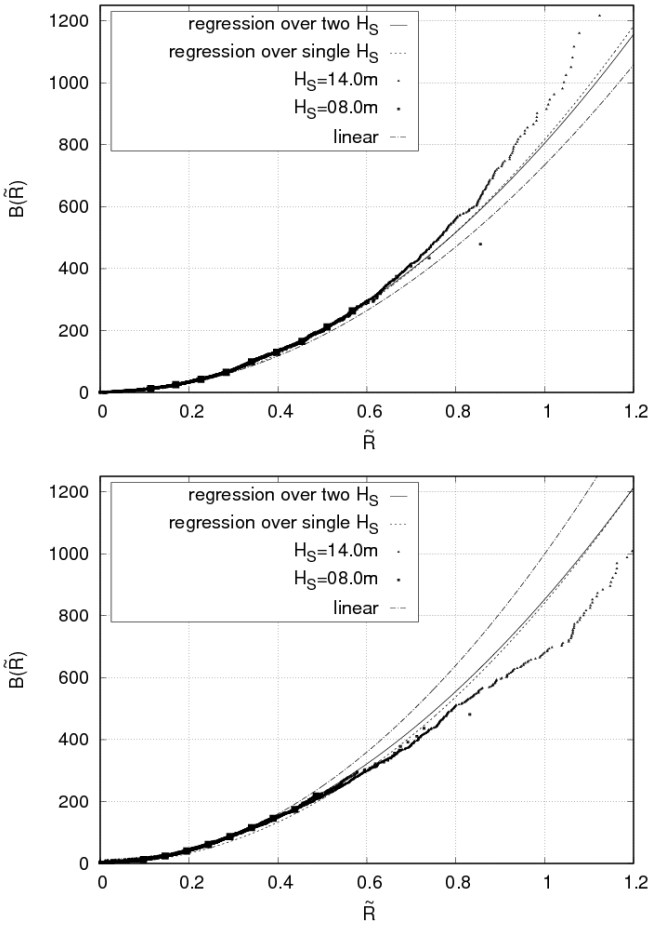

Figure D.10: $B(\tilde{R})$ from regression over B_k (solid line) versus $B(\tilde{R})$ fitted to a single simulation for the 14,000 TEU; hogging (top) and sagging (bottom); filled squares mark the data points for regression

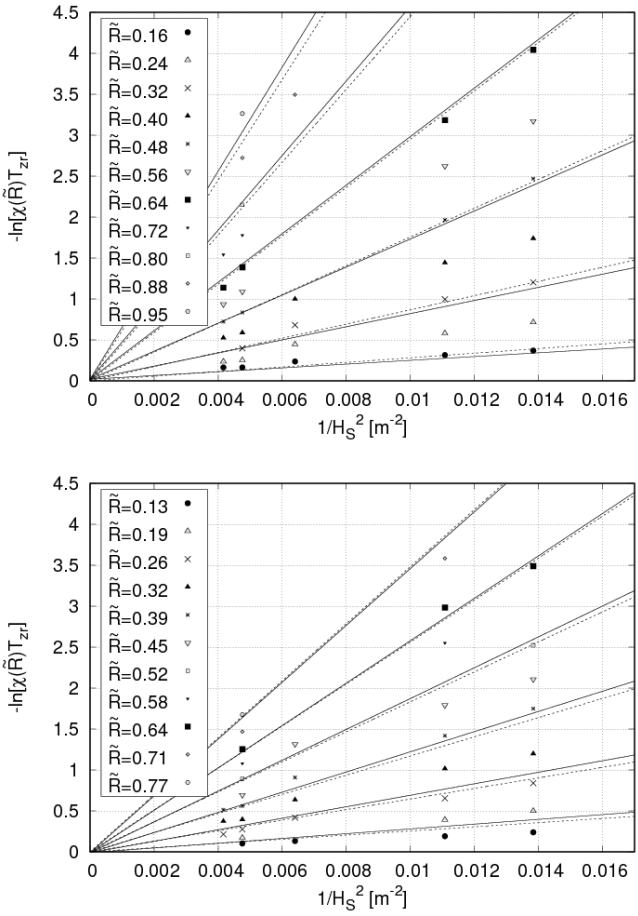

Figure D.11: LNPE of hogging (top) and sagging VBM peaks (bottom), regression results based on a single H_S (solid lines) and two H_S (dashed lines) for the 10,000 TEU containership

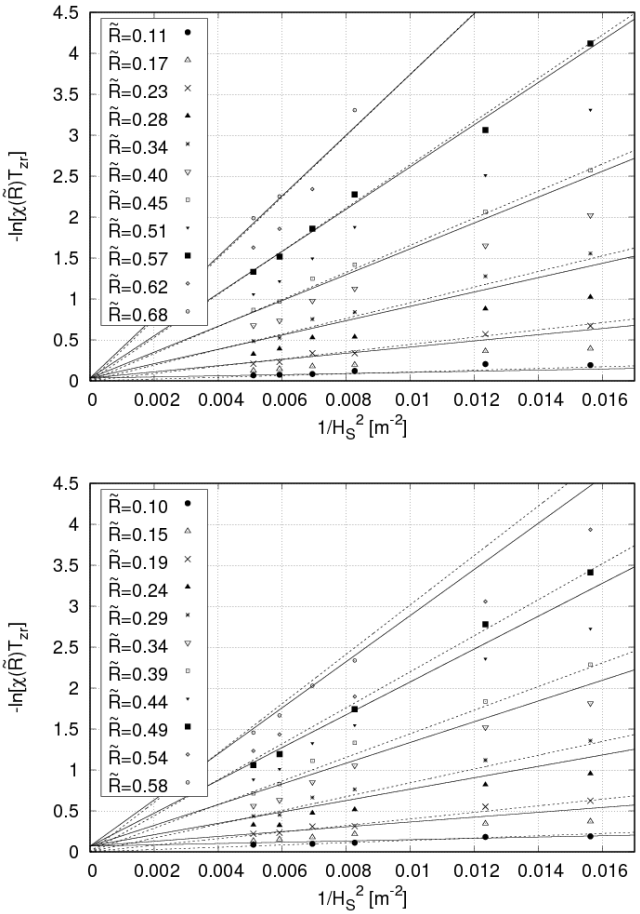

Figure D.12: LNPE of hogging (top) and sagging VBM peaks (bottom), regression results based on a single H_S (solid lines) and two H_S (dashed lines) for the 14,000 TEU containership